INVESTIGATING VISCOUS FLUID FLOW IN AN INTERNAL MIXER USING COMPUTATIONAL FLUID DYNAMICS

ALAN MARCUS HARRIES

Doctor of Philosophy

The University of Aston in Birmingham

June 2000

Thesis Summary

The University of Aston in Birmingham

INVESTIGATING VISCOUS FLUID FLOW IN AN INTERNAL MIXER USING COMPUTATIONAL FLUID DYNAMICS

Alan Marcus Harries

Doctor of Philosophy

June 2000

This thesis presents an effective methodology for the generation of a simulation which can be used to increase the understanding of viscous fluid processing equipment and aid in their development, design and optimisation. The Hampden RAPRA Torque Rheometer internal batch twin rotor mixer has been simulated with a view to establishing model accuracies, limitations, practicalities and uses. As this research progressed, via the analysis several 'snap-shot' analysis of several rotor configurations using the commercial code Polyflow, it was evident that the model was of some worth and its predictions are in good agreement with the validation experiments, however, several major restrictions were identified. These included poor element form, high man-hour requirements for the construction of each geometry and the absence of the transient term in these models. All, or at least some, of these limitations apply to the numerous attempts to model internal mixers by other researchers and it was clear that there was no generally accepted methodology to provide a practical three-dimensional model which had been adequately validated. This research, unlike others, presents a full complex three-dimensional, transient, non-isothermal, generalised non-Newtonian simulation with wall slip which overcomes these limitations using unmatched gridding and sliding mesh technology adapted from CFX codes. This method yields good element form and, since only one geometry has to be constructed to represent the entire rotor cycle, is extremely beneficial for detailed flow field analysis when used in conjunction with user defined programmes and automatic geometry parametisation (AGP), and improves accuracy for investigating equipment design and operation conditions. Model validation has been identified as an area which has been neglected by other researchers in this field, especially for time dependent geometries, and has been rigorously pursued in terms of qualitative and quantitative velocity vector analysis of the isothermal, full fill mixing of generalised non-Newtonian fluids, as well as torque comparisons, with a relatively high degree of success. This indicates that CFD models of this type can be accurate and perhaps have not been validated to this extent previously because of the inherent difficulties arising from most real processes.

Dedication

I would like to dedicate my doctorate to two wonderful people – my parents Gwyn and Betty Harries - who have always exemplified beautiful and inspirational qualities: honesty and hard work ('you reap what you sow'), tenacity ('never give in') and demonstrate each day what unconditional love, an open mind and a kind heart can achieve.

Acknowledgements

I would like to acknowledge the kind support and assistance of Dr Sotos Generalis and also my supervisor Dr M. Wilson. I would also like to thank Dr Matt Overd who is clearly an outstanding friend in every way.

Mostly, however, I would like to show my appreciation and extend my deepest love to the person who completes me – my fiancée Nicki Morris. Thank you for all your help and thank you for being mine for so long. You are a truly wonderful person and, even though I can hardly believe it is possible and just when I think my heart can not take any more, I find myself loving you more each and every day.

I am a vastly fortunate man.

List of Contents

List of Figures

List of Tables

1. Introduction

1.1 Industrial Processing of Viscous Fluids: The Need for Research

The phenomenon of laminar flow of viscous fluids occupies an integral place in many areas of process engineering. The technical and financial success of significant large-scale, multi-million dollar industries depends on the performance of the equipment used in the conveying and mixing of viscous fluids in terms of product quality and performance, and capital related issues. A diverse range of viscous processing equipment is available to achieve the desired process operation and product properties[1]. This equipment typically presents complex process conditions where mass transfer, heat transfer and chemical reactions may occur simultaneously. The complexity of the situation is intensified by the particular challenges inherent in the deviation from Newtonian behaviour of many viscous fluids.

Achievement of the appropriate degree of homogenisation may be the essential factor in systems where product performance relies greatly on the degree of mixing. Mixing, for many technologists, remains more of an art than a science with theoretical studies lagging far behind the practical experience of those involved with mixing processes in industry. A full understanding of the stress, energy exchange and mixing mechanisms that exists within the 'black box' operations that typify the design an operation of much viscous processing equipment has, as yet, not been obtained. Experimental investigation may only proceed within limits and may be overly time consuming and expensive. Mathematical modelling offers the potential for an effective, non-intrusive technique to complement experimental methods in advancing the knowledge and confidence of engineers in many important areas related to design and optimisation.

In an attempt to develop a mathematical tool to increase understanding and aid in the development, design and optimisation of viscous fluid processing equipment this research has been carried out with a view to establishing model accuracies, limitations, practicalities and uses. In order to achieve this, the area which viscous processing is perhaps most commonly associated, the polymer industry, has been chosen for investigative purposes.

Reactive processing of viscous commodity materials, for example, involves the conversion of bulk polymers into high added-value speciality products. The development of improved product

character and confirmation of the feasibility of the process is typically established in a batch process using an internal mixer, such as the Hampden RAPRA Torque Rheometer or Banbury mixer, and may then be transferred to a larger scale batch reactor or, for continuous operation for instance, to a twin screw extruder (TSE) or cavity transfer mixer (CTM). The shear and mixing characteristics, which are imposed upon the reacting medium, have a significant effect upon the progress of the reaction and upon the character of the product. When these phenomena are not fully understood the designer / engineer has little knowledge of:

- the flow, mixing patterns and shearing character
- the effect of the rheology of the fluids
- the effect of altering process variables
- optimising the design of equipment e.g. to reduce the processing time in internal mixers and hence decrease their high power consumption[2] or to prevent polymer degradation by high thermomechanical load or high stress intensity in certain systems.
- the scale up factors necessary to replicate the optimum process conditions to achieve successful scale-up or process transfer.

It is hoped that this research may lead to furthering knowledge in these areas, not only contributing to the body of work on viscous fluid flow simulation and hence aiding the designer and engineers in industry, but also, on a another level, it is hoped that the work will be beneficial in environmental terms as explained below.

Polymers and plastics are a vital part of our everyday lives and we, as a society, entrust that the products we use are non-toxic and safe as well as being engineered to give the desired flawless chemical and physical properties. A subject that has attracted much attention recently is the risk to health from additives and modifiers in bulk polymers used in the food industry. Antioxidants and UV stabilisers, in the presence of extractive media, may migrate out of a polymer in the course of its service life[3,4]. Packages and wrapping, over time, especially those in contact with oils and fats, may release quantities of these additives into our consumables adversely affecting health. In the case of prostheses, bio-incompatible additives can result in severe toxicity problems[5]. One example is the use of the possible carcinogen phthalates in soft PVC toys and teething products for babies which migrate through saliva[6]. Also the performance of polymer products will deteriorate with the loss of antioxidants and stabilisers. This is important in rubbers and plastics used in engineering components where mineral oils and synthetic fluids may reduce the life time of the object to that of the unprotected polymer[7,8]. It is clear, therefore, that the

process by which additives are incorporated in the polymer matrix and the mixing mechanism involved are of great importance. This knowledge gained from this research may lead to the development of an engineering tool which can contribute to this field of knowledge and may lead to improved understanding of mixing and additive binding and hence the production of more environmentally friendly polymers.

1.2 An Engineering Tool: Computational Fluid Dynamics (CFD)

In the last decade researchers have realised the potential of using mathematical models, in conjunction with powerful hardware, to investigate such areas as the processing of viscous fluids. *Computational Fluid Dynamics* has shown itself to be of significant technological and commercial importance by its ability to tackle successfully specific problems in a range of complex geometries and rheologies.

Computational Fluid Dynamics

Three fundamental principles govern the physical aspects of any fluid flow: the conservation of mass; Newton's second law and the conservation of energy. These fundamental principles can be expressed in terms of partial differential equations. Computational Fluid Dynamics can be thought of as the technology of acquiring a numerical solution to the governing equations of fluid flow whilst advancing the solution through temporal space to obtain a numerical description of the complete flow field of interest at any time. The governing equation for Newtonian fluid dynamics, the Navier-Stokes equation, has been known for over a century[9].

1.3 Industrial Applications of Computational Fluid Dynamics

CFD provides engineers with a tool to obtain solutions to a variety of fluid flow, heat transfer and mass transfer problems. The application of CFD has been widespread. Many CFD companies have been established and their software products are specially developed to deal with such a diverse range of problems. The CFD industry is still considered by many to be in its infancy and its various products are continuously and rapidly evolving. An excellent up to date appreciation of the continuously advancing commercial software (CFD codes and their capabilities) for some of the larger companies can be found on the world wide web, for example: Fluent Inc. (FIDAP, FDI, Polyflow)[10], AEA Technology (CFX)[11], CD Ltd. (STAR CD)[12], ICEM[13], CHAM

(Pheonics)[14], Amtec Engineering Inc. (INCA)[15], ADINA R & D (ADINA PATRAN)[16], and PolyDynamics, Inc (POLYCAD 3D)[17].

Polyflow[18], was identified as a commercial CFD package which has been engineered specifically to be used for simulating viscous fluid flow and the processing of polymeric materials (including the ability to represent viscoelasticity) and a suitable way forward for the start of this research. A comparison between Polyflow and other similar software has been recently been compiled[19].

1.4 Generic Code Overview

The combination of a generic commercial solver programme with a powerful pre-processor and post-processor package result in an exciting engineering tool with potentially vast capabilities. A brief description of a general CFD package follows:

- ***pre-processor***

  A Computer Aided Design (***CAD***) package is used to construct a precise two/three-dimensional skeleton of the complex fluid flow domain to be investigated. The post processor also incorporates a mesh generating facility to discretise the flow domain and also to analyse the grid form.

- ***solver***

  The fluid flow problem is specified by defining boundary conditions on a mesh created by the preprocessor and by setting material property data. Other parameters such as those controlling the numerical techniques used by the solver are also set. The solver will then attempt to find a solution to flow equations on each nodal point within the mesh. The many iterative calculations require the use of powerful computer hardware. The data obtained is transferred to the post-processor for analysis.

- ***post-processor***

  The post-processor package allows three-dimensional visualisation and manipulation of the data obtained from the solver. The flow field is open to investigation through parameters such as velocity vectors, shear rates, shear stresses, pressures and other variables.

Further explanation is given in chapter 5.

2. Research Strategy

2.1 Introduction

The first section has outlined the polymer industry's need for greater understanding of shear, mixing, scale up, process transfer and an insight into the effect of altering process variables and equipment design identifying CFD as a possible means to aid progress. In order to establish a strategy for this research a number of preliminary questions were posed under the main theme of "Is CFD a reasonable way forward to benefit industries involved with viscous fluid processing?". Answers to the following questions were obtained from the literature and from preliminary trials.

- Can geometrical complexities found in polymer process machinery be incorporated into the models?

  In initial trials the complex three-dimensional curved surfaces of the rotors of the Hampden RAPRA Torque Rheometer internal batch mixer have been modelled. The problem of rotating surfaces has also been overcome. This leads to the suggestion that even that most difficult of geometries can be simulated. (Details of the Hampden RAPRA Torque Rheometer computational model can be found in the main body of this report).

- What is the current state of progress in this field?

  From the literature reviewed at the beginning of this research it was clear that this area of study had generated considerable interest, however, many of the models presented use limiting approximations, such as simplified two-dimensional geometries, and adequate or widely accepted approaches to these simulations have not been adopted. The inadequacies in the simulation are reflected by the lack of serious experimental verification. Many researchers present their models without giving details of the assumptions made and of assessing the impact of these assumptions and the potential uses of their model. Chapter four, which provides a background to theoretical modelling of viscous processing equipment, contains a summary of the recent work of researchers in this area.

- What are the limitations of the CFD software?

  The well established limiting factors that could control the progress of research using CFD to investigate viscous fluid processing are listed below, although other limitations were expected to be discovered during the course of this investigation:

  1. The high CPU (central processing unit) time required for each simulation. This relates to the size and complexity of a domain and the complexity of the model.

2. The high virtual memory (swap space) and RAM requirement of a model with large densely meshed domains and complex models
3. The present capabilities of the in-house hardware and other available computing power.
4. The capabilities of the CFD package, the numerical methods and the assumption used by the simulation (see below).

2.2 The PhD Plan Flow sheet and Project Statement

In order to convey the detailed research strategy developed during the initial stages of this research in a concise and flowing manner a "PhD Plan Flow sheet" has been created presenting the following information:

- the **aims** identified for this research
- the **objectives** presented in a step by step route through the life cycle of this research
- the **process** to be modelled throughout this research and why it was selected
- the initial **problems** defined and various **solutions** posed in an attempt to overcome these problems

From the data contained within the flow sheet the project statement has been defined:

Project Statement

To create a simulation representing, as close as possible, a polymer processing situation and to assess model accuracies, practicalities, limitations and uses

The flow sheet highlights three very important aspects of this research which are described below:

2.2.1 Model Assumptions

Although theoretical modelling is advancing continuously many assumptions are still employed decreasing model accuracy significantly; in some cases more than others. It is important to identify and attempt to justify *all* assumptions and continue to develop the model to get as close to reality as possible. This will help to determine the accuracy of the model and therefore contribute to an understanding of how useful CFD can be to the viscous processing industry. Hence, an emphasis, in this research, has been given to:

- Identifying assumptions which cause the model to deviate reality

- Justifying the assumptions and providing focus on the assumptions are the most limiting in terms of model credibility
- Identifying and utilising methods to overcome these assumptions where possible and quantifying the necessary computing time (CPU time) and assessing whether the increased complexity is justified.

2.2.2 Experimental Verification of the Simulations

Verification of viscous fluid flow models of process machinery has been an issue partially avoided by past researchers. This is due to the fact that real life conditions found in process machinery are complex and comparing a theoretical model to the practical situation is particularly difficult. A prime objective of this project is experimental verification without which research in this area is of limited use. Ideally we could achieve experimental verification in terms of each of the main outputs obtained from the simulations e.g. velocity vectors / flow patterns, shear stress and rate maps, pressures and temperature profiles (should the model be non-isothermal).

2.2.3 The Application of CFD to Viscous Fluid Processing

In general, and as shown in section 4.2.2, it is fair to say that researchers publish their work on the theoretical simulation of viscous fluid processing equipment without giving enough attention to the practical uses of the numerical description of the flow domain obtained. Although the model may disclose the flow phenomena of a system, allowing the processing situation to be appreciated, research into other uses appears to be frequently neglected. This research, hopefully, may lead to answers for important questions such as can we, using a theoretical simulation, aid in:

- predicting and understanding flow patterns accurately (in conjunction with mechanical models)
- analysing the effect of changing process variables
- understanding mixing mechanisms qualitatively
- understanding mixing mechanisms quantitatively
- predicting equipment performance
- optimising process equipment
- scaling up a batch operation
- transferring a batch process to a continuous process confidently

Alan Harries

Ph.D. Plan - Flow sheet

Date: November 1997

Project Statement: To create a simulation representing, as closely as possible, a polymer processing situation and to assess model accuracies, practicalities, limitations and uses.

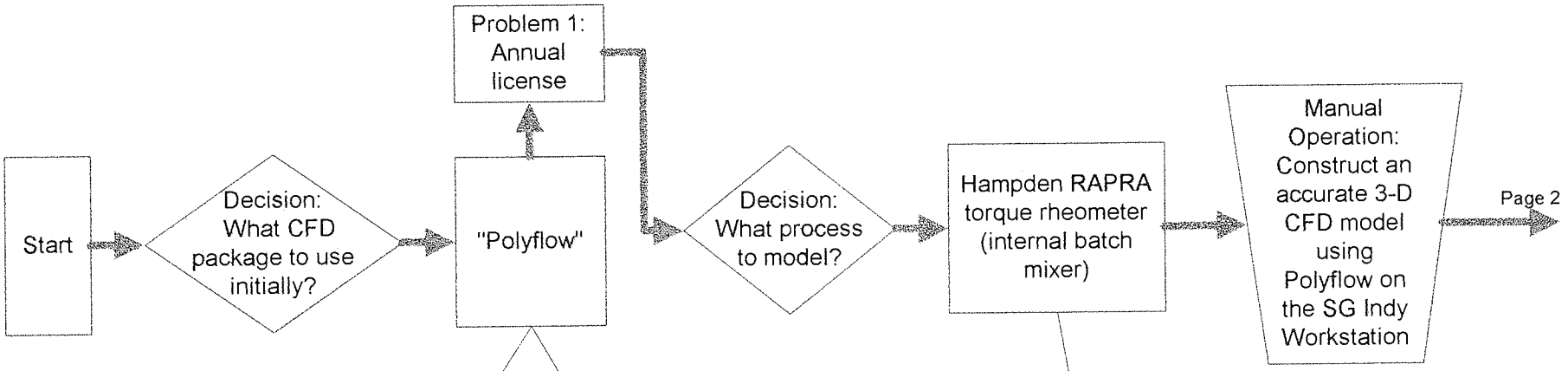

Polyflow has been identified as a CFD package specifically designed for use with polymer processing and viscoelastic fluids and has an established track record at Aston University.

Experimental verification has been achieved for example with some simple 2D models and for the complex 3D Kenics static mixer. However, for other real life processing geometries (with time dependent geometries) verification has been neglected.

Why?
1. It is a "real" processing geometry .
2. Two are owned and have been used extensively by Aston University.
3. The rotors are of a relatively simple design and the chambers are low volume.
4. It is thought that the experimental verification would be easier in this internal mixer than compared to other geometries
5. This geometry has not been investigated by others using CFD.

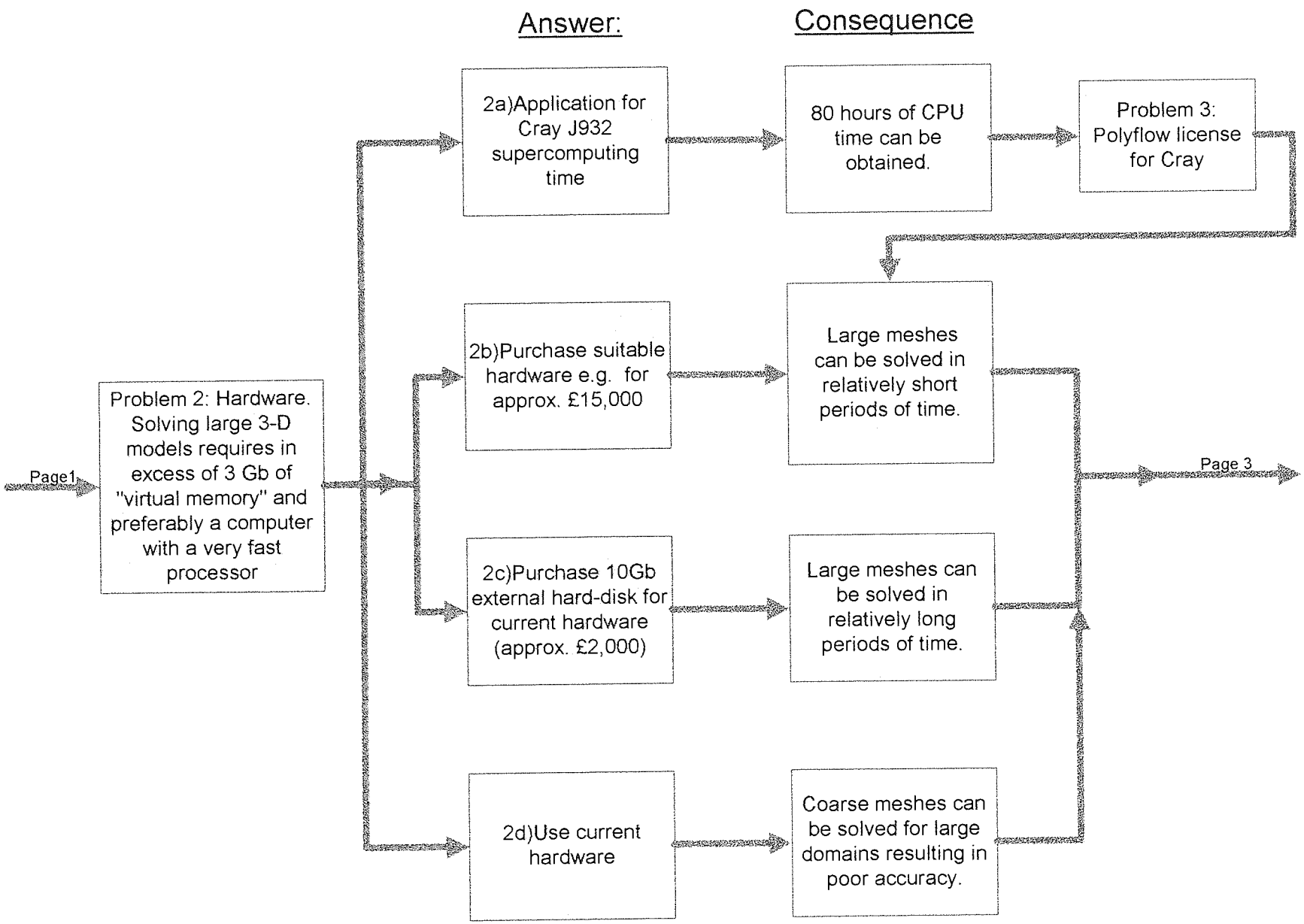
Answer:
Consequence
Page1
Problem 2: Hardware. Solving large 3-D models requires in excess of 3 Gb of "virtual memory" and preferably a computer with a very fast processor
2a)Application for Cray J932 supercomputing time
80 hours of CPU time can be obtained.
Problem 3: Polyflow license for Cray
2b)Purchase suitable hardware e.g. for approx. £15,000
Large meshes can be solved in relatively short periods of time.
2c)Purchase 10Gb external hard-disk for current hardware (approx. £2,000)
Large meshes can be solved in relatively long periods of time.
2d)Use current hardware
Coarse meshes can be solved for large domains resulting in poor accuracy.
Page 3

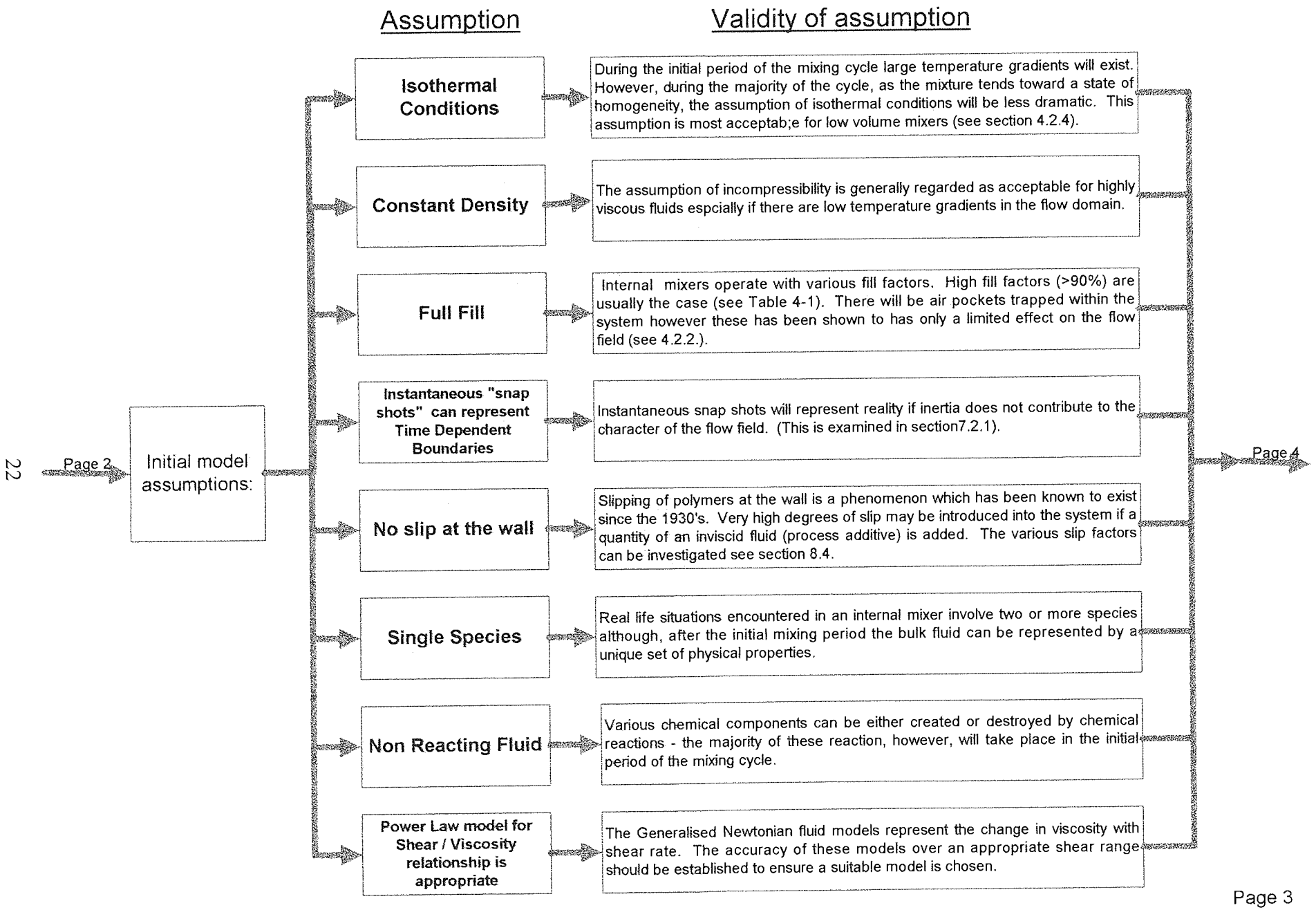
Assumption
Validity of assumption
Page 2
Initial model assumptions:
Isothermal Conditions
During the initial period of the mixing cycle large temperature gradients will exist. However, during the majority of the cycle, as the mixture tends toward a state of homogeneity, the assumption of isothermal conditions will be less dramatic. This assumption is most acceptab;e for low volume mixers (see section 4.2.4).
Constant Density
The assumption of incompressibility is generally regarded as acceptable for highly viscous fluids espcially if there are low temperature gradients in the flow domain.
Full Fill
Internal mixers operate with various fill factors. High fill factors (>90%) are usually the case (see Table 4-1). There will be air pockets trapped within the system however these has been shown to has only a limited effect on the flow field (see 4.2.2.).
Instantaneous "snap shots" can represent Time Dependent Boundaries
Instantaneous snap shots will represent reality if inertia does not contribute to the character of the flow field. (This is examined in section7.2.1).
No slip at the wall
Slipping of polymers at the wall is a phenomenon which has been known to exist since the 1930's. Very high degrees of slip may be introduced into the system if a quantity of an inviscid fluid (process additive) is added. The various slip factors can be investigated see section 8.4.
Single Species
Real life situations encountered in an internal mixer involve two or more species although, after the initial mixing period the bulk fluid can be represented by a unique set of physical properties.
Non Reacting Fluid
Various chemical components can be either created or destroyed by chemical reactions - the majority of these reaction, however, will take place in the initial period of the mixing cycle.
Power Law model for Shear / Viscosity relationship is appropriate
The Generalised Newtonian fluid models represent the change in viscosity with shear rate. The accuracy of these models over an appropriate shear range should be established to ensure a suitable model is chosen.
Page 4

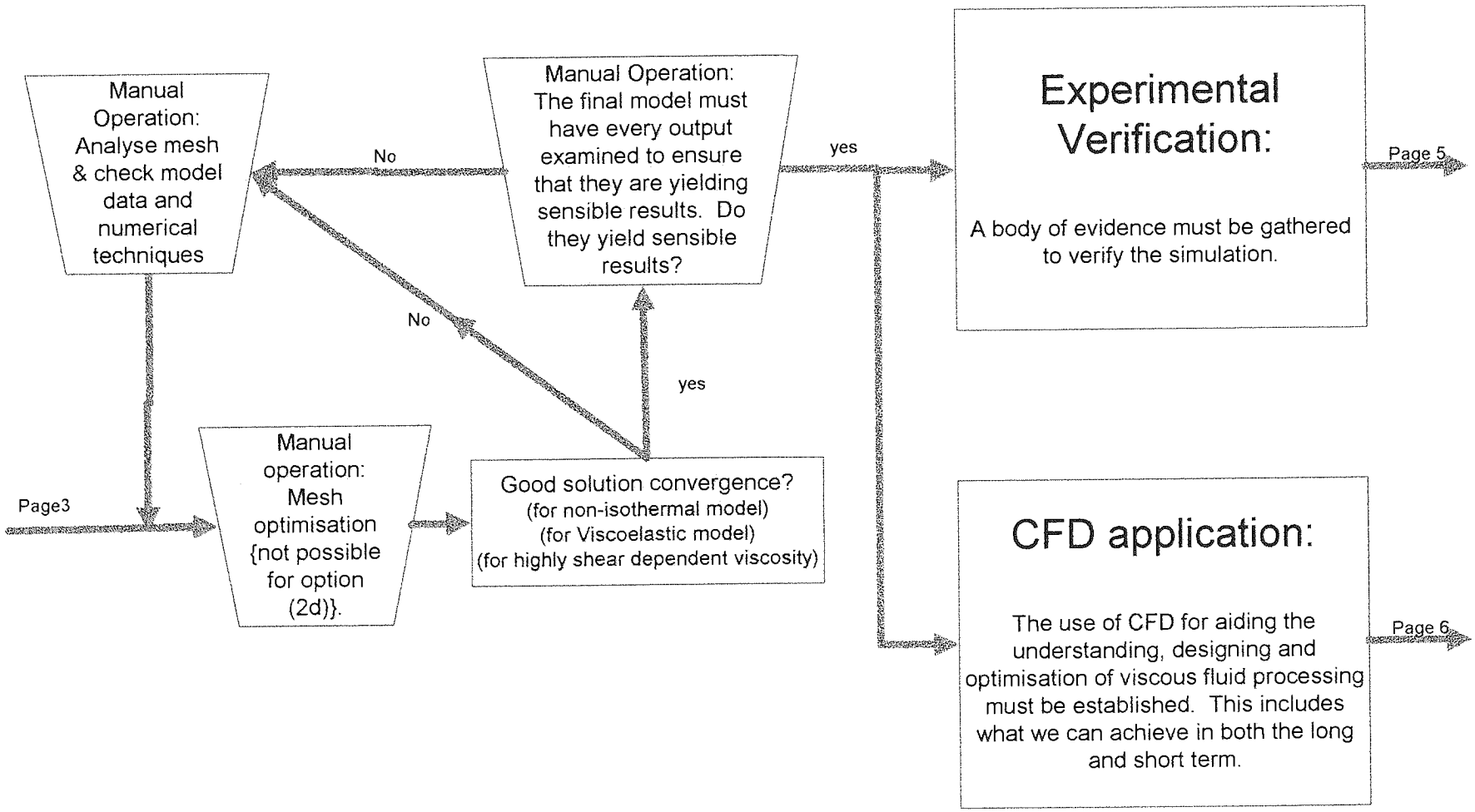
Manual Operation: Analyse mesh & check model data and numerical techniques
No
Manual Operation: The final model must have every output examined to ensure that they are yielding sensible results. Do they yield sensible results?
yes
Experimental Verification:
A body of evidence must be gathered to verify the simulation.
Page 5
No
yes
Page3
Manual operation: Mesh optimisation {not possible for option (2d)}.
Good solution convergence?
(for non-isothermal model)
(for Viscoelastic model)
(for highly shear dependent viscosity)
CFD application:
The use of CFD for aiding the understanding, designing and optimisation of viscous fluid processing must be established. This includes what we can achieve in both the long and short term.
Page 6

Experimental Verification of the Simulation

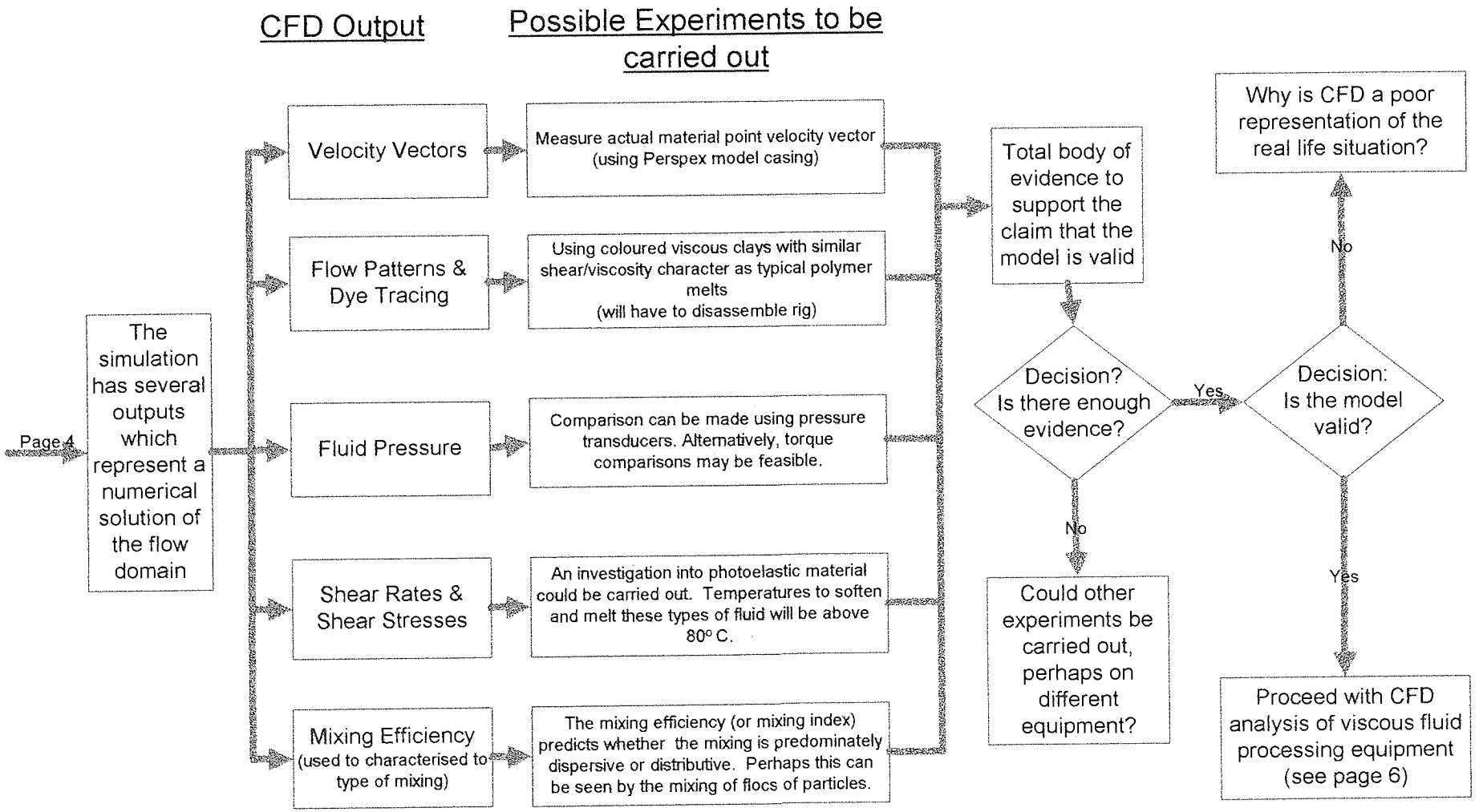

Application of CFD to aid in the investigation of Viscous Fluid Processing

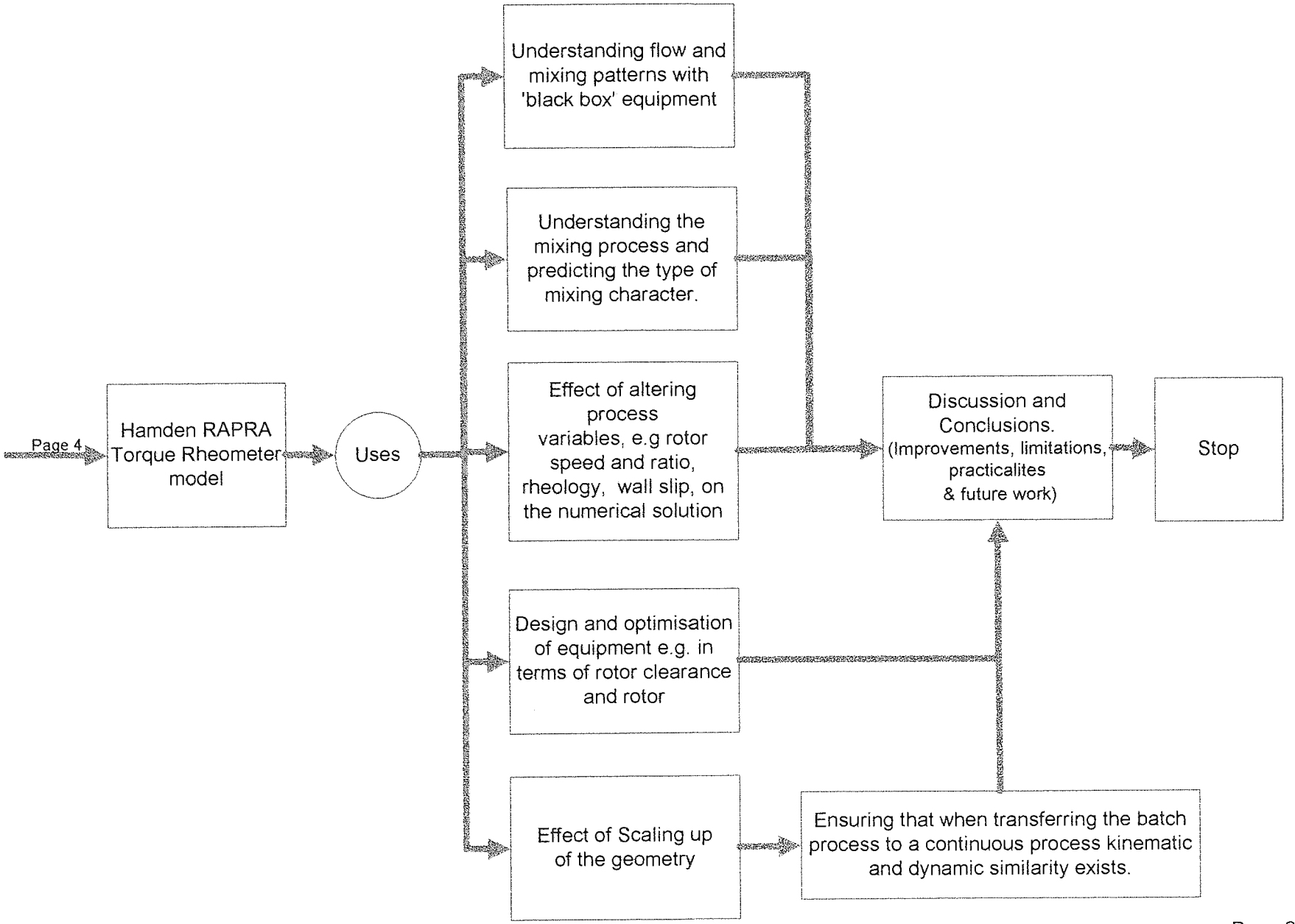

2.3 *Time Scale for Project*

Table 2-1 has been constructed to enable the reader to appreciate the time and effort devoted to each aspect of this research.

Table 2-1 ***Project Schedule Chart***

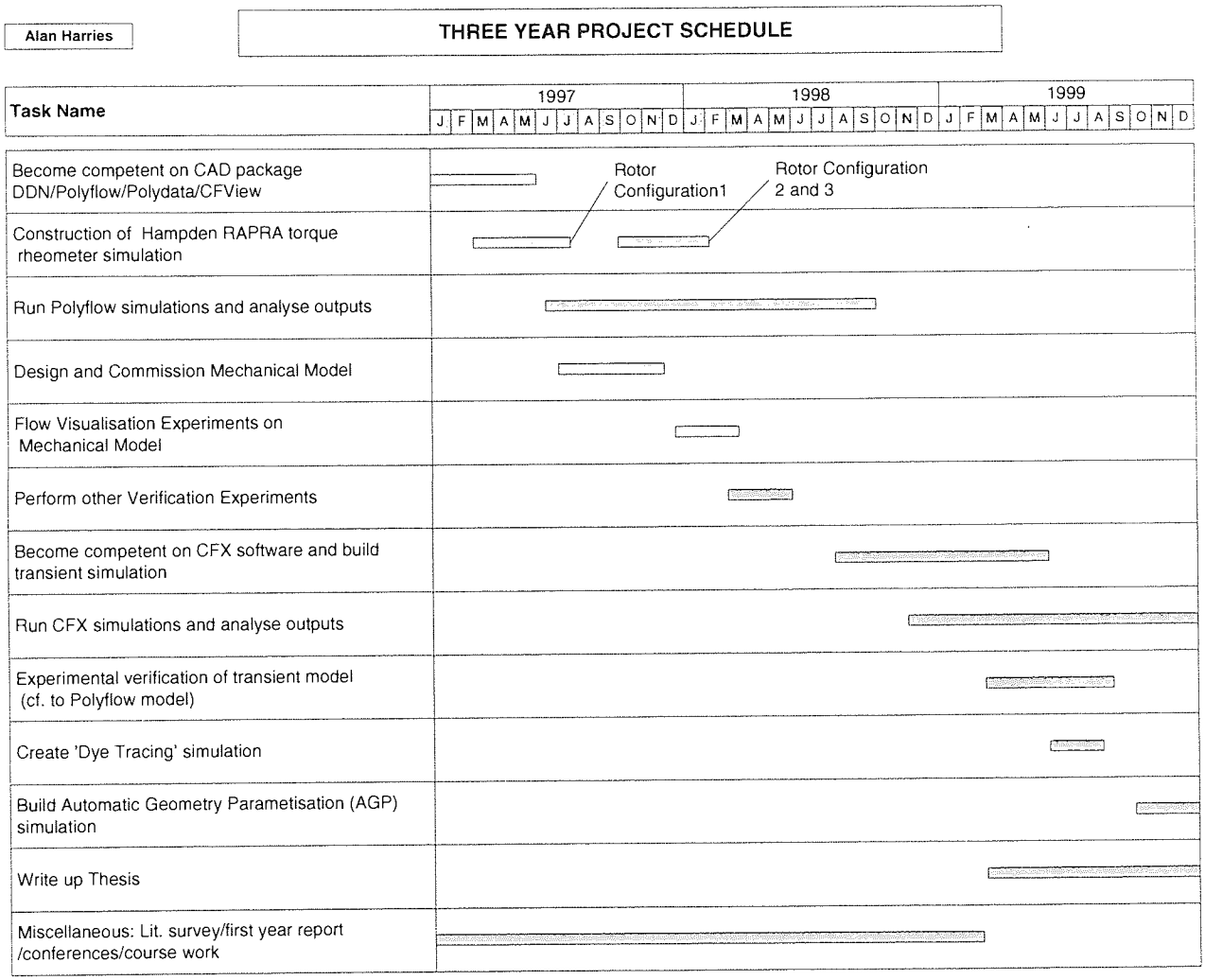

3. Rheology and Viscous Fluid Processing

3.1 Rheology

Defined generally as the study of internal stresses and strains in fluids, rheology plays an important part in many day to day chemical engineering situations. Knowledge of the fundamentals of this subject is vital if the processing of polymers is to be investigated.

Shear and elongational flow

- When (hypothetical) layers of a liquid flow over each other we have what is referred to as *shear flow*
- The shear stress (σ) is the force per unit area which produces or results from this flow
- The shear rate ($\dot{\gamma}$) is the velocity gradient normal to the flow direction

Elongational flow, or extensional flow, occurs when the velocity gradient is in the direction of the flow. The difference between shear and elongational flow may be more clearly understood if we envisage a liquid drop in each flow type; in shear flow the drop rotates deforming slightly, however, in elongational flow the drop is stretched out into along thin elongated form. Solid particles may be seen to align in the direction of flow thus minimising the resistance to shear flow but maximising the resistance in elongational flow.

Newton's law of viscosity – Defining a Newtonian fluid

- The only stress generated when a liquid flows, ignoring inertia, is the shear stress
- This shear stress is directly proportional to the shear rate (i.e. constant viscosity)
- Shear stress appears and disappears instantaneously when the flow starts or stops

The viscosity for a Newtonian fluid is hence defined by:

$$\mu = \frac{\sigma}{\dot{\gamma}} \left(= \frac{kgs^{-2}m^{-1}}{s^{-1}} = kgs^{-1}m^{-1} \right) \tag{3-1}$$

Non-Newtonian Fluids

In reality many fluids, dispersions, emulsions and especially polymers and their solutions exhibit non-Newtonian properties varying substantially from the ideal Newtonian model; this is due to stresses other than shear appearing. It is this type of fluid we shall be concentrating our efforts on

in order to construct mathematical and mechanical models that represent a *realistic* industrial process.

It is important to bear in mind that viscosity is, in reality, a function of shear rate (which in turn is a function of shear stress), temperature, time, pressure, concentration, molecular parameters such as molecular weight (and its distribution) the presence of additives (plasticisers, fillers, slip agents, mould release agents, pigments and dyes, stabilisers, products of decomposition and other impurities) and finally factors relating to processing history (orientation, residual stresses, etc.).

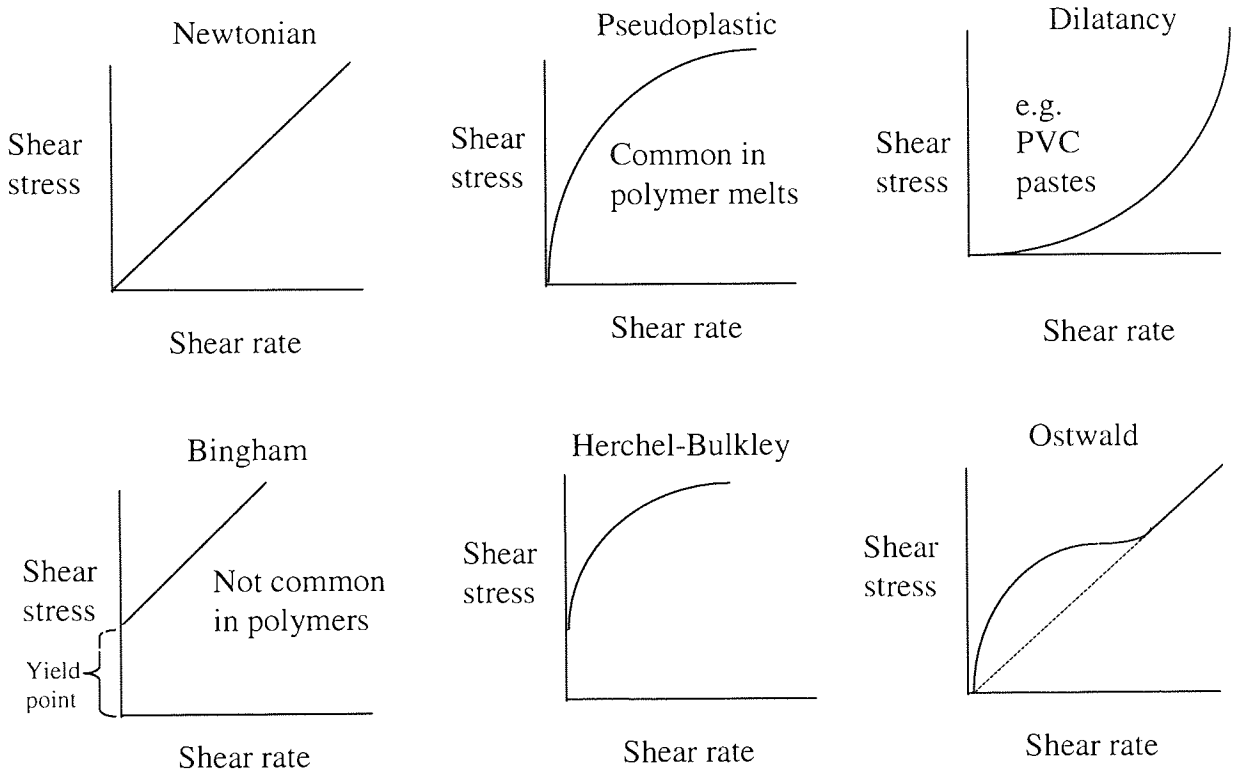

Figure 3-1 ***Shear stress against shear rate for Newtonian and common non-Newtonian fluids***

Rheology Models

Using such equipment as a Haake Viscometer we can obtain plots of shear stress against shear rate. Therefore, from equation 3-1, we can determine the viscosity at any value of shear rate. Plotting these values of viscosity against shear rate (or shear stress), on a $\log_e$ scale, usually produces curves of the form depicted by Figure 3-2 for a typical pseudoplastic material. Examining each of the three distinct regions we can make the following deductions:

1. Below a threshold of shear rate the viscosity is constant i.e. Newtonian behaviour
2. As the shear rate increases the viscosity begins to fall i.e. shear thinning

3. The curve develops into a straight line i.e. power-law model (see equation 3-3)
4. Eventually, at high enough shear rates, the viscosity begins to level out reaching a constant value.

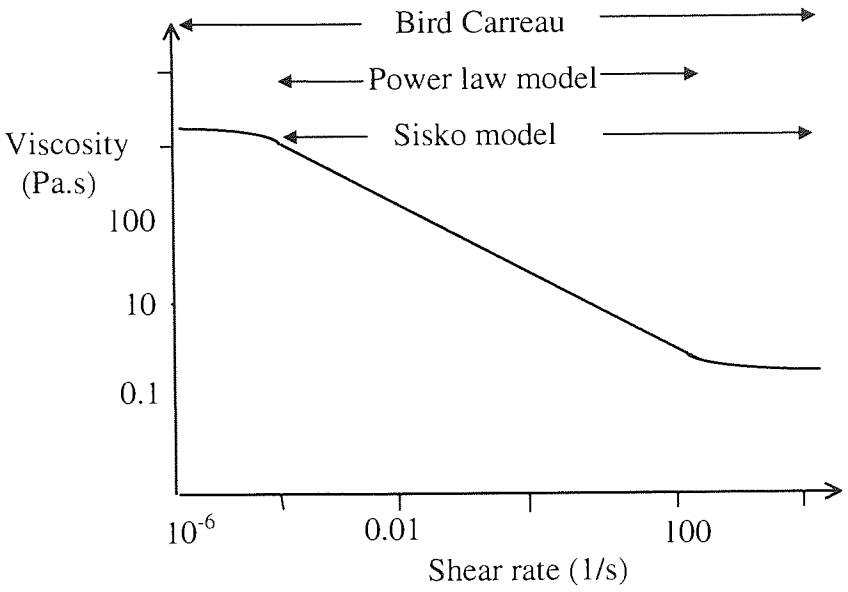

Figure 3-2 ***Viscosity against shear rate plot for a non-Newtonian pseudsoplastic liquid.***

The *Bird-Carreau model*, describing the entire plot, for non-shear thickening fluids is given by

$$\frac{\mu - \mu_\infty}{\mu_0 - \mu_\infty} = \frac{1}{1 + \left[\kappa \dot{\gamma}\right]^m} \tag{3-2}$$

Where

μ_0 = Viscosity at zero shear rate

μ_∞ = Viscosity at infinite shear rates

κ = Bird-Carreau model constant

m = Bird-Carreau model exponent

It is important to note that the value of viscosity at infinite shear rates (μ_∞) *cannot* be obtained by extrapolating, since shear thickening (dilatancy - power index greater than unity) often occurs in the high shear rate regions[20].

This equation is simplified, with some simple redefinitions, for more realistic engineering conditions, where we have high shear rates, resulting in the *Sisko model* (equation 3-3).

$$\mu = K\dot{\gamma}^{n-1} + \mu_\infty \qquad (3\text{-}3)$$

Where

1-n = m

K = μ_0 / κ^m

If the value of the shear range of interest does not extend into the regions characterised by the Newtonian plateaux then equation 3-3 reduces to the *power law model.*

$$\mu = K\dot{\gamma}^{n-1} \qquad (3\text{-}4)$$

A problem has been identified by Blair[21,22] which should be noted. Shear stress and shear rates have fixed dimensions, however, a change in dimension seems to be implied in the power law equation for all values of n other than unity. This is overcome by the assumption that K has compensating dimensions i.e. $M\,L^{-1}\,T^{n-1}$. Caution should be exercised when comparing evolution curves and other flow characteristics with values of K for fluids with different values of n. Numerically K is the value of the apparent viscosity (or shear stress) at unit shear rate and this numerical value will depend on the units used e.g. the value of K at a shear rate value of $1s^{-1}$ will be different from that of a shear rate of $1h^{-1}$.

It is important to remember that the behaviour of structured liquids, such as polymers, cannot always be adequately described by the power law model at the higher shear rates; in which case the Sisko model is preferable. Typical shear rate values present in polymer extrusion and processing are quoted[23] to be in the range of 10^0-$10^2 s^{-1}$ which indicates that the power law model may be appropriate for theoretical simulations (this is investigated later).

When increased shear rates lead to an increased viscosity or shear thickening the power law gradient in Figure 3-2 becomes positive and the phenomenon is termed dilatancy.

A *yield stress* may be encountered at low shear rates. As the shear rate falls towards some critical value, i.e. the yield stress, the viscosity may increases asymptotically to infinity. To account for the phenomenon of yield stress for a Newtonian fluid the *Bingham model*, as shown by equation 3-5, can be used.

$$\mu = \frac{\sigma_y}{\dot{\gamma}} + \mu_n \tag{3-5}$$

Where

σ_y = yield stress

μ_n = Newtonian viscosity

The Herchel-Bulkley model is a combination of the power law and Bingham models and describes non-Newtonian flow after a yield stress is exceeded.

$$\mu = \frac{\sigma_y}{\dot{\gamma}} + K\dot{\gamma}^{n-1} \tag{3-6}$$

There are exceptions to these general behaviours for instances when time dependency comes into play. For example, when stirring some paints, at a constant shear rate, we may notice a decrease in viscosity which is retained for a period of time after stirring has stopped. This is known as *thixotropy*. The opposite, when an increase viscosity is retained for a period of time, is *Rheopexy*.

Viscoelastic Fluids

A true fluid flows when subjected to a shear field and the motion ceases as soon as the stress is removed. In contrast, an ideal Hookean solid, subjected to a stress, returns to its original state as soon as the stress is removed. Materials exhibiting viscoelastic characteristics have some of the properties of both a solid and a liquid. Most polymer melts, solutions of high molecular weight and other fluids such as showergels and shampoos are viscoelastic, possessing the elastic response associated with solids. Since viscoelasticity is of primary importance when dealing with polymers it is this type of fluid which, ideally, should be modeled when representing a "real life" polymer processing situation. It should be noted, however, that although Polyflow, unlike many other commercial packages, has the capability to model viscoelasticity, the computational power required is great. Viscoelastic fluids are split into two categories, linear and non linear (steady state) viscoelasticity.

Linear elasticity

This is a measure of the elastic response at low stress where the fluids do not experience a change in their microstructure. Doubling the stress in the linear category does indeed double the strain. The concept of microstructure change is brought clearer into our minds if we think of an initially random polymer matrix being altered producing "layers" aligned with the direction of shear or

elongational flow (high rates of shearing can lead to "clump" formation resulting in shear thickening).

Sinusoidally varying stress (or strain) is resolved into two components, namely, a liquid and solid component. They are characterised by assigning *loss and storage moduli.* These moduli are functions of the applied mechanical excitation. The *creep modulus* monitors the response to a step change in stress and is equal to the resulting time-dependent strain divided by the applied stress. Other moduli do exist, defining stress build up and decay but loss, storage and creep are the most commonly used when the liquid microstructure does not change.

Non-linear elasticity

Non linear elasticity can be found in most viscoelastic processing situations, where high stresses are involved, resulting in a change in the fluid's microstructure. These changes are usually reversible when the polymer is no longer experiencing the stresses. The *first normal-stress difference* (N_1) is the most quoted parameter when dealing with viscoelasticity in steady state flow. The example most commonly used to illustrate this phenomenon is the *Weissenburg effect*[24] where a vertical rotating rod, partially immersed in a very viscoelastic liquid, is seen to have liquid climbing up its shaft. Die swell is another classic example, and indeed problem, as seen in the polymer extruder industry. Other manifestations include vortex enhancement in contraction flow, recoil in swirling flow and drag reduction in turbulent flow[25].

Viscoelastic liquids have a high resistance to stretching, their elongational viscosity is always much greater than three times the shear viscosity, and consequently they are quite ductile. This principle allows the manufacture of man-made-fibres.

Viscoelastic fluids are modelled using the same theory outlined above, however, tensor descriptions (or at least vectors) replace the simple algebraic terms. The equations used to reperesent viscoelastic materials are presented in Chapter 6. A comprehensive discussion on this subject (beyond the scope of this work) and the associated theory is given by Bird, Armstrong and Hassenger[26].

3.2 Theory of Mixing in Viscous Systems

Mixing is one of the most common operations carried out in the chemical processing industry. The reduction in the degree of non-uniformity, or gradient of a property in a system such as concentration, viscosity, temperature and so on, are all achieved by mixing. Moving material from one region to another not only results in an improved degree of homogeneity but greater heat and mass transfer coefficients, often where a system undergoes a chemical reaction. Good and efficient mixing is vital to the processing industry. The BHR group have recently gone as far as to say that current mixing practices found in process plants throughout the western world need a radical overall if enhanced production efficiencies and environmental improvements are to be made ensuring complete reactions between different substances and reducing wastes and emissions [27].

In general, mixing is characterised as two separate regimes:

1. ***Turbulent mixing***

   This is the reduction of scale of segregation (see below) depending on random turbulent motion.

2. ***Laminar mixing***

   This is the reduction of scale of segregation or striation thickness by laminar flow deformation i.e. cutting, folding, shearing or stretching. *Striation Thickness* is the average distance between adjacent interfaces of materials to be mixed by a laminar mechanism. It is laminar mixing which we are concerned with in this project.

Mixing Equipment in the Polymer Industry

Products from polymeric materials (plastics and rubber) are not only produced in a certain shape but at a suitable degree of homogeneity in composition and properties. Common machinery used to accomplish this can be put into two categories:

1. Batch Mixers

Since the first Banbury type internal batch mixers were developed in the 1920's the internal mixer has seen various modifications in design, however, the basic principle remains unchanged. To increase productivity, to combat ever increasing energy costs and to improve mixing (hence product quality) the rotor design, rotor speed and cooling capacity have been improved as well as mechanical changes. At present the application of this processing device extends from small-scale laboratory (Hampden RAPRA Torque Rheometer - see Figure 3-3) and

pilot plant scale testing and development work to large scale commercial use in the polymer and rubber industries (Banbury type). Examples of these large-scale industries include the manufacturing plastics such as of polyvinylchloride (PVC), acrylonitrile-butadiene-styrene (ABS) and polyolefin carbon black masterbatches and the processing of rubbers. Large-scale internal mixers are particularly suitable to processes that involve mixing sticky and blocky materials. Their advantages over continuous processes stem from the fact that they are not restricted by the size and shape of the material to be mixed (rubbers are uneconomical to powderise) and the mixing time and procedure for material can be selected freely[28]. Large-scale mixers used in the tyre industry have a capacity of between 240-620 litres and in the technical rubber sector the batch volume is usually around 50 - 200 litres. Recently the use of internal mixers has received a fresh impetus with the production of highly filled thermoplastic compounds and the reprocessing of secondary polymer materials[29]. *White* gives an excellent review of the development of the internal mixer[30].

The design of the rotors significantly affects plastication and mixing[31] and the four-winged rotor was created resulting in higher productivity but poor distributive mixing when compared to its standard two wing counter part. Intermeshing rotor and variable clearance internal mixer have more recently been developed which give arise to additional nipping and shearing between the rotors. These are used for the softer more technical rubbers. The rotors in non-intermeshing mixers usually rotate at different speeds (frictional), however, the intermeshing mixer has an inherent limitation which confines the operation to synchronous rotation. Although it has been postulated that this operation, where by the blades rotate at the same speed, will give rise to equal shearing character in each chamber material transfer between the two chambers may be affected.

2. Continuous Mixers

Continuous mixing machines have been developed during the past 40 years, due to the rapidly increasing scale of production of thermoplastics (particularly PVC and polyethylene) around the middle of the century. An extremely wide variety of sizes and shapes now exist[32]. Continuous mixers can be either static or dynamic. Static mixers rely on the motion of the fluid via a series of channels or pathways to achieve mixing. Examples include the Kenics, which is based on simple shear for stretching, cutting and stacking, the Multiflux, which rely on acceleration and deceleration between trapezoidal blocks for stretching, cutting and stacking and the Ross (ISG) which utilises several small intertwined tubes[33]. Dynamic mixers, although less energy efficient than the static mixers, provide good stretching, folding and reorientation.

These devices have many varied applications including the generation of large interfaces enhancing reaction between phases and the dispersion of additives increasing homogenisation. Examples include extruders, cavity transfer mixers and continuous flow stirred tank reactors (CFSTR).

Mixing technology has progressed far in advance of its associated theory. However, with the onset of researchers exploring the flow field found in mixing situations, with the aid of CFD and high powered computer hardware, theoretical studies are progressing steadily.

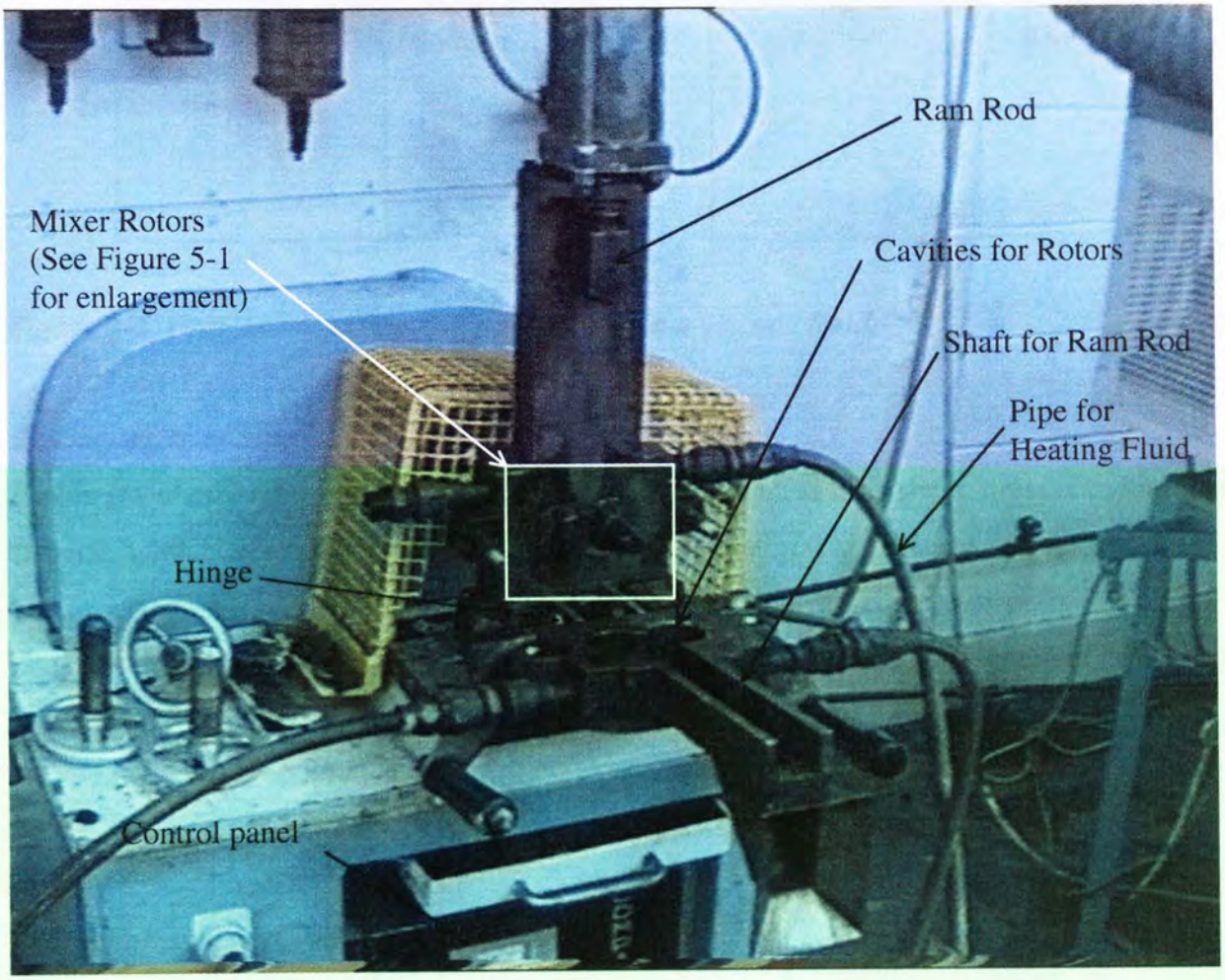

Figure 3-3 ***The Hampden RAPRA Torque Rheometer internal batch mixer, owned by Aston University, in its open position.***

Figure 5-1a is an enlargement of the "boxed" rotors.

Mixing Analysis

Two separate mixing actions are available for analysis.

1. Distributive mixing

This is frequently referred to as extensive mixing and involves spatial distribution of a component or floc of particles without altering their size or form significantly as depicted in Figure 3-4. This is achieved by interruption of streamlines.

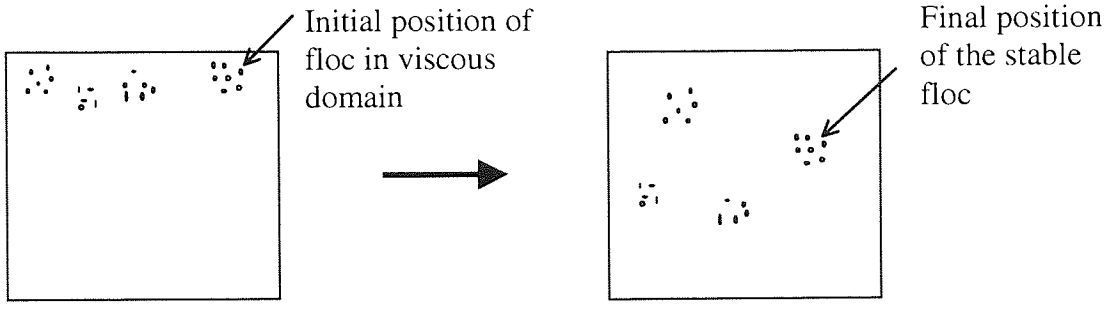

Figure 3-4 ***Distributive mixing of particulates in a viscous fluid.***

2. Dispersive mixing

This is frequently referred to as intensive mixing and requires high shear stresses to "intimately" disperse a component or floc of particles into the bulk material as depicted by Figure 3-5.

The hypothetical layers in the continuous phase have a sufficient velocity gradient between them to break down conglomerates resulting in a "spreading action".

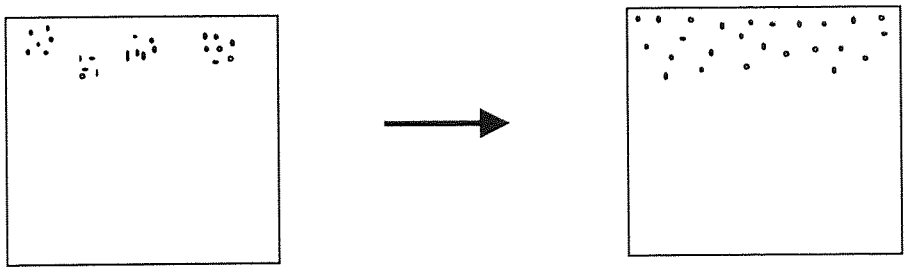

Figure 3-5 ***Dispersive mixing of particulates in a viscous fluid.***

An uneven work distribution leads to uneven dispersion, so it is highly desirable that the work distribution should be as uniform as possible.

Perfect Mixing

Mixing in general processing situations combines both distributive and dispersive mixing to various degrees. If we take the example of different mixing elements in a twin screw extruder train we discover that the staggered *mixing discs* region, with their chopping apertures, exhibit an overall distributive mixing characteristic. However, the *kneading block* region, with its high shear generating "smearing" action, exhibits an overall dispersive mixing characteristic. Thus, a combination of the two mixing mechanisms, for the required amount of time, will result in good overall mixing. Particulate mixing, however, can never reach "perfect mixing"; no amount of mixing will lead to the formation of a uniform mosaic. This ideal goal is more attainable with two fluids where the local concentration of each point in the domain tends to the same value.

Energy Input

All mixing processes require the input of energy. Excessive energy input and mixing, which equipment designers try to eliminate, can result in the following:

- High operational costs
- More frequent maintenance, shutdowns and equipment wear
- Excessive heat generation leading to degradation
- Unwanted attrition
- May produce agglomeration

Appendix 1 contains a brief summary of some other useful terms associated with laminar mixing.

Scale-up and process transfer

Effective scale-up and process transfer of mixing equipment from the laboratory to the industrial scale is a major challenge. Considerable effort has been devoted to determining and quantifying scale up factors. The aim is to achieve, using these appropriate factors, similarity between a test/pilot scale rig and the desired full-scale units. This will eliminate the need for costly (in terms of time and money) intermediate units and experimental trials. The similarity of the mixers is considered in three areas:

1. Geometric similarity

This is achieved in two units if the ratios of various key lengths, e.g. D_c/D, are constant (where D is the rotor diameter and D_c is the rotor/barrel clearance).

2. *Kinematic similarity*

When the ratio of fluid velocity vectors at two fixed points in two geometrically similar units are constant, kinematic similarity exists. Also the paths of fluid motion (flow patterns) must be alike[34].

3. *Dynamic similarity*

This is achieved only if the forces at two fixed points in two geometrically similar units are constant. There are several types of forces and each has to be considered separately. These include viscous forces, normal stresses (in the case of viscoelastic fluids) and others such as gravitational forces, inertial forces and surface tension forces. The ratios of these forces can be expressed as dimensionless groups that serve as similarity parameters for scale up of mixing equipment[35].

In the polymer industry, particularly for extruder design, scale-up rules have been identified as early as 1953 and since then many different mathematical models have been developed dealing with solids conveying, melting, pumping, dispersion, distribution and reaction. For example Carley and McKelvey[36] rules predict that "Output and Power Consumption are directly proportional to the Diameter Ratio^{3}" (for proportional increase in channel depth and width and constant screw speed). This rule is used in industry but applies to Newtonian full fill melt situations.

Maddock's "square root rule"[37] is the second widely used scale-up rule. The system works well in terms of melting and solid conveying, however, it yields a shear rate which is too high, not scaling the mixing phenomena appropriately. Table 3-1 gives a comparison between these two scale-up rules used by industry. S is called the scale up factor and is the diameter ratio D/d where D and d are the diameters of the larger and smaller extruder respectively.

	Scale-Up Rule	
	Carley & McKelvey	Maddock
Diameter	$D = d \times S$	$D = d \times S$
Channel Depth	$H = h \times S$	$H = h \times S^{0.5}$
Screw Speed	$N = n \times S^{0}$	$N = n \times S^{-0.5}$
Output Rate (per min)	$Q = q \times S^{3}$	$Q = q \times S^{2}$
Shear Rate	$\dot{\gamma} = \dot{\gamma} \times S^{0}$	$\dot{\gamma} = \dot{\gamma} \times S^{0}$
Circum. Speed	$V = v \times S$	$V = v \times S$
Residence time	$T = t \times S^{0}$	$T = t \times S^{0}$
Power Consumption	$P = p \times S^{3}$	$P = p \times S^{2.5}$

Note: Upper case and lower case denotes the larger and smaller extruder respectively.

Table 3-1 ***A comparison of scale up rules for distributive mixing in twin screw extruders***

Other researchers' models favour Carley and McKelvey but it is fair to say no rules produce ideal final scale extruder conditions whether it be problems with too much pumping and not enough melting or problems with the mixing and hence the product character.

There have been numerous investigations into transferability and attempts to describe the mixing process in internal mixers. Many of these investigations, however, consider only parts of the process, leading to a lack of coherent solutions[38].

4. Theoretical Modelling of Viscous Fluid Flow

4.1 Fundamentals in Laminar Flow Modelling

4.1.1 Introduction of Flow Modelling

As an engineering tool, for investigating the behaviour of a variety of fluids under many varied situations, CFD may appear as an excellent method of yielding information not easily obtainable by experimental methods. CFD codes are extremely difficult to write, case specific and, without powerful preprocessors and postprocessors, are limited in terms of domain complexity and interpretation of the results. Commercial CFD packages, on the other hand, overcome these problems and have the benefit that the user need not become involved with the extremely complex mathematics, numerical methods and programming background that are required to model complex fluid flow. Although this means that the user can concentrate on becoming competent with other important aspects, for example mesh generation techniques, the down side is that the background is very easily neglected. This lack of understanding and appreciation can mean that inappropriate choices and assumptions can be made when defining the flow problem in hand. This may lead to the full potential of CFD not being fully exploited or not being correctly used. It is also important to understand the capability of CFD, how accurately it can perform and what results it can offer when applied to a certain scenario.

This section serves as an introduction to the *general case* of CFD modelling and the *specific case* of the modelling of the Hampden RAPRA Torque Rheometer using Polyflow.

4.1.2 Applying CFD to a General Case Flow Problem

When addressing a fluid flow problem one begins by selecting the working differential equations that describe the continuous variations of flow parameters throughout a system. These are the time averaged Navier-Stokes Equation (momentum equation) and the continuity equation model of flow of fluid. If the fluid is turbulent by nature then the well known k-ε model is an example of a model that can be used the represent the effect on viscosity. In three dimensions turbulent flow there are six equations (three momentum equations, one continuity and one equation each for k and ε) and six unknowns (one velocity vector in each of the three dimensions, pressure, k (turbulent kinetic energy) and ε (turbulent dispersion rate)). Compressible flow problems will require the equation of state that relates pressure to density. Non-isothermal systems will require

some form of energy equation and if chemical reactions take place some equation involving the conservation of chemical species will be needed.

The next task is the discretization of the flow field. At this stage the differential equations are transformed into algebraic forms where the continuous variations of flow variables are represented by values at discrete locations in time and space[39]. There are several techniques that can be employed for space discretization e.g. the finite difference method (finite analysis network - FAN), the finite volume methods, the spectral method and finite element method. There are other methods of solving a given flow field e.g. the boundary element method which is used for inviscid flow simulation, however, the finite element method is used by 'Polyflow'. The discrete locations in space are provided by *nodes* on a computational grid called a *mesh*. Whatever the method used to perform this discretization, the subsequent solution procedure is essentially independent of the means of discretization for a high mesh density[40]. The solution of the simultaneous equations for the flow variables for each of the nodes is obtained using linear matrix techniques.

4.1.3 Applying CFD to a Specific Case: The Hampden RAPRA Torque Rheometer

Engineers who use commercial CFD codes may fall prey to numerous pitfalls jeopardising their research and producing unnecessarily poor results from their simulations. Reasons for this include a lack of in-depth understanding of several important areas such as:

- The derivation of all equations which are to be solved
- The meaning of various terms in equations
- Any approximations included in the model and the domino effects of combined approximations
- Any assumptions made when using various equations and any subsequent consequences

Errors in the simulations of engineers who do not spend time studying these issues may never be identified and as a consequence time and money will be wasted as well as generating a poor reputation for CFD which could have been avoided. This is an inherent disadvantage of 'black box' commercial codes.

In order to obtain the required knowledge, as listed above, the derivations of the fundamental equations used in the simulation of the Hampden RAPRA Torque Rheometer have been studied

and are presented below complete with explanations and justifications of approximations and assumptions employed by the model.

Conservation of Mass / Continuity Equation

A mass balance, for a typical viscous fluid processed in the Hampden RAPRA Torque Rheometer, is considered over a small stationary volume element in rectangular co-ordinates as shown in Figure 4-1.

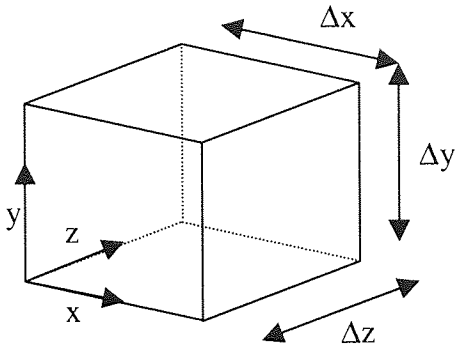

Figure 4-1 ***A small volume element for a Hampden RAPRA Torque Rheometer mass balance***

The rate of mass accumulation is equal to the rate of mass in to the element minus the rate out of the element. By addressing each direction separately and adding the terms the complete balance is achieved:

$$\Delta x\Delta y\Delta z\frac{\partial \rho}{\partial t} = \Delta y\Delta z\left[(\rho v_x)|_x - (\rho v_x)|_{x+\Delta x}\right] + \Delta x\Delta z\left[(\rho v_y)|_y - (\rho v_y)|_{y+\Delta y}\right] + \Delta x\Delta y\left[(\rho v_z)|_z - (\rho v_z)|_{z+\Delta z}\right] \tag{4-1}$$

Dividing by the volume of the element and taking the limits we find

$$\frac{\partial \rho}{\partial t} = -\left(\frac{\partial \rho v_x}{\partial x} + \frac{\partial \rho v_y}{\partial y} + \frac{\partial \rho v_z}{\partial z}\right) \tag{4-2}$$

This equation of continuity may be rewritten in terms of a 'divergence' of the mass flux ($\rho \mathbf{v}$)

$$\frac{\partial \rho}{\partial t} = -(\nabla \cdot \rho \mathbf{v}) \tag{4-3}$$

Assuming constant fluid density equation 4-3 reduces to

$$(\nabla \cdot \mathbf{v}) = 0 \tag{4-4}$$

The assumption of ***constant fluid density*** is an important issue that requires justification especially when the simulation is non-isothermal. Constant fluid density implies that the fluid is incompressible in the case of an isothermal system. No fluid is truly incompressible, however, engineers frequently use this assumption resulting in considerable model simplification and almost no error[41] when dealing with dense fluids. For non-isothermal models a substantial change in temperature may affect the density significantly; this is considered in more depth later.

Equation of Motion / Momentum Balance

A momentum balance, for a typical viscous fluid processed in the Hampden RAPRA Torque Rheometer, is considered over a similar small volume element as depicted in Figure 4-1. The rate of accumulation is equal to the rate of momentum in to the element minus the rate of momentum out of the element plus the sum of the forces acting on the system.

The rate of accumulation of momentum, in the x direction , within the element is given by

$$\text{rate of accumulation of momentum (x-direction)} = \Delta x \Delta y \Delta z \left(\frac{\partial \rho v_x}{\partial t} \right) \qquad (4\text{-}5)$$

Momentum transfer results from two mechanisms which are described below in terms of the 'x' direction; the 'y' and 'z' directions will be handled analogously.

Momentum transfer by convection

The rate of momentum in the 'x' direction into the element by bulk flow is expressed by

$$\begin{aligned} \text{momentum flux by convection} = {} & \Delta y \Delta z (\rho v_x v_x |_x - \rho v_x v_x |_{x+\Delta x}) \\ & + \Delta x \Delta z (\rho v_y v_x |_y - \rho v_y v_x |_{y+\Delta y}) \\ & + \Delta x \Delta y (\rho v_z v_x |_z - \rho v_z v_x |_{z+\Delta z}) \end{aligned} \qquad (4\text{-}6)$$

Momentum transfer by molecular mechanisms

Momentum enters the element via velocity gradients. This momentum flux may be considered as stresses. Figure 4-2 depicts the 'x' component of momentum transported through each surface.

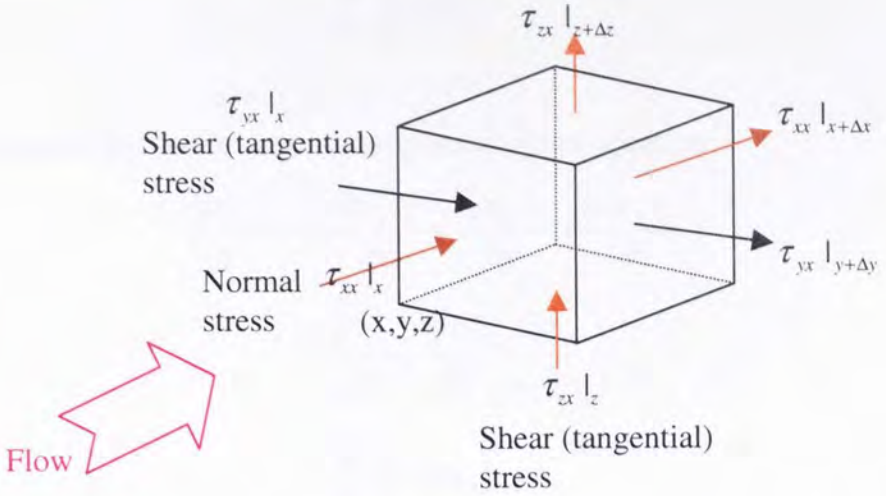

Figure 4-2 ***Momentum transfer by shear and normal stresses in a small volume element***

The summation of all six terms gives:

$$\begin{aligned}\text{molecular momentum flux} = {} & \Delta y\Delta z(\tau_{xx}|_x - \tau_{xx}|_{x+\Delta x}) \\ & + \Delta x\Delta z(\tau_{yx}|_y - \tau_{yx}|_{y+\Delta y}) \\ & + \Delta x\Delta y(\tau_{zx}|_z - \tau_{zx}|_{z+\Delta z})\end{aligned} \tag{4-7}$$

The forces which act on the system come from two sources:

Pressure

Fluid pressure over the area normal to the flow in the x direction is given by

$$\text{pressure in 'x' direction} = \Delta y\Delta z\left(p|_x - p|_{x+\Delta x}\right) \tag{4-8}$$

Gravity

For completeness the force due to the 'x' component of gravity on the fluid volume is presented although it will only effect the flow field if there are changes in fluid density in the system; it is given by:

$$\text{force due to gravity} = \Delta x\Delta y\Delta z\rho g_x \tag{4-9}$$

Combining equations (4-5) – (4-9) in the overall momentum balance, dividing by the volume of the element and taking the limits results in:

$$\begin{aligned}\frac{\partial \rho v_x}{\partial t} = & -\left(\frac{\partial \rho v_x v_x}{\partial x} + \frac{\partial \rho v_y v_x}{\partial y} + \frac{\partial \rho v_z v_x}{\partial z}\right) \\ & -\left(\frac{\partial \tau_{xx}}{\partial x} + \frac{\partial \tau_{yx}}{\partial y} + \frac{\partial \tau_{zx}}{\partial z}\right)\end{aligned} \tag{4-10}$$

$$-\left(\frac{\partial p}{\partial x}\right)+(\rho g_x)$$

A similar treatment for the 'y' and 'z' components gives equation

$$\frac{\partial \rho v_y}{\partial t}=-\left(\frac{\partial \rho v_x v_y}{\partial x}+\frac{\partial \rho v_y v_y}{\partial y}+\frac{\partial \rho v_z v_y}{\partial z}\right) \tag{4-11}$$

$$-\left(\frac{\partial \tau_{xy}}{\partial x}+\frac{\partial \tau_{yy}}{\partial y}+\frac{\partial \tau_{zy}}{\partial z}\right)$$

$$-\left(\frac{\partial p}{\partial y}\right)+(\rho g_y)$$

$$\frac{\partial \rho v_z}{\partial t}=-\left(\frac{\partial \rho v_x v_z}{\partial x}+\frac{\partial \rho v_y v_z}{\partial y}+\frac{\partial \rho v_z v_z}{\partial z}\right) \tag{4-12}$$

$$-\left(\frac{\partial \tau_{xz}}{\partial x}+\frac{\partial \tau_{yz}}{\partial y}+\frac{\partial \tau_{zz}}{\partial z}\right)$$

$$-\left(\frac{\partial p}{\partial z}\right)+(\rho g_z)$$

For convienence we combine equations 4-10 to 4-12 to give equation 4-13.

$$\frac{\partial \rho \boldsymbol{v}}{\partial t}=-[\nabla\cdot\rho\boldsymbol{v}\boldsymbol{v}]-\nabla p-[\nabla\cdot\boldsymbol{\tau}]+\rho\boldsymbol{g} \tag{4-13}$$

Where $-[\nabla\cdot\rho\boldsymbol{v}\boldsymbol{v}]$ is the dyadic product of $\rho\boldsymbol{v}$ and $\boldsymbol{v}$ and denotes the rate of loss of momentum per unit volume.

Rearranging equation 4-13 yields equation 4-14 which reduces to equation 4-15 where, in this form of the equation of motion, the small fluid volume is moving with the fluid and is accelerated by forces acting on it. This is Newton's second law which states that the mass multiplied by acceleration is equal to the sum of the forces.

$$\left(\frac{\rho\partial \boldsymbol{v}}{\partial t}+\frac{\boldsymbol{v}\partial\rho}{\partial t}\right)^{1}+[\rho\boldsymbol{v}(\nabla\cdot\boldsymbol{v})+\rho(\boldsymbol{v}.\nabla)\boldsymbol{v}+\boldsymbol{v}\boldsymbol{v}\nabla\cdot\rho]=-\nabla p-[\nabla\cdot\tau]+\rho\boldsymbol{g} \tag{4-14}$$

[1]Using the assumption of constant density as stated in equation 4-4

$$\frac{\rho D\boldsymbol{v}}{Dt}=-\nabla p-[\nabla\cdot\tau]+\rho\boldsymbol{g} \tag{4-15}$$

$\frac{\rho D\boldsymbol{v}}{Dt}$ =is the mass per unit volume multiplied by the substantial time derivative of the velocity vector with respect to time (i.e. acceleration)

∇p = pressure gradient of element per unit volume

$[\nabla \cdot \tau]$ = viscous force on element per unit volume

ρg = gravitational force per unit element per unit volume

The nine components of viscous force are given by

$$\tau_{xx} = -2\mu \frac{\partial v_x}{\partial x} + \frac{2}{3}\mu(\nabla \cdot v) \tag{4-16}$$

$$\tau_{zz} = -2\mu \frac{\partial v_z}{\partial z} + \frac{2}{3}\mu(\nabla \cdot v) \tag{4-17}$$

$$\tau_{yy} = -2\mu \frac{\partial v_y}{\partial y} + \frac{2}{3}\mu(\nabla \cdot v) \tag{4-18}$$

$$\tau_{xy} = \tau_{yx} = -\mu\left(\frac{\partial v_x}{\partial y} + \frac{\partial v_y}{\partial x}\right) \tag{4-19}$$

$$\tau_{yz} = \tau_{zy} = -\mu\left(\frac{\partial v_y}{\partial z} + \frac{\partial v_z}{\partial y}\right) \tag{4-20}$$

$$\tau_{zx} = \tau_{xz} = -\mu\left(\frac{\partial v_z}{\partial x} + \frac{\partial v_x}{\partial z}\right) \tag{4-21}$$

Assumptions and simplifications for the isothermal Hampden RAPRA Torque Rheometer model

The assumption of uniform density (incompressible fluid), as mentioned previously, is used again in the equation of motion (equation 4-15). Other possible assumptions relating to isothermal conditions are discussed below.

- *Steady state*

To overcome the problem of the time dependent geometry, due to the rotors turning, a complete representation of the process will be made by considering several steady state instantaneous 'snap shots' in time. The analysis of each will provide a description of the process in terms of various defining quantities.

- *Single species*

When two or more fluids of similar rheologies are mixed the interfaces between the two will be random depending on how the materials are loaded into the mixer. Although the model could incorporate several subdomains each one defined by the rheology of the fluid contained within, realistic representation is limited by the stochastic nature of the situation. The best achievable approximation would be to define the mixture by a set of physical properties that described the

fluid after it had been partially mixed. The majority of the mixing cycle continues after the mixture is partially homogenised. In the case of two dissimilar fluids, for example, an inviscid lubricant is added to the main viscous medium, then another problem arises – wall slip.

- *No slip at the wall*

The assumption of no slip at the wall is commonly used when modelling polymer processing equipment. However, one case that will undoubtedly result in a high degree of wall slip is during the addition of an inviscid lubricant to a viscous major phase. This will affect the shearing and hence mixing significantly. Figure 4-3 illustrates the apparent slip at the wall caused by a thin layer of a lubricant forming at the outer wall surface.

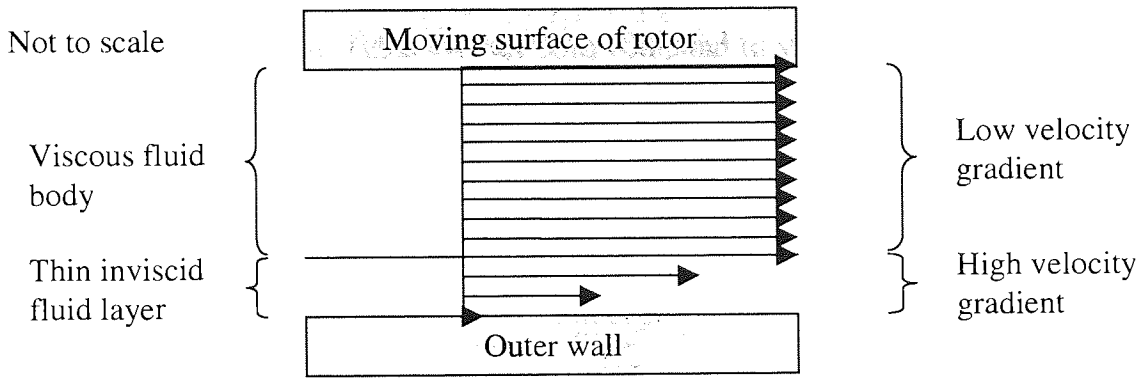

Figure 4-3 ***Diagrammatic explanation of apparent wall slip due to inviscid lubricant***

A full investigation of slip can be found in a subsequent chapter. The investigation includes tests to see how viscous fluids adhere to the wall when the rotors are turned using flow visualisation experiments. The incorporated of slip into the model and the affect of the flow field is also examined.

- *Single phase*

The initial period of the mixing cycle involves complex phase transitions where solids soften and plasticate. However, during the majority of the cycle, phase transitions will have already taken place. It is this period of the mixing cycle that is critical to the to the productivity and character of the final product and it is this period which is intended to be investigated using the Hampden RAPRA Torque Rheometer simulation. There may be solid phases that do not melt, such as powdered additive and impurities. The effect of these additives on the system after the initial mixing period (during the majority of the mixing cycle) is assumed to be taken into account by the rheological parameters set in the model. Inhomogeneity of particulate distribution will cause the fluid flow field to change. The viscosity increase resulting from the presence of spherical

particulates in dilute dispersions is represented in terms of dispersion volume fraction, ϕ, by what is usually referred to as Einstein's equation.

$$\eta_{rel} = \frac{\eta_D}{\eta_L} = \frac{dispersion\_viscosity}{liquid\_viscosity} = 1 + \alpha\phi \qquad (4\text{-}22)$$

For a low enough viscosity (for $\phi < 0.05$) α is equal to 2.5. Similarly, any gaseous phase is assumed not to affect the flow field significantly if it occupies a small enough percentage of the total chamber volume (see full fill).

- *Full Fill*

Internal mixers, depending on the task in hand, operate at different material fill factors. For small-scale laboratory mixers full fill is usually the case, however, for full-scale internal mixers 100% full fill is not common. Table 4-1 has been compiled to summarise the 'usual' fill factors and the relative batch sizes for common materials mixed in internal mixers[42].

Table 4-1 ***Fill factors and batch sizes of common materials processed in internal mixers***

Material	Fill Factor	Relative Batch Size
Polyethylene	0.9	1.0
Polyethylene master batch	0.91	1.15
Polystyrene/SBR	0.91-0.95	1.15-1.23
Rubber Stock	0.91	1.2
Rubber tread stock	0.91	1.29
'Easy-processing' rubber stock	1.0	1.86
Unplasticised PVC	0.86-0.98	1.45-1.7
Plasticised PVC (25% filler)	0.96-1.0	1.65-1.97
Soft PVC flooring (55% filler)	0.99	2.08
Soft PVC flooring	0.99	2.67
Vinyl/asbestos floor tile	0.99-1.0	2.55-2.7

In industrial scale internal mixer operations less than 10% in of the chamber volume is usually air pockets. The presence of these voids in the domain of large-scale mixers will effect the accuracy of the results from CFD simulations assuming full fill. Attempts by researchers to include voids in internal mixer simulations are discussed in the literature review that follows. It should be noted that there has been a tendency to increase ram pressure over the last 20 years or so[43] to reduce voids in the composition with the aim of increasing the speed of engagement of the materials with the rotors and contact between components.

- *Non reacting fluid*

Polymeric materials may change their chemical structure during the mixing cycle and as a consequence the physical properties will change by some degree. This change in molecular form may be due to physical conditions such as high shear or high temperatures causing chain lysis or product degradation or it may result from chemical reactions. It may be the case that if the material reacts the relevant physical properties may not be altered significantly and so the flow field will remain the same to all intents and purposes. This shall be the assumption for this research. If this is not the case and known reactions are taking place, which will result in considerable physical property change (which may be compounded by the associated temperature rise or fall), then it is possible to model this reaction, in Polyflow, as long as it occurs in the bulk of the fluid i.e. not an interfacial reaction. It should be noted that a transient model is required to model reactions.

- *Non Newtonian behaviour*

When we consider the viscous forces, the possibility of assuming that the fluid is Newtonian presents itself. However, realistic shear gradients imposed on a viscous fluid will affect the viscosity dramatically as discussed in chapter 3. As seen from equations 4-16 to 4-21 stresses are a function of fluid viscosity which in turn is a function of shear rate. Therefore, generalised Newtonian models shall be investigated and also viscoelastic fluid properties.

- *Inertia*

The inertia term in the momentum equation (equation 4-14) can have a negligible effect on high viscous flow fields and is often ignored to reduce computational effort. This is illustrated in section 7.2.1. The Reynolds number (equation 4-23) can be used as a guide to determine whether the inertial forces are significant compared to the viscous forces (Re<<1). The Reynolds number can be defined in terms of different parameters dependent on the particular process in question. An internal mixer takes a form similar to a stirred tank hence I have used equation 4-23 to check that the Reynolds number is suitably low to allow inertia terms to be ignored.

$$\mathrm{Re} = \frac{N \cdot L^2 \cdot \rho}{\mu} \tag{4-23}$$

Where

Re = Reynolds number

N = Number of rotor revolutions per second

L = Characteristic length of rotor (diameter)

ρ = Density of fluid (kg/m^3)

μ = Maximum viscosity of fluid (kg $s^{-1}m^{-1}$)

Hence for a typical polymer melt mixed at full rotor speed of 65 revs per minute the Re is equal to

$$= \frac{1.083 \cdot 0.00144 \cdot 1150}{3049}$$

$$= 0.588 \times 10^{-3}$$

- *Isothermal Conditions*

After the temperature stabilises in the mixing cycle, isothermal conditions may exist. For small scale mixers White *et al*[44] show that it is reasonable to assume isothermal conditions (see section 4.2.2). For steady state models, examining flow patterns and the mixing mechanism isothermal conditions will be assumed. Although the author feels that this is an important area since temperature affects rheology (and other important properties such as specific heat capacity and heat conduction coefficient), taking into account temperature changes will complicate the model and increase the computational demand notably.

Equation of Change for Non Isothermal Conditions / Energy Balance

Using the same volume element as in Figure 4-1 at any given time equation 4-24 will apply.

Rate of accumulation of internal and kinetic energy	=	Rate of internal and kinetic energy in by convection	-	Rate of internal and kinetic energy out by convection	+	Net rate of heat addition by conduction	-	Net rate of work done by systems on surroundings	(4-24)

The kinetic energy is the energy due to the motion of the fluid while the internal energy component comes from the internal motion of the molecules and the energy interactions between molecules. Internal energy is a function of temperature and density. It has been assumed potential energy, energy due to chemical reaction and other forms of energy and energy transport such as radiative, nuclear and electromagnetic, are negligible.

The rate of accumulation of energy within the element is given by:

$$\text{rate of accumulation} = \Delta x \Delta y \Delta z \frac{\partial}{\partial t}\left(\rho \hat{U} + \tfrac{1}{2}\rho v^2\right) \qquad (4\text{-}25)$$

Where $\hat{U}$ is the internal energy per unit mass.

The net rate of energy input by convection of internal and kinetic energy is given by

$$\text{energy input by convection} = \Delta y\Delta z\left\{v_x\left(\rho\hat{U}+\tfrac{1}{2}\rho v^2\right)|_x - v_x\left(\rho\hat{U}+\tfrac{1}{2}\rho v^2\right)|_{x+\Delta x}\right\} \quad (4\text{-}26)$$
$$+\Delta x\Delta z\left\{v_y\left(\rho\hat{U}+\tfrac{1}{2}\rho v^2\right)|_y - v_y\left(\rho\hat{U}+\tfrac{1}{2}\rho v^2\right)|_{y+\Delta y}\right\}$$
$$+\Delta x\Delta y\left\{v_z\left(\rho\hat{U}+\tfrac{1}{2}\rho v^2\right)|_z - v_z\left(\rho\hat{U}+\tfrac{1}{2}\rho v^2\right)|_{z+\Delta z}\right\}$$

The net rate of energy input by conduction is given by

$$\text{net rate of energy input by conduction} = \Delta y\Delta z(q_x|_x - q_x|_{x+\Delta x}) \quad (4\text{-}27)$$
$$+\Delta x\Delta z(q_y|_y - q_y|_{y+\Delta y})$$
$$+\Delta x\Delta y(q_z|_z - q_z|_{z+\Delta z})$$

Where q_x is one of the three components of the heat flux vector $\boldsymbol{q}$.

The work done by the whole volume against gravity (potential energy) and the work done on the surfaces due to pressure and viscous forces are given by equations 4-28, 4-29 and 4-30 respectively. Note that the rate of doing work is equal to a force multiplied by a velocity in the direction of that force.

$$\text{work done against gravity} = -\rho\Delta x\Delta y\Delta z(v_x g_x + v_y g_y + v_z g_z) \quad (4\text{-}28)$$

$$\text{work done against pressure} = -\Delta y\Delta z(pv_x|_x - pv_x|_{x+\Delta x}) \quad (4\text{-}29)$$
$$-\Delta x\Delta z(pv_y|_y - pv_y|_{y+\Delta y})$$
$$-\Delta x\Delta y(pv_z|_z - pv_z|_{z+\Delta z})$$

$$\text{work done against viscous forces} = \quad (4\text{-}30)$$
$$-\Delta y\Delta z\left\{(\tau_{xx}v_x+\tau_{xy}v_y+\tau_{xz}v_z)|_x - (\tau_{xx}v_x+\tau_{xy}v_y+\tau_{xz}v_z)|_{x+\Delta x}\right\}$$
$$-\Delta x\Delta z\left\{(\tau_{yx}v_x+\tau_{yy}v_y+\tau_{yz}v_z)|_y - (\tau_{yx}v_x+\tau_{yy}v_y+\tau_{yz}v_z)|_{y+\Delta y}\right\}$$
$$-\Delta x\Delta y\left\{(\tau_{zx}v_x+\tau_{zy}v_y+\tau_{zz}v_z)|_z - (\tau_{zx}v_x+\tau_{zy}v_y+\tau_{zz}v_z)|_{z+\Delta z}\right\}$$

Subtituting equations 4-25 - 4-30 into equation 4-24, dividing by the volume of the element and taking limits as Δx, Δy and Δz tend to zero gives

$$\frac{\partial}{\partial t}\rho\left(\hat{U}+\tfrac{1}{2}v^2\right) = -\left(\nabla\cdot\rho\boldsymbol{v}\left(\hat{U}+\tfrac{1}{2}v^2\right)\right) - (\nabla\cdot\boldsymbol{q}) + \rho(\boldsymbol{v}\cdot\boldsymbol{g}) - (\nabla\cdot p\boldsymbol{v}) - (\nabla\cdot[\boldsymbol{\tau}\cdot\boldsymbol{v}]) \quad (4\text{-}31)$$

On rearrangement equation 4-32 is formed from which the substantial derivative of $\left(\hat{U} + \frac{1}{2}v^2\right)$ is obtained as shown by equation 4-33. The two forms of the energy equations 4-31 and 4-33 represent the energy change in a fluid from a stationary observer and an oberver moving with the fluid respectively.

$$\rho\left[\frac{\partial}{\partial t}\left(\hat{U} + \tfrac{1}{2}v^2\right) + \boldsymbol{v}\nabla\cdot\left(\hat{U} + \tfrac{1}{2}v^2\right)^{1}\right] + \left(\hat{U} + \tfrac{1}{2}v^2\right)\nabla\cdot\rho = \tag{4-32}$$

$$-(\nabla\cdot\boldsymbol{q}) + \rho(\boldsymbol{v}\cdot\boldsymbol{g}) - (\nabla\cdot p\boldsymbol{v}) - (\nabla\cdot[\tau\cdot\boldsymbol{v}])$$

[1]Using the assumption of constant density as stated in equation 4-4

$$\rho\frac{D}{Dt}\left(\hat{U} + \tfrac{1}{2}v^2\right) = -(\nabla\cdot\boldsymbol{q}) + \rho(\boldsymbol{v}\cdot\boldsymbol{g}) - (\nabla\cdot p\boldsymbol{v}) - (\nabla\cdot[\tau\cdot\boldsymbol{v}]) \tag{4-33}$$

4.2 Literature review

4.2.1 Introduction

The idea of using simplified mathematical models to investigate the flow of material within an internal mixer has been around since the late 1950's. Reviews of these early models and of those leading up to the early 1990's and some research into experimental flow visualisation, can be readily found[45,46]. This review, however, concentrates on the recent work which has advanced the field of mathematical modelling in an attempt to overcome the complexities of a transient, non isothermal, mixing dependent flow situation of a complex rheological material with a free surface flow regime in a complex geometry.

4.2.2 Theoretical Modelling of Internal Batch Mixers

The simulation of internal mixers has been approached in either one of two directions. Firstly are those researchers who model two-dimensional representations of either part or whole sections of a mixer using in-house codes. The other school of thought comes from those who have identified the potential of commercial codes which offer highly sophisticated mesh generation, result processing and powerful equation solvers to model three-dimensional models. Some of these packages, however, may not be as flexible as in house codes when dealing with such a specialist field.

In house codes have been used extensive by Nassehi, Freakley and Ghoreishy *et al* to develop a two-dimensional finite element simulation of a Banbury type mixer. The geometries mostly used

in their investigations consist of either a whole or part of a single chamber rotor mixer. Transient, simulations of Carreau type fluids are obtained using the assumption that the outer chamber rotates around a stationary rotor[47,48]. This assumption produces, the author believes, a fundamentally different flow field than that found in real mixers. This claim can be substantiated if one considers two situations involving a simple mixer. The first mixer has a stationary rotor and chamber rotating at a constant angular velocity 'x'rads^{-1}. If a full slip condition is imposed on all walls then, even though the chamber rotates, the fluid will remain stationary. If we consider the second case, where the chamber is stationary, as with real mixers, and the rotor has an angular velocity 'x'rads^{-1}, if the walls have a full slip condition the fluid in front of the rotors will experience a force and therefore the flow field will become active. Their simulation, however, has been partly validated by measuring rotor peak pressures for no slip conditions, these being in the region of $1.8*10^6$ Pa. This is in good agreement with previously published experimental measurements of peak pressure around $1.8*10^6$ - $2.0*10^6$ Pa for various rotor positions[49]. Their work has addressed important factors such as the adiabatic temperature rise from viscous dissipation (assuming no heat leaves through the boundaries), non-Newtonian rheology and partial wall slip[50] (using Navier slip condition and coefficients of $1.0*10^{-7}$mPa^{-1}s^{-1}and $2.0*10^{-6}$mPa^{-1}s^{-1}). In addition to the Banbury, narrow tip and wide tip blades (Francis Shaw type) have been modelled[51], although critical evaluation of each type of rotor was not in their scope of work. Most interesting, however, are the attempts to model mixing dependent rheology based on the particulate concentration[52] and the attempts to model free surfaces[53] within the chamber. These free surfaces, representing air trapped in the fluid are modelled by defining an initial position (such as a quarter of the flow field) and tracking their position over a number of time steps equivalent to several seconds of mixing time. Very recently Nassehi and Ghoreishy have extended their model to represent a twin rotor mixer with a friction ratio of 1:1.125 presenting free surface tracking corresponding to 0, 30, 60 and 90 degree rotation of the right rotor[54]. To achieve the conversion to the time dependent geometry of a twin rotor mixer a technique called the Arbituary Lagrangian Eularian (ALE) scheme has been used. In the developed method a pre-processor is used to generate a number of finite element meshes which represent each time step and the different stages of rotation of the blades. The solution of the governing equations starts from an initial configuration and proceeds from mesh to mesh. This overcomes problems of a purely Lagrangian remeshing techniques which would over-distort the mesh elements if it was applied to twin rotor internal mixers. The man hours involved in creating each separate geometry is perhaps why these researchers have presented a 90 degree rotation of the blades and have remained firmly in two-dimensions. The authors comment that their work

could be extended to three dimensions but would need a super computer to find the numerical solutions.

A commercial code has been used to model a three-dimensional internal mixer by Manas-Zloczower, *et al* who have modelled the BB-2 Banbury mixer (which is one of the most common high intensity industrial batch rubber and plastic mixers) using the finite element package FIDAP. Most notable is their investigation of the influence of rotor speed, rotor speed ratio and initial relative position of the rotors[55] which was investigated by analysing the average values of six sequential two-dimensional geometries for a power law fluid ($K = 9.87 \times 10^4$ N $s^{0.22}/m^2$ and $n = 0.22$). A mixing time of 8 minutes was assumed since the isothermal assumption is less "dramatic" after long enough mixing times. A comparison of two-dimensional[56] and three-dimensional models was made and although the patterns are very similar there are discrepancies indicating that only the three-dimensional models should be used when accurate flow field patterns, shear stresses and elongational flow components are required. The flow fields are said to be in agreement with flow visualisation investigations of other researchers. The work on particle distribution / tracking and the evolution of the distance between pairs of particles in the mixing chamber[57] has been given a high priority in their work. The identification of the best mixing performance of several rotor orientations for even (both rotors rotating at 60 rpm) and uneven (60/40 rpm) rotor speeds has been attempted. This was achieved by analysing a complete rotor cycle which was represented by a sequence of two-dimensional pseudo steady state 'snap shots' every 5 degrees (72 for even speed and 216 for uneven speed). The anti-symmetric configuration was the best operating mode among the three even speed cases tested. The performance of the uneven speed cases fell in-between the even speed cases. It appears that this analysis may restrict simulations to simple friction ratios since a friction ratio of 8:9, for example, will required the modeller to create 648 separate meshes to achieve a similar degree of accuracy.

A VIC counter rotating twin rotor internal mixer (Variable Intermeshing Clearance) has been modelled under isothermal conditions using the finite element package FIDAP by Yang and Manas-Zloczower[58]. The whole cycle has been represented by nine meshes each differing by a rotor angle of 20 degree each containing 20243 nodal points taking 23000s of CRAY supercomputing time. It is interesting to note that the average values for various parameters calculated for each successive geometry do not differ by more than 3%. The effect of changing intermeshing distance on dispersive and distributive mixing was investigated. It was concluded that the average shear rate increases by 9% and the mixing index (see chapter 6.4 for a

explanation of the mixing index) increases by 1% by decreasing the clearance between the two rotors from 6.5mm-1mm. The evolution of particle motion was also used to assess mixing by a pairwise correlation function and by analysing the particle concentration. Several assumptions are used when calculating the paths of the mass-less points (hypothetical particles) such as, neglecting friction and Van der Waals force. A limitation of this work is the large number of man-hours required to construct each separate three-dimensional geometry, 18 in all, representing a 20 degree increment. These increments are large (30 degrees for the three-dimensional Banbury model) and since the flow field changes significantly over a few degrees (as concluded from my own work) the accuracy of this work is put into question. It is also unclear from the work presented how each flow field for each mesh are linked together. More recently chaotic features in polymer processing equipment[59] have been investigated expanding on the particle distribution work to include, for example, Lyapunov exponents.

The assumption of full fill, which may not exist when the material to be mixed may be too viscous to enable the chamber to be completely filled, has also been challenged by Manas-Zloczower and Wong[60] using a two dimensional finite element study. These extra surfaces complicate matters greatly introducing new boundaries to the situation. The simulation dictates that the chamber and rotors have non-slip boundaries, however, the voids have a constant normal stress and a tangential stress-free boundary condition along their surface depending on their location. The evolution of the void regions was followed by integrating the velocity vectors along the void surface. The integration method was the simple Euler method (i.e. an explicit integration scheme). The results show that the pressure patterns are very similar to the full fill case. The voids do not affect the mixing character (mixing index); trends are very similar - but this work only deals with small voids. Larger voids would lead to a "cut circuiting" effect.

CFD modelling of the internal rotor mixer has been attempted by several other research groups; their main model assumptions and conclusions have been summarised below:

White and Kim[61] have applied the hydrodynamic lubrication theory and the Finite Analysis Network (FAN), a finite difference form, to model the non-Newtonian, non-isothermal three-dimensional flow in a Banbury type internal mixer in a flattened out mixing chamber where the chamber wall is considered to move. The chamber is assumed to be set at a constant temperature by a cooling fluid and the rotor is considered to be adiabatic. They show that large-scale internal mixers (Farrel 27 Banbury - 700mm rotor diameter) tend to operate adiabatically while the small-scale machines (Haake Rheocord - 20mm rotor diameter) are close to isothermal. They note that

20% of material moves axially 70% moving circumferentially with the rest moving between the rotors. The influence of rotor flight angle, other rotor parameters and power law exponent on material flux in various directions, was investigated. Unfortunately little experimental verification is presented. White *et al* have applied their model again to the study of non-Newtonian behaviour[62] and seven different rotor types[63], this time basing their model on cylindrical co-ordinates. Separate simulations for the region between the rotor and the mixing chamber and for the inter-rotor region have been carried out and the results are matched at the boundaries between the two regions. The effects of non-Newtonian flow is quoted to have only a small effect on material fluxes with the transfer flux form one chamber to another and the axial flux decreasing by around 1% for most of the different rotor designs for power law exponents of 0.6 and 0.2.

Min and Suh[64] also have used the hydrodynamic lubrication theory in their attempts to model an internal mixer.

Osswald and Gramann suggest that the FAN (finite difference method) is unsuitable to model a twin rotor mixer adequately and the finite element cumbersome since many meshes have to be generated to represent a complete rotor cycle. In order to address this situation Osswald and Graham have used the boundary element method to model the mixing of a Newtonian fluid in a two-dimensional Banbury twin rotor batch mixer under isothermal conditions[65]. The mathematical manipulation of the governing equations results in boundary integrals, allowing the solution of moving boundary problems without domain meshing. Osswald *et al* have extended their modelling techniques to incorporate the non-isothermal nature of the process[66] and, more recently, multi-fluid domains to analyse the effect of varying fluid viscosity ratios[67] (although in this work multi-fluid domains are only presented for horizontal layers of Newtonian fluids flowing between two horizontal parallel plates and drops experiencing pure shear flow under isothermal conditions).

Malkin *et al* [68] have modelled the flow in the area around a simplified rotor tip in order to determine an optimum rotor clearance value. A power law fluid was simulated under non-isothermal conditions using the finite element method and the chamber was assumed to move relative to a stationary wall. Malkin *et al* acknowledge that the model is applied to a situation where the mixture is homogeneous and its fluid properties change monotonously without possible jumps in passing from one phase to another. The optimum rotor clearance value was previously investigated by Shinti[69] who defined a parameter to assess the amount of dispersive mixing as the

product of the shear stress magnitude and the volumetric throughput. Malkin *et al*, however, has used a parameter to calculate the effective dispersive mixing by quantifying the specific energy increase. This is the product of the shear stress magnitude and the average shear rate, and the volumetric throughput. The predicted optimum value was reported to agree with experimental work as does the average temperature/time graph. A similar simple geometry setup was used by Meisser and Poltersdorf[70] and their model temperature and torque plots again time give similar trends although the model tends to under-predict torque values.

4.2.3 Other Process Equipment Theoretical Models

Other polymer processing equipment has received attention from investigators using flow simulations. The twin screw extruder has been given the most attention. *Wilson et al* have successfully tackled generalised Newtonian fluid flow where efforts has been concentrated on the construction of two and three dimensional models of both conveying and mixing regions of a twin screw extruder [71,72,73,74]. A comprehensive review of the work of other researchers analysing viscous flow fields found in processing machinery has been compiled until 1996 by *Bruce*[75]. The study shows considerable growth in this area of research in recent years, coinciding with the advance in computer hardware, software and interest from large engineering companies.

Other geometries have also been tackled, such as the single screw cavity transfer mixer[76], although, in this study, the clearance between the stator and the rotor has not been incorporated into the model.

The literature on experimental verification and investigations into wall slip are located in chapter 6 and in chapter 8 respectively.

5. The Hampden RAPRA Torque Rheometer Simulation

The following chapter contains a brief modelling process overview, a section on the construction of the finite element mesh and an insight into the strategy of modelling a real and complex geometry. It serves only to give the reader an appreciation of the various components of the model and practical modelling considerations such as mesh optimisation.

5.1 Modelling Process Overview

The following steps were carried out in order to achieve a working simulation of the Hampden RAPRA Torque Rheometer:

1. Obtaining the exact dimensions of the geometry to be modelled using a suitable measuring device such as digital callipers accurate to $\pm$ 0.01mm.
2. Creating the three-dimensional CAD skeleton on the pre-processor package ICEM -DDN.
3. Transferring the CAD skeleton to the finite element meshing package ICEM - PCUBE and commencing with face and block generation. This process includes assigning faces to any curved surfaces created in DDN, designating surface families, defining boundaries and fluid domains, choosing the number of grid points and their distribution and finally generating the mesh.
4. Viewing the mesh in ICEM - LEO where it can be inspected and the element form can be analysed.
5. Defining the nature of the flow problem (e.g. generalised non-Newtonian, steady state and isothermal), setting boundary conditions, choosing numerical solver techniques and their associated convergence criteria. This is accomplished in Polydata, which is the interface between the ICEM package and the Polyflow 'solver'.
6. Creating a material property data file. This includes, for example, defining the fluid's shear rate dependence on viscosity.
7. Solving the flow domain using the Polyflow solver programme on in-house workstations.
8. Finally, processing the results from Polyflow on the graphics package CFVIEW where the predicted flow / mixing and shearing character can be examined.

5.2 The Construction of the Finite Element Mesh

The Hampden RAPRA Torque Rheometer rotors, Figure 5-1, are recreated in three-dimensions as illustrated by Figure 5-2. These are identical; any apparent discrepancies between the two pictures are due to the slightly differing viewing angles and perspectives.

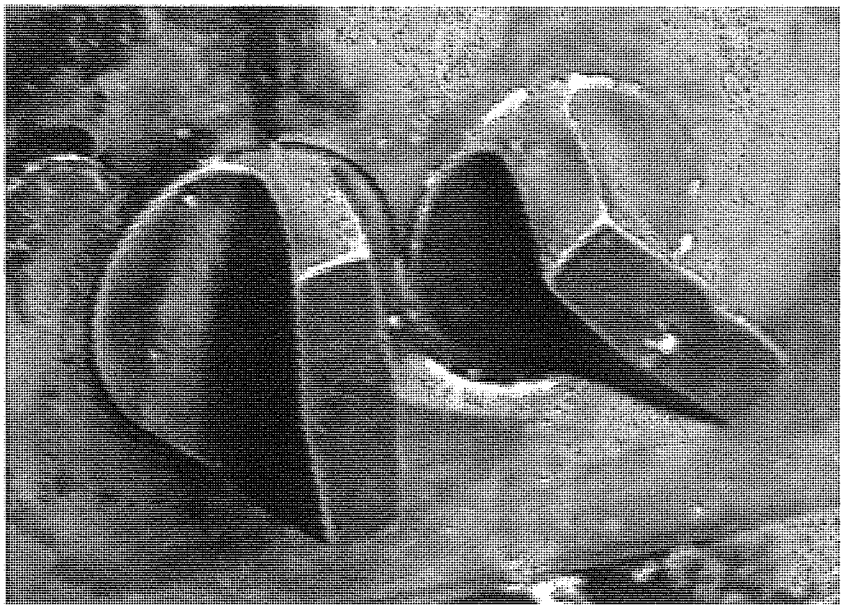

Figure 5-1 ***Hampden RAPRA Torque Rheometer internal batch mixer rotors***

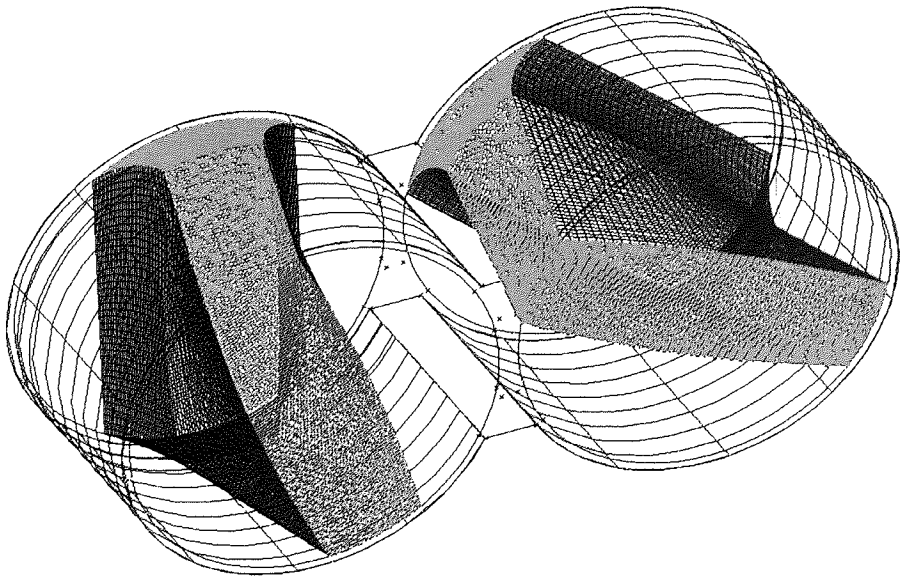

Figure 5-2 ***Three-dimensional Hampden RAPRA Torque Rheometer CAD skeleton***

The creation of the Hampden RAPRA Torque Rheometer finite element mesh is a complex procedure. A detailed description of the various mesh generating procedures for simple geometries is presented within the ICEM manuals[77]. Figures 5-1 to 5-12, however, illustrate the main features of the finite element mesh construction technique for this specific case introducing various concepts and meshing terms.

Block generation

Vertices created on the CAD structure are redefined in the mesh generating package and linked together to form edges. These edges, which can be curved and distorted to fit the CAD structure, are joined together to form faces. Finally, since we are working in three dimensions, blocks are created in which the virtual fluid will flow as shown by Figure 5-3.

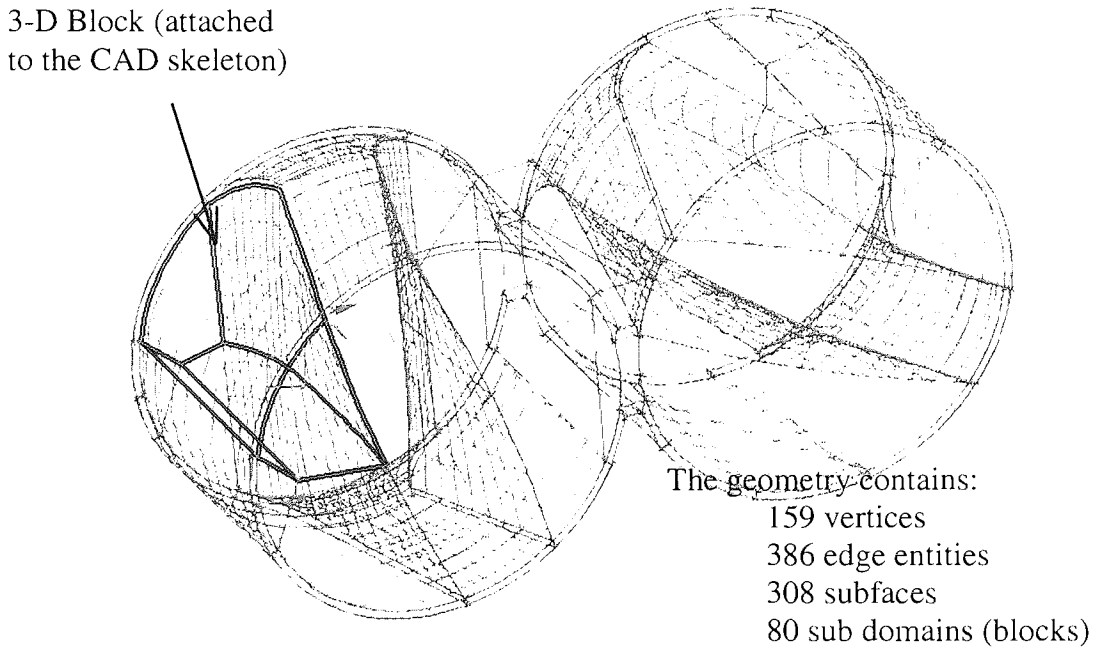

Figure 5-3 ***The completed "blocking" for the meshing process***

Node Distribution

Good node distribution is essential, especially when dealing with large domains. It is also desirable to minimise the node density. The corresponding reduction in CPU time will be particularly beneficial if many simulations using the geometry are envisaged, however, a high enough mesh density must be maintained to avoid excessive errors – the concept of mesh optimisation is focused on later in this section. Good node distribution is facilitated by good

block design. Higher densities of nodes are distributed where high parameter gradients are predicted to exist. Figure 5-4 depicts node distribution.

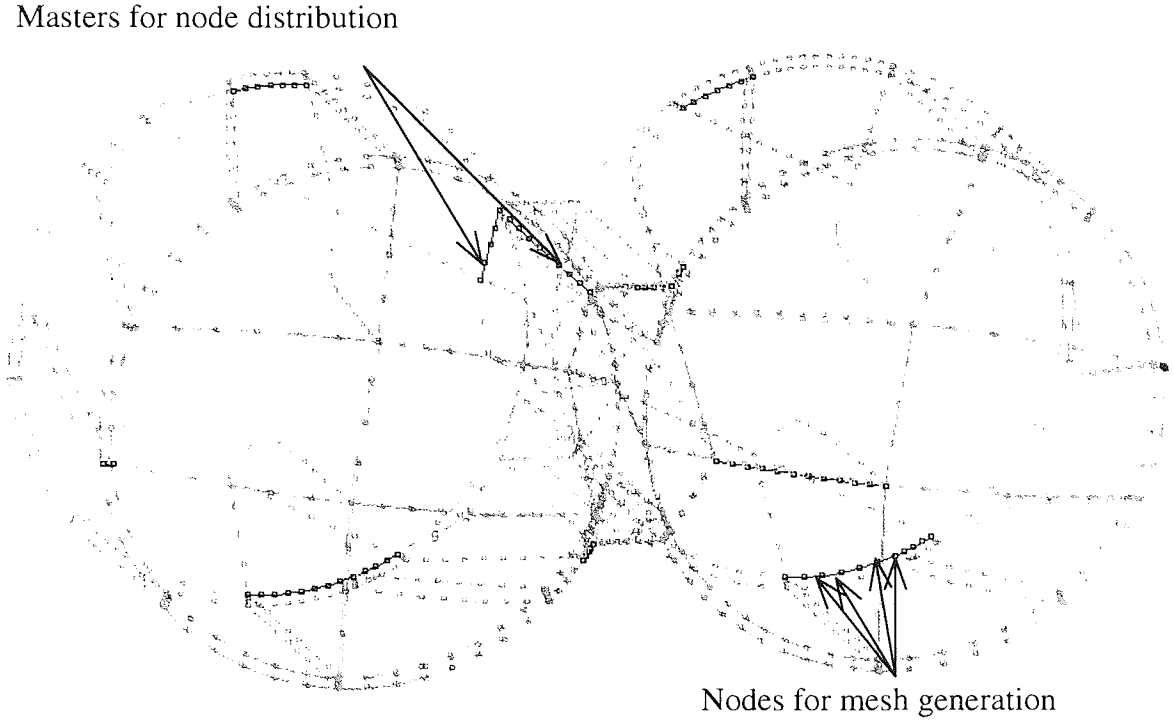

Figure 5-4 ***Node distribution for the meshing process***

Boundary definition

Fluid domains, surface families and boundary definitions have to be defined before the process can be completed. The five boundary sets used for the meshing process, as viewed in ICEM-LEO, are illustrated by Figure 5.5 - Figure 5.9

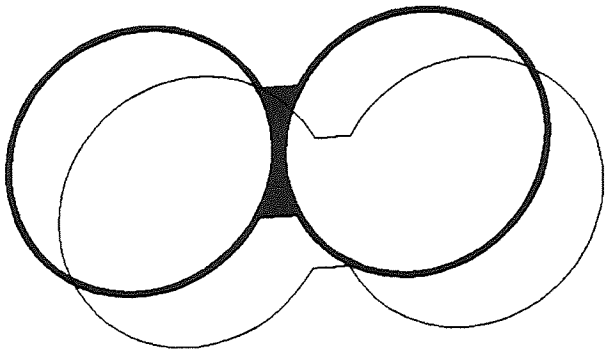

Figure 5-5 ***Mesh boundary 1***

(The back solid wall has an inside radius of 19.74mm)

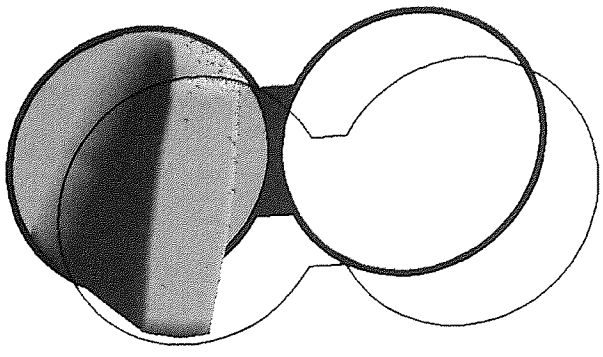

Figure 5-6 ***Mesh boundaries 1 & 2***

(The left rotor rotates clockwise at 32.6 rpm –see Table 7-1).

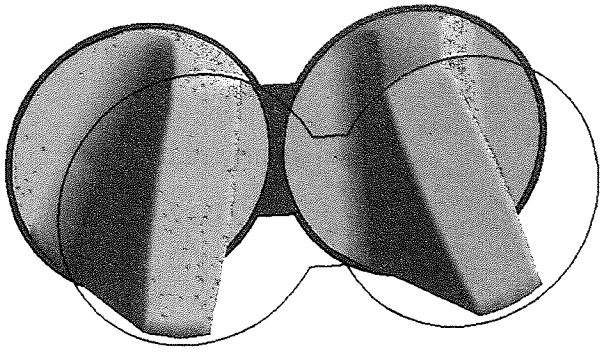

Figure 5-7 ***Mesh boundaries 1, 2 & 3***

(The right rotor rotates counter-clockwise at 21.7 rpm).

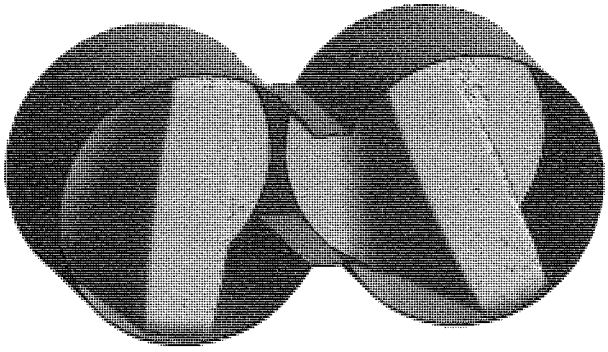

Figure 5-8 ***Mesh boundaries 1, 2, 3 & 4***

(The outer chamber wall has a rotor clearance of 0.81mm).

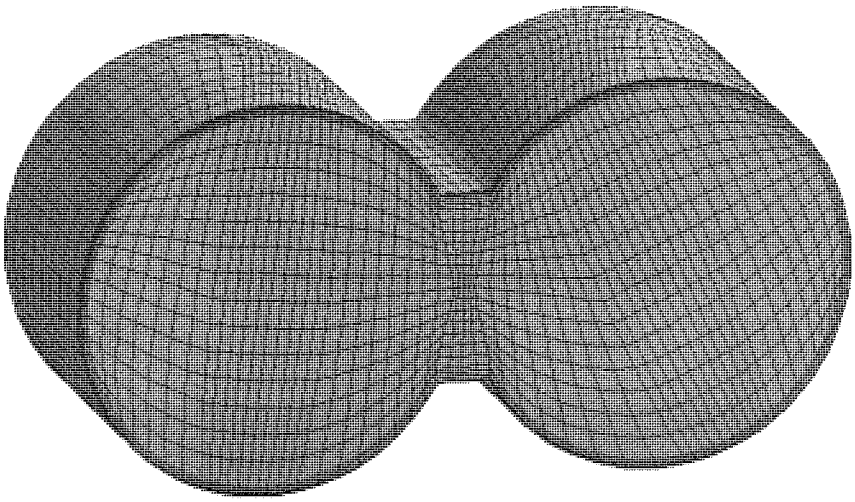

Figure 5-9 ***Mesh boundaries 4 & 5 with generated mesh***

(The front wall has a rotor clearance of 0.69mm).

Mesh Creation

A preliminary mesh, shown in Figure 5-10, has a small number of nodes (approximately 1500) and is very coarse. This mesh may be easier to appreciate than a dense mesh representing curved rotors which can appear very irregular.

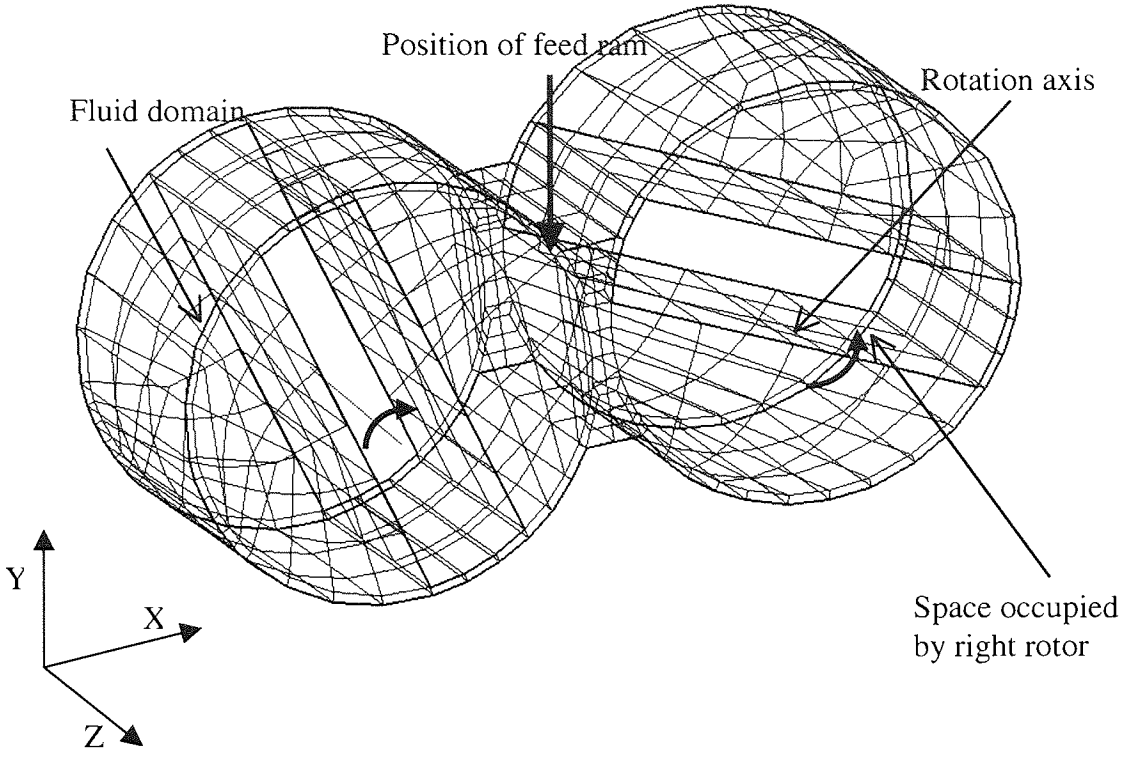

Figure 5-10 ***A coarse mesh for the simplified batch mixer geometry***

5.3 Modelling Strategy

The simulation was constructed in three separate stages each increasing in complexity until an accurate geometric representation of the process was obtained. This was necessary since the geometry's complex curving three-dimensional surfaces and the narrow clearances between rotor and the chamber wall presented difficult challenges. Splitting the process into three sections provided milestones to aim towards and provided an opportunity for mesh testing at the end of each stage. Figures 5.11a, b & c show the development of the model.

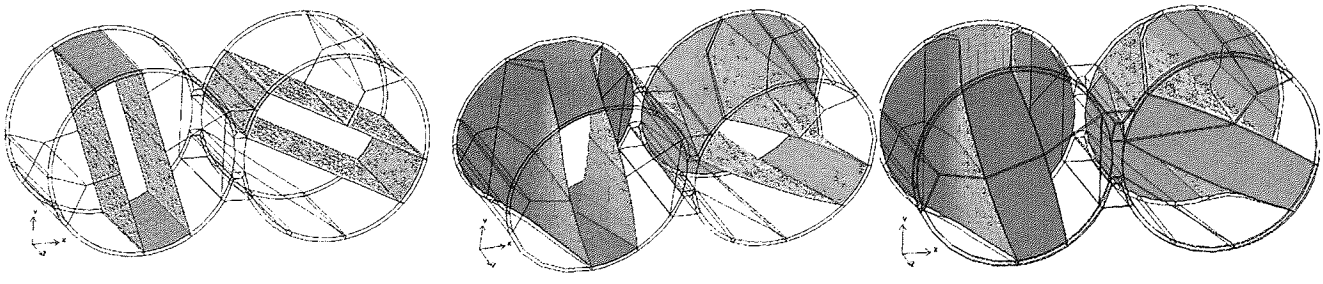

Figure 5-11a, b & c ***The three stages in the progression of the internal mixer geometry.***

The first geometry employed simplified rotors to obtain a numerical description of the internal mixer domain. The second geometry incorporated the back wall and the curved surfaces as found in the real unit. The final model also includes the front wall that had previously been ignored.

5.4 Standard Model Conditions

Every experiment using the Hampden RAPRA Torque Rheometer simulation was carried out after defining various conditions and setting key parameters. Each of these must be carefully chosen depending on the test run in hand and factors involving optimizing time and resources and accuracy required. Each run is, therefore, accompanied by an appropriate data sheet to record pertinent information. Appendix 2 contains the data sheet template used for each simulation together with a summary of model units.

5.5 Alternate Internal Mixer Rotor Configurations

The problem of modelling a rotating geometry can be overcome by taking a series of instantaneous snap shots that equate to real life motion. The situation is complicated due to the fact that the left-hand rotor rotates 1.5 times as fast as the right-hand rotor. Therefore, when taking 20-degree increments to represent one complete cycle we find there are 38 rotor configurations as shown in Appendix 3. Due to the rotational symmetry of each blade the number of unique configurations is reduced to 19. There are two reasons for not undertaking the task of modelling each configuration separately. The first reason for this is that each separate increment requires a new finite element mesh to be constructed. This would take a considerable amount of time since the model involves dealing with such a complex geometry involving complex curved surfaces, large numbers of skewed blocks and multiple block layers. This is considered by some to be the major obstacle for the finite element method[78]. Figure 5-12a and 5-12b give an example of the complex block shapes required for a Hampden RAPRA Torque Rheometer configuration.

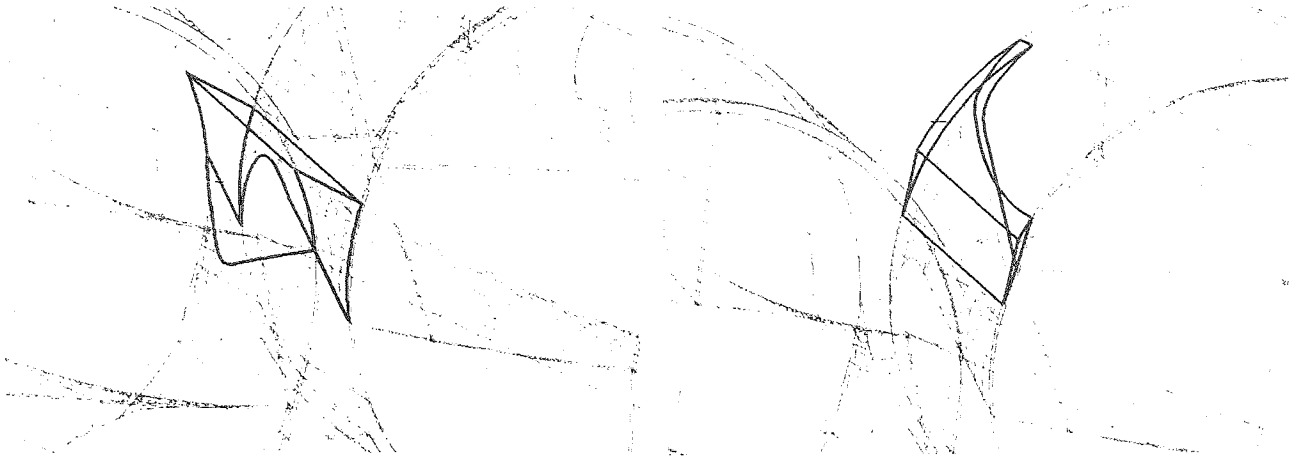

Figure 5-12a & b ***Complex blocks constructed for rotor configuration 3***

The second and most important reason was discovered after choosing to model the most extreme rotor configurations; these are:

- Rotor Configuration 1: One rotor 'horizontal' and one 'vertical' – Figure 5-2
- Rotor Configuration 2: Both rotors 'vertical' – Figure 5-13a
- Rotor Configuration 3: Both rotors 'horizontal' – Figure 5 –13b

It was found that the shear and mixing characteristics do not differ significantly between each of the three models - as reported in more detail in the next section (Table 5-1). A similar behaviour in flow and mixing characteristics for varying rotor configurations in processing equipment has been noted by Manas-Zloczower et al [79,80]. Hence, in quantifying the effect of altering the rheology, process variables, scale and rotor design on the flow field it is satisfactory to assume only one configuration is required to represent the entire mixer.

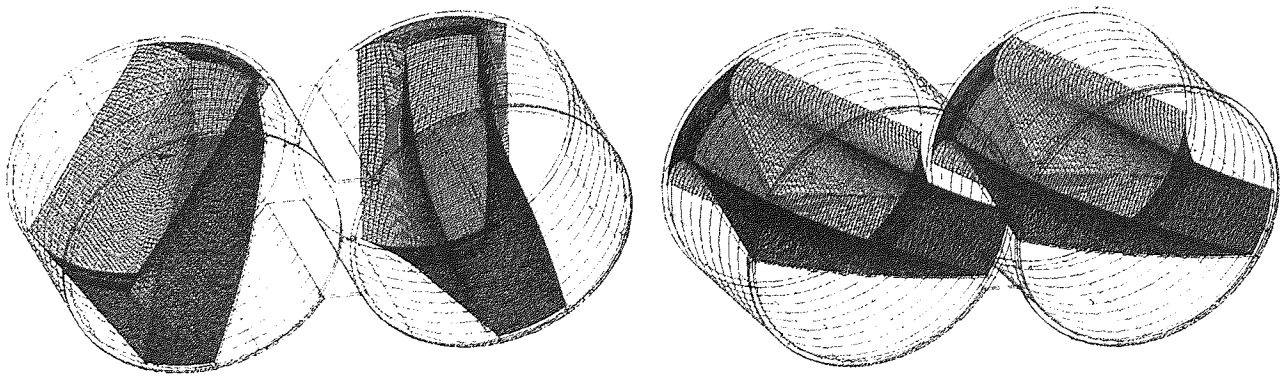

Figure 5-13a & b ***Model Rotor configurations 2 and 3***

It should be noted that the rotors in the actual Hampden RAPRA Torque Rheometer are arranged so that the one rotor will never be perfectly vertical or horizontal when the other one is either horizontal or vertical. Hence, the theoretical models have been constructed to mimic the actual rotor configurations found rather than the perfect case. Rotor configuration 3 represents the position of maximum overlap between the rotors.

5.6 Mesh Optimisation

5.6.1 Introduction

Care should be taken in defining the number of nodes for each mesh. There are four areas to consider when optimising a mesh:

- Mesh size

  This reflects the total number of nodes in any given mesh. An increase in the number of nodes will refine the mesh and as a consequence increase the *accuracy* of the results, the *swap space* requirement and the *CPU demand.*

- Solution accuracy

  The accuracy of the results will initially increase rapidly as the number of nodes increases, eventually stabilising until a point is reached where an increase in mesh density will have a negligible effect on the solution. This can be observed by monitoring the average value parameters.

- Swap space and RAM

  Swap space is the amount of 'virtual' memory required for the calculation to proceed. As mesh density increases the swap space and RAM demand increases. The amount of swap space allocation on any computer can be adjusted to fill a proportion of its hard disk. There are obvious limits to swap space and RAM and as a consequence a computer cannot solve any problem that requires more swap space or RAM than it can provide. The swap space setting on most computers is low, however, due to the high computational demands of this research, the swap space of the computational hardware at Aston has been set at approximately 5Gb (with 192Mb of main memory).

- CPU time

  The CPU time increases with mesh density. It is an important consideration when optimising a mesh. Therefore, a balance must be made between an acceptable accuracy and the 'time per iteration' of a specific flow problem

Coarse meshes yield results that only indicate general trends. If an accurate model is desired, which will give reliable and precise values of specific parameters, then the number of nodes has to be increased until optimization is achieved. Figures 5.14a, 5.14b, 5.15a and 5.15b illustrate the numerical inaccuracies of meshes with too few nodes. Note how only a general picture of the flow situation is determined from the results of a low-density mesh as compared to the corresponding results of a more refined mesh.

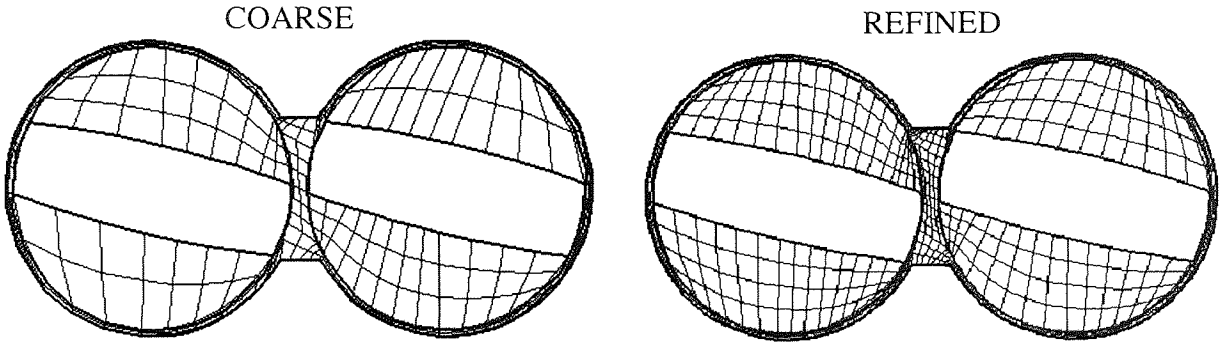

Figure 5-14a & b ***'Z' plane cross sections of a coarse and refined mesh at z = 15mm.***

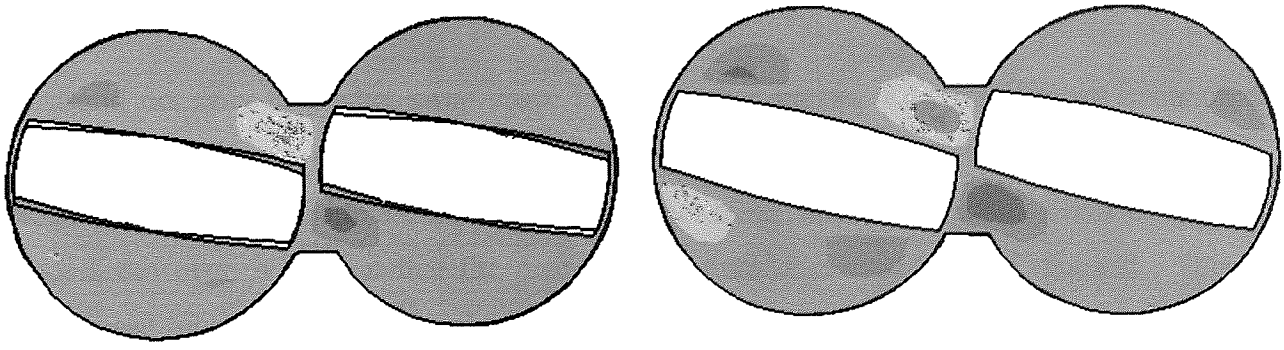

Figure 5-15a & b ***'Z' plane cross sections of a coarse and refined mesh at z=15mm showing 'z' (axial) plane velocity contours***

Along with numerical inaccuracy, geometric inaccuracy is another problem that arises when a mesh with too few nodes is used. This is illustrated by Figure 5-16 where the form of a sphere improves with increasing node density. Geometrical inaccuracies are important when

considering the Hampden RAPRA Torque Rheometer simulations since small clearances occur between the rotor and the outer chamber.

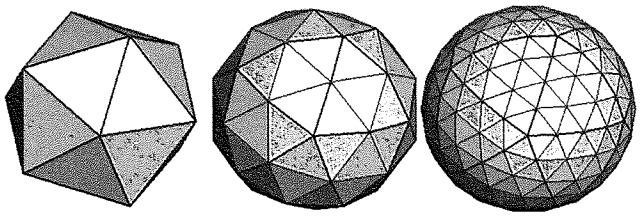

Figure 5-16 ***The effect of increasing the number of nodal points on the geometric form of a sphere.***

5.6.2 Mesh Optimisation Results

Appendix 4 holds the various parameters calculated to enable optimisation of the three rotor configuration meshes. Figures 5-17 to 5-20 are plots of the relevant data. From the plot of swap space against mesh density, Figure 5-17, we can note several points of interest:

- Swap space does not increase linearly with the number of nodes used for a mesh.
- The trend-line equations are useful to predict swap space requirement for any given number of nodes.
- Each rotor configuration requires different amounts of swap space for any given number of nodes. This is due to differing block numbers and arrangement. Therefore, it is clear that maximum mesh density depends on mesh design.
- Rotor configurations 2 and 3 have a superlative block arrangement.

It is useful not only to predict swap space but to predict solving time for a given simulation. Several external factors complicate matters relating to CPU time prediction. Figure 5-18 has three *predicted* CPU times lines, one for each configuration. When compared to *real* CPU times recorded, however, it is clear that the predictions are underestimating CPU demand. This is partly caused by simultaneous use of the computer hardware by other users. Nevertheless, with the trends predicted, combined with experience, it is possible to estimate the actual CPU times to a reasonable degree of accuracy.

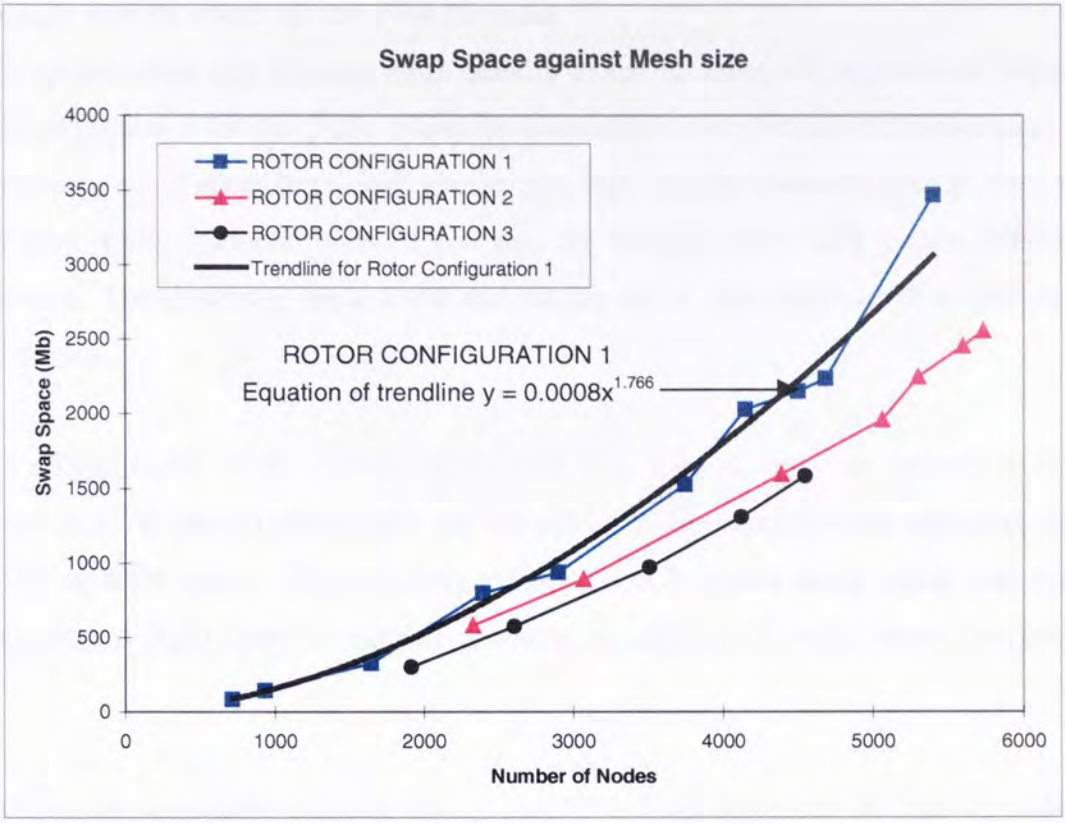

Figure 5-17 ***Graph of swap space requirement for various mesh sizes and rotor configurations***

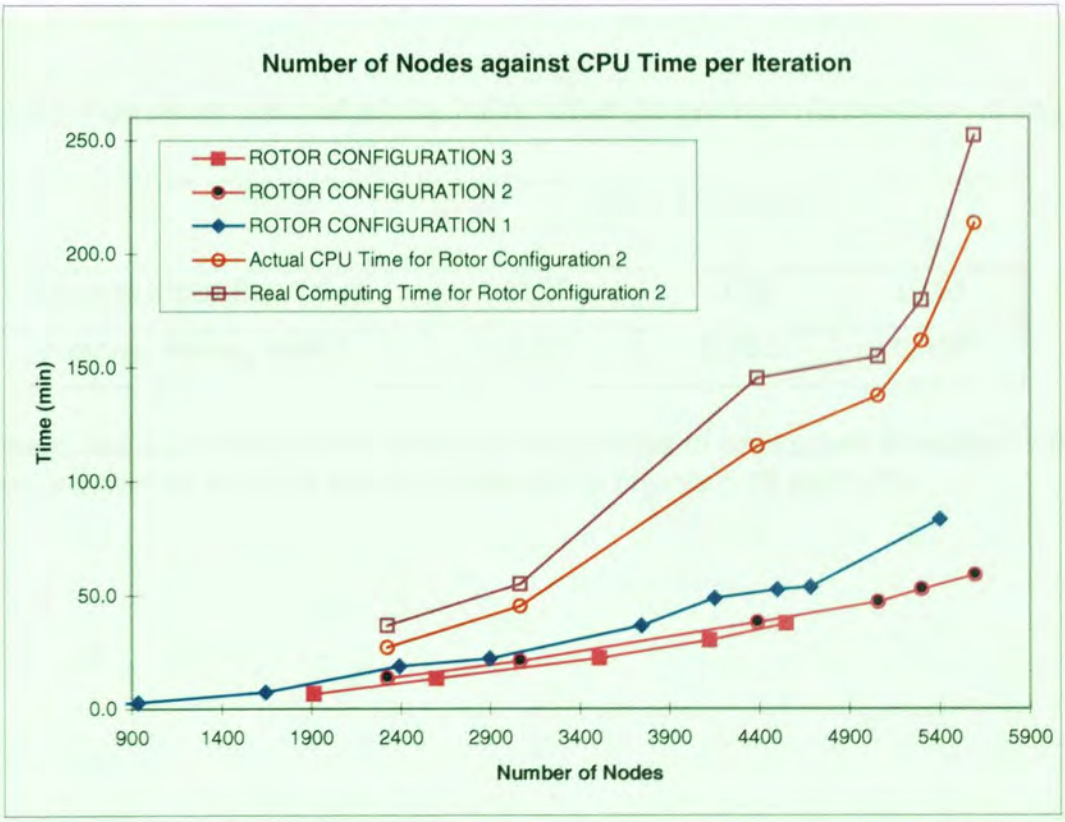

Figure 5-18 ***Graph of CPU requirement per iteration for various mesh sizes and rotor configurations***

Mesh Density and its effect on the Flow Domain

The mesh optimisation data relating mesh density to the accuracy of the solution (Appendix 4) are plotted in Figures 5-19 and 5-20. Since the simulations have modelled a Newtonian fluid the average shear rate and shear stress data give curves with similar characteristics so only the shear rate data have been produced here. However, the mixing index data yields different curve characteristics. The shear rate, shear stress and mixing index parameters are discussed in depth in the next chapter.

For rotor configuration 1 the average shear rate falls from a value in excess of 16 s^{-1} and stabilises at 12 s^{-1} at around 4000 nodes and the curve for the mixing index oscillates stabilising around 0.52 at 4500 nodes. Rotor Configuration 2 and 3 appear more stable and even when employing around 2000 nodes reasonable accuracy is achieved for both shear rates and mixing index.

All three rotor configurations stabilise at very similar average shear rate and mixing index values as can be seen by Figures 5-19 and 5-20 (taking into account the scale of the Y-axis). The apparent stabilising values of average shear rate and mixing index are summarised in Table 5-1.

Table 5-1 ***Average shear rate and mixing index values for rotor configurations 1,2 and 3***

	Rotor Configuration		
	1	2	3
Average Shear Rate* (s^{-1})	12.07	11.85	12.07
Average Mixing Index*	0.523	0.522	0.519

* These shear rate and mixing index values quoted thought to be accurate to within +/-0.01 with confidence provided by from the stability of the trends Figures 5-19 and 5-20.

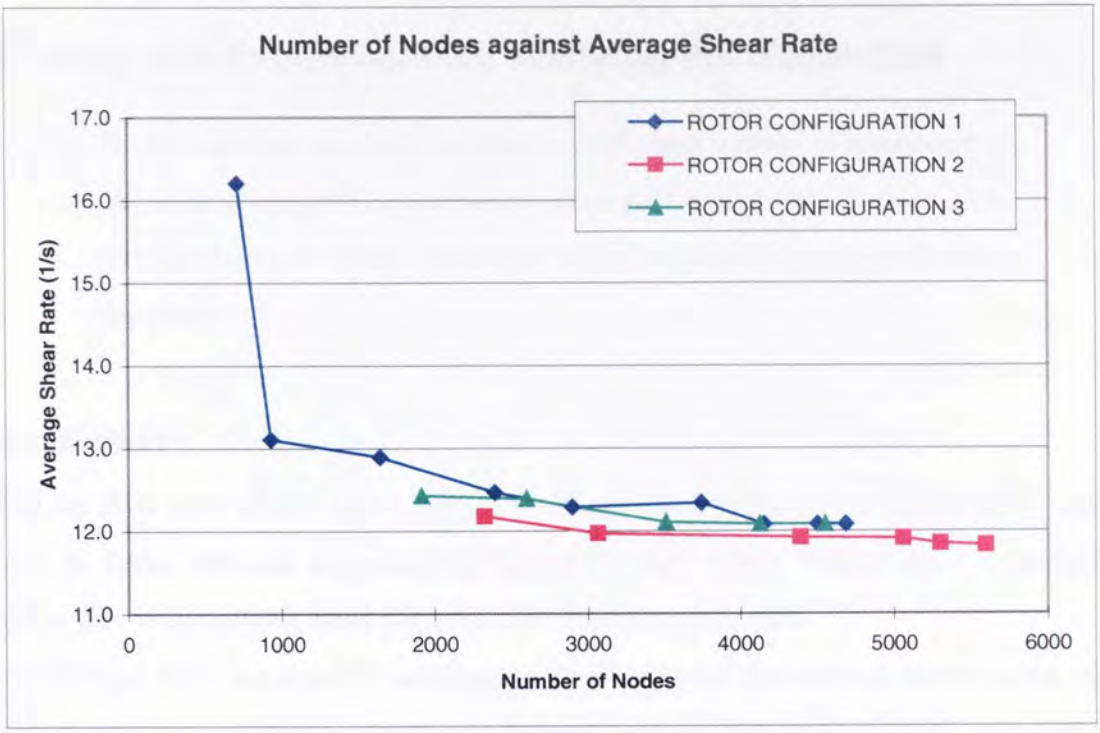

Figure 5-19 ***Graph of average shear for various mesh sizes and rotor configurations***

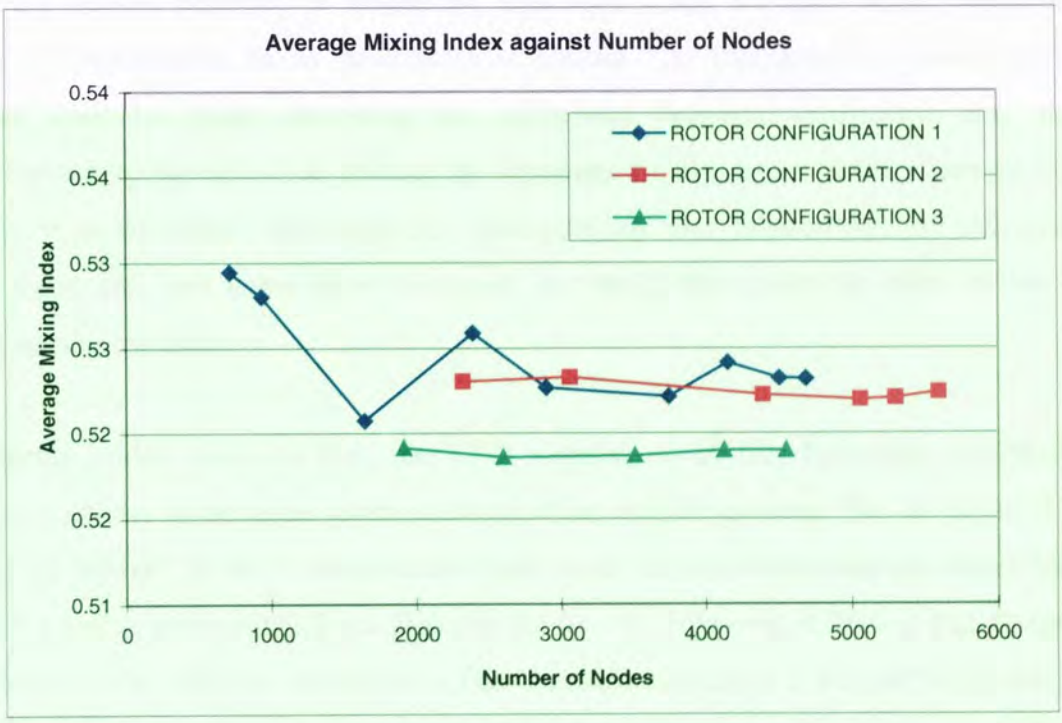

Figure 5-20 ***Graph of average mixing index for various mesh sizes and rotor configurations***

In conclusion, taking into account the graphs reproduced in this section and by observing various contour patterns (as per Figure 5-14 & 5-15), it appears that meshes that have approximately 4500 nodes give accurate results.

6. Exploring and Experimentally Verifying the Simulation

In this section we find qualitative and quantitative comparisons of the simulation with experimental observation and data derived from the mechanical model constructed for validation and verification purposes.

6.1 Introduction

Exploring the flow field within the Hampden RAPRA Torque Rheometer via the CFD simulation goes hand in hand with the experimental investigations. Flow visualisation experiments, as described in this section, have been performed to achieve two goals.

- To understand flow and mixing mechanisms involved with the internal mixer operation,
- To make direct comparisons with the 'virtual' mixer and hence verify and validate the simulation.

Determining model accuracy is extremely important since without model verification and validation the confidence in its predictions is limited. At this point a noteworthy semantic distinction shall be made describing the difference between verification and validation. Verification can be thought of as solving the equations rightly, and validation can be thought of solving the right equations. Although this difference has been pointed out, for convenience and to avoid repetition, both terms have been used separately throughout the body of this thesis to convey a similar meaning.

A hypothesis which purports that the CFD simulation of the Hampden RAPRA Torque Rheometer provides an accurate representation of the real life process, like all physical theories, can never be proven. Even if experiments agree with the hypothesis one can never be entirely sure that the next experiment will not disprove the theory. However, a finding that disagrees with the predictions will disprove the theory. The simulation presents a number of predictions that could, in principle, be disproved by observation; that is if the experiment itself yields accurate information. Therefore, it is clear that no one experiment will serve the purpose of model verification, rather, a series of specific experiments will be necessary in order to collect a body of evidence to establish model validity. In order to achieve this goal each output from the numerical solution should be considered in turn. The four principle dependent variables from the coupled mass and momentum balances are:

- The velocity vectors in the x direction
- The velocity vectors in the y direction
- The velocity vectors in the z direction
- The system pressures (forces)

These principle variables must be examined and appropriately verified by experimental methods. All other outputs from the simulation, e.g. shear rate and mixing efficiency, are derived from these principle variables, hence, if the principle variables are proved to be reliable their reliability is transferred to all the other outputs. Since, in this simulation, the shear dependency of viscosity is taken into account via the power law model – Equation 3-4, it is appropriate to assess this ideal also. The last section in this chapter summarises the points discussed from each section and puts forward a case, based on the body of evidence collected, to support model validity.

As previously mentioned experimental verification of theoretical CFD models for viscous fluid flow in real geometries and process situations has, generally, been neglected. The literature does reveal some interesting work on the way to 'proving' that CFD models of viscous processing equipment, if used correctly, accurately represent reality. The Kenics static mixer has been modelled in 3 dimensions, using the Polyflow codes, and the resultant velocity vectors have been used to calculate trajectories and hence the paths of 8000 hypothetical particles. The results were compared to an experimental model in an attempt to replicate the mixing patterns predicted by the theoretical model. An extremely good match was found for various cross sections taken along the length of the mixer[81]. Simulations of highly viscous polymer processing equipment involving precise and complete three-dimensional *time dependent geometries*, however, have not been satisfactorily verified. This may be put down to several possible reasons:

- CFD users assume that CFD is 100% accurate and therefore no reason to proceed with verification experiments.
- Constructing mechanical models require considerable time, effort and money.
- Comparing CFD results directly to sensors and meters on existing processing devices used in industry is difficult and provides little supporting evidence. For example, it is quite common practice for researchers to offer a comparison of the high pressures found between the chamber wall and rotor tip in their simulation and that from a pressure sensor in the experimental model as evidence of model validity[82,83,84]. Although the comparisons maybe of the same order of magnitude or better, these values of pressure, even if accurate, say nothing about the rest of the domain.

- Some models may have used inappropriate assumptions, equations, numerical methods or discretisation resulting in comparisons that may be poor.
- CFD can not be satisfactorily verified!

In previous research into the flow of polymeric material in twin screw extruders using CFD, conducted at Aston by Wilson *et al,* a problem was encountered that limited verification. A mechanical model of a closely intermeshing co-rotating twin screw extruder (CICo-TSE) was employed to study the flow patterns in the mixing disc region. The mixing disc apertures have a radius of only a few millimetres and this prevented any serious, reproducible findings. The screw channels, however, within an extruder are a good situation to model since their geometry is simple, the geometry does not change with time and model validity can be assessed by experimentation since access is not restricted by other moving parts. A serious attempt to quantitatively validate model results in the axial and azimuthal direction for the flow of corn syrup screw channels in a twin screw extruder, including the nip region, has been made by Sernas, Karwe et al using Laser Doppler Anemometry (LDA) yielding "fairly close agreement" between the CFD predictions and LDA results[85,86]. The LDA technique has previously been used quite commonly to determine point velocities in stirred tanks[87].

6.2 Flow / Mixing Study and Velocity Vector Verification

6.2.1 Mechanical Model

As part of the validation procedure a mechanical model of the Hampden RAPRA Torque Rheometer, with a transparent outer case allowing visualisation of the process was designed and constructed. The model was designed with the following considerations:

- Low cost.
- Material to be completely transparent.
- Simple to machine.
- Material must not degrade by chemical or physical conditions experienced in the mixer.

Two outer casings were considered:

1. Simple rectangular Perspex case with removable Perspex front cover (making construction and cleaning easy) to be fitted over existing rotors - allowing total visibility of mixing mechanisms.

2. Simple rectangular steel case with removable toughened glass front cover - allowing the process to be viewed from the front only but allowing processing at realistic temperatures (above 100°C).

The first option was chosen allowing complete flow visualisation. Scaled diagrams, including dimensions, are given in Figure 6-1 and Figure 6-2. Should it be considered necessary to investigate mixing at higher temperatures in any future investigations the second design could also be manufactured easily and at a low cost.

Flow visualisation techniques have been used to understand the mixing phenomenon for such mixing equipment as the Banbury internal mixer[88] and the Haake Buchler Rheocord laboratory mixer[89]. Although flow visualisation has been carried out in conjunction with CFD simulations comparisons have been weak as far as the author is aware. One advantage of choosing the Hampden RAPRA Torque Rheometer to carry out flow visualisation investigations is that the "material viewing area", when observing the process normal to the plane of rotation, is very good. Another advantage of modelling the Hampden RAPRA Torque Rheometer is that its simple non-intermeshing rotor design will result in a less complicated mixing action hence making the verification task one that is possible.

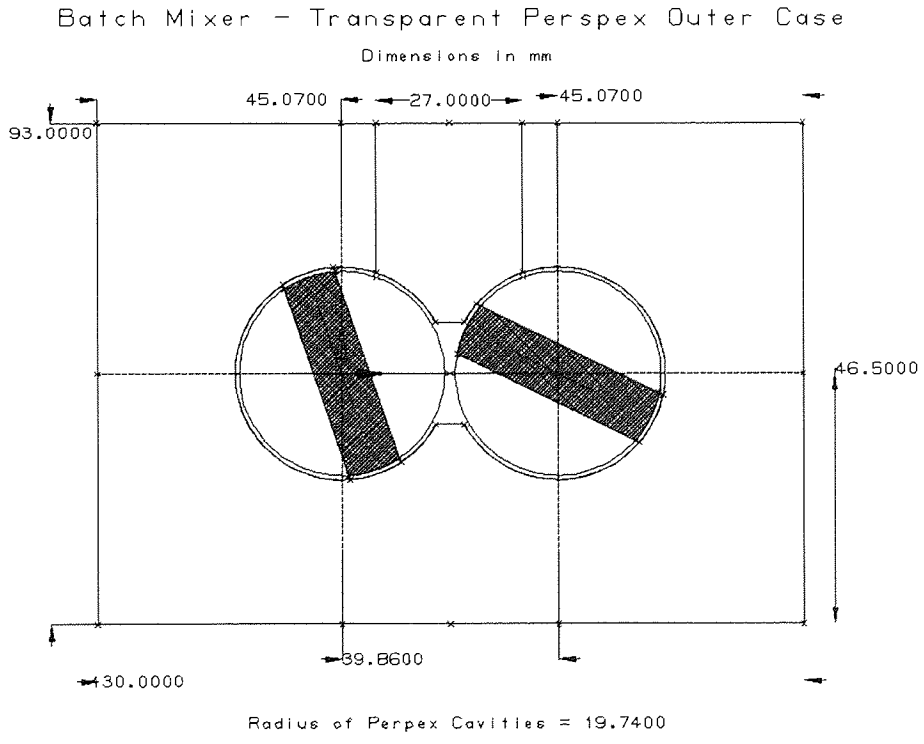

Figure 6-1 ***Scaled representation of the Hampden RAPRA Torque Rheometer transparent outer case - Front view***

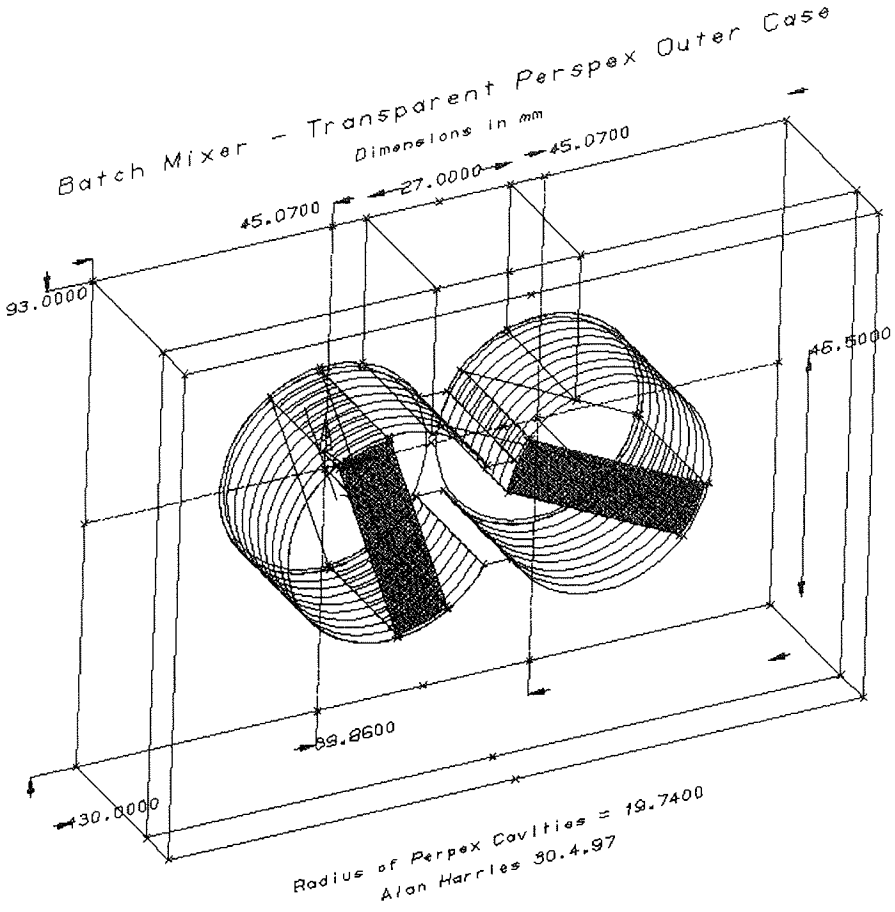

Figure 6-2. ***Scaled representation of the Hampden RAPRA Torque Rheometer transparent outer case - Isometric view***

6.2.2 Qualitative Study on Mixing

A variety of experiments were performed by the author using a selection of materials used in various proportions and arrangements in order to investigate the flow and mixing mechanisms within the Hampden RAPRA Torque Rheometer and to verify the CFD simulation. Trials involved either transparent viscous fluids (as follows in section 6.2.3) or distinctly coloured viscous fluids. Experiments using the coloured fluids involved careful packing of two coloured 'clays' with identical physical properties[#] of various proportions and arrangements into the cavities between the rotors and the outer chamber wall. Voidage was always kept to a minimum as much as possible since the simulation assumes full fill. After mixing for a number of turns the mixture and the Perspex chamber wall were carefully separated. The mixed clays were sliced into thin sections with a narrow gauge wire and, by observing the fine cross sections, the laminar mixing patterns were revealed. This technique of revealing the inner flow patterns overcomes the

[#] Composition of Coloured Doh (%vol): 50% Flour, 40% Water, 8% Salt, 1.5% Tartar, 0.5% Vegetable Oil.

problems experienced by flow visualisation experimentalist who viewed their mixtures as they are being mixed (when using opaque materials only the outer surfaces can be seen and the patterns are soon obscured beyond comprehension by smearing).

The theoretical simulations modelled two types of fluids:

1. Hypothetical viscous fluid representing a typical viscous polymer
2. Specific viscous fluids used for experiments with the mechanical model

When simulating the mixing of the actual fluids used in trials (clays and gels) in the Hampden RAPRA Torque Rheometer it was necessary to input their material properties into the programme. Hence, the material properties of these fluids needed to be experimentally determined. The shear dependency of viscosity for these fluids was determined using the Haake viscometer (as outlined in chapter 3). Appendix 5 contains the plots from data gathered for the fluids used. It can be seen that the use of the power law is perfectly adequate to describe their shear dependency of viscosity. Appendix 5 also focuses on the importance of using the correct shear range when determining the power law constants. Table 6-1 presents a comparison of the power law constants for common polymer melts[90], viscous coloured 'clay' and the transparent gels used.

Table 6-1 ***Power Law constants for polymer melts, the doh mix and the transparent gel.***

	Poly-propylene*	Poly-styrene*	LDPE*	HDPE*	Coloured 'doh'**	Gel**
Index	0.5	0.32	0.45	0.4	0.36	0.4114
Factor	4400	15600	4800	18900	1933.5	54.57

*at 200°c (typical mix temperature)
** at ambient temperature

Note: The density of Polypropylene and coloured 'doh' is 800 kg/m^3 and 1150 kg/m^3 respectively.

To study the mechanism of material transfer between rotor chambers an experiment was devised employing different coloured clays packed in the separate chambers. A material interface in the central plane was created as indicated in Figure 6-3. By observing the interface deformation it was discovered that the material flux across the central plane alternates from left to right depending upon the rotor configuration at a certain point in time. The transfer takes place at the base of the central plane and this new material entering a chamber takes a form resembling an elongating sickle. As the mixing progresses this elongation continues, as seen in Figure 6-3.

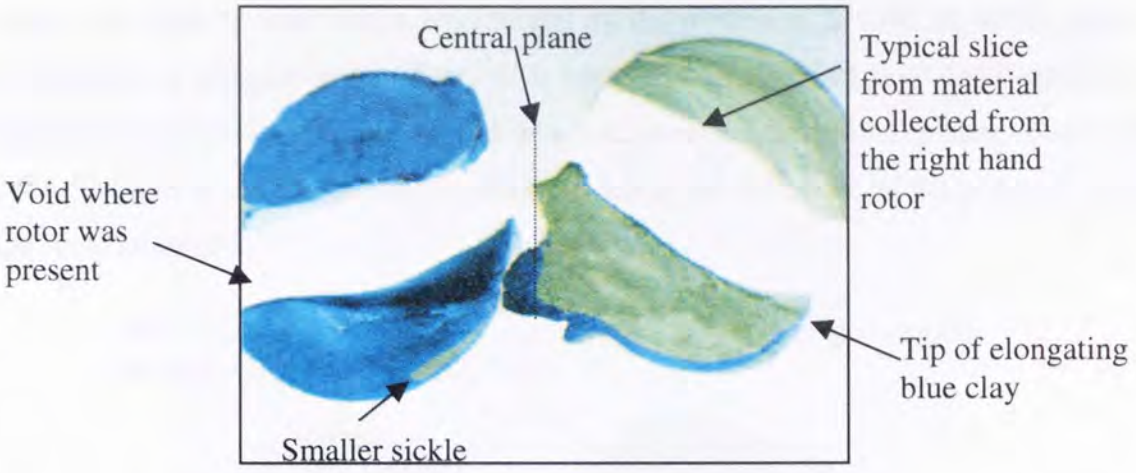

Figure 6-3 ***Material transfer after 2π revolutions of the Mechanical Model***

A similar material transfer pattern is predicted by the simulation. Material streamlines generated from the left-hand rotor, as illustrated by Figure 6-4, continue until they contact a solid body e.g. the right-hand rotor. It is important to bear in mind when studying streamlines that the model represents a snap shot in time. The material will never 'catch up' to a rotor, as one may interpret from the diagram, since the rotors are continuously rotating. However, this type of analysis produces a good qualitative insight to mixing mechanisms. For this particular rotor configuration the majority of the flow follows the rotor with a small percentage being driven into the neighbouring chamber. When viewed from above the material streamlines in Figure 6-4 tend to bend slightly towards the back of the chamber due to the small amount of axial flow induced by the rotor curvature.

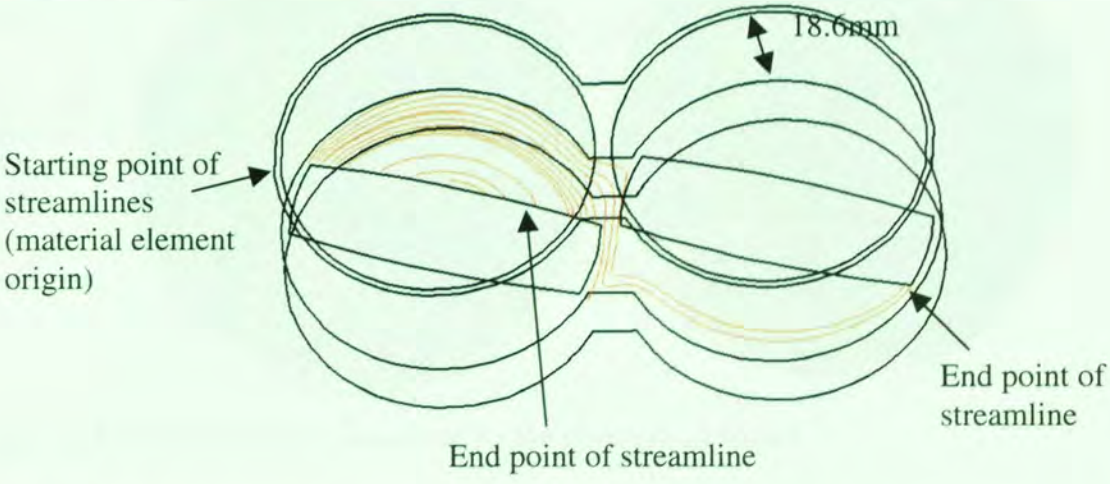

Figure 6-4 ***Material transfer in the simulation- rotor configuration 3***

After several rotations 'horse shoe' patterns appears as shown in Figure 6-5. What resembles 'material folding' is actually caused by a velocity differential as shown by the simulation. Figure

6-6 discloses the velocity distribution engendered by the motion of the rotors, which takes the form of Poiseuille or pressure driven flow. It is noted that this type of flow contrasts with that found between the tip and the chamber wall which is shear dominated i.e. planar couette flow. The velocity profiles at the tip are slightly concave due to the influence of the pressure gradient across the rotor landwidth.

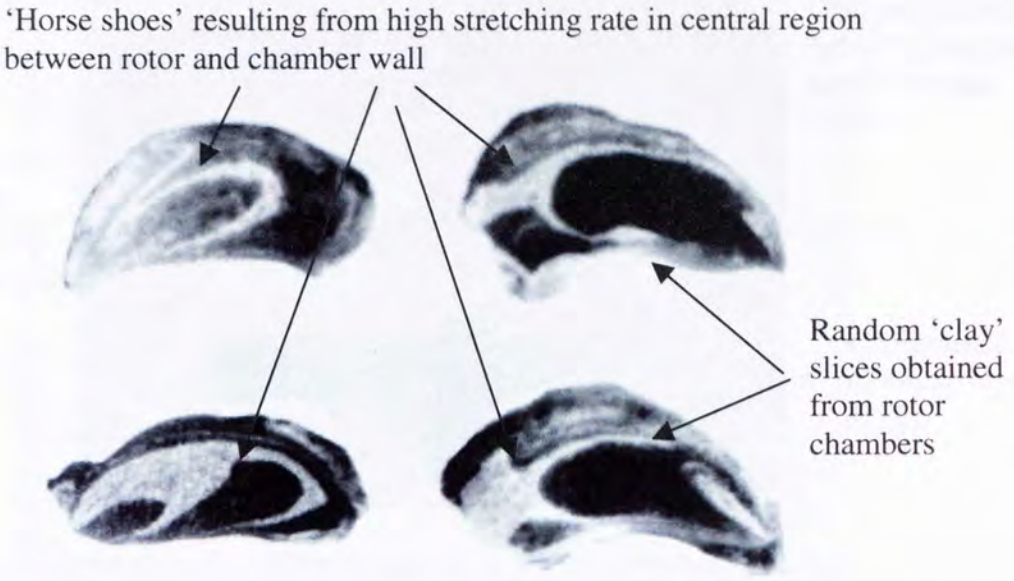

Figure 6-5 ***Mixing patterns after 8π revolutions in the mechanical model***

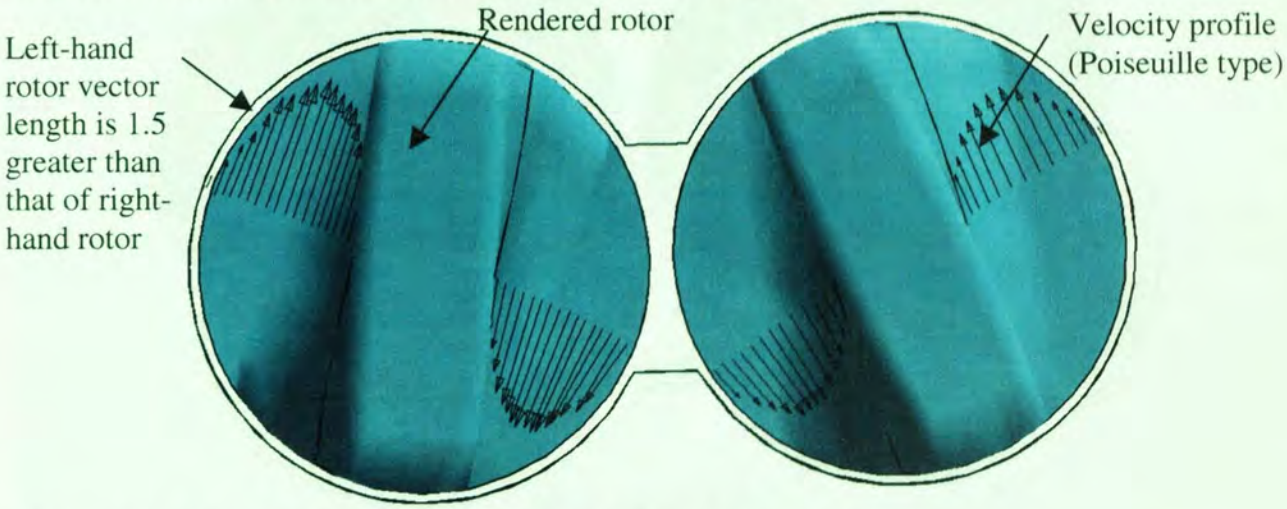

Figure 6-6 ***Velocity profiles predicted by the theoretical model***

When viewing the mixing process in the mechanical model normal to the plane of rotation it can be noted that doh layers are periodically forced into the area between the Perspex cover and the main Perspex case. This occurs if either too much clay is packed into the chamber or if the screws that hold the cover secure are not tightened sufficiently. These compressed layers are

preserved as they are generated and can be seen to extend around the edge of the chamber Similarities between these preserved layers and material streamline close to the front wall in the CFD model can clearly be seen; see Figure 6-7 and Figure 6-8.

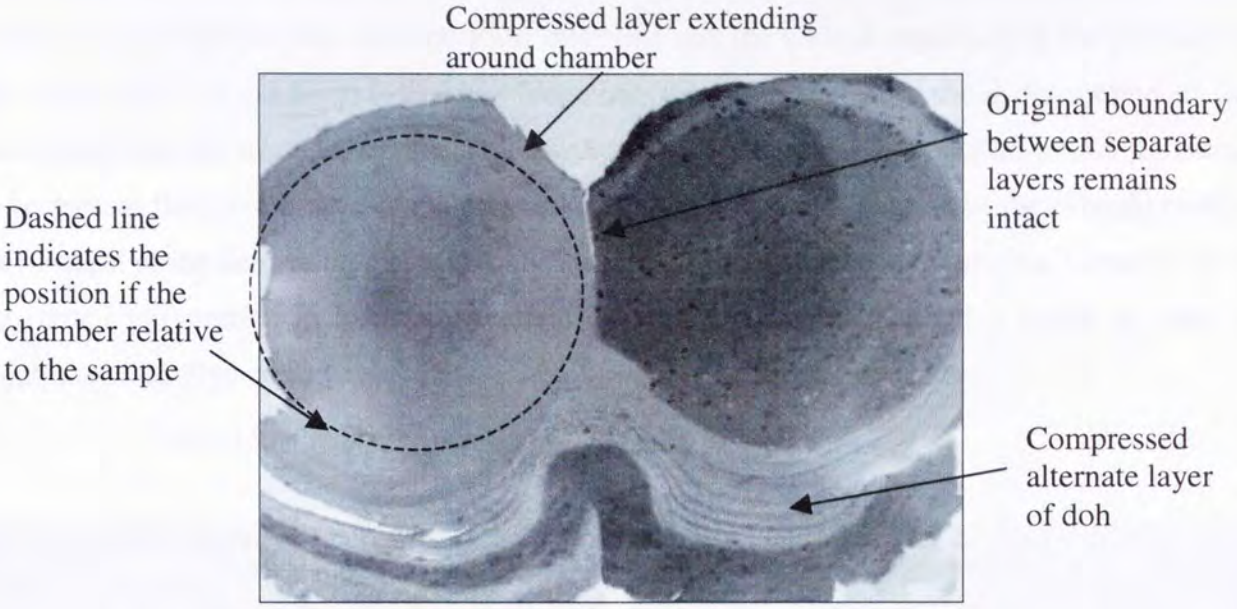

Figure 6-7 ***Material transfer after 18π revolutions in the Mechanical Model***

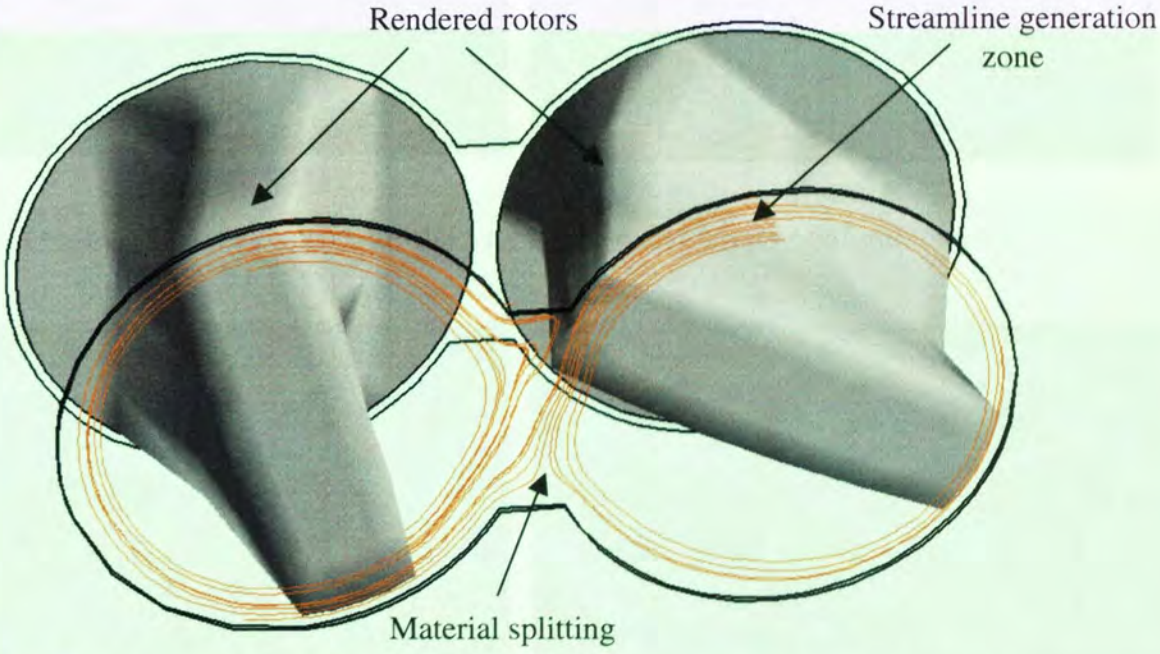

Figure 6-8 ***Material transfer in the simulation - rotor configuration 1 at z=24.3mm***

Various qualitative experiments have been performed but one series of tests in particular were realised to provide both a stage by stage account of the initial mixing period and to provide a better qualitative comparison for the simulation. Figure 6-9 *(frames A – J)* is the product of these trials represents the first nine snap shots or frames taken to reveal how a horizontal plane of doh

is mixed into the bulk phase at various advancing time increments. The tenth frame characterises the mixing after 12π rotations.

Care was taken to ensure that rotor configurations 1, 2 and 3 were each represented by two 'snap shots'; one representing the rotor position modelled and the second representing the position of the rotors after a short period of time. Together, the two snap shots show the motion of the deforming material around a simulated configuration. If the simulation is used to plot a number of vectors, at the co-ordinates of the material boundary of the first snap shot, they should predict the position of the deforming material in the second. If the two snap shots and the vector plots of the rotor configuration in hand are overlaid one obtains a good qualitative match as seen in Figures 6-10 to Figure 6-13.

Dotted line indicates position of doh strip at t = 0 s

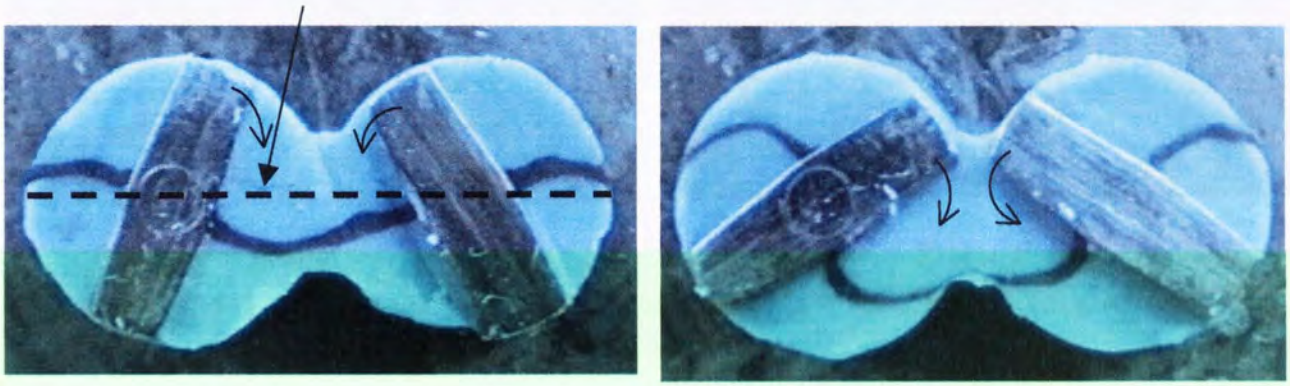

Frame A *Frame B*

Frame A represents the motion of the deforming plane about rotor configuration 2

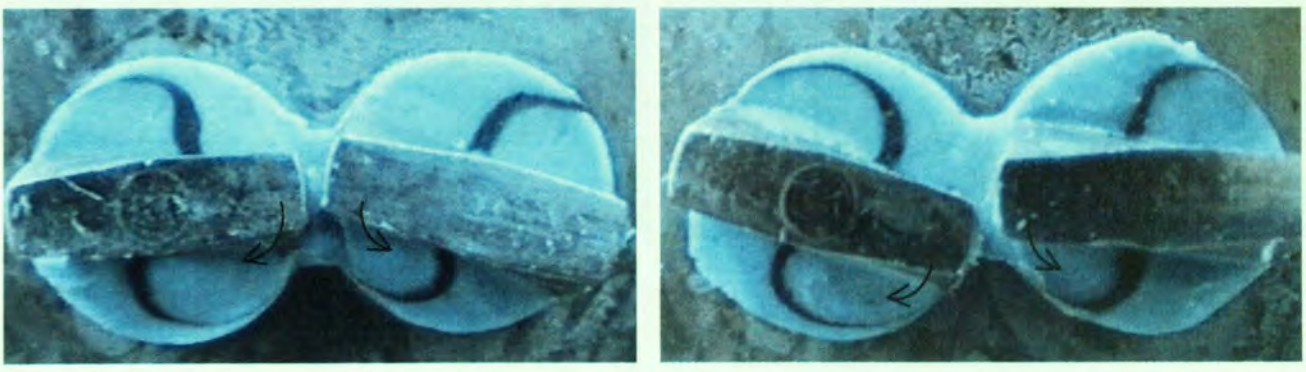

Frame C *Frame D*

Frame C and D represent the motion of the deforming plane about rotor configuration 3

Frame E

Frame F

Frame G

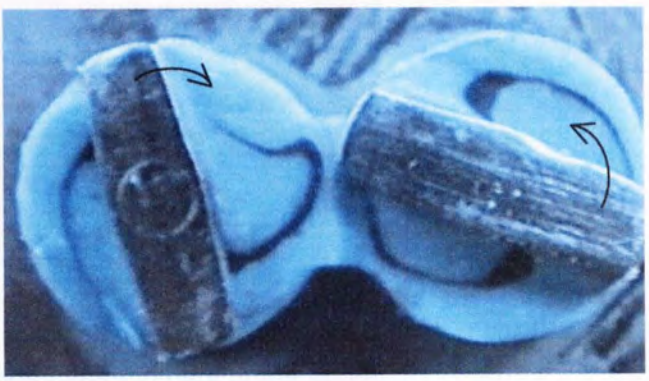

Frame H

Frame G and H represent the motion of the deforming plane about rotor configuration 1

Frame I

Frame J

Figure 6-9 ***The deformation of a horizontal plane in the internal mixer –Frames A-J***

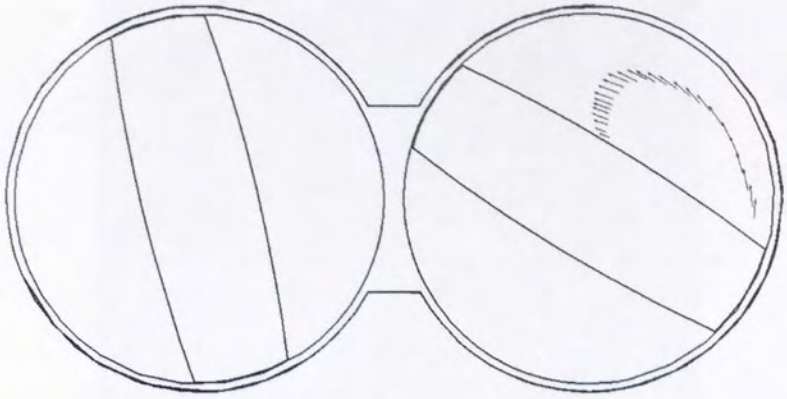

Figure 6-10 ***Velocity vectors plotted around Frame G***

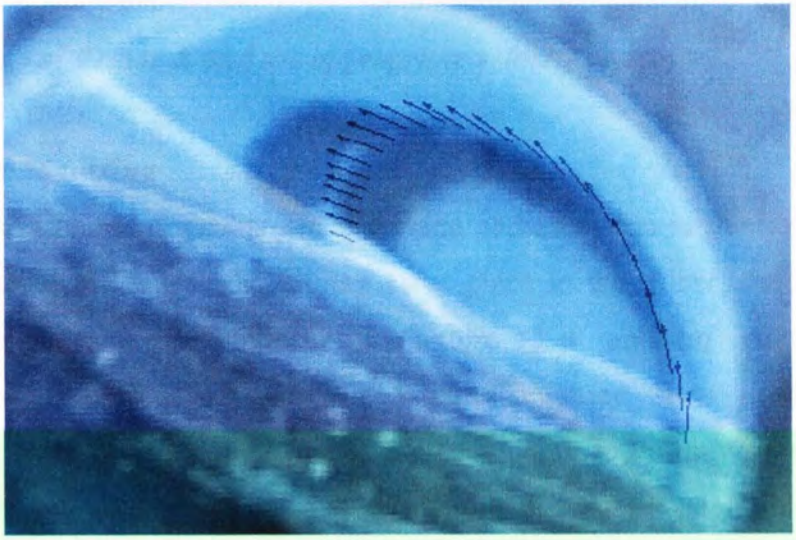

Figure 6-11 ***Overlay of Frame G and H and Velocity Vectors***

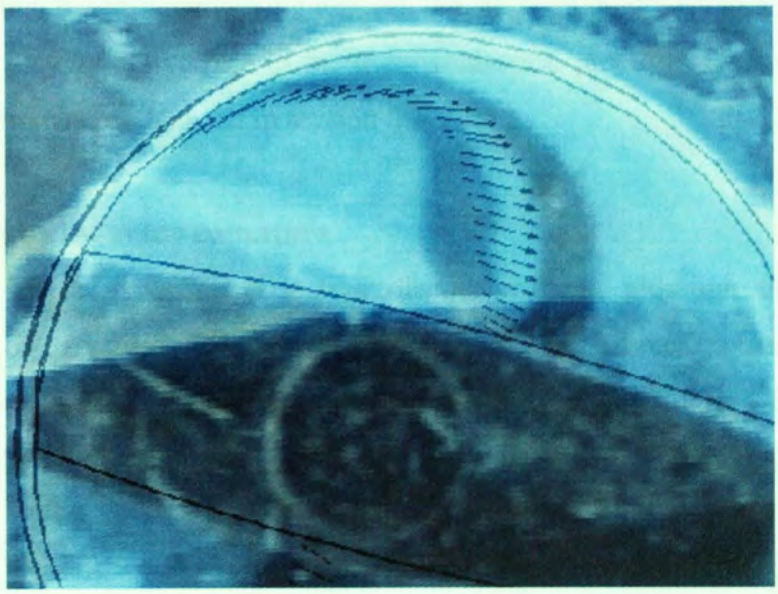

Figure 6-12 ***Overlay of Frame C and D and the appropriate velocity vectors***

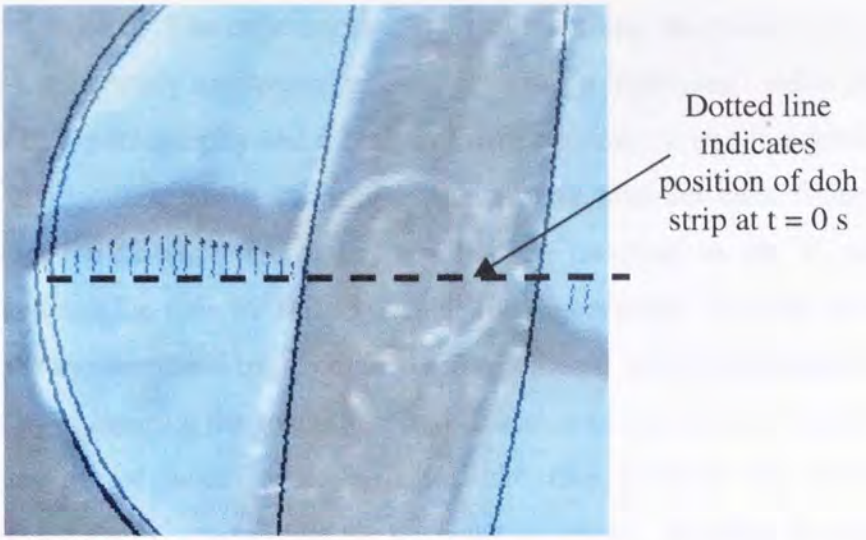

Figure 6-13 ***Overlay of Frame A and the appropriate velocity vectors***

Action of diffusion in mixing

Diffusion can be an important mechanism in mixing and its action in internal mixers has been considered. It is evident that, as the mixing takes place in the mixer, the striation thickness decreases and the shear stresses reduce the mixture to a 'uniform' colour. At this point homogenisation is achieved. As with the viscous coloured clays used in experimental investigations the majority of polymer blends are considered to be immiscible. However, an interfacial composition gradient exists due to the finite (usually negligible) solubility of a polymer in every other polymer. The diffusion coefficients are of the order of 10^{-13} cm^2s^{-1} [91] so a striation thickness of the order of 10^{-5} cm (0.1μm) will have a diffusion scale of time equal to 10^3 seconds. Hence, when the laminar mixing reduces the striation thickness to a small enough scale then diffusion will play an active role in the homogenisation process. Diffusion coefficients in these types of simulations can be seen in section 8.3.2.

Axial flow induced by the rotor curvature

Whilst performing these experiments it was discovered that, although the rotors posses a substantial amount of curvature, material transfer in the axial (z) direction was poor. Examining the CFD model prior to the practical experiments identified this anomaly. Distributive mixing could be improved by altering the rotor design. This is examined in more depth in a later section.

6.2.3 Quantitative Assessment of Velocity Vectors

The aim of the second type of experiment performed was to *quantify* the velocity of material elements within the mechanical model, thus, enabling direct comparisons to be drawn from all

three rotor configurations simulated. The experiments involved recording the motion of a small spherical inert particles in a completely transparent viscous gel using a high-speed video camera. A macro lens allowed close up photography and a built in timer, accurate to one hundredth of a second, provided means of recording small changes in the mixing time on each frame. By inspecting the freeze frames the distance and direction a particle travelled in the 'x' and 'y' directions could be measured and the time for this to occur. The co-ordinates from the particle's point of origin, i.e. where the measurement began, could then be entered into the simulation and a vector calculated. Hence, by comparing the magnitude and direction of the velocity vector from the simulation the accuracy of the model could be assessed. One problem that arose was obtaining an accurate value for the 'z' co-ordinate for the point of origin. To solve the problem the particle was viewed from above and callipers used continuously measure the position of a particle in the 'z' direction. The accuracy of this method was estimated to be in the region of +/- 1mm. Fortunately, the 'x' and 'y' velocity components do not vary significantly within a +/- 1mm axial variation in the majority of the domain. Table 6-2 presents the data obtained from examining the motion of fourteen real and simulated particles and quantifies any discrepancies between the CFD simulation and the real system.

Table 6-2 ***Velocity vector comparison between the CFD model and experimental values***

Location of Particle Origin*		Velocity					
Co-ordinates** (mm)		Point Trajectory (deg)			Vector Magnitude (mm/s)		
'x'	'y'	Exp.	Sim.	%diff.	Exp.	Sim.	diff.
[1]42.22	11.37	291.8	287.9	1.1	35.5	38.7	3.2
[1]53.76	6.47	329.0	328.8	0.1	33.2	38.5	5.3
[1]43.81	9.56	294.3	295.4	0.3	35.8	36.8	1.0
[2]28.02	6.32	204.6	205.6	0.3	25.3	36.5	11.2
[2]25.33	-7.58	145.5	143.6	0.5	30.3	34.5	4.2
[2]25.96	6.32	203.6	205.8	0.6	34.5	37.7	3.2
[3]30.54	-7.11	125.7	128.7	0.8	36.1	37.3	1.2
[3]39.71	-16.11	89.7	92.7	1.0	27.8	33.1	5.3
[3]42.16***	-13.90	82.2	86.0	1.1	38.6	40.3	1.7
[1]9.22	6.95	140.0	142.3	0.6	47.4	53.3	5.9
[2]13.80	5.37	159.5	162.9	0.9	45.7	55.3	9.6
[2]14.75	2.37	175.2	173.16	0.6	53.7	52.3	1.4
[1]16.17	8.05	150.2	138	3.4	31.6	34.3	2.7
[2]14.43	-3.32	202.6	198.7	1.1	52.6	51.6	1.0
			mean	0.9		mean	4.0

Notes:

* All vector origins were taken at z = 15mm (+/- 1mm)
** Co-ordinates taken from the left-rotor axis
*** Vector was taken at z = 12 mm (+/- 1mm)
[1] Rotor Configuration 1
[2] Rotor Configuration 2
[3] Rotor Configuration 3

The range for the point trajectory is 0 –360 deg where zero equates to a particle moving vertically upwards.

Discussion of experimental technique and results

Several problems had to be overcome to enable this technique to produce results which were as accurate as possible. For example, to limit the number of air bubbles present, the gel was carefully added into the horizontal rotor chamber and the liquid level allowed to even out. Any air entrapment was eliminated by using a hypodermic needle and a syringe. The chamber was then positioned vertically and slowly fitted over the rotors. The rotors are quite complex in their design and air had a tendency to enter into the gel as the gel was being displaced by the volume of the rotors. Loading excess gel in the chambers alleviated this problem. Another difficulty encountered was the gel's tendency to cloud after a short period of time. This was solved by electroplating and cleaning all surfaces and therefore eradicating the grease and oil which had caused the gel to cloud.

The time, and hence distance a particle was allowed to travel when measuring a specific vector, was kept to a minimum (approximately 0.2 s). The reasons for this are twofold. Firstly, the accuracy of the trajectory measured would diminish, and secondly, to keep the position of the rotors true to any one of the three configurations examined. As a consequence of minimising the time the accuracy of the vector magnitude may have suffered.

Initially, the path of a small metal disc (approximately 2mm in diameter) was tracked, however, although the trajectory compared well to the model, the magnitude of the vector was considerably underestimated (up to 20mms^{-1}). This led to the conclusion that either the model was over predicting vector magnitudes or that the particle was not being dragged along effectively with the fluid. The experiments using a 1mm plastic spherical particle, as seen from Table 6-2, again compared well with the trajectories computed by the simulation and this time the value of the experimental and simulated velocity magnitude compared more favourably. The difference in the values ranges from 1mms^{-1} to 11mms^{-1}. It is clear that the particle form contributes to the

discrepancies between magnitudes. Therefore we can deduce that significant drag forces act on these particles and this contributes to the differences observed in table 6-2. This observation improves our confidence in the simulation.

Note that these particles are very large relative to powdered additives and drag forces become less significant as the size of the particle decrease.

6.2.4 Qualitative Pressure Analysis

Pressure is the fourth dependent variable we are concerned with in terms of model validation. If the pressure contours in the simulation are examined we can get a reasonable idea whether or not these predictions are sensible. Like all model outputs pressure can be observed via several different techniques. Pressure contours, plots and point values on various 'slices' or 'cuts' through the domain all reveal the pressure gradients that contribute to driving the fluid flow. A good appreciation of the pressure character can be obtained from the pressure contours on the rotor surfaces as shown in Figure 6-14. The greatest pressure occurs at the rotor tips with the left-hand rotor producing the maximum force as anticipated. A steep pressure gradient exists over the rotor ends with the lowest pressures existing in the wake of the rotors.

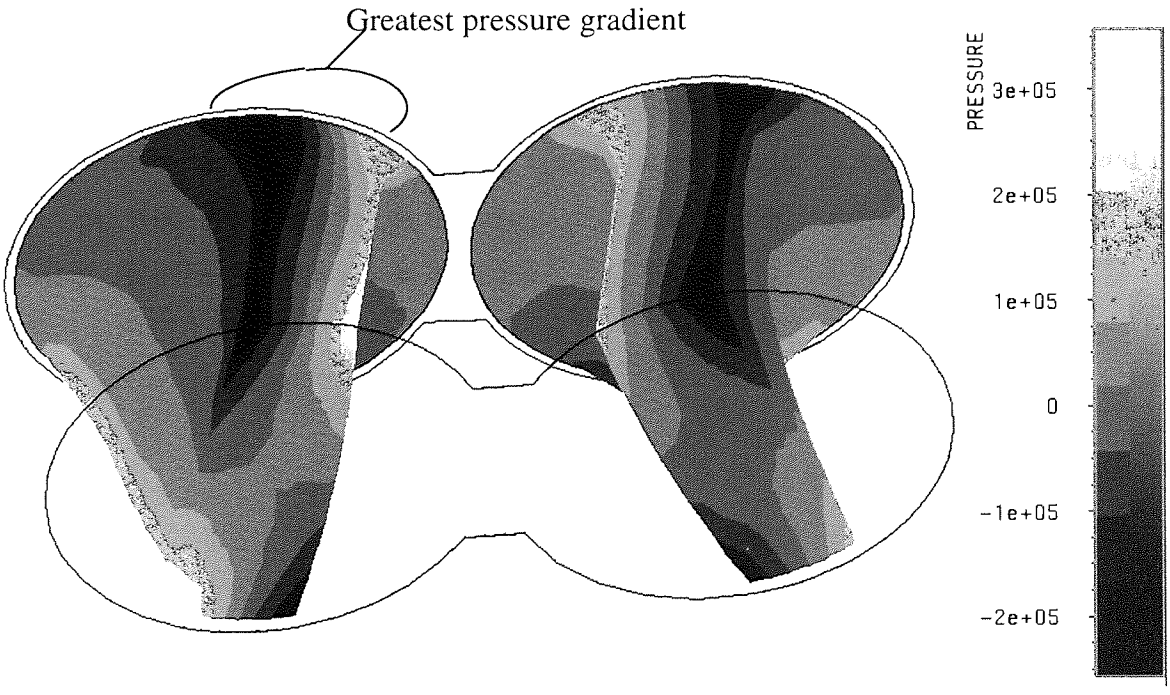

Figure 6-14 ***Pressure contours on the rotor surfaces of rotor configuration2***

A simple experiment involving the mixing of a gel with a high air bubble content shows, after reaching a steady state, that the larger bubbles accumulate in the regions with the lowest

'pressure' i.e. behind the rotor tips (Figure 6-15). The smaller bubbles circulate close to a fixed locus relative to their closest rotor. When comparing the pressure contour diagram in Figure 6-14 to the real situation which it represents, similarities can be observed. Note how the lowest pressure regions, which correspond to the greatest accumulation of air, are found behind slower right-hand rotor tips in both figures.

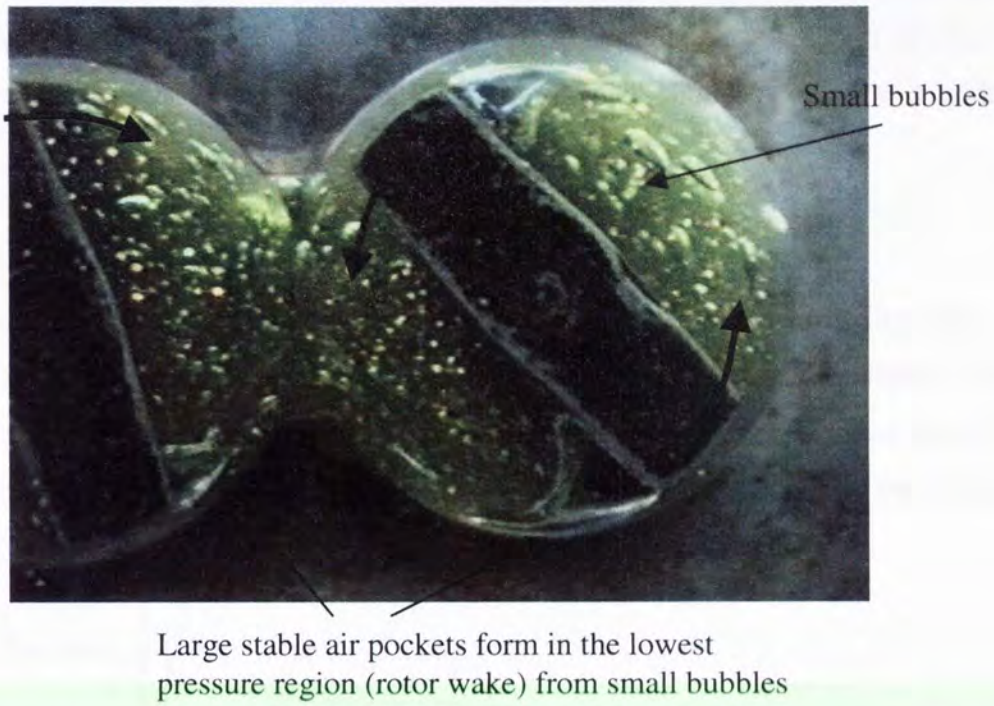

Figure 6-15 ***The mixing of a semi-transparent viscous gel with a high bubble content***

Figure 6-16 is a pressure contour diagram for rotor configuration 3. A similar pressure gradient pattern, as compared to rotor configuration 1, is found on the tip in view of the left-hand rotor. However, the right-hand rotor edge in view is found in the central 'transfer' or 'bridge' region and consequently the gradient is less dramatic.

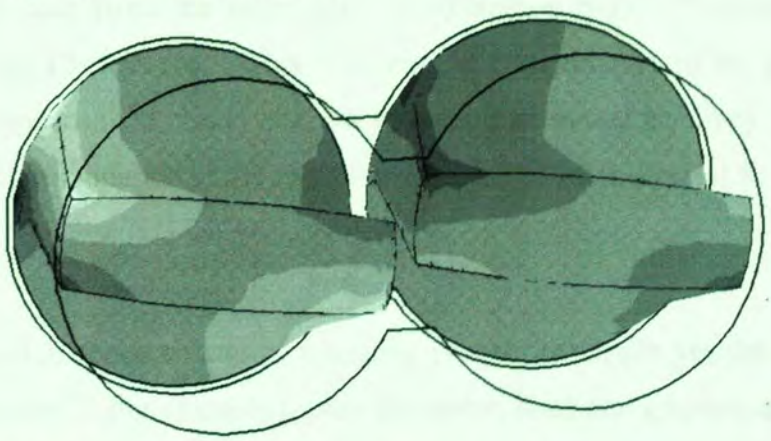

Figure 6-16 ***Pressure contours on the rotor surfaces of rotor configuration 3***

6.2.5 Quantitative Pressure Analysis

Data collected from pressure sensors on the outer wall of an internal mixer chamber can provide further evidence for model validity. However, as previously mentioned, these data should not be used as the sole evidence of model validity. General values of maximum pressure found in small-scale internal mixers range from 0.2MPa to 7.0MPa[92,93,94&95]. The maximum pressures found in the Hampden RAPRA Torque Rheometer occur within the lower part of this range. Ideally, a different approach representative of the whole domain should be used when validating the pressures.

Torque and Power Consumption

The Hampden RAPRA Torque Rheometer calculates the torque over the mixing cycle. The purpose of this is to give an operator an indication of homogeneity. A typical torque – time plot produced will take the form as shown by Figure 6-17. The peak corresponds to the initial period of polymer plastication and the plateau, i.e. constant rotor torque, corresponds to the mixing of a relatively 'uniform' mixture.

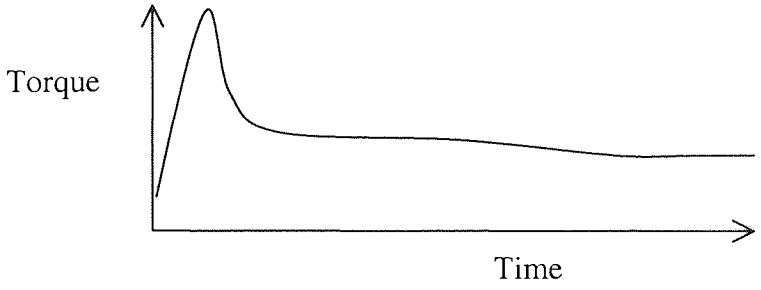

Figure 6-37 ***A typical torque – time graph for the mixing in an internal mixer***

Torque '**T**' is related to the product of the force '*F*' over a small area on the mixer surface '*s*' and the distance of this area from the rotor axis 'r_a' (equation 6-1). Theoretically this can be programmed into the CFD codes. This will enable comparisons to be made between the simulations and the mechanical model in order to determine model accuracy. The investigation into torque and the codes inputted in the simulation are presented in chapter 8.

$$\mathbf{T} = -\int_{Stotal} \mathrm{F} \cdot \mathrm{r_a} \cdot \mathrm{ds} \qquad (6\text{-}1)$$

The power consumption characteristic of a mixing process is simple yet the information it can provide is quite valuable[96]. For example to size the motor, shaft and gearbox as well as providing a basis for comparison in the evaluation of different mixer designs for mixing rate and efficiency[97]. The Power number *Po* is given by the following equation and is independent of scale for laminar mixing.

$$Po = K_p Re^{-1} \tag{6-2}$$

The constant K_p can be expanded to take account of various geometrical ratios.

The average shear rate in a system undergoing mixing can be the basis for the description of its power consumption[98]. The average shear rate '$\dot{\gamma}$' is directly proportional to rotor speed 'N' and the proportionality constant k_s in this relationship is determined from experimental data. The average shear rate is also be used to define the viscosity 'μ_a' and hence the Reynolds Number. To determine 'k_s' from experimental data involves three steps:

1. Plotting a torque against rotor speed graph from which the power number can be calculated for any N using equation 6-3
2. Plotting log power number 'Po' against log Reynolds number 'Re' to determine the Reynolds number as for the value of 'Po' calculated in step one given which the viscosity can be found (equation 6-4).
3. Plotting a viscosity against shear rate graph from which the average shear rate can be determined and therefore 'k_s' can be found by substitution of the shear rate and the rotor speed into equation 6-5.

$$Po = \frac{2\pi NT}{D^5 N^3 \rho} \tag{6-3}$$

$$Re = \frac{ND^2\rho}{\mu_a} = \frac{N^{2-n}D^2\rho}{K(k_s)^{n-1}} \tag{6-4}$$

Since $\mu_a = K(k_s N)^{n-1}$ (power law equation)

$$\dot{\gamma} = k_s N \tag{6-5}$$

It follows that the power consumption can be written as

$$Po = K_p \left(\frac{N^{2-n}D^2\rho}{K(k_s)^{n-1}} \right)^{-1} \tag{6-6}$$

There is potential here for the CFD model to improve on this method in terms of accuracy and time since the average shear rate can be computed directly as can the torque.

6.3 Strain, Shear Rates and Shear Stresses

Polymers are sheared and plasticised in the high stress regions that exist between the rotor tips and the chamber and to a slightly lesser extent between the rotor blades when they meet in the centre of the chamber. These high shear zones can be seen experimentally by the breaking up of flocs of particles in a fluid medium and by the various theoretical models which can show the distribution of the shear stress and shear rates at any point within the domain. High shear coupled with extensional flow, which is found in these regions, act together to break down agglomerates and gels. A floc of particles such as carbon black, used for colouring and tinting plastics, for protection against sunlight and thermal ageing and for electrical conductivity, must have a good degree of not only intensive mixing that results from high shear stress but also good extensive mixing. We have seen distributive or extensive mixing take place in the sickle shape area between the rotor and the chamber wall.

Strain

Strain in **pure extensional flow** is defined as the ratio of extension to original length (equation 6-7).

$$\varepsilon = \frac{\Delta l}{l} \tag{6-7}$$

Strain can also be defined in terms of displacement U.

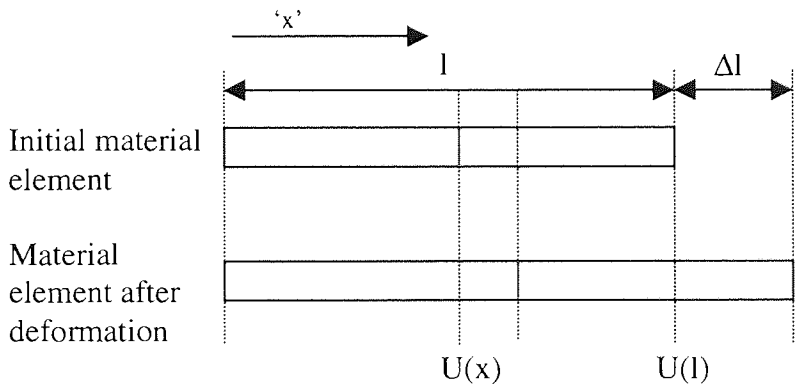

Figure 6-48 ***Strain in the extension of a material element***

Assuming homogeneous deformation the displacement in the 'x' direction is given by equation 6-8 and therefore another definition of strain is derived as shown by equation 6-10.

$$U(x) = \frac{x}{l}\Delta l \tag{6-8}$$

$$\frac{dU}{dx} = \frac{\Delta l}{l} \tag{6-9}$$

$$\varepsilon = \frac{dU}{dx} \tag{6-10}$$

By inspection of a square element of dimensions 'h x h' in the 'x-y' plane under pure shear, as shown in Figure 6-19, we can define for this system the following equation:

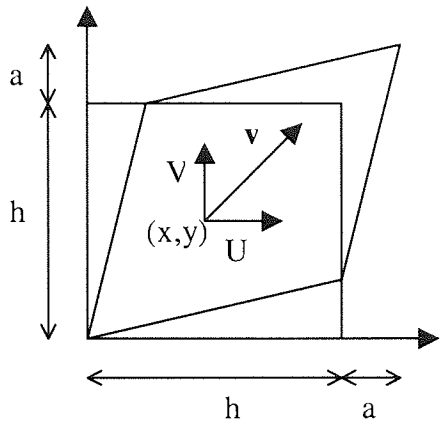

Figure 6-19 ***Strain in the pure shear of a material element***

$$\gamma = \frac{dU}{dy} = \frac{dV}{dx} \tag{6-11}$$

The strain in a general continuous medium is defined through a field of the displacement gradient $\boldsymbol{U}$(x,y,z) with coordinates:

U(x,y,z) V(x,y,z) W(x,y,z)

Strain in this three dimensional flow can be viewed by expressing the nine components of deformation with three defining the extension (or compression) and six defining the shear. The displacement gradient tensor $\nabla \boldsymbol{U}$ is given by:

$$[\nabla \boldsymbol{U}] = \begin{bmatrix} \partial U/\partial x & \partial U/\partial y & \partial U/\partial z \\ \partial V/\partial x & \partial V/\partial y & \partial V/\partial z \\ \partial W/\partial x & \partial W/\partial y & \partial W/\partial z \end{bmatrix} \tag{6-12}$$

To represent local deformation the tensor is made symmetrical by having half the sum of two tensors each transposed with respect to each other. The deformation or strain tensor is given by equations 6-13 and 6-14.

$$\varepsilon = \frac{1}{2}\left(\nabla \boldsymbol{U} + [\nabla \boldsymbol{U}]^T\right) \tag{6-13}$$

$$\varepsilon_{ij} = \frac{1}{2}\left(\frac{\partial U_i}{\partial x_j} + \frac{\partial U_j}{\partial x_i}\right) \tag{6-14}$$

where $U_i = (U, V, W)$ and $x_i = (x, y, z)$

So for the conditions described by Figures 6-18 and 6-19 :

$$\varepsilon_{xx} = \frac{\Delta l}{l} \tag{6-15}$$

and

$$\varepsilon_{xy} = \varepsilon_{yx} = \gamma \tag{6-16}$$

The definition of the tensor ε is valid if the terms are small e.g. if equation 6-15 and 6-16 are less than 5%. This is not the case for polymer flow in the Hampden RAPRA Torque Rheometer and so the rate of strain tensor $\dot{\varepsilon}$ or $\boldsymbol{D}$ is used. The *rate of deformation* or *rate of strain tensor* is given by:

$$\boldsymbol{D} = \lim_{dt \longrightarrow 0} \frac{[\varepsilon]_t^{t+dt}}{dt} \tag{6-17}$$

where $\mathrm{d}\boldsymbol{U} = \boldsymbol{u}dt$

$$\boldsymbol{D} = \frac{1}{2}\left(\nabla \boldsymbol{u} + [\nabla \boldsymbol{u}]^T\right) \tag{6-18}$$

and

$$\boldsymbol{D}_{ij} = \frac{1}{2}\left(\frac{\partial u_i}{\partial x_j} + \frac{\partial u_j}{\partial x_i}\right) \tag{6-19}$$

Applying knowledge of deformation or strain it is possible to perform a check on the shear rate predicted by the simulations to ensure that sensible results are being produced. For example, the shear at the rotor tip can be approximated if the assumption that the flow is that of two-dimensional planar couette type and there is no slip at the walls. The clearance between the rotor and the chamber wall is 0.81mm. The speed of the left rotor is 3.414 $rads^{-1}$ and the radius of the rotor is 18.36mm, hence the tip speed from equation 6.20, is 62.68 mm/s

$$v = r\omega \tag{6.20}$$

Hence the approximate shear rate is equal to 62.68/0.81 = **77.4** $\mathbf{s^{-1}}$. The shear rate obtained from the same point at the top of the rotor is **81.4** $\mathbf{s^{-1}}$. As anticipated the shear rate obtained from the

simulation is slightly higher than that of our approximation since there are additional components that contribute to this value such as flow in the 'z' direction.

Stress Fields

The stress field generated within a domain is represented at each point by the stress tensor. This stress tensor has already been introduced in chapter 4 along with the conservation of momentum equation. When assessing stresses between varying systems one has six separate components to consider. Tensors can be mathematically manipulated and reduced to give various scalar quantities. It would be convenient to have a similar single term which represents the stress tensor. However, from the literature, it appears that there is no treatment commonly used that can to be used to make comparisons between systems. One definition that has been recently used is by Kajiwara *et al*[99] in the study of twin screw extruders is given by:

$$\tau_{scalar} = \sqrt{(\tau_{\max})_{xy}^2 + (\tau_{\max})_{yz}^2 (\tau_{\max})_{zx}^2} \tag{6-21}$$

$$(\tau_{\max})_{xy} = \sqrt{4\tau_{xy}^2 + (\tau_{xx} - \tau_{yy})^2} \tag{6-22}$$

$$\tau_{scalar} = \sqrt{4(\tau_{xy}^2 + \tau_{yz}^2 + \tau_{zx}^2) + (\tau_{xx} - \tau_{yy})^2 + (\tau_{yy} - \tau_{zz})^2 + (\tau_{zz} - \tau_{xx})^2} \tag{6-23}$$

Any single value derived from a tensor must be derived from the its trace as shown in the following equations:

$$I = tr\tau = \sum_i \tau_{ii} \tag{6-24}$$

$$II = tr\tau^2 = \sum_i \sum_j \tau_{ij}\tau_{ji} \tag{6-25}$$

$$III = tr\tau^3 = \sum_i \sum_j \sum_k \tau_{ij}\tau_{jk}\tau_{ki} \tag{6-26}$$

The trace of the tensor, or the tensor square or cubed, gives an invariant because their values are independent of the choice of co-ordinate system to which the components are referred. Combining these three can form scalars. The most common are the invariants I_1, I_2 and I_3 given by:

$$I_1 = I \tag{6-27}$$

$$I_2 = \tfrac{1}{2}(I^2 - II) \tag{6-28}$$

$$I_3 = 1/6(I^3 - 3I*II + 2III) = \det \tau \qquad (6\text{-}29)$$

As a check to determine whether equation 6-23 is a true invariant, and therefore suitable to use as a way of expressing stress at any point in the simulation, combinations of I_1, I_2 and I_3 were substituted into equation 6-23. It was found that the stress 'τ_{scalar}' is an agglomeration of the first and second invariants:

$$\sigma = 2I_2 - I_1^2 + I_1 \qquad (6\text{-}30)$$

where

$I_1 = \tau_{xx}^2 + \tau_{yy}^2 + \tau_{zz}^2$

$I_2 = \tau_{xx}^2 + \tau_{yy}^2 + \tau_{zz}^2 + 2\tau_{xy}^2 + 2\tau_{yz}^2 + 2\tau_{zx}^2$

Equation 6-23 has been used in the next chapter as a parameter to aid in assessing dispersive mixing for a variety of situations.

As an aside Figure 6-20 is offered as an example depicting the viscosity distribution across a slice through rotor configuration 2 where it can be seen how significantly the viscosity decreases in the high shear regions.

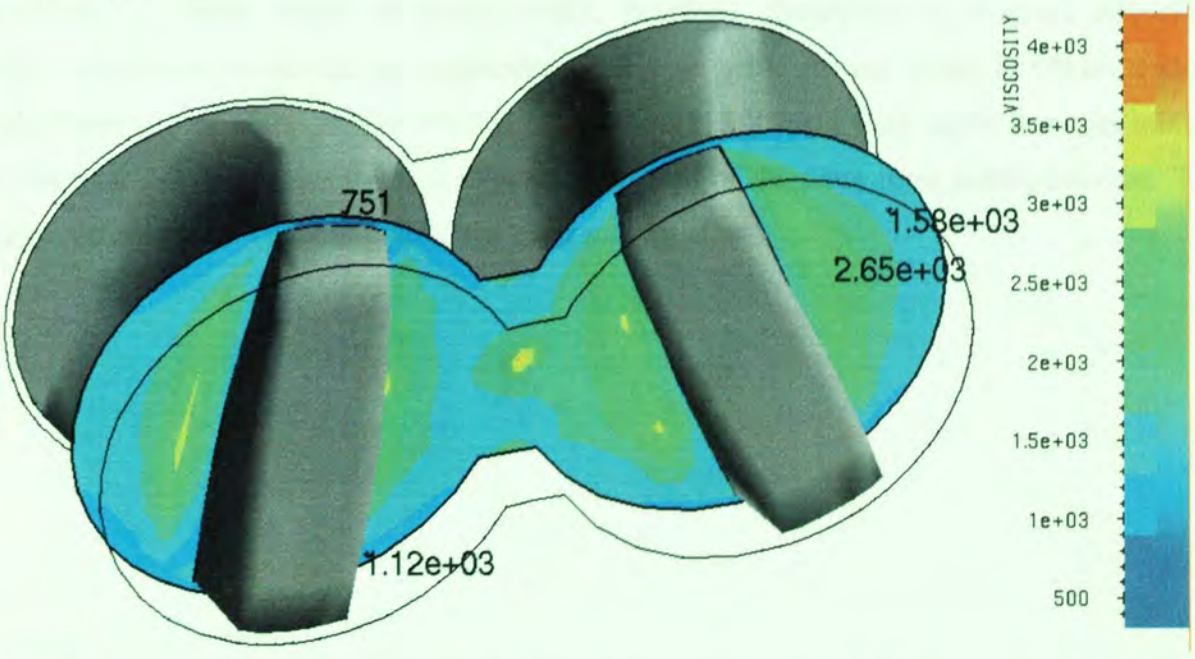

Figure 6-20 ***Viscosity contours and local values on a slice through the Hampden RAPRA Torque Rheometer domain (K = 3000, n=0.4)***

6.4 Mixing Efficiency

The mixing index, or mixing efficiency as it is sometimes referred to, is given by:

$$\lambda = \frac{|\boldsymbol{D}|}{|\boldsymbol{D}| + |\omega|} \tag{6-31}$$

Where $|\boldsymbol{D}|$ is the magnitude of the rate of deformation tensor and $|\omega|$ is the magnitude of the vorticity tensor equation 6-32 and 6-33 respectively.

$$|\boldsymbol{D}| = \sqrt{2\boldsymbol{D}_{ij}\boldsymbol{D}_{ij}} \tag{6-32}$$

$$|\omega| = \sqrt{2\omega_{ij}\omega_{ij}} \tag{6-33}$$

where $\boldsymbol{D}$ is given in equation 6-19

$$\omega_{ij} = \frac{1}{2}\left(\frac{\partial u_i}{\partial x_j} - \frac{\partial u_j}{\partial x_i}\right) \tag{6-34}$$

A mixing index value of unity corresponds to pure elongation while a mixing index value of zero corresponds to pure rotation. A value of 0.5 corresponds to simple shear situations. Elongational flow has been shown, through experimental study, to be more effective than simple shear in the dispersive mixing of solid agglomerates in viscous liquids (Manas-Zloczower and Feke[100, 101]) and in the dispersive mixing of liquids with high viscosity ratio and low interfacial tension (Elmendorp[102]). High values of mixing index, therefore, corresponding to good dispersive mixing. Shear stresses should be considered closely with the mixing index to obtain a more complete assessment of dispersive mixing. Figure 6-21, 6-22 and 6-23 show how the mixing character of the system alters through the central section of the three rotor configurations. The velocity vectors are provided alongside the local mixing plots.

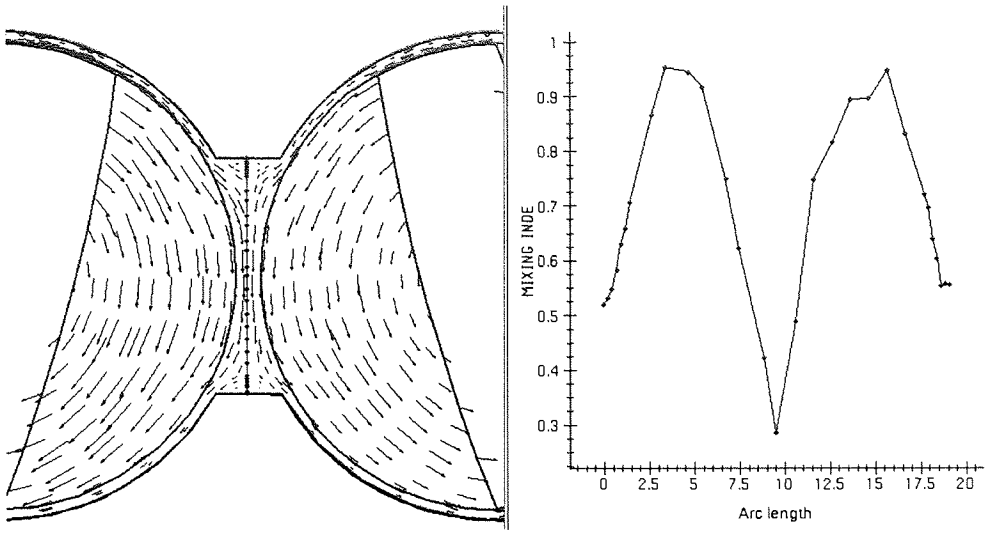

Figure 6-21 *Mixing index values plotted along an arc for rotor configuration 2*

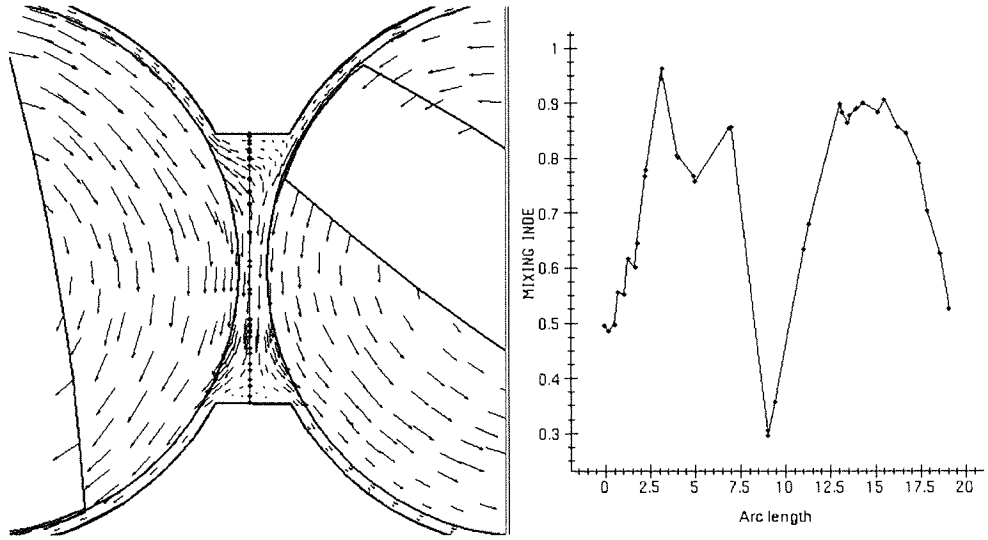

Figure 6-22 *Mixing index values plotted along an arc for rotor configuration 1*

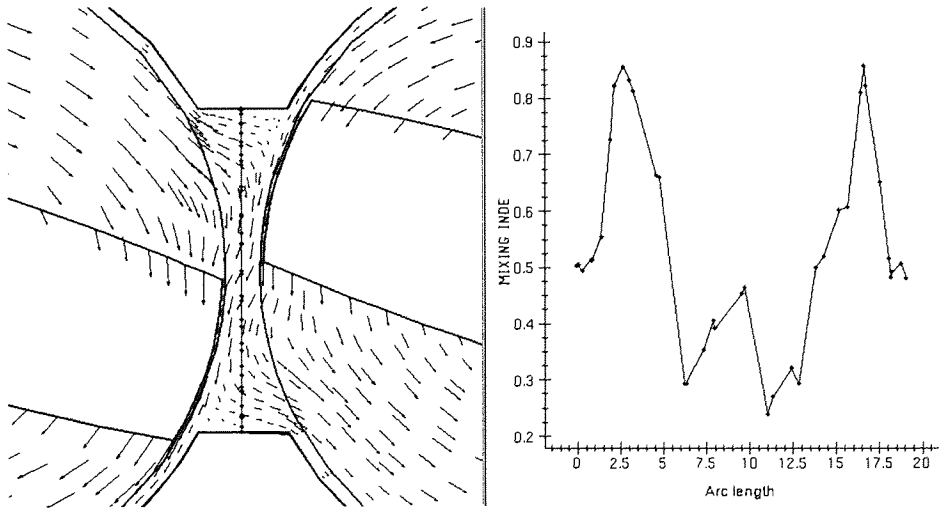

Figure 6-23 *Mixing index values plotted along an arc for rotor configuration 3*

6.5 Conclusions

The qualitative experiments, performed in order to give an indication of model validity, provide substance to support the hypothesis that the simulation represents reality accurately. The quantitative experiments, to determine the trajectories and velocity magnitudes of real particles in a transparent viscous fluid and enable comparisons to be made with infinitely small hypothetical particles that move with the fluid as it flows in the simulation, produced interesting results. Over 90% of the trajectories compared are within 1.1% of each other. The difference in velocity magnitudes range between 11.2 and 1.0mms^{-1} with 78% of the results being under 5.3 mms^{-1}. Discrepancies in the velocity magnitude comparisons are attributed to drag since the experimental values are almost always less than those predicted by the model. Validation of the theoretical model continues in chapter 8 where torque and dye tracing simulations are examined.

The evidence collected is considered to be transferable to other similar Hampden RAPRA Torque Rheometer models, e.g. that use different rotor speeds and rheologies.

7. Application of the Simulation

We have already seen how a validated simulation can be obtained and be used in understanding flow patterns and mixing processes in an otherwise 'black box' operation. This section investigates how a simulation may be used to qualitatively and quantitatively assess the influence of important design and optimisation factors such as operating conditions, fluid rheology, equipment design and process scale.

7.1 Quantifying the Effect of Changing Process Variables

7.1.1 Rotor Speed

The speed at which the rotors rotate within the internal mixer affects the mixing and the compounding process in several important ways. One consequence of increasing rotor speed is the effect on the shear rate and the associated increase in the stresses experienced by the material which is being processed. Although increasing stresses improves the break down of agglomerates (dispersive mixing) there may be a limit on the maximum shear stresses permitted due to the risk of polymer degradation. Another consequence of faster rotor speeds will be the higher rate of viscous heating. A high viscous heating rate will result in a reduced plastizisation time and a decrease in the heat input required (or an increase in the cooling duty required depending on the process and its scale). Rotor speeds could therefore be optimised to achieve the shortest feasible processing time depending on the thermal and stress sensitivity of the material and, of course, other parameters which are considered within this chapter.

The Hampden RAPRA Torque Rheometer has two rotor speed settings (Table 7-1). Both these speed settings and two other speeds have been simulated using rotor configuration 2 and the relationship between rotor speed and shear rate / stress established (Figures 7-1 and 7-2).

Altering the Cartesian velocity boundary condition for the two rotors does not change the flow patterns only the magnitude of the vectors. This is due to the high kinematic viscosity of the polymeric materials, which prevents significant flow by inertia. The magnitude of the pressure field increases proportionally with the rotor speed, the character of the velocity profiles, however,

is not noticeably affected even near the rotor tips where high pressure gradients exist. These attributes are congruent with several experimentalists who have drawn similar conclusions from their own work which suggest that, when mixing highly viscous fluids, rotor speeds have very little effect on the number of revolutions required to achieve a specified degree of laminar mixing[103,104]. Figures 7-3 and 7-4 show the pressure and velocity fields of two simulations with varying rotor speed. To aid comparison the cross sections are both taken at 'z' = 12.51mm, the vector magnitudes have been scaled down by 1/32 and the pressure ranges are identical.

The average shear rate is directly proportional to the rotor speed (Figure 7-1) and also the model shows that the average mixing index is independent of rotor speed. This confirms the above statements concerning the fact that the flow patterns do not change with rotor speed. This implies that if a mixing operation requires 'x' number of rotations to reach a state deemed to be homogenised in terms of distributive mixing then doubling the rotor speed will halve the processing time. The shear stresses increase with rotor speed however this is not a linear function; this is attributed to the fact that the shear rate is a function of shear stress and viscosity.

Table 7-1 ***Hampden RAPRA Torque Rheometer rotor speeds***

High Speed		Low Speed	
Left Rotor	Right Rotor	Left Rotor	Right Rotor
65.2 rpm anticlockwise (6.828 rad s^{-1})*	43.37 rpm clockwise (4.608 rad s^{-1})*	32.6 rpm anticlockwise (3.414 rad s^{-1})*	21.68 rpm clockwise (2.304 rad s^{-1})*

* Values determined using a high-speed video recorder and video timing equipment.

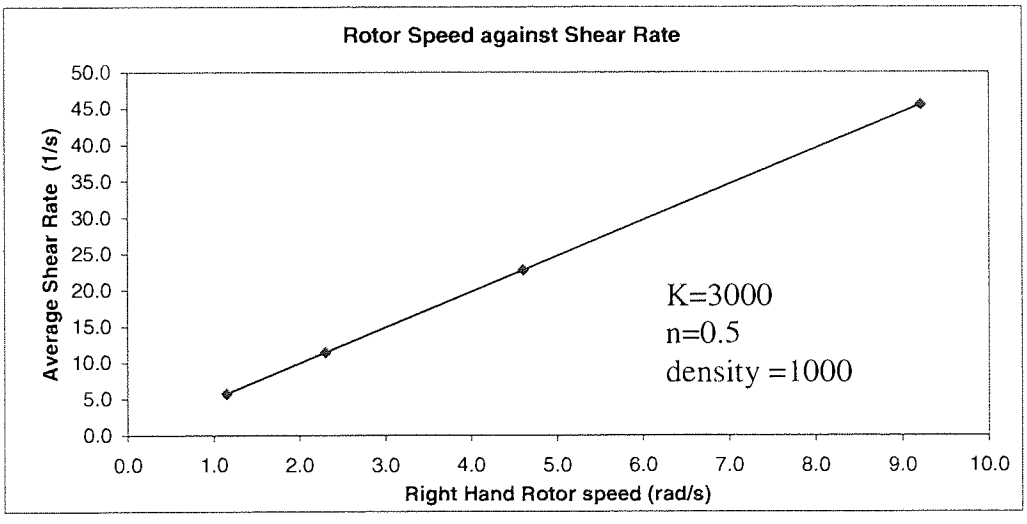

Figure 7-1 ***Rotor speed against average shear rate for rotor configuration 2***

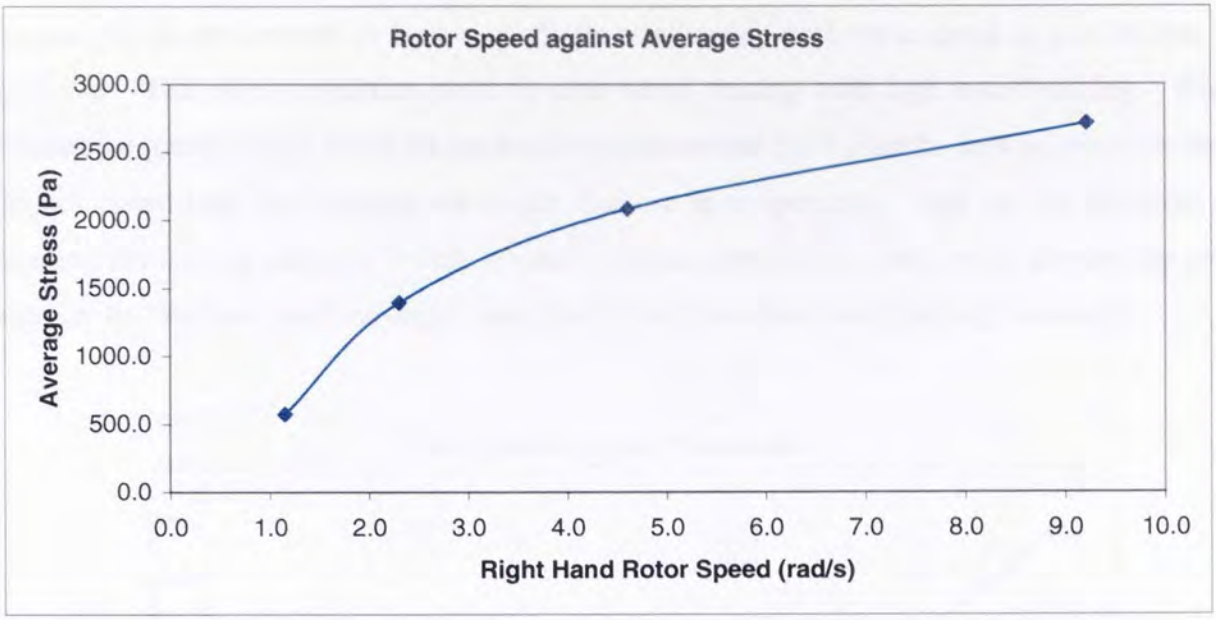

Figure 7-2 *Rotor speed against average shear stress for rotor configuration 2*

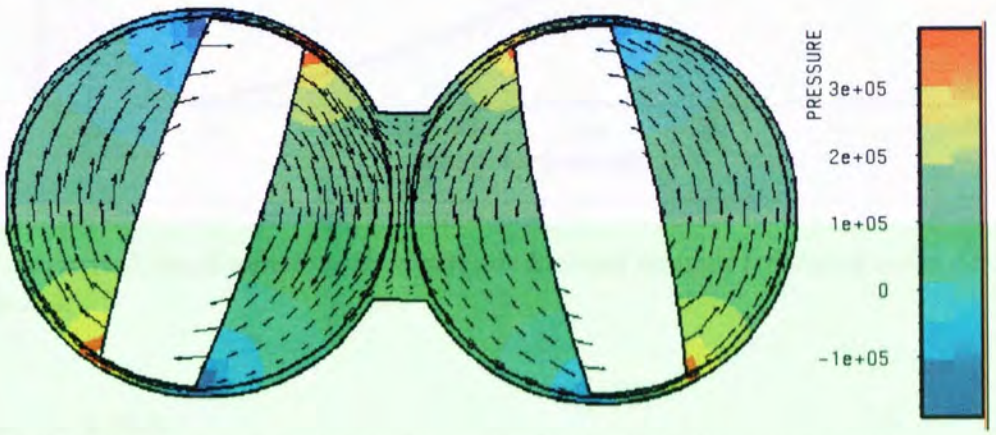

Figure 7-3 *Right-hand rotor speed = 4.608 rad/s : Velocity and pressure fields*

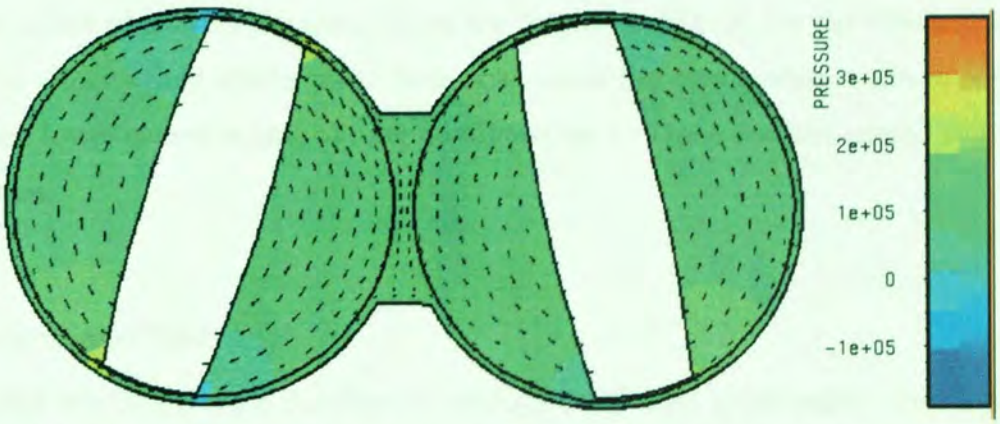

Figure 7-4 *Right-hand rotor speed = 1.152 rad/s: Velocity and pressure fields*

Viscous heating can be seen to have a quadratic relationship with rotor speed as can be seen by Figure 7-5. This is an important point to note when dealing with high speed mixing. When operating the rotors at high speed the productivity is increased but it must be kept in mind that there is an associated limit that corresponds to the increase in temperature. This can be alleviated by increasing the cooling capacity (which results in higher operational costs) or by altering the rotor design i.e. tip clearance and land-width (which will alter the mixing and shearing character).

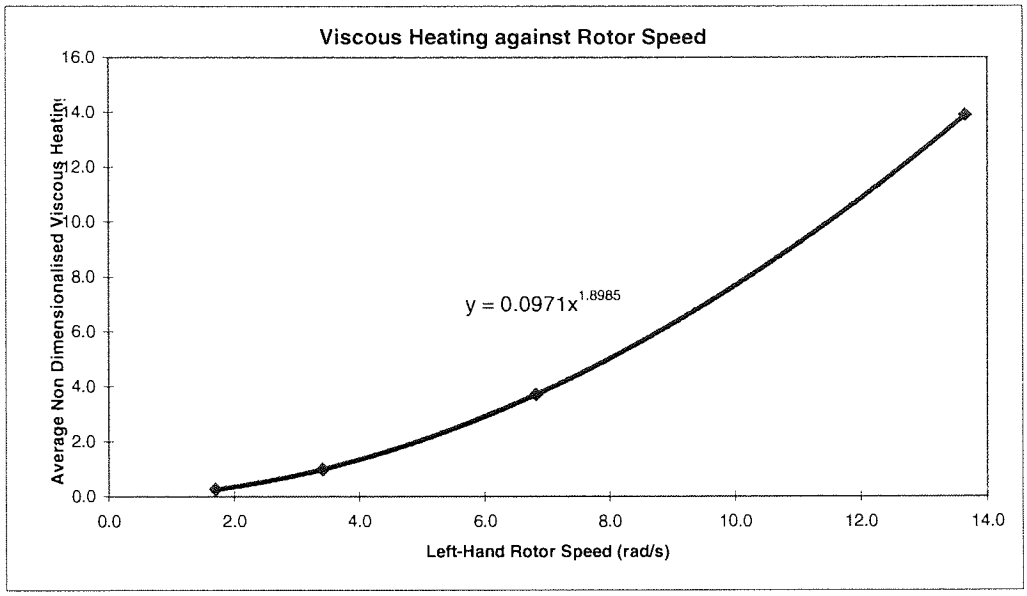

Figure 7-5 ***Average Non-dimensionalised viscous heating against left-hand rotor speed for configuration 2.***

7.1.2 Rotor Direction

The Hampden RAPRA Torque Rheometer has *counter-rotating* mixing blades, however, this may not always be the case with other internal mixers; consequently the simulation was used to observe the affect of altering the direction of the rotors. In Figure 7-6 the effect of *co-rotating* rotors on the velocity field can be seen. Note how, under this new system, vortices are formed in the upper and lower central region of rotor configuration 3. These vortices extend similarly in the axial direction.

7.1.3 Rotor Speed Ratio

The Hampden RAPRA Torque Rheometer employs a 3:2 rotor speed ratio. This breaks up the simple repeating motion of a simple 1:1 rotor ratio improving randomness in the system and, therefore, the distributive mixing. The down side of this design is the loss of even stress and heat

generation in the two separate chambers. Perhaps optimum rotor speed ratios and starting configurations could be determined using particle distribution simulations.

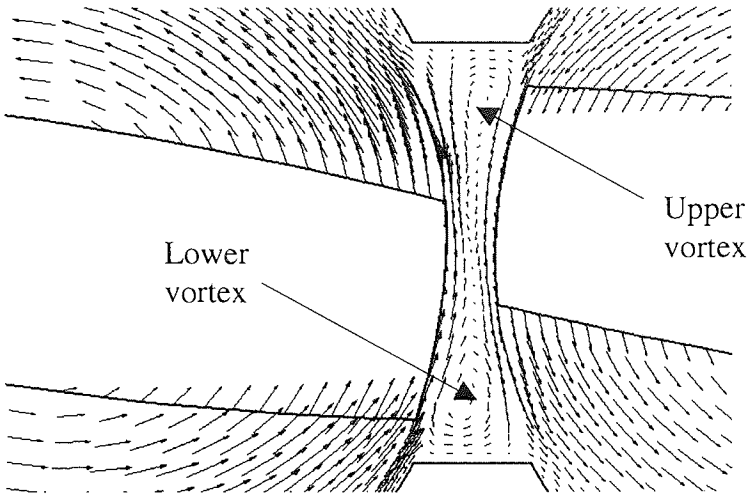

Figure 7-6 ***Velocity field for co-rotating scenario***

7.2 Fluid Rheology

The viscosity of most viscous fluids, especially polymers, is highly shear dependent. The power law model, which gives an accurate representation of most of the viscous fluids used in experimental work over small shear ranges, has been investigated. The power law has two variables. These are the power law factor and the power law exponent. When the power law exponent for a particular fluid is found to be a value greater than unity it indicates that the fluid is shear thickening (dilatant); this type is not common in the polymer industry. A value of the exponent equal to unity defines the fluid as shear independent i.e. Newtonian; this is rare in viscous fluids. Values of the exponent less than unity give the fluid a shear thinning character (pseudoplastic); as the value approaches zero the effect of shear on the fluid viscosity is increased (see section 3.1 and equation 3.4). *Harby et al* comment that useful laboratory trials of many popular mixers in this area are only sketchily documented and research into understanding the influence of non-Newtonian properties on mixing rates and power consumption would be welcomed[105]; this remains a grey area.

The investigation presented in this section reveals information on:

- The effect of rheology on flow patterns, mixing and shearing character. An appreciation of this, for example, may be important if a mixer is designed for a variety of fluids.

- The limits on the degree of shear thinning which can be applied to the theoretical model. Increasing non-linearities, which are associated with the decrease of the power law exponent, make the problem specified increasingly difficult for the numerical methods to solve. Many polymers will have power law exponents which approach 0.1 and this may be difficult or even impossible to solve to an acceptable degree of accuracy within complex three-dimensional domains.
- The practical modelling considerations. These are the convergence *level* and convergence *rate* achievable. For example, as shown in more detail in this section a Newtonian fluid problem will solve in two iterations using the 'Polyflow' solver. In this research, however, it has been noted that decreasing the power law exponent significantly increases the number of iterations required to solve the problem increasing the total CPU time by a factor up to twenty!

7.2.1 Power Law Factor

Varying the power law factor in an isothermal simulation does not change the flow field. This is true as long as the power law factor represents a highly viscous fluid and therefore prevents significant flow by inertia. These statements are qualified by the contents of Table 7-2 which illustrates how the mixing index remains unchanged for power law constants of 10 and above. These findings agree with several deductions made by experimentalists concerned with the mixing of viscous fluids who remark that viscosity of near Newtonian fluids has a negligible effect on the number of revolutions required to achieve a specified degree of mixing[106,107]. The increasing non-linearities incurred when a power law constant of around 0.01 and below is modelled make the flow field more challenging to solve. The stresses (Figure 7-7) and the viscous heating generated, however, will both increase with increasing power law factors.

Table 7-2 ***Power law constant against average mixing index for rotor configuration 2***

Rotor Configuration 2	Power Law Constant						
	20,000	4400	1000	100	10.0	1.0	0.1
Average Mixing Index*	0.48689	0.48689	0.48689	0.48689	0.48689	0.48688	0.48222

*when n=0.5

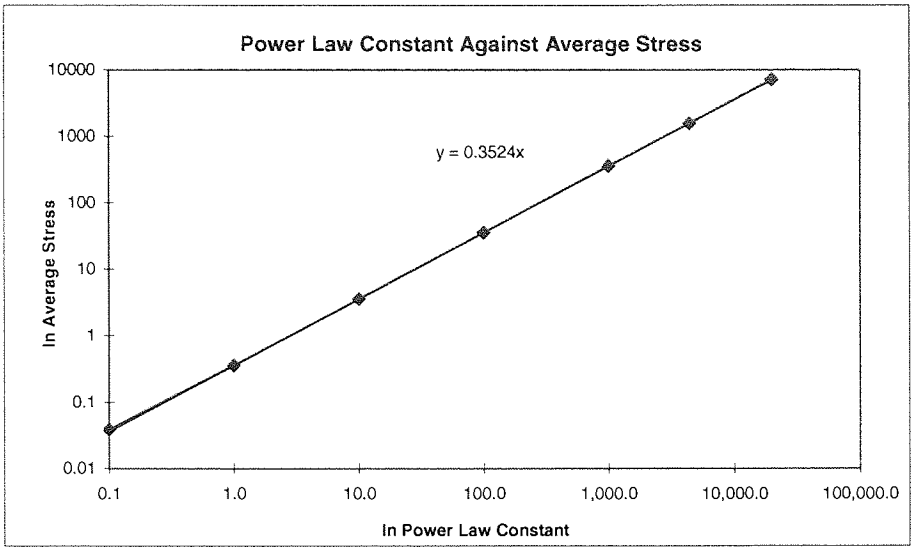

Figure 7-7 ***Power law constant against average stress for rotor configuration 2***

7.2.2 Power Law Exponent

There is a substantial shift in the velocity profile in the 'x-y' plane when the power law exponent is varied as can be seen from the example given in Figure 7-8 (refer to Figure 6-6). In the axial or 'z' direction a considerable dampening of the flow is observed. This is reflected in Table 7-3 where the mixing and shearing character are seen to be functions of the power law exponent. Figures 7-9 and Figures 7-10 present this data more clearly. The average shear rate decreases by approximately 20% as we decrease the exponent from unity to 0.1 when the power law factor K is equal to 3000 and the rotor speed is low. As discussed in the previous chapter values of the mixing index tending toward unity would represent good dispersive mixing (depending on shear stress magnitudes). The mixing efficiency analysis suggests a move from a performance better than simple shear to a relatively poor dispersive mixing character as the fluid viscosity becomes more shear dependent. The change in the axial flow patterns as the power law exponent decreases can be seen on a slice at z = 15 mm in Figures 7-11 to 7-20. Figure 7-21 represents a quantification of the change by depicting a plot of axial flow from a point within the domain corresponding to maximum 'z' velocity for the Newtonian case. Altering equipment design or process operating conditions can compensate for this decrease in axial flow / distributive mixing, for example, by increasing rotor curvature.

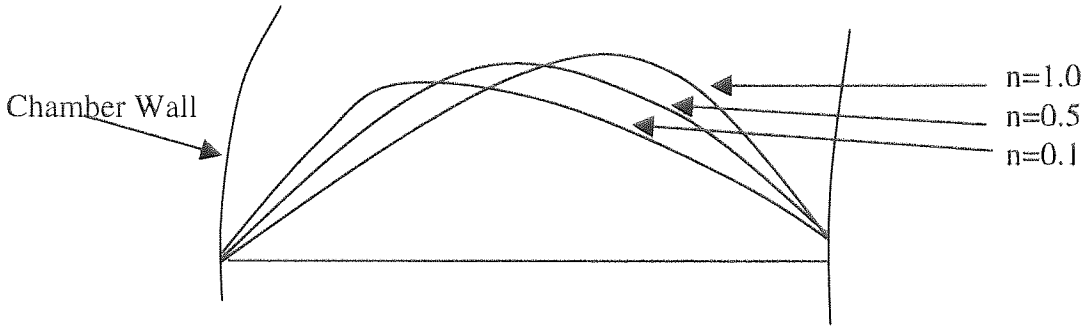

Figure 7-8 *Velocity profile variation along a 'x-y' plane at z=15mm for rotor configuration 2 for different power law exponents*

Table 7-3 *Investigation into fluid rheology for rotor configuration 2 - average parameters against power law index*

Power Law Index	Shear Rate(1/s)	Mixing Index
1	11.9184	0.5222210
0.9	11.7569	0.5176776
0.8	11.5836	0.5118053
0.7	11.3953	0.5041673
0.6	11.1862	0.4942000
0.5	10.9475	0.4868894
0.4	10.6685	0.4622805
0.3	10.3393	0.4352213
0.2	9.95859	0.3930386
0.1	9.56481	0.3239338

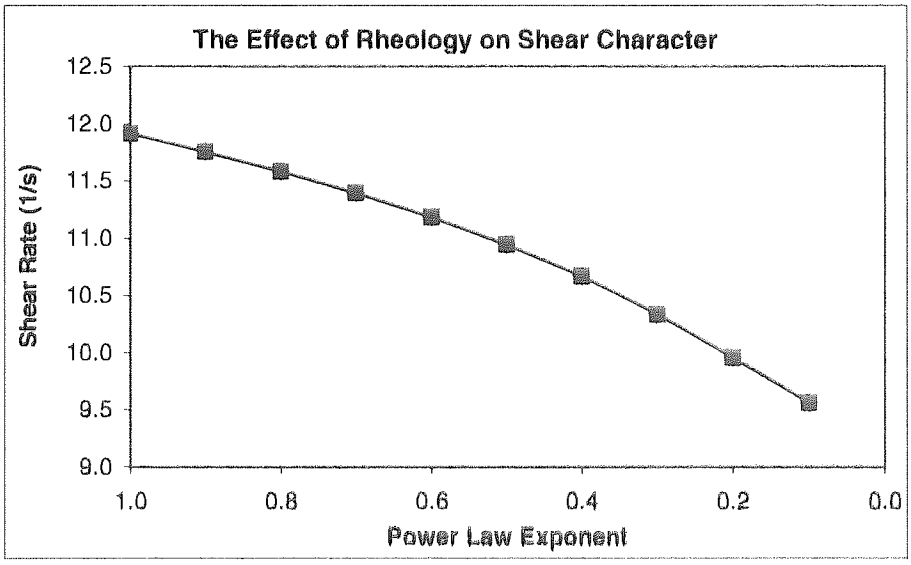

Figure 7-9 *Power law index against average shear rate for rotor configuration 2*

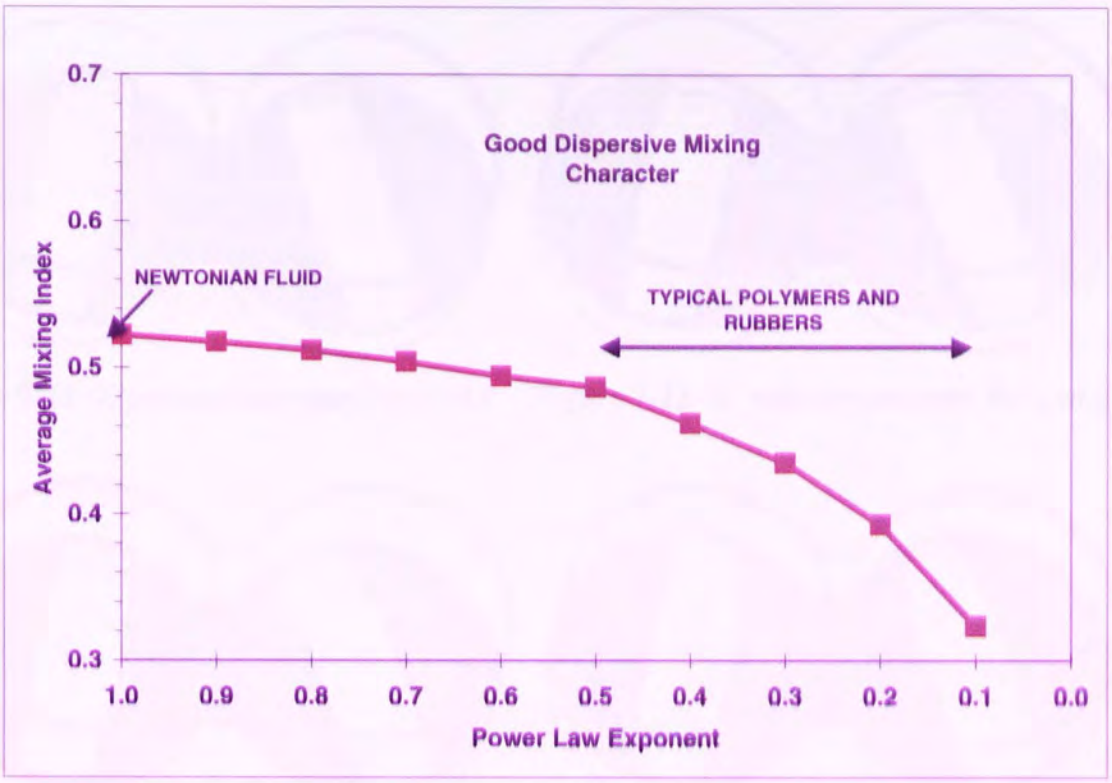

Figure 7-10 *Power law index against average value of mixing index for rotor configuration2*

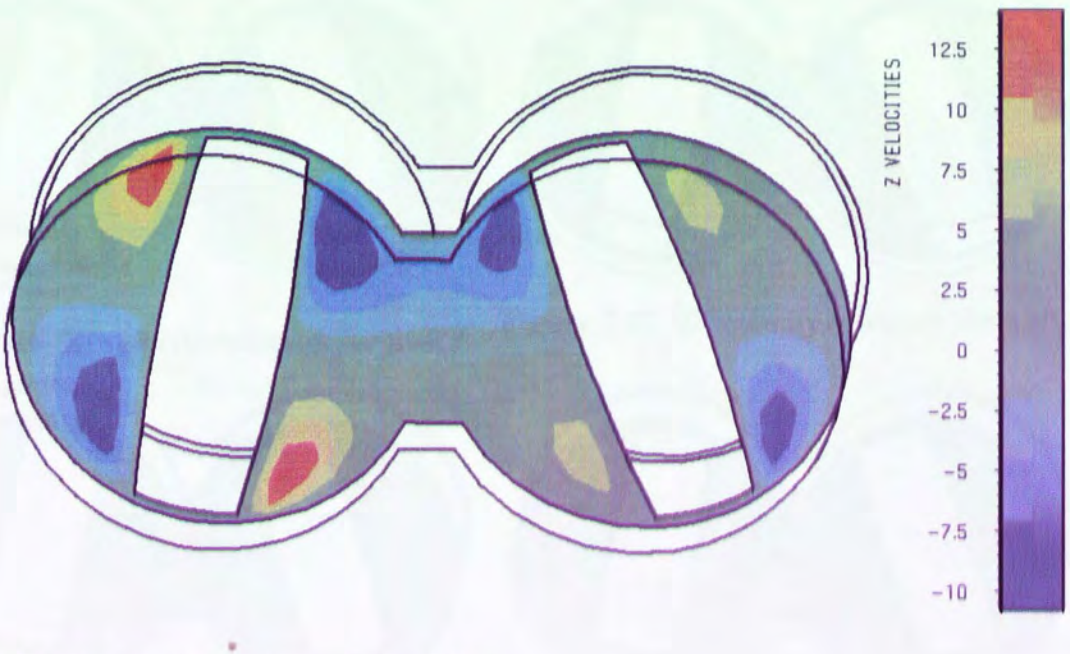

Figure 7-11 *'Z' velocity contours for n=1.0*

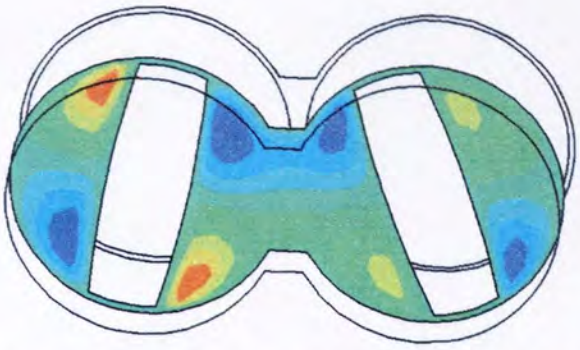

Figure 7-12 *'Z' velocity contours for n=0.9*

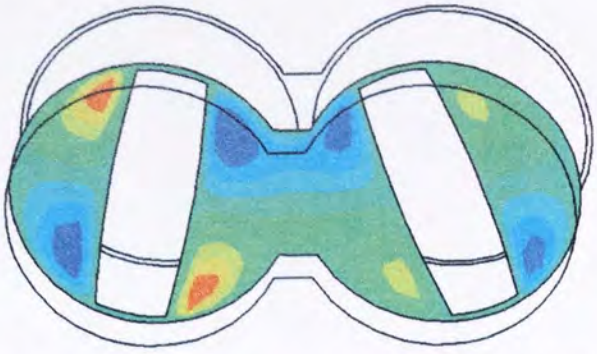

Figure 7-13 *'Z' velocity contours for n=0.8*

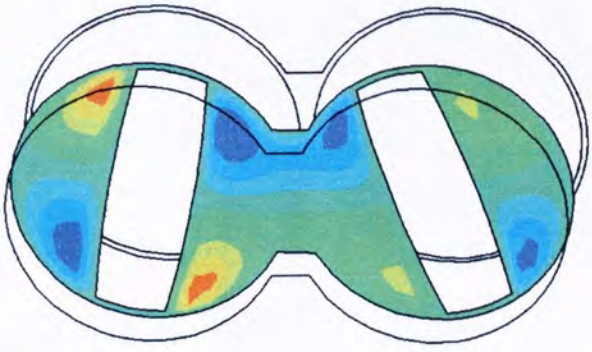

Figure 7-14 *'Z' velocity contours for n=0.7*

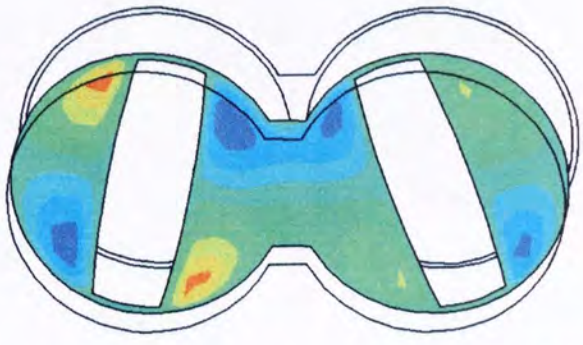

Figure 7-15 *'Z' velocity contours for n=0.6*

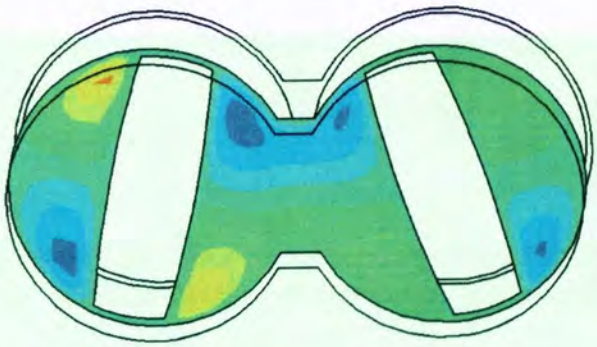

Figure 7-16 *'Z' velocity contours for n=0.5*

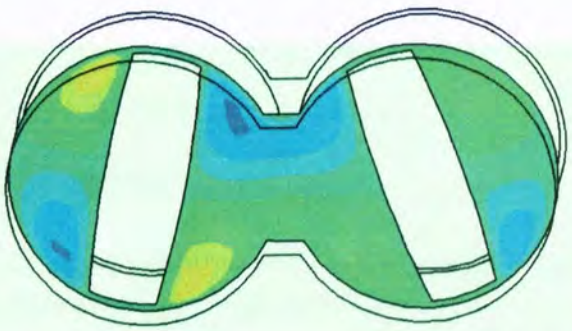

Figure 7-17 *'Z' velocity contours for n=0.4*

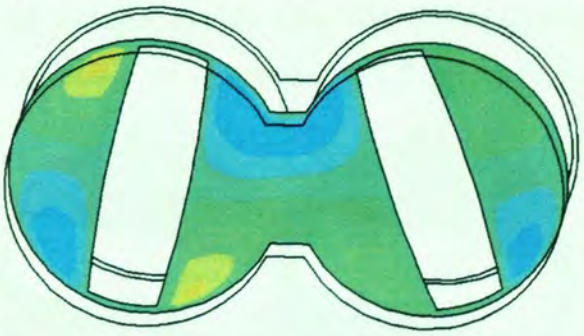

Figure 7-18 *'Z' velocity contours for n=0.3*

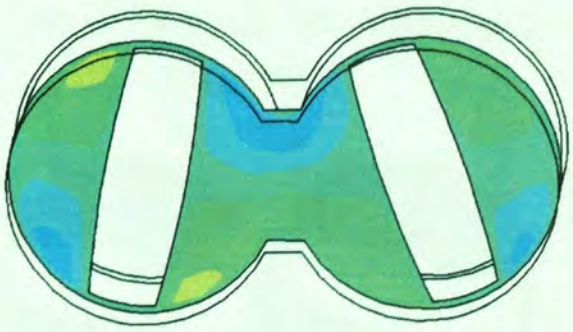

Figure 7-19 *'Z' velocity contours for n=0.2*

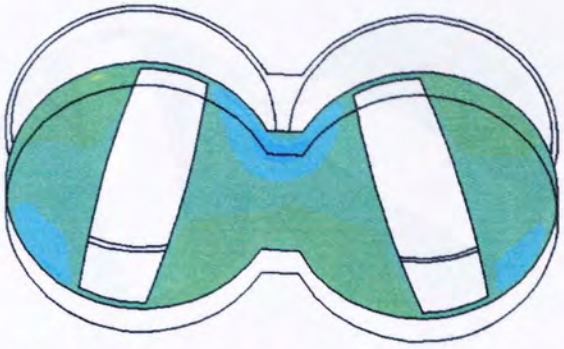

Figure 7-20 ***'Z' velocity contours for n=0.1***

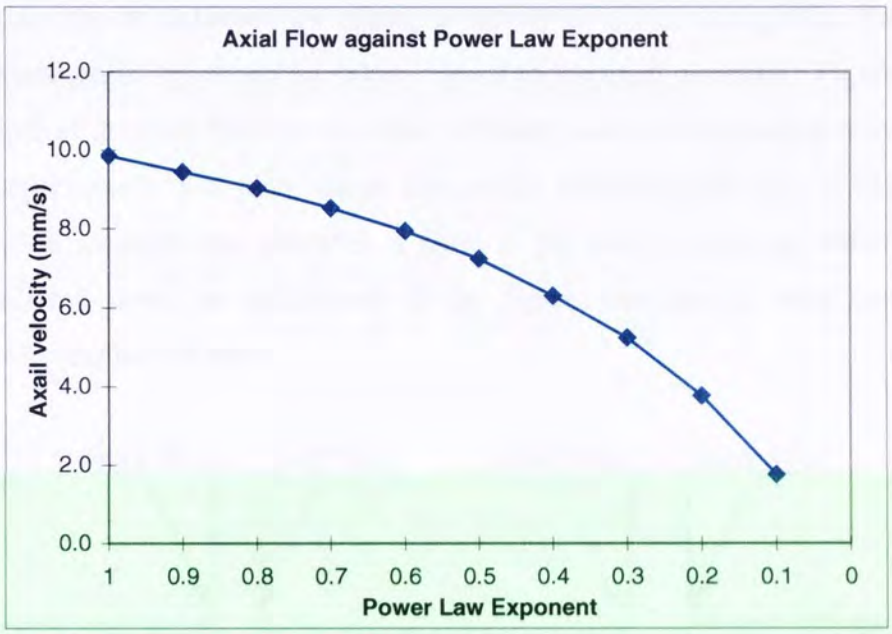

Figure 7-21 ***Axial flow from a point within the domain corresponding to maximum 'z' velocity for the Newtonian case against power law exponent for rotor configuration 2.***

Figures 7-22 and 7-23 are presented to illustrate the contrast in axial flow between the Newtonian case and a power law fluid representing a typical polymer (n=0.3) for rotor configuration 1 and 3. A similar flow dampening effect can be seen as with rotor configuration 2.

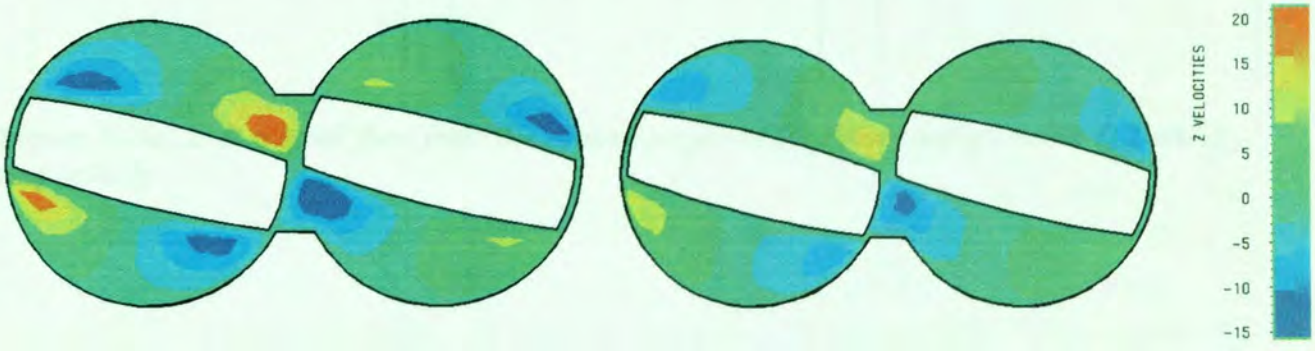

Figure 7-22 ***Z' velocity contours for n=1.0 and n=0.3 for rotor configuration 3***

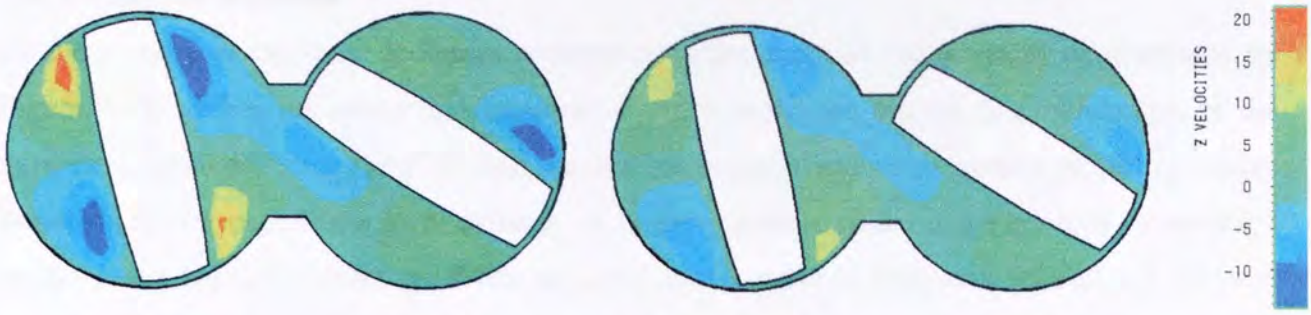

Figure 7-23 ***Z' velocity contours for n=1.0 and n=0.3 for rotor configuration 1***

Flow examination can be achieved by taking a variety of slices through the domain although most slices reproduced in this thesis are taken normal to the axial direction. Figures 7-24a, b and c give an example of the flow field for the three different rotor configurations from an alternative slice which is represents a 'y-z' plane taken through the central region (at x = 19.9mm). As the rotor configuration changes one observes a shift in the mixing patterns which change from overall re-circulating flow, as highlighted in the figure, through an axial dampening to an inversion of the re-circulation route.

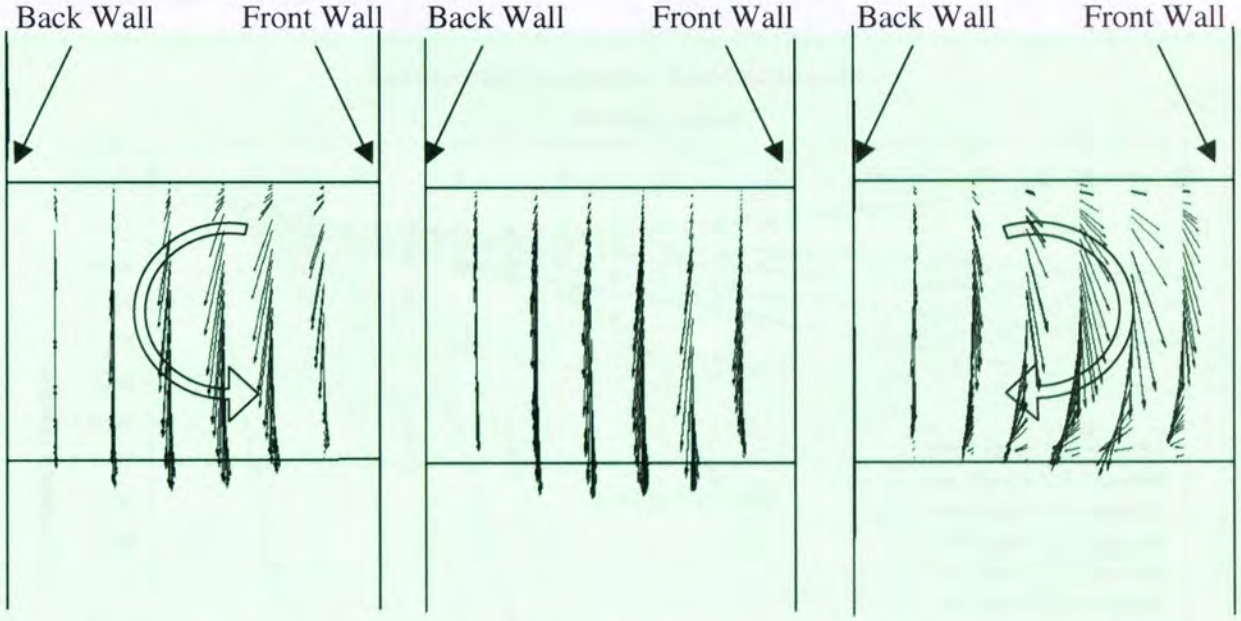

Figure 7-24a, b & c ***Axial flow from the central y-z plane for rotor configuration 1, 2 and 3 respectively***

Simulation Practicalities

As the power law exponent decreases convergence rates decrease considerably as illustrated by Figure 7-25. When the power law exponent is equal to 0.5 we see the first indications of the numerical methods "struggling" to find the correct solution and consequently requiring twelve iterations to converge to the level defined. A further decrease of the exponent to a value of 0.4 results in the solution diverging. When the maximum number of iterations defined, e.g. 20, was reached the calculation was stopped. This particular case, with 3000 nodes solved on a Digital 500au workstation –SPECfp95 20, used 41.5 hours of real CPU time and 40 hours of actual CPU time.

At this point the Newton Raphson was substituted for the Picard iteration scheme which, although using more CPU time, is thought to sometimes be useful when the limits of the Newton Rhapson method are reached[108]. This iteration scheme enabled the lower values of the exponent to be successfully simulated although many iterations were required (not shown on graph) for the simulation to reach a good convergence level. The simulation of these highly shear sensitive fluids using the Picard iteration scheme requires considerable time to solve which can be field limiting for research in this area.

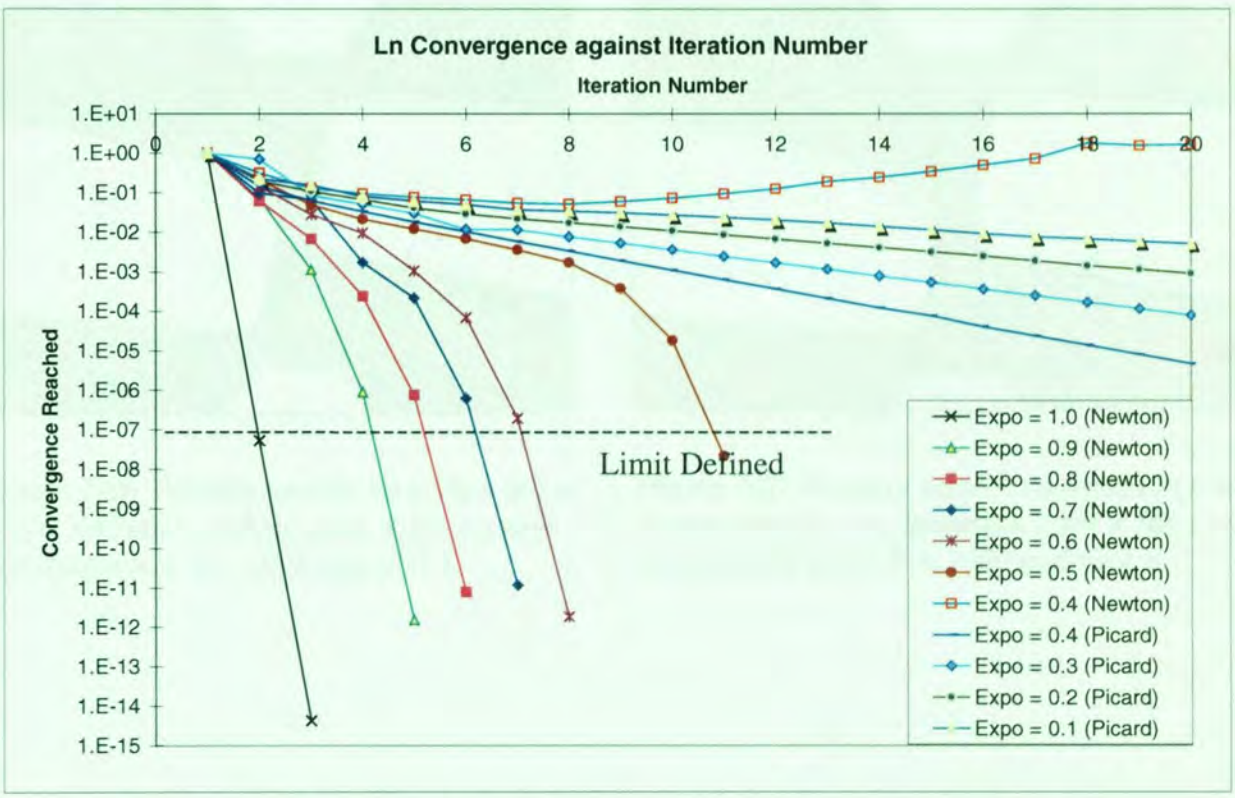

Figure 7-25 ***A graph illustrating convergence character for varying power law exponents for rotor configuration 2***

7.2.3 Yield Stress

Many highly viscous fluids to a greater or lesser extent must experience a certain critical shear stress before they will flow. The Bingham model or Herchel Bulkley model can be used to represent such a fluid as given by equations 3-5 and 3-6 respectively. The effect of this phenomenon within an internal mixer can be partly appreciated by Figures 7-26 and 7-27. The region between the two rotors becomes more stagnant when a critical shear rate of 10 s^{-1} is defined. Even when both rotor tips are within this central region, as in rotor configuration 3, the motion of the fluid is still dampened although the flow patterns remain very similar. The implications of yield stress, in terms of distributive and perhaps dispersive mixing efficiency as well as viscous heating, should be considered if the rheology of the fluid being modelled has a significant critical yield stress. *Kaylon*[109] comments how it maybe inappropriate to use the power law for all materials processed by a twin screw extruder, for example, highly filled suspensions of polymeric composites will not flow until a critical stress magnitude is reached of approximately 20 Pa (This value is exceeded throughout this flow domain).

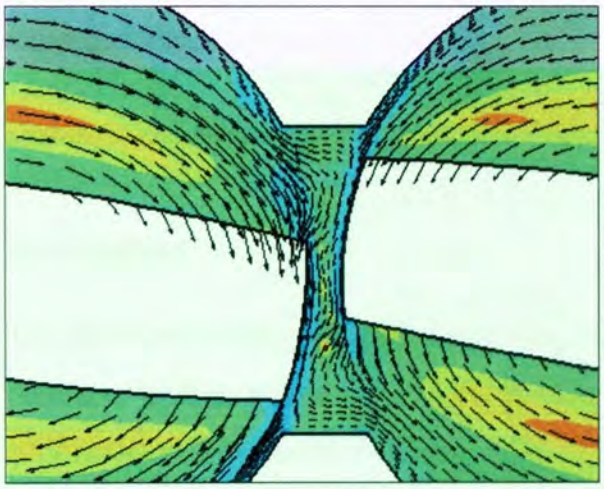

Figure 7-26 ***Velocity vectors on a slice at z = 15mm on rotor configuration 2 for a power law fluid when K = 3000 and n=0.3.***

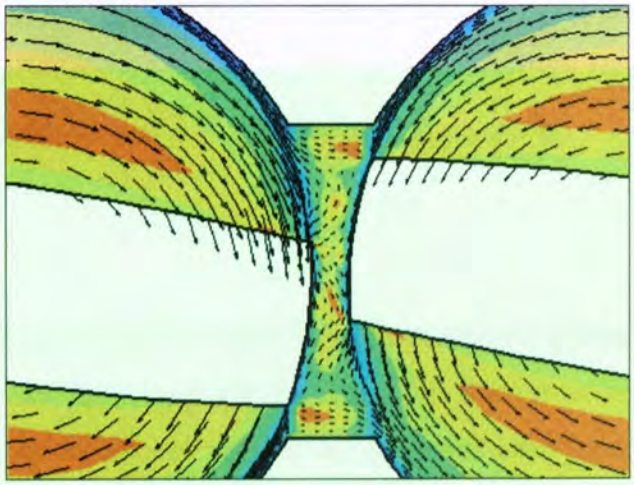

Figure 7-27 ***Velocity vectors on a slice at z = 15mm on rotor configuration 2 for a Herchel Bulkey fluid when K = 3000 and n=0.3.***

7.2.4 Viscoelasticity

Polymers exhibit viscoelastic properties when sheared. It would be desirable to determine the relative magnitude of these extra stresses generated when a viscoelastic fluid is sheared compared to that of the shear stresses. This will aid in assessing their impact on dispersive mixing within the internal mixer.

Viscoelastic Simulation Overview

A total stress tensor is introduced in place of the shear stress tensor and is equal to the sum of the shear stress component and the extra stress component. This extra stress component '$\mathbf{T_e}$' can be derived from a choice from several viscoelastic models. These models stem from one of two model groups which deal with the non-linear character brought about by the fluid memory in very separate ways. One is the differential viscoelastic model and the other is the integral viscoelastic model. The differential model has been used for this investigation since, although the integral model is thought to represent the situation more realistically, it involves calculating the integral time along each flow line. This is more computationally demanding and the concept of historical time in a pseudo steady state 'snap shot' used for the Hampden RAPRA Torque Rheometer simulations is not physically sound.

Details of the differential viscoelastic models available in Polyflow are given in Appendix 6.

Investigation

The total stress tensor components and the extra stress tensor components were calculated at four points, or probes, within the domain at various locations around the tip of the left hand rotor in configuration 2 as shown in Figure 7-28. This was carried out for five different left-hand rotor speeds (see Appendix 6 for the data obtained in this analysis). Figure 7-29a is a plot of the total and extra stress for the point corresponding to maximum stress against rotor speed and Figure 7-29b is a plot of the percentage of the extra stress for each of the four points' stress against rotor speed. The investigation shows that at very low rotor speeds the shear stresses dominate. However, with increasing rotor speed, the extra stresses from the viscoelasticity terms increase more rapidly than shear stresses. It is this rapid increase in the viscoelastic stress that makes finding a converged solution very difficult at realistic rotor speeds. The instabilities that exist for even the simplest viscoelastic models available in Polyflow present a considerable obstacle to overcome especially for complex three-dimensional geometries where the poor element form

hinders solver performance. This unfortunately resulted in the premature termination of this line of investigation, although, a discussion of a new route to a viscoelastic model of an internal mixer is given later on in this thesis.

These results suggest that one should exercise caution when assessing stresses for evaluating dispersive mixing efficiency. Although, for comparisons of various equipment configurations and operating conditions, the model still will reveal useful trends.

Figure 7-28 ***Probe location for viscoelastic extra stress investigation on rotor configuration2***

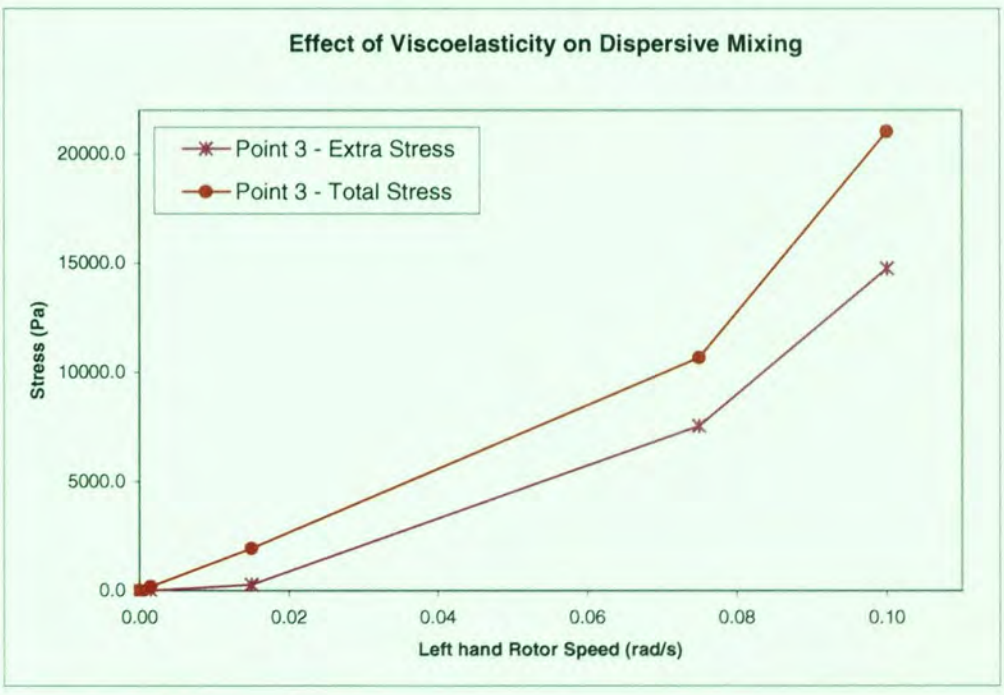

Figure 7-29a ***The total and extra stress against rotor speed for various probes around a rotor tip***

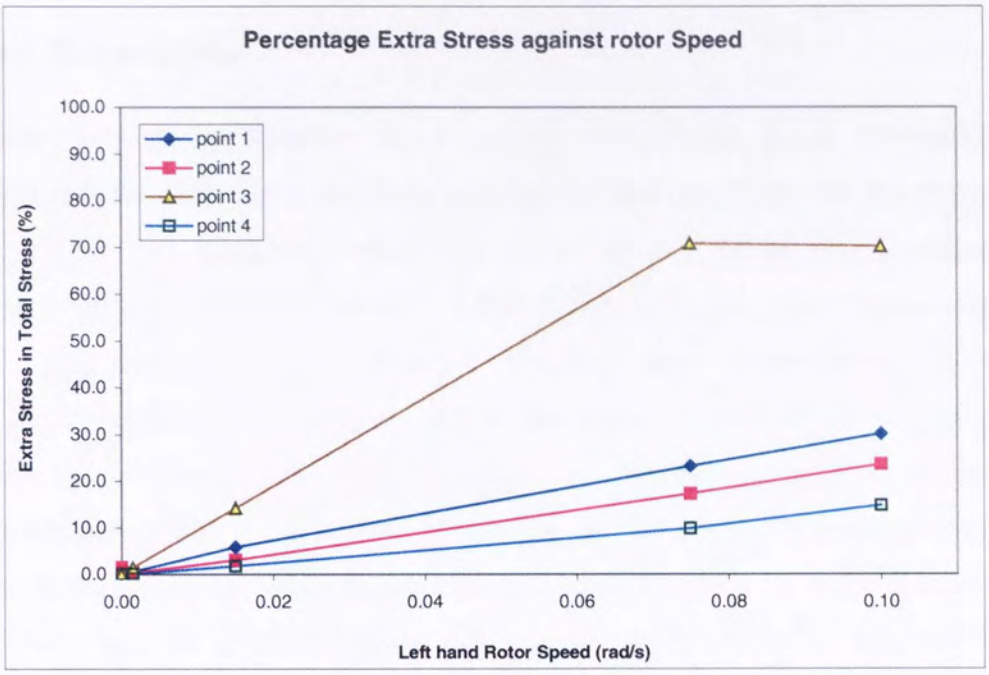

Figure 7-29b *The percentage of extra stress against rotor speed for various probes around a rotor tip*

7.3 System Temperature

The simulation uses the assumption that a uniform temperature exists throughout the fluid domain. Although for small scale processing equipment this assumption is less dramatic[110] it is still desirable to take into account energy changes in the system and the corresponding effects on viscosity and density (and also the constants in the energy equation). The temperature variations are greater during the initial mixing process. However, temperature uniformity is gradually reached as the mixing process continues and at this point the complexities of non-isothermal behaviour can be ignored as previously discussed. A uniform change in temperature will, of course, alter fluid properties. Varying rheological properties will cause a change in the mixer's performance as shown in the examples in this chapter. However, it is the non-uniformity of temperature that may exist in practice which will intensify the effect on the mixer's flow field.

A pseudo steady state non-isothermal simulation has been used although the added complexities in this type of simulation can only provide limited useful information. The temperature assigned to the fluid (from which the fluid properties are calculated) and the boundaries is 298°K and the only heat source stems from the viscous heating term. The energy equation is presented in chapter 4. The data from the converged solutions can be used to provide temperature contour plots. It was observed that the viscous heating is greatest around the rotor tips as anticipated.

The question of computational practicalities raised by including the energy equation into the solver is reported and this information is used for comparative purposes with later investigations involving non-isothermal simulations in chapter 8. The non-linear character of a non-isothermal simulation may limit the model's capabilities, for example, it may restrict the rheology that can be modelled. In addition the number of iterations needed for a suitable convergence level will increase. This has been examined and the results presented in Figure 7-30.

The CPU demand from these non-isothermal simulations was high, so, in order to reduce CPU time, a central plane of symmetry was inserted in the model (at 'x' = 19.9mm) eliminating the need for one half of the mesh. This was reasonable, since rotor configuration 2 is almost symmetrical. Since the number of nodes is reduced by one half the CPU time required for each simulation decreases considerably. At the 'plane of symmetry' boundary the normal velocity component and the tangential force component are set at zero. It was clear that the numerical method used to solve the equations (Picard) has a low convergence rate approximately equal to

three times slower than the isothermal model and this is expected to increase proportionally with the number of nodes in the mesh. Although at this stage it was pleasing to see that even the extreme cases can be solved if a good modelling strategy is employed.

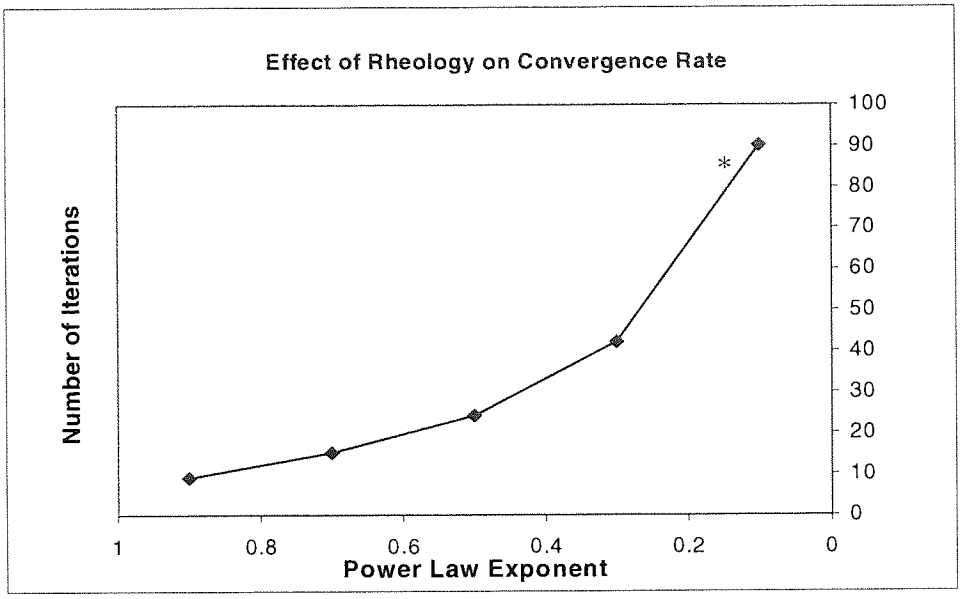

Figure 7-30 ***The number of iterations plotted against power law exponents for rotor configurations 2 with a plane of symmetry.***

* Convergence = $1x10^{-6}$ (The convergence of all other simulations is $1x10^{-8}$)

Another important consideration, which should be kept in mind when introducing new equations to the model, is the swap space required of the simulation. Taking an example of a mesh containing 4683 nodes (rotor configuration 1) the swap space requirement rises from 2.30 Gb to 2.84 Gb after introducing the energy equation into the model.

7.4 Internal Mixer Design -Rotor Clearance / Landwidth

Two important design criteria for internal mixers are the rotor tip clearance and the rotor land-width; the rotor tip clearance being the distance between the tip and the chamber wall and the rotor land-width being the width of the rotor tip. Both the rotor tip clearance and the rotor land-width can act on the system in similar directions for any set conditions e.g. altering these variables to increase both the total stresses imposed on the fluid and viscous heating. In order to quantify the response of the flow field from changing these types of rotor specifications the following investigations have been carried out:

The investigations involved flow field analysis of four separate geometries each corresponding to different rotor specifications that differ in the scale of the rotors in the 'x' and 'y' planes; the resulting rotor clearances and land-width for each geometry can be found in Table 7-4. Each simulation used a typical polymer rheology (polypropylene at 200°C). The data gathered attempts to quantify the effect of varying rotor clearance and land-width on shear stress, shear rate, viscosity and viscous heating, and involves computing both the average values of key parameters over the whole domain and various point values (Table 7-5). The point values, or 'probes', correspond to the maximum shear areas located at the rotor tips. The results of the simulations are presented in Figure 7-31 to 7-34.

It is clear that the level of shear stress at the rotor tips is proportional to the rotor clearance, and the volume of fluid that these high stresses act upon is inversely proportional to the rotor clearance. It is reasonable to assume, therefore, that there will be some optimum value of rotor clearance at which the product of shear stress per unit volume and the volume of fluid that these high stresses act upon will be greatest. To illustrate this situation the volume for each rotor geometry is plotted on Figure 7-33. The investigation into optimum rotor design would be perhaps better represented by investigations involving the average stress magnitude over the volume between the rotor tip and the chamber and the mass flow rate over the rotors. Due to the confines of the software used for the simulations, however, this was not feasible at this stage. A renewed effort into this subject can be found in section 8.6.2.

Table 7-4 ***Rotor tip clearance and land-width dimensions for geometry investigation***

	Simulation Geometry			
	1	2	3	4
Rotor radius (mm)	17.8112	18.3621	18.93	19.1994
Chamber radius (mm)	19.74	19.74	19.74	19.74
Rotor tip clearance (mm)	1.9288	1.3779	0.81	0.5406
Rotor tip width (mm)	9.3472	9.6363	9.9343	10.0757
Fluid volume ratio*	3.57	2.55	1.50	1.00

* Volume above a rotor tip (geometry 'x'/geometry 4)

Table 7-5 ***Probe locations for geometry investigation***

	Probe co-ordinates (mm)		
	x value	y value	z value
Left rotor tip Probe	7.2546	16.86	12.7993
Right rotor tip Probe	37.48	18.2197	12.7993

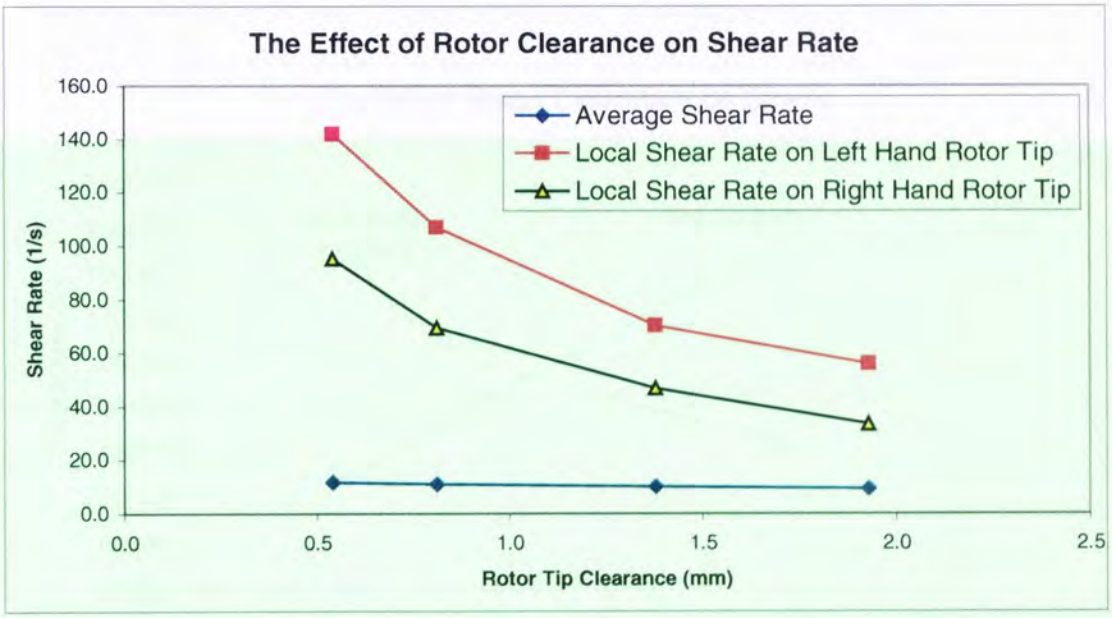

Figure 7-31 ***Rotor tip clearance against shear rate for rotor configuration 2***

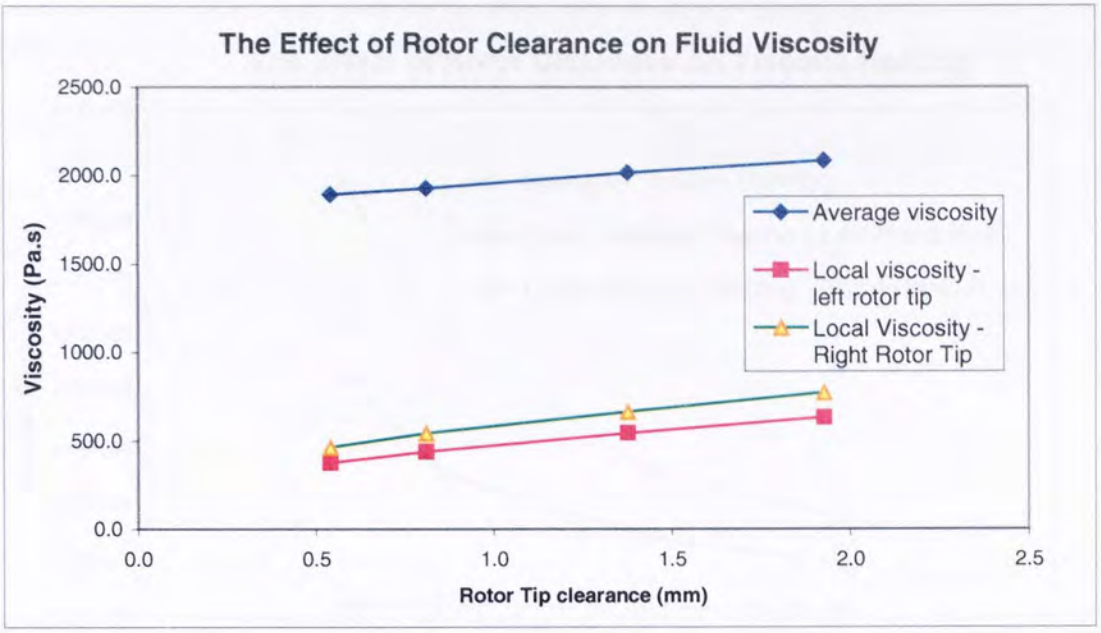

Figure 7-32 ***Rotor tip clearance against viscosity for rotor configuration 2***

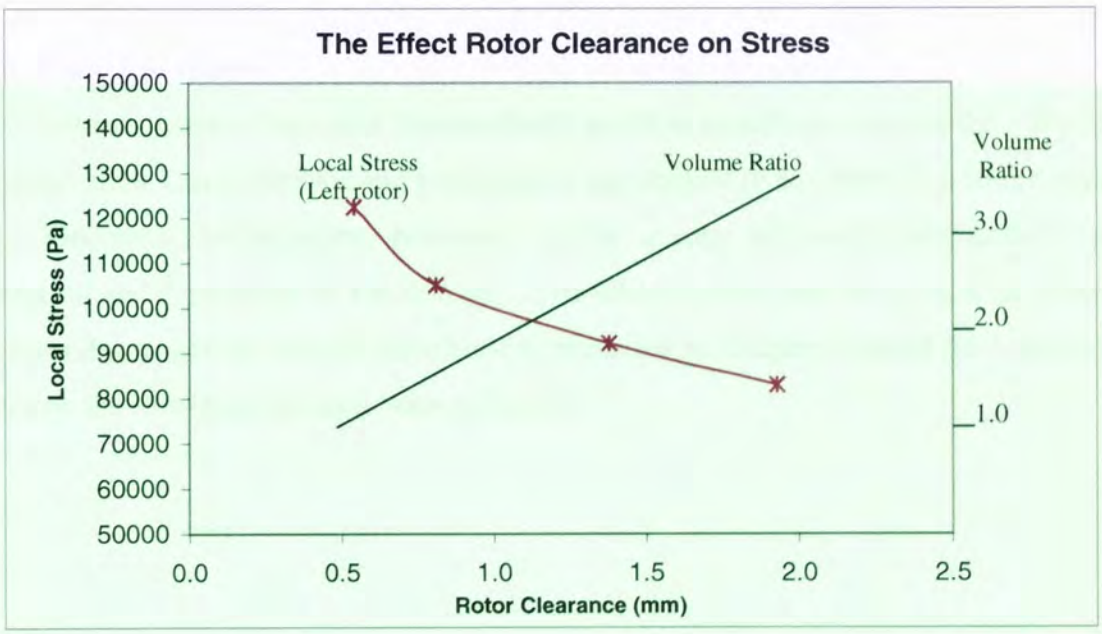

Figure 7-33 ***Rotor tip clearance against shear stress for rotor configuration2***

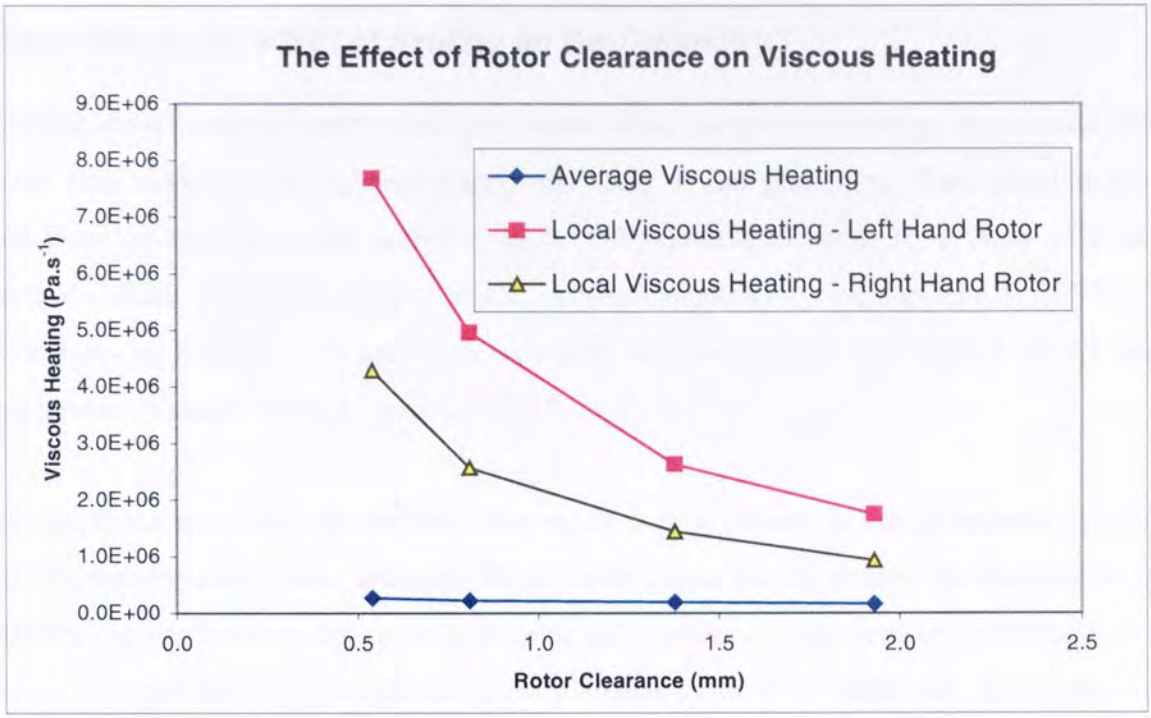

Figure 7-34 ***Rotor tip clearance against viscous heating for rotor configuration 2***

Note on Rotor Curvature

Rotor curvature is another important design criteria and it is possible to analyze the effect of rotor blade curvature on certain key system performance parameters in an effort to promote good axial mixing. Geometry discretisation, however, can be a long and sometimes difficult process depending on the complexity of the domain. The investigation into the pursuit of overcoming this arduous discretisation obstacle have been is presented in Chapter 8 where the impact of rotor curvature on the flow field has also been addressed.

7.5 Quantifying the effect of Scaling up the Geometry

Theoretical investigations into process equipment scale involve comparing simulations that are identical with regard to all variables except the scale of the geometry. Two simulations were created from the original model scaled in each of the three dimensions by a factor of 2 and 0.5 respectively. Each simulation used a typical polymer rheology (polypropylene at 200°C). The cross sections in Figures 7-35 and 7-36 represent the results from the original model and the similar geometry scaled down by a factor of 0.5.

It is clear that the magnitude of each velocity vector is proportional to the distance away from the axis of its nearest rotor. Also, although the rotor tip speed has decreased for the smaller scaled simulation, the gap between the rotor tip and the outer-wall has decreased proportionally as well. Therefore, it is not surprising to find that flow and shear patterns are identical. As a result mixing index values, shear rate magnitudes and pressure contours are also identical. This statement is affirmed by Figures 7-35 and 7-36 – note the scale provided in each figure.

It should be noted that altering the scale of the geometry may become important in terms of transforming the flow field in these isothermal models if the viscosity of the fluid modelled decreased or the scale was increased beyond a certain threshold so as to invoke significant inertial forces. This subject is investigated in section 8.6.2.

Also noteworthy is the fact that heat generation and dissipation will differ between varying scales and therefore heat loads on heat transfer fluids will change. This situation cannot be adequately represented by a pseudo steady state model given by an instantaneous snap-shot; a time dependent model is required. The scaling of non-isothermal flow simulations of screw and kneading disc elements in a twin screw extruder has been discussed by White and Chen[111]. They report that, in the case of non-isothermal flows, the scale of the process is an important consideration since the larger machines have a tendency to generate greater temperatures due to viscous heating. This tendency of large scale devices to experience a temperature build up is due to the fact that "the volume of the machine per unit length increases with the square of the scale up factor and the surface area of the barrel and screw increases linearly, hence, heat dissipation becomes increasingly important and then a dominant factor as machines becomes larger".

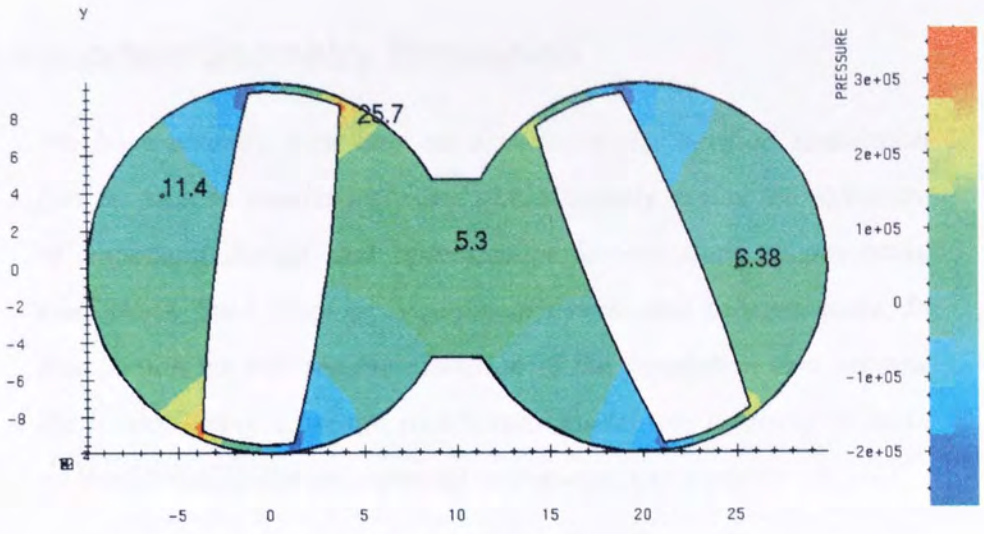

Figure 7-35 ***Smaller scale: Pressure contours and local shear rate values***

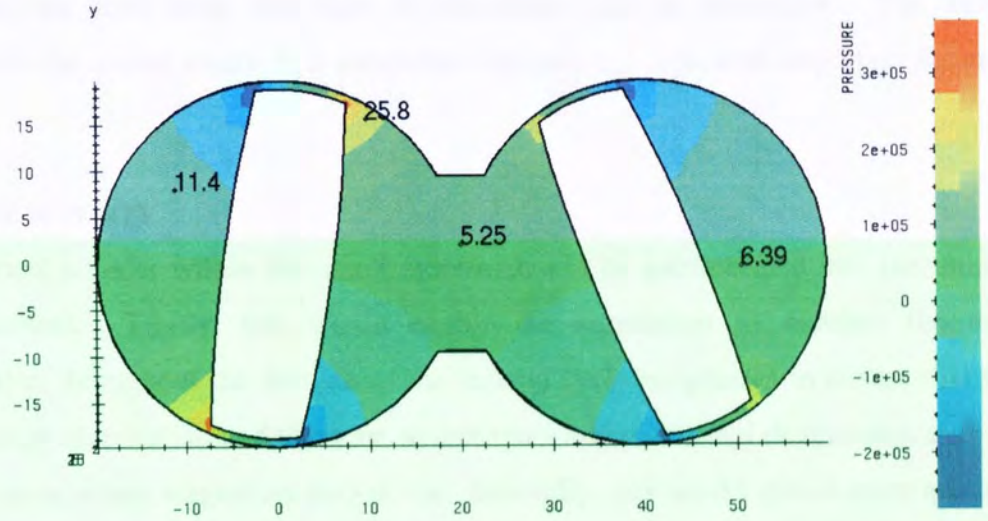

Figure 7-36 ***Larger scale: Pressure contours and local shear rate values***

8. Time Dependent Geometry Simulation

We have already seen how an experimentally verified simulation can be used to qualitatively and quantitatively assess the influence of important design and optimisation factors such as operating conditions, fluid rheology, equipment design and process scale. In this section we will see the extension of the simulation to overcome the limitations of a pseudo steady state model and in doing so build on model validation and open up new avenues to explore.

8.1 Introduction

Until now investigations have been pursued, with some success, via pseudo steady state models. However, as we have seen, this type of simulation can be restricting. The lack of time dependency in the model results in a simulation that can not cope with important features. These are:

Transfer of energy

Ideally heat transfer within the mixer system should be incorporated into the model for two main reasons. Firstly, this would enable the simulation to monitor the temperature distribution throughout the domain as the mixing cycle progresses to ensure that there is an even energy distribution and there are no hot spots where thermal degradation may take place or cold spots where stagnation may occur. Secondly, this would give a more accurate model since the change in important physical properties such as viscosity and density (and others like specific heat capacity, wall slip and chemical properties) due to temperature fluctuations will be taken into account. Thermal gradients within a system will inevitably alter flow and mixing patterns and the performance of the equipment in question. Decreasing the viscosity of a fluid will also lower the shear stress and adversely affect dispersive mixing. The extent of the overall effect of thermal gradients and temperature on the system will of course be dependent on their magnitude. The thermal in-homogeneity that exists within any internal mixer during the initial mixing and plasticizing period will be great. However, for the majority of the mixing cycle the effect will be less dramatic. The thermal gradients that exist in the Hampden RAPRA Torque Rheometer during the more stable period of the mixing cycle are unknown. Their effect may turn out to be negligible. This is an area that needs to be explored.

Conversion of species via chemical reaction

The reactions that may take place within practical processing situations will alter the physical properties of the fluid. The changing mix of species, linked with temperature, may, for example, induce significant viscosity gradients and this change in viscosity will alter the flow and mixing patterns.

Viscoelastic models

If the additional stresses generated by viscoelastic fluids are to be included in the simulation then viscoelastic models are required. Accurate viscoelastic models require the inclusion of time as a parameter.

Particle tracking

Tracking hypothetical particles, by integrating velocity vectors with respect to time, could be used to examine distributive mixing as time progresses.

Dye Tracing

Tracking the position of a theoretical mass scalar through the domain, similar to particle tracking, can be useful to analyse mixing qualitatively and for model validation purposes.

Two phase models

The entrapment of gases (or solids) within the bulk polymer phase is a challenge which, in order to be studied effectively, needs the inclusion of time in the models so the position of the minor phase can be tracked.

Simulations that include time will yield greater in-depth flow field appreciation. All rotor configurations can be analysed and the effects of altering various key variables of the system can be modelled and monitored throughout the stages of temporal advancement rather than by three representative configurations.

8.2 Time dependent geometry meshing techniques

Two possible routes have been identified by the author, that are potentially superior to other techniques employed by other researchers modelling internal mixers, to model the time dependent geometry of the Hampden RAPRA Torque Rheometer. These are the transient or sliding grid technique and the mesh superposition technique (MST). Both of these techniques take a mesh defined to represent the situation in question and automatically define new meshes linked to any number of time steps which represent the whole cycle of rotation. For accuracy the time step or degree of rotation can be quite small and of the order of 10^{-3}s or 0.5° respectively. The question that immediately arises is 'how can the large number of time steps required to model one rotor cycle be practical when one step requires many hours of CPU time?' For example, a simulation of an optimised Hampden RAPRA Torque Rheometer mesh for a viscous fluid with a power law exponent of 0.3 will take greater than 24 hours to reach a good convergence level using Polyflow 3.5.0.1 on a Digital 500au workstation. Also, as seen in chapter 7, the number of iterations for a non-isothermal simulation can increase significantly e.g. by a factor of two to reach a similar conversion level for a fluid with a power law exponent of 0.5. The MST, as incorporated in the very latest version of Polyflow (3.6), is a practical solution for Newtonian, isothermal two-dimensional simulations. Techniques can be used to reduce CPU by, for example, using less accurate linear velocity and constant pressure interpolation and this latest version of Polyflow boasts improved code performance. For this research, however, this particular route would be highly impractical. The MST technique does, however, appear promising for future research in this area since it allows simulations of intermeshing equipment, unlike the sliding grid technique, and of course hardware and software are continuously and rapidly improving. Also, for modelling a twin screw extruder, MST, when used in conjunction with 'Polyfuse', offers the potential to represent the whole length of the screw train using various separate conveying and mixing modules. These modules, once constructed, could be easily rearranged as desired to aid in determining optimum screw configurations. The sliding grid technique, as used by CFX[112] commercial codes, presents a more pragmatic possibility for modelling the Hampden RAPRA Torque Rheometer since their codes offer far greater efficiency in terms of both CPU and swap space requirement.

8.2.1 Transient/sliding grid technique and unmatched grids

The sliding meshing technique, originally developed to model flow within continuous flow stirred tank reactors (CFSTR), makes use of *unmatched* grids. Regular grids must have each cell within the main body of the domain either aligned and perfectly connected to another cell or

defined as an external boundary. However, with unmatched grids internal boundaries can be defined within the main body of the domain. These boundaries do not need cells which match on either side. The dummy cells that surround each block or boundary are used to transfer information via interpolation techniques. Therefore, unmatched boundaries can slide past one another in transient simulations and the mesh can behave as a regular mesh at any given time step regardless of the way the cells overlap. This idea may become clearer when we consider the Hampden RAPRA Torque Rheometer mesh.

The mesh was constructed in three main parts; the two identical left and the right rotors (Figure 8-1a and b) and the chamber wall (Figure 8-2a and b). The mesh around the two rotors fits into the two voids in the chamber section with a clearance of 0.001mm. When the rotors are translated into their correct position the boundary between them appears 'unmatched'. Figure 8-3 illustrates an example of a small section of one of the unmatched grid used for the transient/sliding grid model. These unmatched grids around each rotor can be altered relatively easily/quickly and are not constrained by the chamber grid.

Figure 8-1a) ***Left/right rotor fluid domain.*** **b)** ***Left/right rotor wall boundary on its own.***

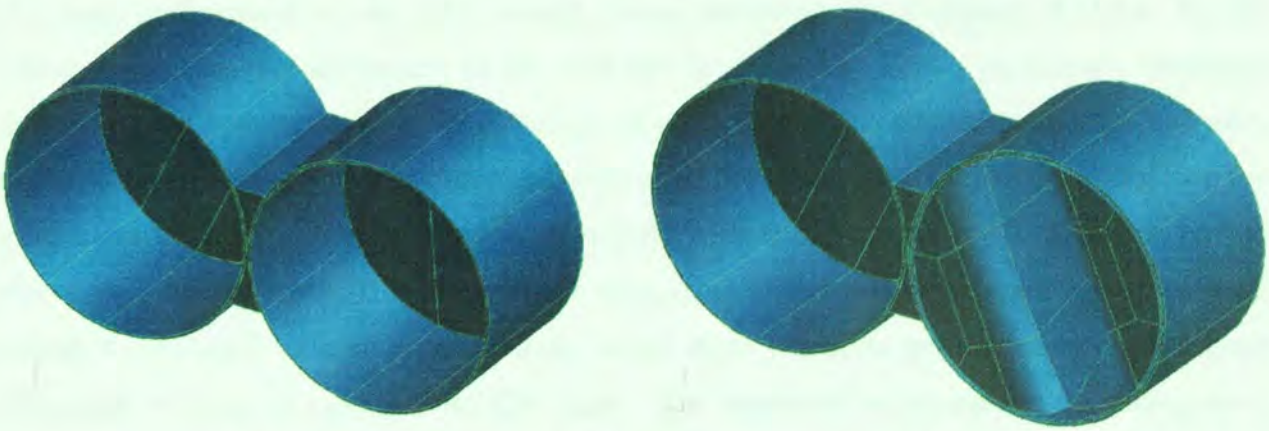

Figure 8-2a) ***Rear angled view of outer shell of simulation geometry*** **b)** ***Rear angled view of outer shell of simulation geometry with left-hand rotor in position***

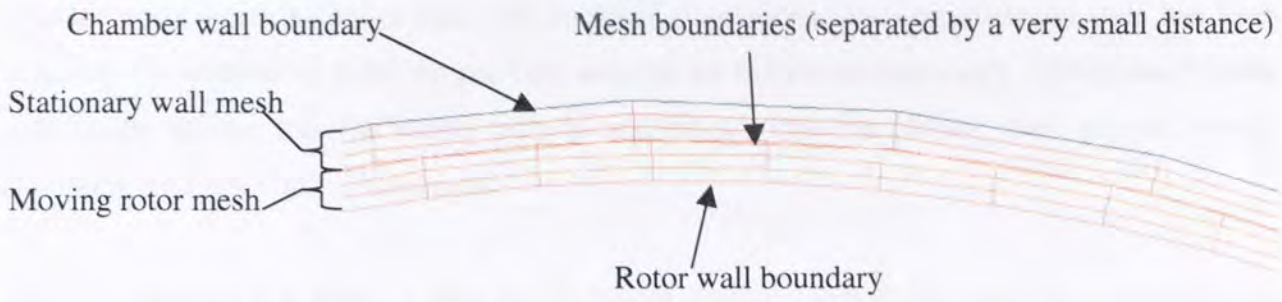

Figure 8-3 ***A section of the unmatched grid around a rotor tip***

8.2.2 Solver performance

The improvement in performance gained from using CFX to model the Hampden RAPRA Torque Rheometer as opposed to Polyflow is substantial. Firstly the swap space requirement for CFX simulations is very much less than for Polyflow simulations. Secondly, although a CFX simulation requires more iterations to reach a certain convergence level than Polyflow, the total CPU time required is considerably less. Table 8-1 offers a comparison between the performance of two commercial solvers solving identical problems.

Table 8-1 ***Solver performance for the Hampden RAPRA Torque Rheometer simulations***

	Hampden RAPRA Torque Rheometer simulation	
	Polyflow version 3.5.0.1	CFX 4.2
Swap space (≈5500 nodes)	3500Mb	<<64Mb
No. iterations *	20	700
Total CPU Time *	80 hours	<0.1hour

* for a fluid where K = 3000 and n = 0.3 with typical convergence of 10^{-4}

The high performance of the CFX solver, when modelling the Hampden RAPRA Torque Rheometer, means that the density of the mesh can be increased. This is particularly beneficial since it is good practice to have a high density of nodes around unmatched boundaries and also, although the previous mesh was optimised, increasing the mesh density will tend to improve the accuracy of the results. The quality and form of the cells within the mesh will also be improved with a high density mesh. This is important since large differences in adjacent cell sizes make finding a converged solution more difficult, hence, more iterations are needed to reach a good conversion resulting in a greater total CPU time. The number of nodes used in the sliding mesh simulations analysed in this chapter was 21,867.

Another point worth noting is that with transient simulations, once quasi-steady state has been achieved, the number of iterations per time step can be reduced considerably. Quasi steady state simulations assume that the inertia term is negligible. This has already been proved for the Hampden RAPRA Torque Rheometer.

The next question that arises is 'how do the results compare to both the previous simulation and the mechanical model?'

8.3 Simulation Validation

The simulation of internal mixers using a three dimensional sliding grid has not been undertaken by researchers until now so the results were approached cautiously. On first inspection it appeared that sensible results were obtained. The transient nature of the simulation and the fact that 'USER FORTRAN' routines allow CFX solver code manipulation means that other validation techniques such a dye tracing and torque calculations can be implemented. However, to determine the accuracy of the model it was firstly compared to the mechanical model and the previous Polyflow simulation.

8.3.1 Velocity Vector Comparisons

In order to compare directly both solver simulations and the mechanical model, velocity vectors have been obtained at locations within the domain as used in Table 6-2. The results of this investigation are presented in Table 8-2.

The average difference between the Polyflow simulation and the mechanical model for the point trajectories and velocity magnitudes calculated from the data in Table 8-2 is 0.88% and 4.06mm/s respectively. The average difference between the CFX simulation and the mechanical model for the point trajectory and velocity magnitude is 0.98% and 3.98mm/s respectively. The average difference between the Polyflow simulation and the CFX simulation for the point trajectory and velocity magnitude is 0.85% and 1.24mm/s respectively. These values indicate very similar model accuracy. The relative closeness of the velocity magnitudes from the two simulations add weight to the conclusion previously drawn that drag, due to the presence of the real particles in the fluid, at least partially causes the discrepancies observed in these validation experiments.

Table 8-2 ***Velocity vector comparison between the CFD model and experimental values***

Location of Particle Origin*		Velocity					
Co-ordinates** (mm)		Point Trajectory (deg)			Vector Magnitude (mm/s)		
'x'	'y'	Exp.	Polyflow	CFX	Exp.	Polyflow	CFX
[1] 42.22	11.37	291.8	287.9	289.0	35.5	38.7	36.7
[1] 53.76	6.47	329.0	328.8	328.3	33.2	38.5	38.0
[1] 43.81	9.56	294.3	295.4	297.3	35.8	36.8	34.7
[2] 28.02	6.32	204.6	205.6	204.4	25.3	36.5	35.5
[2] 25.33	-7.58	145.5	143.6	149.0	30.3	34.5	34.8
[2] 25.96	6.32	203.6	205.8	203.5	34.5	37.7	36.1
[3] 30.54	-7.11	125.7	128.7	132.3	36.1	37.3	35.5
[3] 39.71	-16.11	89.7	92.7	94.1	27.8	33.1	34.6
[3] 42.16***	-13.90	82.2	86.0	87.6	38.6	40.3	40.1
[1] 9.22	6.95	140.0	142.3	147.8	47.4	53.3	51.9
[2] 13.80	5.37	159.5	162.9	156.0	45.7	55.3	56.3
[2] 14.75	2.37	175.2	173.16	175.0	53.7	52.3	52.1
[1] 16.17	8.05	150.2	138.0	145.4	31.6	34.3	37.7
[2] 14.43	-3.32	202.6	198.7	196.7	52.6	51.6	52.0

Notes:

* All vector origins were taken at z = 15mm (+/- 2mm)
** Co-ordinates taken from the left-rotor axis
*** Vector was taken at z = 12 mm (+/- 2mm)
[1] Rotor Configuration 1
[2] Rotor Configuration 2
[3] Rotor Configuration 3

The range for the point trajectory is 0 –360 deg where zero equates to a particle moving vertically upwards.

8.3.2 Dye Tracing Validation Technique

Another method of assessing model predictions is by comparing flow and mixing patterns.

Mixing Patterns – Experimental Method

Two viscous fluids of identical physical properties with different colouring are packed into the mixer chambers whilst the rotors are configured 'vertically'. The minor phase, in the form of a thin horizontal plane, is positioned within a bulk or major phase. When the rotors are turned the mixing patterns are formed and can be revealed by examining the various clay slices as seen in chapter 6.

Mixing Patterns – Simulation Method

In the simulation the horizontal plane of the minor phase was modelled by inserting a number of new blocks within the discretized domain. Within each new block the mass scalar was defined. This mass scalar source term represented the dye in the model. The source term 'S_L' added to satisfy the laminar equations is given by

$$S_L = \frac{\partial \rho \Phi}{\partial t} + \nabla \cdot (\rho U \Phi - \Gamma_\Phi \nabla \Phi) \qquad (8\text{-}1)$$

The scalar diffusion coefficient of the minor phase in the bulk phase 'Γ_Φ' was defined as zero.

Results

Figures 8-4 and 8-5 present an example from the results of these trials from which we can see that the predictive model reveals very similar patterns to that obtained from the experimental model. When studying this type of simulation it is worth noting that the horizontal plane of blocks, that contains the 'dye', will rotate with their associated rotor, therefore, the motion of the fluid appears (due to numerical diffusion) to either 'drag out' or 'leave behinds' the dye from the block. Hence it is the outer bounds of the dye that should be considered. This can be a limitation to this validation method since as time advances the domain will become totally permeated by the dye. This statement may become clearer by appreciating the figures in the section on slip where the dye can be seen to occupy a large percentage of the domain.

The discrepancy between Figures 8-4 and 8-5 two is largely due to wall slip. The effect of slip on this type of simulation is examined later.

Figure 8-4 ***A slice through a two coloured clay mixture revealing the deformation of a horizontal plane after a 1/2π rotation of the left rotor***

Figure 8-5 ***A slice through a simulation representing a two coloured clay mixture revealing the deformation of a horizontal plane after a 1/2π rotation of the left rotor***

8.3.3 Torque Validation Technique

As elaborated on previously, torque comparisons appear to be a good way to compare model predictions with reality. In order to enable the model to calculate torque it was necessary to write a 'USER FORTRAN' programme. This ability of CFX, to allow the users to input their own ideas into the code, affords good flexibility. The programme created is given in Appendix 7. Torque data, taken directly from the Hampden RAPRA Torque Rheometer mechanical model, has been used in a wide variety of investigations at Aston by *Al-Malaika et-al,* for example, in the compounding of polypropylene[113] and polystyrene [114]. This data can be used for comparing the torque values obtained from mixing in a real system to that predicted by the simulation. The operating conditions, as used by *Al-Malika et al*, for these experiments are:

Operating temperature - 180°c,

Operating Speed – high (see Table 7-1)

Mixing time – 10 mins

The power law data for polypropylene and polystyrene are given in Table 6-1. This data is given at 200°C and therefore must by adjusted to compensate to allow for the 20°C temperature difference. The power law index is not particularly sensitive to temperature change. *Griskey*[115] comments that '*n* can be assumed to be relatively constant, provided that the temperature does not change by more than 30°C' and provides a number of examples to substantiate his claim. The constant value of *n* for polypropylene melts can be seen in polypropylene viscosity and shear rate plots for a number of different temperatures[116]. The viscosity 'μ', or consistence term '*K*' in the power law equation, changes drastically with temperature for polymer melts and can be

evaluated in terms of the activation energy E and the ideal gas constant R as shown in equation 8-2. The activation energy of polymers is much larger than typical viscous liquids and increases with chain rigidity and the size of lateral branches. The constants for a number of polymer melts are given by *Agassant et al*[117]. Using this equation the viscosity is calculated below for both polypropylene and polystyrene.

$$\mu = \mu_0 * \exp \frac{E}{R}\left(\frac{1}{T} - \frac{1}{T_0}\right) \tag{8-2}$$

Polypropylene

$$\mu = 4400 * \exp \frac{3.7 * 10^4}{8.314}\left(\frac{1}{453} - \frac{1}{473}\right)$$

$$\mu = 4400 * 1.51$$

$$\mu \approx 6600 Pa.s$$

Polystyrene

$$\mu = 15600 * \exp \frac{9.6 * 10^4}{8.314}\left(\frac{1}{453} - \frac{1}{473}\right)$$

$$\mu = 15600 * 2.94$$

$$\mu \approx 45900 Pa.s$$

Simulation Results

Using the data above simulations were carried out representing a homogeneous and isothermal mix after 10 minutes of processing time with the residuals decreasing by six orders of magnitude. Figure 8-6 presents torque contours plotted on a rotor surface and Figure 8-7 presents the total torque calculated over the 2.8s rotor cycle for polypropylene mix and polystyrene mix. Table 8-3 summarises the average torque values for the simulated and the experimental work.

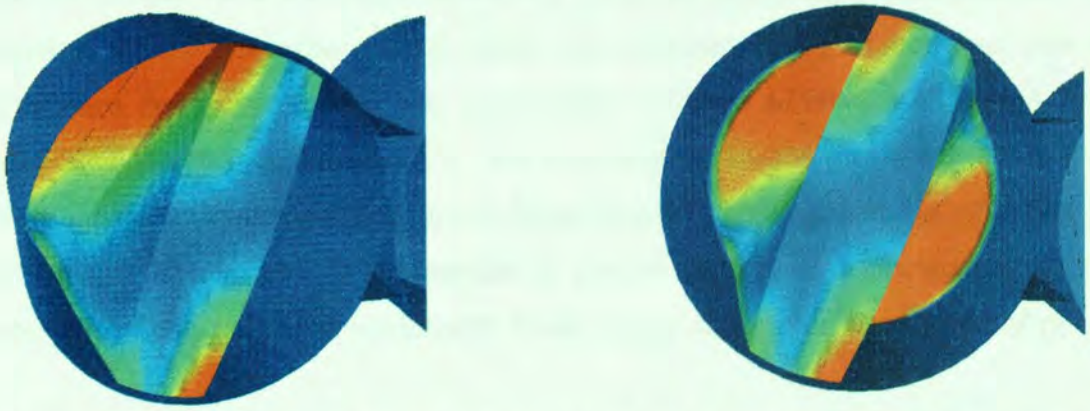

Figure 8-6 ***Torque contours plotted on a rotor surface for two different viewing perspectives***

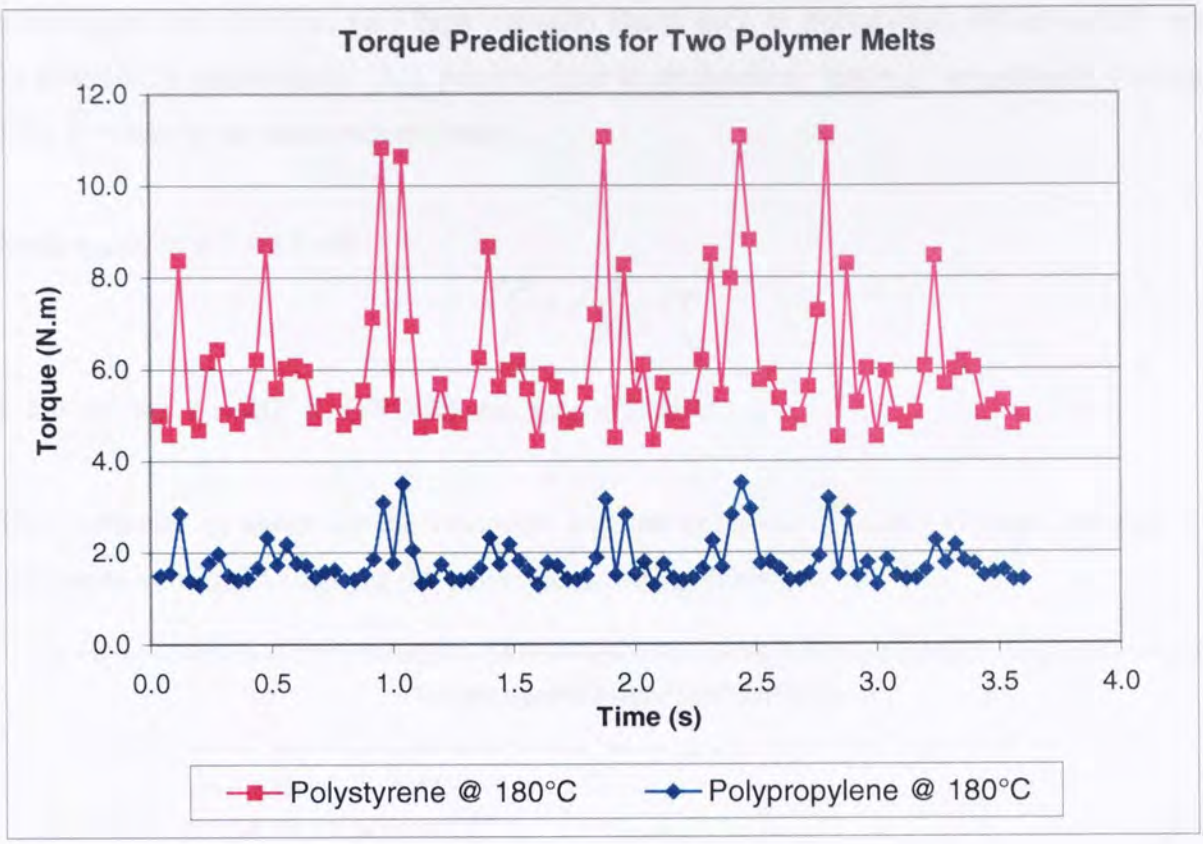

Figure 8-7 ***Torque against time for polystyrene and polypropylene melt simulations at high speed***

Table 8-3 ***Experimental and predicted torque values for two polymer melts***

	Polypropylene Melt @ 180°C	Polystyrene Melt @ 180°C
Experimental reading after 10mins	~2.0 N.m	~12.5 N.m
Simulation average over cycle	1.8 N.m	6.0 N.m

The predicted torque value compares favourably with that determined experimentally for the polypropylene melt. The experimental value was expected to be higher than that of the simulation since the polypropylene was compounded with an additive AATP (1-Acryloyl-4-acryloyoxy-2,2,6,6-tetramethylpiperidine). The experimental torque plot from the 20% AATP mix is very similar and marginally higher (2.5N.m after 10 minutes) than that of a 10% AATP mix (2.0N.m after 10 minutes). It is reasonable to assume that a lower concentration, i.e. tending to pure polypropylene, will have a relatively lower torque value after 10 minutes of processing time.

The torque is a function of rotor speed and the viscosity as defined by the power law; Figures 8-8 and 8-9 show the dependence of torque on these variables. The viscosity can be a function of

temperature and therefore very high viscosity fluids such as polystyrene are drastically affected by changes in temperature. A 1 percent error in temperature reading can produce a 25 percent error in viscosity as demonstrated below.

From equation 8-2 we have

$$\frac{\Delta\mu}{\mu} = -\frac{E}{RT^2}\Delta T \tag{8-3}$$

If $E = 10^5$ and T =400 °K, E/RT=25 and $\Delta\mu/\mu = 25\Delta T/T$.

This difficulty in assessing the viscosity, and the presence of additives, may account for the difference in torque values for the polystyrene mix in Table 8-3.

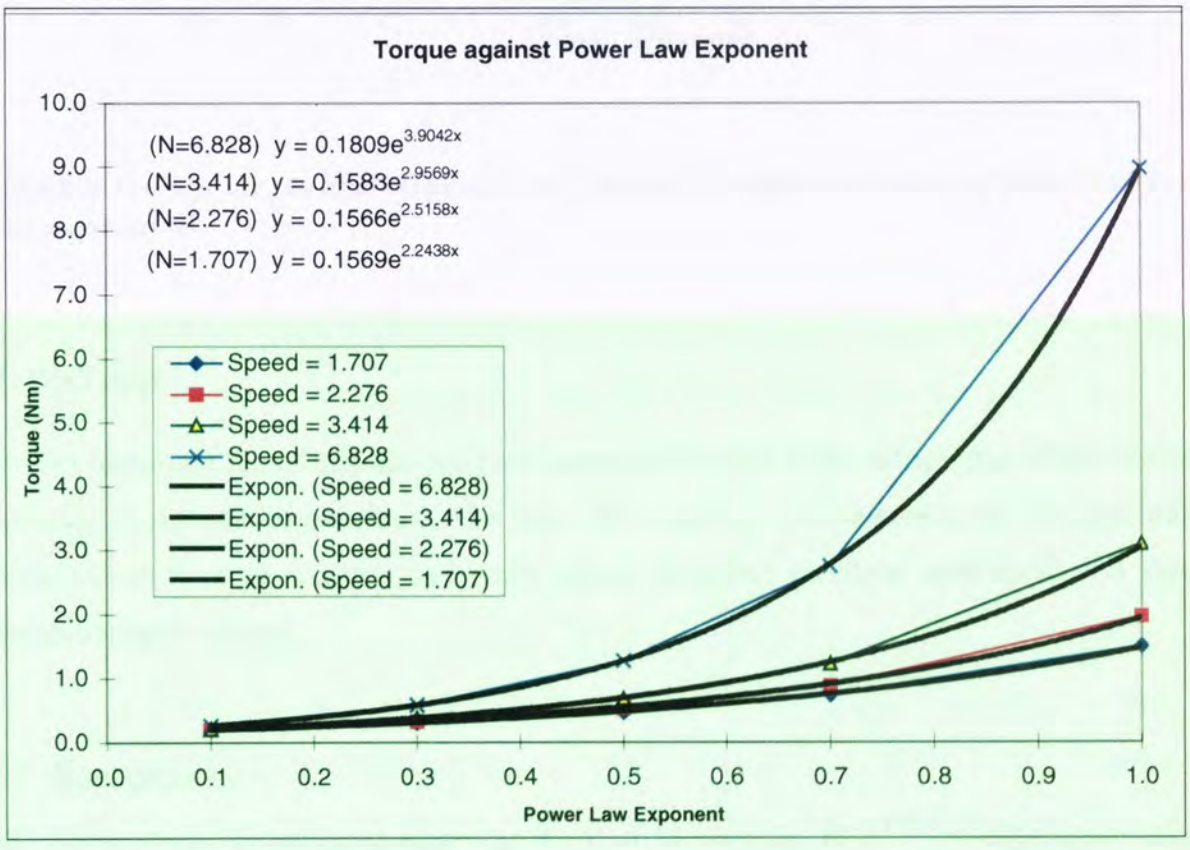

Figure 8-8 ***Average torque against power law exponent for different values of the left hand rotor speed when K=3000***

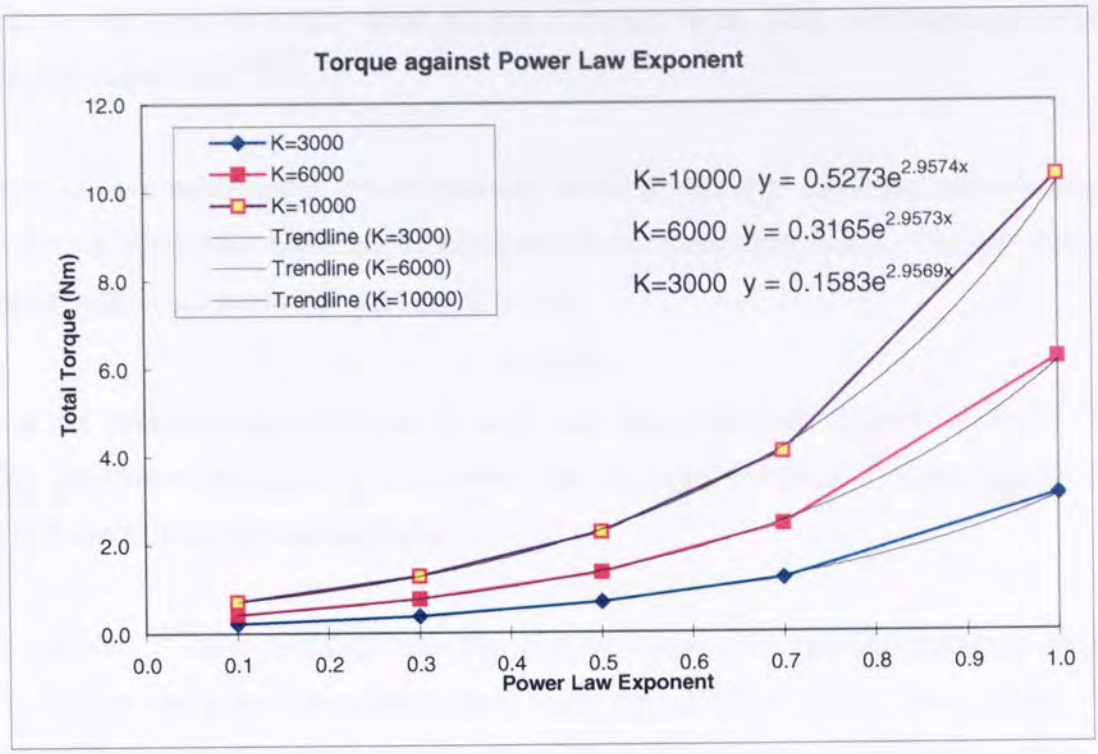

Figure 8-9 ***Average torque against power law exponent for different values of power law factor at low rotor speed***

8.4 Wall Slip

One very important factor that has not been assessed in depth is the detrimental effect of slip on processing equipment performance. To date, the majority of researchers in this area do not include slip in their simulations and hence ignore its effect on shear rates/stress and various material transport criteria.

8.4.1 Background

Wall slip has been documented since the work of Mooney in 1931[118]. At high shear stresses polymer-melt flows violate the standard no-slip hydrodynamic boundary condition at solid surfaces. Wall slip has long been suspected of significantly contributing to melt fracture instabilities observed in polymer melt extrusion processes. Melt fracture is a macroscopic change in the surface morphology that varies from small-scale roughness (100μm) to large-scale distortion of the entire extrudate[119]; the well-known 'sharkskin' effect. The onset of slip depends on the material of construction of the boundary, strongly suggesting that the wall-polymer interaction is important[120,121]. These experiments and others indicate that the no-slip condition

seems to be valid until the shear stress reaches a critical value. Also wall slip may be inversely proportional to pressure[122,123].

Kalyon *et al* have investigated the relationship between wall slip and shear stress at the wall in the processing of polymer melts/highly filled suspensions and other fluids. The wall slip velocity 'u_s' against wall shear stress 'τ_w' data are fitted by:

$$u_s = \beta \tau_w \tag{8-4}$$

Where β is a material constant or the Navier's wall slip coefficient (9.6×10^{-8} m $Pa^{-1}s^{-1}$ [124,125,126] for filled polydimethylsiloxane with a power law factor of $6888 Pa.s^{0.48}$ and a density of 1050 kgm^{-3}) and can be temperature dependent.

Other researchers[127] have postulated that the relation between slip velocity and shear stress at the wall may follow the power law model above some critical stress for the onset of slip. *Mhetar and Archer*[128] studied slip using a planar couette shear flow cell on a bare silica surface. A log-log plot of slip velocity and shear rate shows several power law regimes. Slip velocity was again found to be a strong function of the chemical nature of the surface. The consensus now seems to be that, unlike simple small-molecule liquids, polymers violate the no-slip condition when wall shear stresses exceed a value around 0.1 MPa in entangled melts sheared over metal surfaces. Data from several of these studies show that the critical shear stress for apparent slip in entangled melts is virtually independent of molecular weight for a given polymer type. In entangled solutions, the critical stress for apparent slip is lower and depends strongly on the concentration.

The studies of *Leger et al*[129] into slipping high molecular weight polymer melts involve the measurement of the velocity of particles near to the wall, through near field velocimetry techniques, and reveals three different regions of friction. At low shear rates ($<10^{-1}$), there is a small amount of slip, due to the strong entanglement between surface-anchored chains and the polymer in the bulk. Critical slip velocity is obtained by increasing shear (10^{-1}-10^{0}), the shear / slip velocity data does not match a linear correlation but power law relationship and this may be due to the untangling of the anchored chains with the bulk polymer. The final region is where there is a large amount of slip due to the high shear rates. This is due to there being almost full untangled, polymer chains. *Leger et al* also conclude that molten polymer flow is limited by solid surfaces. Stainless steel can prove to be a rough surface, whereas treated with silica this can promote slip. Altering the surface chemistry of the solid surface affects the amount of polymer

interactions with the surface (chemical grafting and polymer adsorption) and therefore indirectly affects the amount of slip of the liquid.

Other studies have shown that the critical shear rate for the onset of slip to be in the order of: γ=0.15s^{-1} for poly(di methyl siloxane) in contact with a stationary octadecyltrichlorosane covered quartz plate during shear flow[130].

The effects of solid content, particle size, type of solid particle material and temperature on the slip velocity and slip layer thickness in concentrated suspensions has been investigated by *Soltani* and *Yilmazer*[131]. Small particles (around 5μm) did not show slip at any packing fraction of the solution. All other particles did show slip velocity with a linear relationship to the increasing shear rate and the increasing temperature. The slip layer thickness increased linearly with particle diameter. The increase in slip velocity with increasing temperature was primarily due to the decrease in the shear viscosity.

8.4.2 Investigation

The mechanical model discloses the phenomenon of wall slip at the wall boundaries. A section of the Figure 8-4 has been reproduced below to highlight the amount of slipping of the coloured clay mix after π/2 rotations of the left-hand rotor. The result of slip along the rotor wall can clearly be seen. The slip on the Perspex chamber can also be seen in practice and is of a similar magnitude. The simulation *command file** has been altered, as detailed below, to incorporate a wall slip as a linear function of wall stress. The dye-tracing model has been carried out specifying the Navier's slip coefficient β = 9.6x10^{-8} m $Pa^{-1}s^{-1}$), as derived by *Kalyon et al*, and a broad range of other coefficients. The results (Figures 8-11 – Frames A - E) can be compared to Figure 8-10. The simulation has also been used to determine the effect of slip on transport properties and shear character.

*The command file is written to define the flow problem for the CFX solver. A typical command file is give in Appendix 8

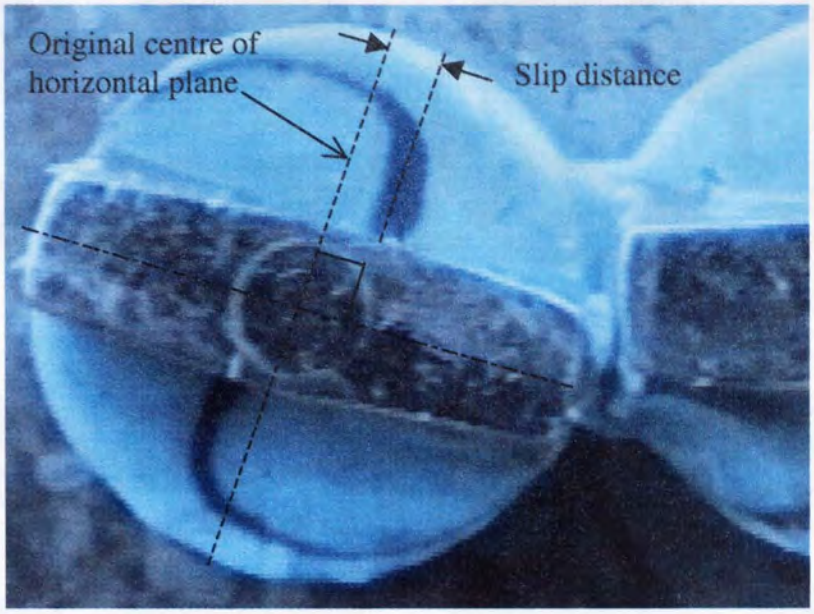

Figure 8-10 ***A slice through a two coloured clay mixture revealing the deformation of a horizontal plane after a 1/2π rotation of the left rotor.***

8.4.3 Slip Simulation

The default model assumes that there is no-slip at the wall i.e. zero wall velocity. Full slip boundary condition, i.e. zero wall stress, can be enforced onto any wall boundary using the command file keyword 'no slip'. Another method of adding wall slip to the simulation is by using an algebraic slip model whereby the velocity boundary conditions may be specified. Velocity boundary conditions may be specified by the user in the form:

$$AU_i + B\tau_i = C_i \qquad i = 1,2,3 \qquad (8\text{-}5)$$

Where $\tau_i = \left(\mu \frac{\partial U_i}{\partial y} \right)_w$ and is the wall shear stress. The default is no-slip i.e. A=1, B_i=0, C_i=0.

If $B_i = 0$ and $C_i \neq 0$ a moving wall is boundary condition is specified. If $C_i = 0$ and B is equal to the Navier slip coefficient then we have a form of the desired equation 8-4.

Results

The results from` the simulations are presented in Frames A-E of Figure 8-11 and Table 8-4

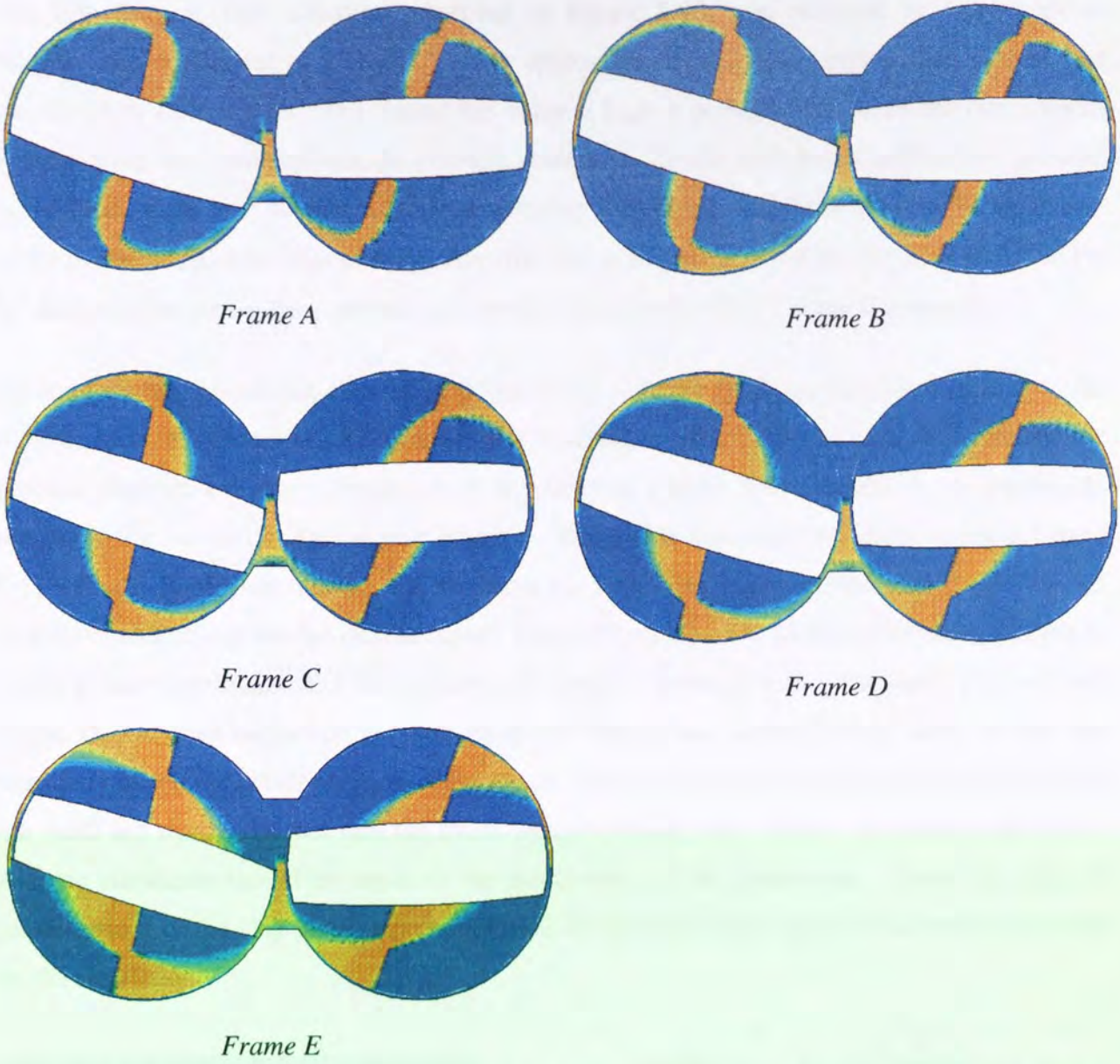

Figure 8-11 ***Prediction of the deformation of a horizontal plane after a ½ π rotation of the left rotor for different Navier slip coefficients.***

Table 8-4 ***Navier slip coefficient and slip quantity after ½ π rotation of the left rotor for slip investigation and frames A-E in Figure 8-11***

Navier Slip Coefficient	Frame in Figure 8-11	Slip distance** mm
1.0E-20	*Frame A*	0.0
1.0E-7*	*Frame A*	0.0
1.0E-6	*Frame B*	3.0
1.0E-5	*Frame C*	5.6
5.0E-5	*Frame D*	7.8
1.0E-4	*Frame E*	12.6
1.0E-2	*Frame E*	12.6

* Representing polymer - wall interaction.

** Slip distance as per Figure 8-10 measured from A4 stills.

The slip distance, from situation presented by Figure 8-10, was recorded as 4mm with an estimate slip coefficient of 2.0E-6. This is approximately one order higher than that of that calculated by *Kalyon et al.* The reason this value is high is perhaps because of the very smooth Perspex walls and rotor surfaces, the possible presence of grease from hands and the low pressure of the fluid. It is clear, however, that by accounting for slip the simulation mimics the behaviour of the experimental trial more closely. Also that the slip conditions defined by $\beta = 8.9*10^{-8}$ $m.Pa^{-1}s^{-1}$ do not influence the flow substantially in the Hampden RAPRA Torque Rheometer.

To compare the dye tracing simulation (Figure 8-11 – Frame B) to a clay mix (Figure 8-4) the figures representing both situations have been overlaid. Figure 8-12 - Frames A-E presents the process diagrammatically. Frame A is the original Figure 8-4. Frame A is graphically transformed to reveal its edges to give Frame C. Frame B is the same simulation output as Figure 8-11 - Frame B with the colours that represent the minor and major phases altered to make the process of identifying the dye outline easier. Frame D has been edited following the dye edges to create a clear representation of the predicted dye pattern. Frame E is the over lap of Frame C and Frame D. On close inspection the rotor boundary lines of the simulation may seem, at first, not to exactly match the actual position of the rotors. This is not due to errors in the construction of the mesh but due to the fact that the rotors are curved and both 'slices' are taken at z=15mm. Also an allowance should be made for the perspective of the photograph. Given the inherent imperfections of the clay packing process Frame E shows the high degree of accuracy produced by the simulation.

Frame A

Frame B

Figure 8-12a ***Direct comparison between the simulation with slip and the clay mixture***

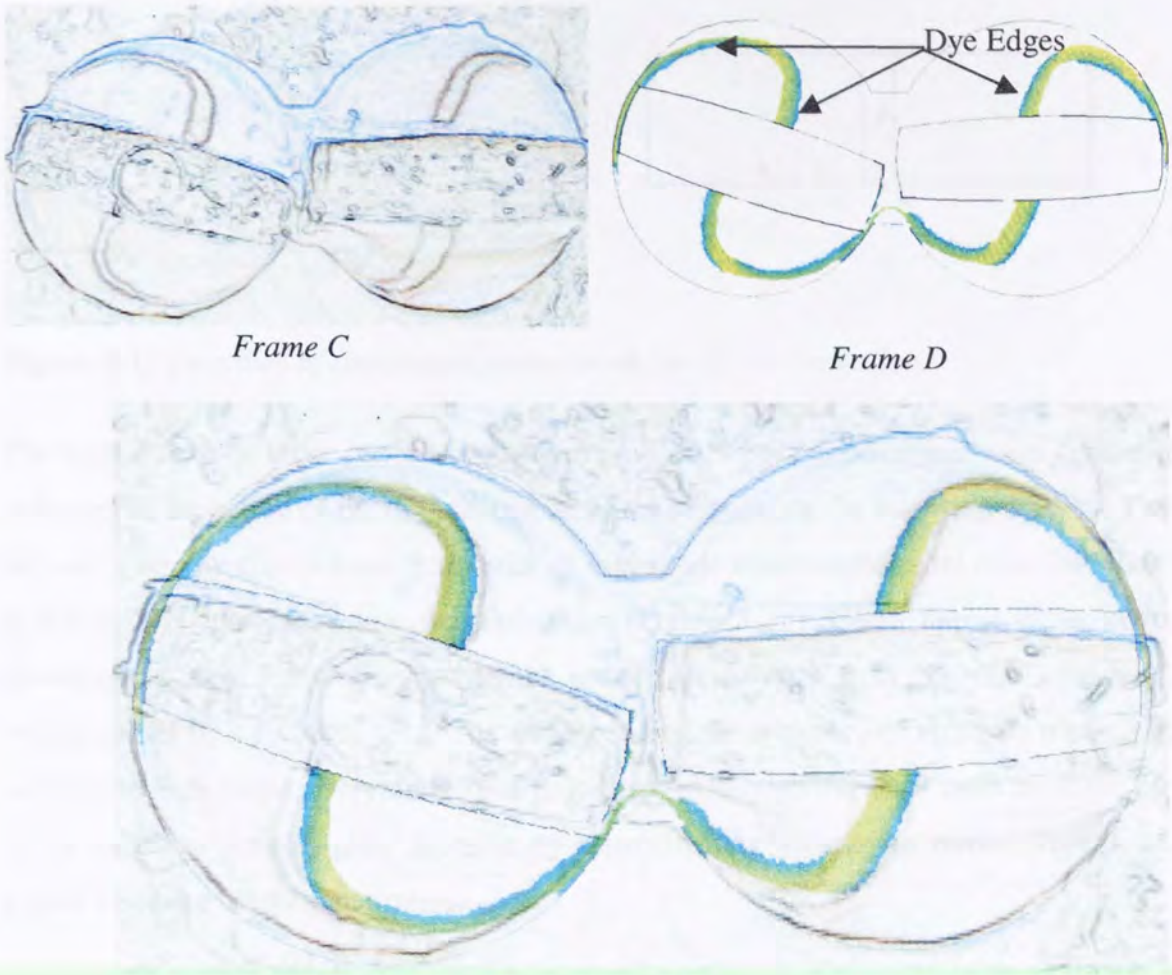

Frame C *Frame D*

Frame E

Figure 8-12b ***Direct comparison between the simulation with slip and the clay mixture***

8.4.4 The Effect of Full Slip on the Flow Field

From the slip-stick phenomenon one can conclude that full slip or very high degrees of slip may be intermittently present at the wall. To determine how slip could possibly effect shear rate, viscosity, pressure, and mass flux a number of probes were inserted into the domain of the simulation to gather data at various key positions. The positions of the probes are shown below:

Table 8-5 ***Co-ordinates of probes used for slip investigation***

Probe	X co-ordinate(m)*	Y co-ordinate (m)*	Z co-ordinate (m)*
Probe 1	0.0000	-0.0195	-0.0125
Probe 2	0.0400	-0.0195	-0.0125
Probe 3	0.0199	0.0000	-0.0125
Probe 4	0.0000	0.0000	0.0005
Probe 5	0.0000	0.0150	0.0005
Probe 6	0.0150	0.0000	0.0005

*Originating from the centre of the left rotor's front face (i.e. point of axis).

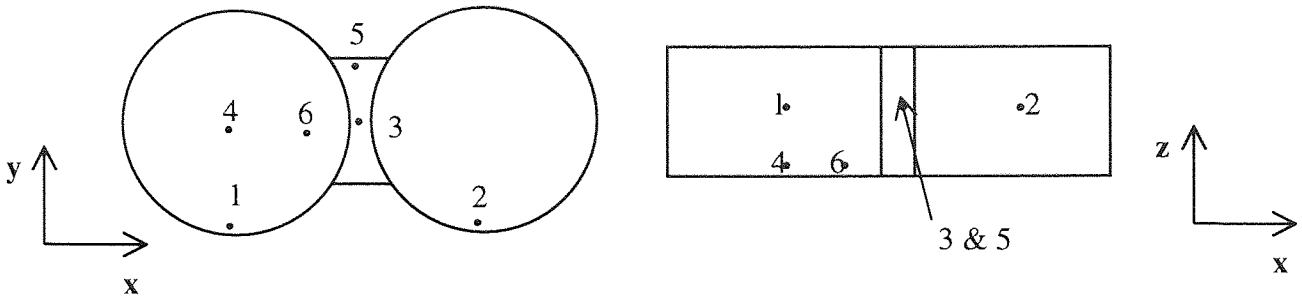

Figure 8-13 ***Location of simulation probes used for slip investigation***

The high shear rate areas generated where the rotor tips pass the chamber walls (probes 1 and 2) and meet in the centre of the domain (probe 3) are responsible for intensive mixing. These shear rates decrease by approximately an order of magnitude and become more constant when full slip at the wall is introduced into the simulation (Figure 8-14). Wall slip may, however, be an advantage in areas least influenced by the action of the rotors, such as probe 5, where the shear rate increases by a factor of two. The corresponding shear stress and viscosity plots, Figure 8-15 and Figure 8-16 respectively, have been presented. Although the shear rates decrease by a factor of 10 the shear stresses only decrease by approximately a factor of three. This is due to the higher viscosity at low shear rates.

The effect of wall slip on the fluid flow in the azimuthal direction can be appreciated by the dye trace simulations (see Figure 8-11). The mass flux in the axial direction is given by Figure 8-17. The axial flux at the edges of the chamber has increased significantly with the introduction of slip at the wall as shown by Probes 1 and 5 while the pattern remains similar at the centre of the domain (Probe 3). This would suggest that slip may improve axial flow and therefore distributive mixing, however, when using theoretical probes the user must be aware of their limitations. Although they are useful for generating quantitative results any conclusion drawn should be backed up by other techniques when analysing a parameter which may vary greatly over small length scales. Analysing contour plots on various slices is one way to check to see if the axial mass flow is improved with slip.

A more useful quantitative method has been devised to assess material transport and is presented in the section on rotor design where the axial flow component is addressed again.

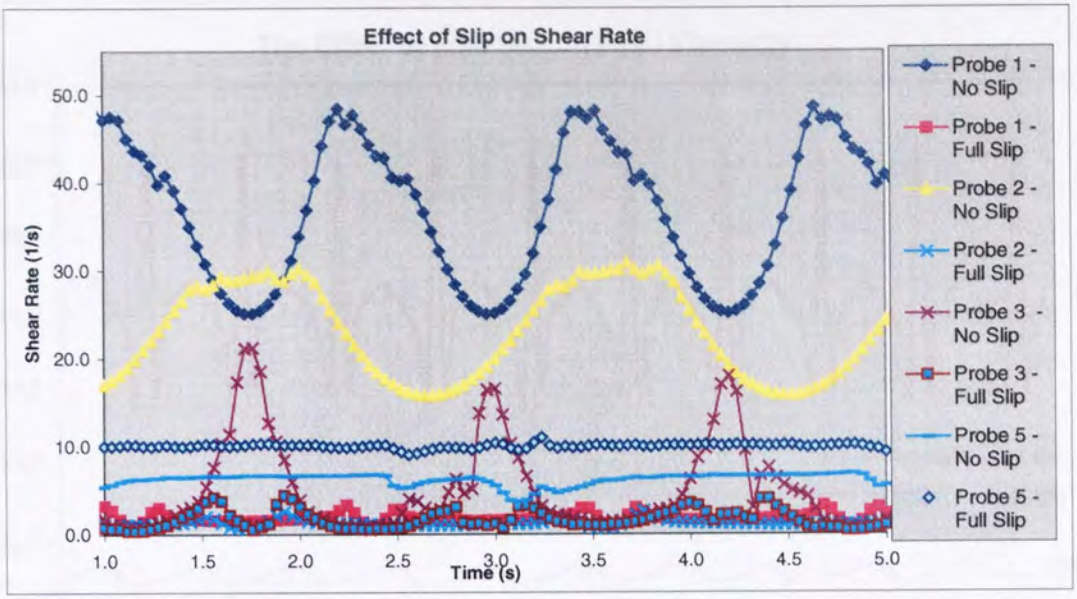

Figure 8-14 *The effect of full slip on shear rate (K=3000 n=0.3)*

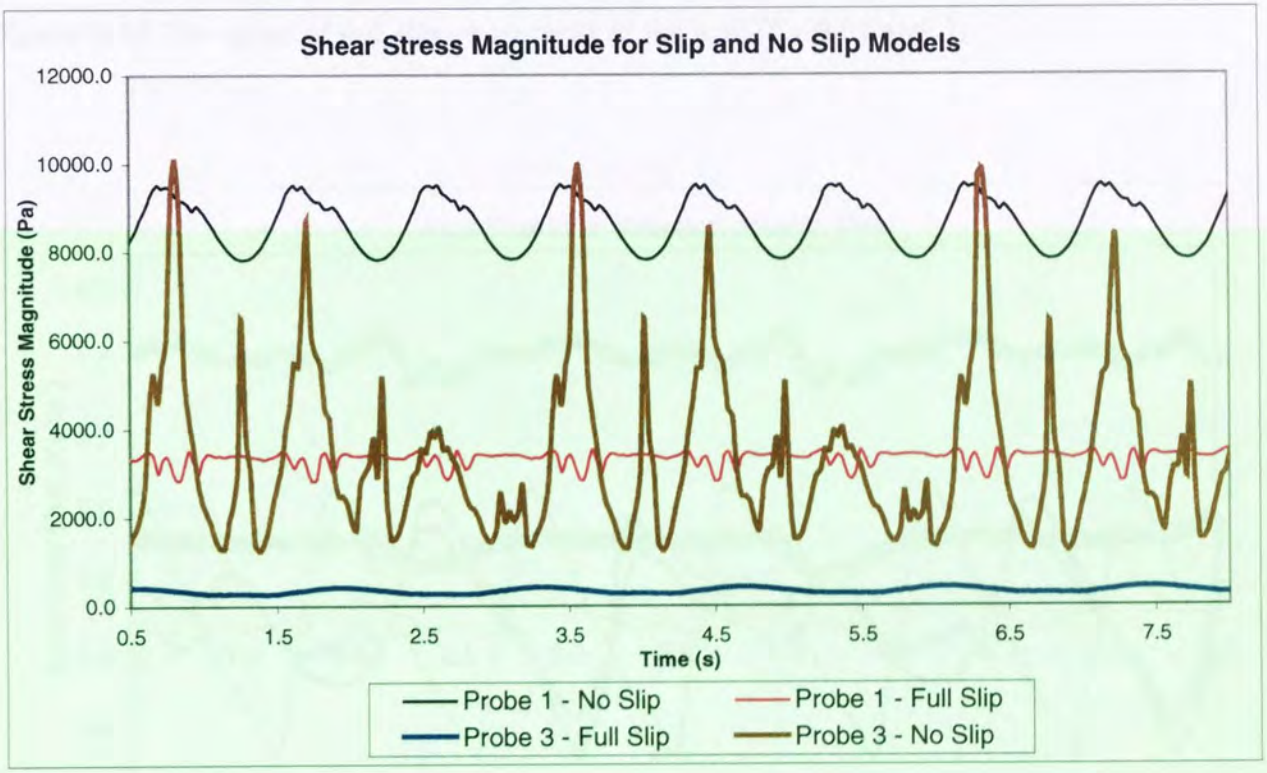

Figure 8-15 *Shear stress Magnitude against time plot for no slip and full slip simulations (K=3000 n=0.3)*

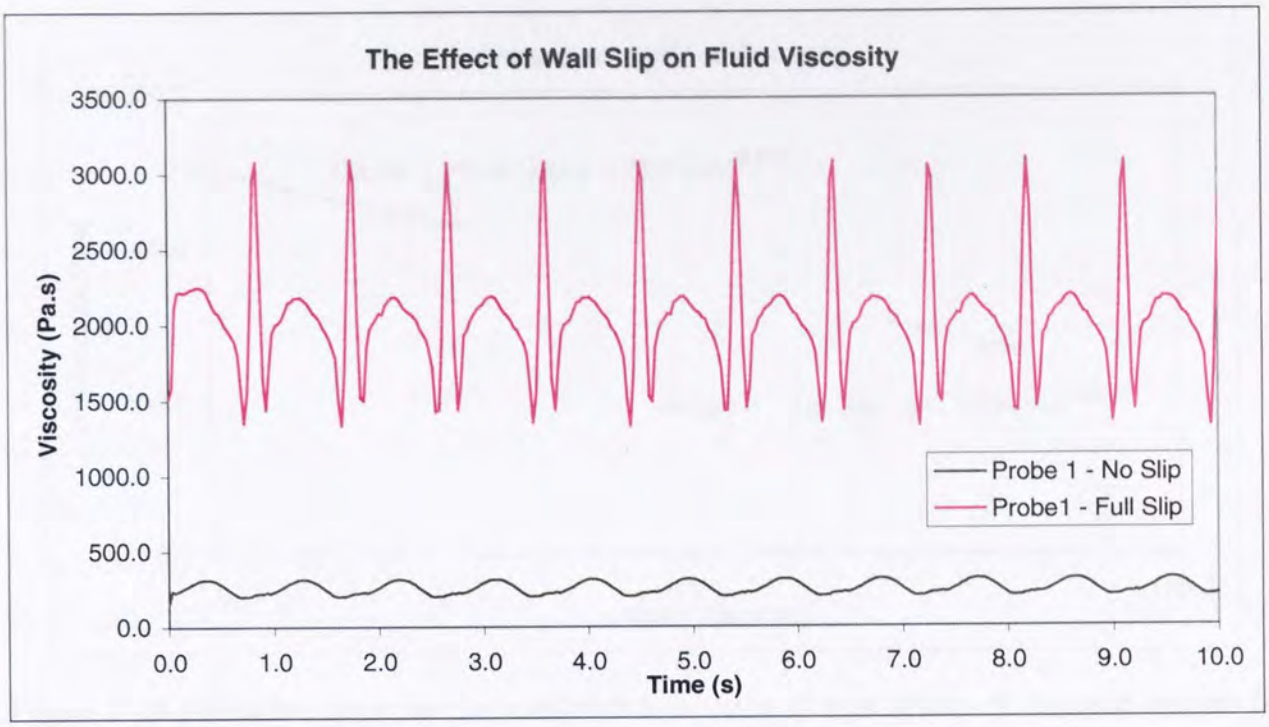

Figure 8-16 *The effect of full slip on viscosity at the wall (K=3000 n=0.3)*

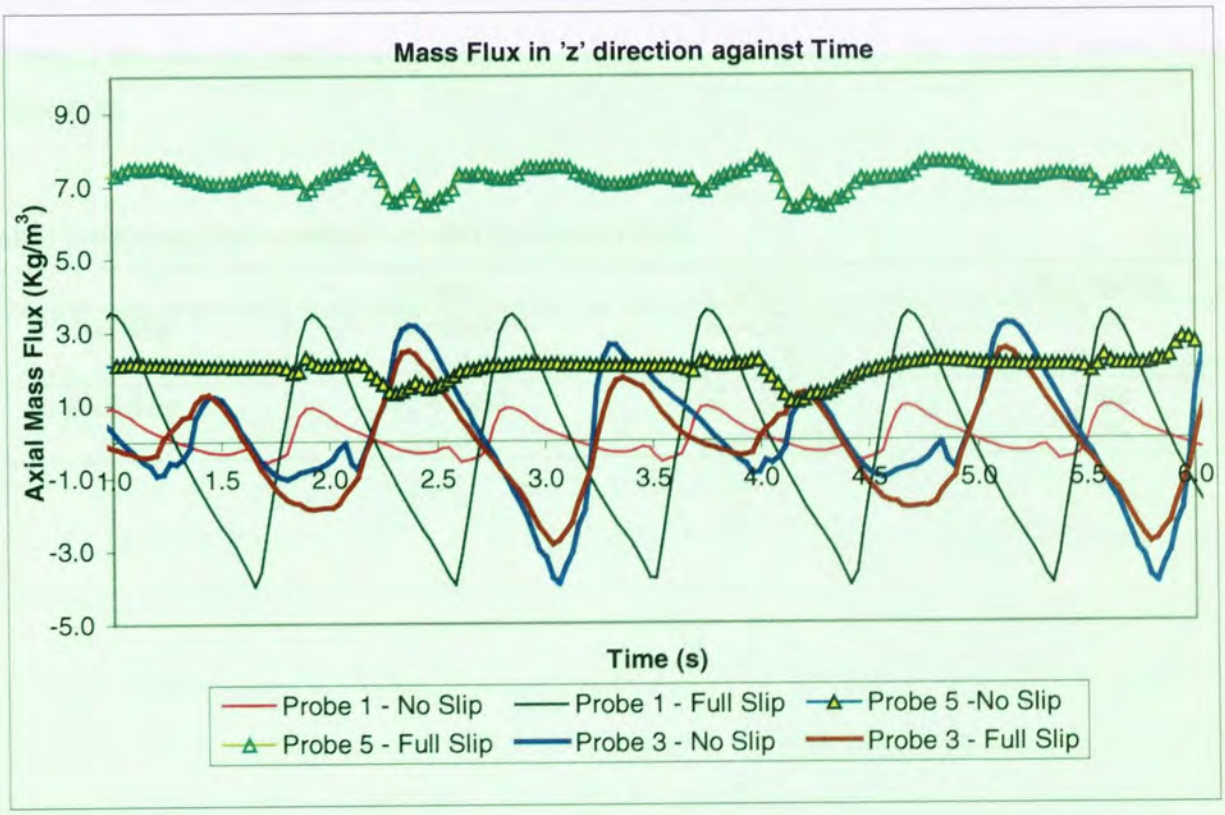

Figure 8-17 *Mass flux in an axial direction against time plot for no slip and full slip simulations (K=3000 n=0.3)*

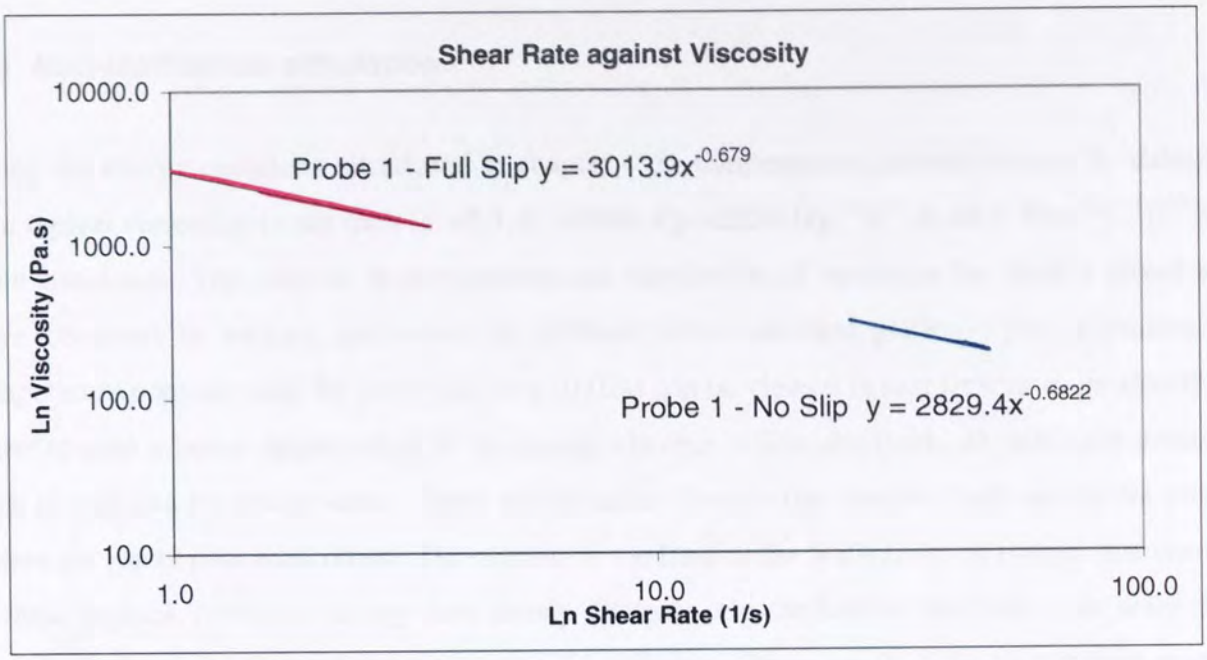

Figure 8-18 ***Validation of power law constants in an area of high shear - ln viscosity against ln shear rate for no slip and full slip simulations***

Using probes to investigate shear rates allows the accuracy of the model to be examined. When plotting the shear rate and viscosity data produced at various time steps for a region of high shear (Probe 1) the line of best fit (see Figure 8-18) can be compared to the original model inputs (Table 8-6).

Table 8-6 ***Power law constant - model accuracy check***

	Input	Output	% Change
No Slip	K =3000	K =3013.9	0.46
	n = 0.3	n = 0.3210	7.00
Full Slip	K =3000	K =2829.4	5.68
	n = 0.3	n = 0.3188	6.26

8.5 Non-isothermal simulation

Using the energy equations introduced in chapter 4 the temperatures increase caused by shearing of a typical viscous polymer melt (n =0.3, K =3000, Cp =2500 $Jkg^{-1}°C^{-1}$, k =0.5 $Wm^{-1}°C^{-1}$)[132] has been simulated. The increase in temperature and distribution of energy as the fluid is mixed has been observed in various animations of different cross-sectional planes. The animation of temperature contour plots for each time step (0.02s) can be viewed in real time or more slowly in order to gain a better appreciation of the energy changes within the fluid. In particular areas of high energy can be clearly seen. These are the areas close to the chamber wall and in the centre where the rotors pass each other. The motion of the fluid at the walls tends to restrict this energy to these regions, however, energy does slowly dissipate into the bulk of the fluid. The areas that experience the least temperature rise are also identifiable. These are the volumes of fluid nearest the rotor centre or axial region. For qualitative purposes the temperature was monitored at four distinct regions (Probes 1-4 in Figure 8-13). The temperature at these locations was plotted against time and is presented in Figure 8-19. Probe 1, positioned close to the left chamber wall, experienced a temperature increase each time the rotor tip passed. The heat is then transported away by the motion of the fluid, however, the overall effect is a steady temperature increase. Probe 2, positioned close to the left chamber wall, exhibits peaks and troughs similar to that of Probe 1 but of a lower frequency corresponding to the lower speed of the right hand rotor. Probe 3, located at the centre of the domain, reveals a more complicated pattern induced by the interaction of the rotors. The symmetry within the motion of the rotors can be seen every 2.8 seconds. The whole cycle, three turns of the left rotor and two of the right rotor, takes 5.6 seconds but, since each rotor has two identical tips, patterns are repeated twice. Probe 4, located at the front face of the left rotor and coinciding with the rotor's point of axis, experience the highest energy build up. This is due to the fact that the rotor is continuously in contact with the blade at this point and the fluid is relatively stagnant; this region would be the most prone to developing a 'hot spot' and may cause product degradation.

The initial stabilisation period (approximately 2.8 seconds) of the oscillations seen in Figure 8-19 is a result of the solution advancing to the point where quasi steady-state is achieved. The number of iterations was set at a low value (100) as the simulation was programmed to run for a relatively long period of time (700 time steps). Although the temperature increases may appear to be small it is worthwhile noting that several factors can make the impact of viscous heating much greater. For example, other polymers or rubbers (especially at low temperatures and during

the initial mixing period) may have a far greater viscosity than the materials modeled by the author. Also other rotor designs may cause greater magnitudes of stress and in large-scale equipment a similar angular velocity will produce much greater tip speeds resulting in greater shearing.

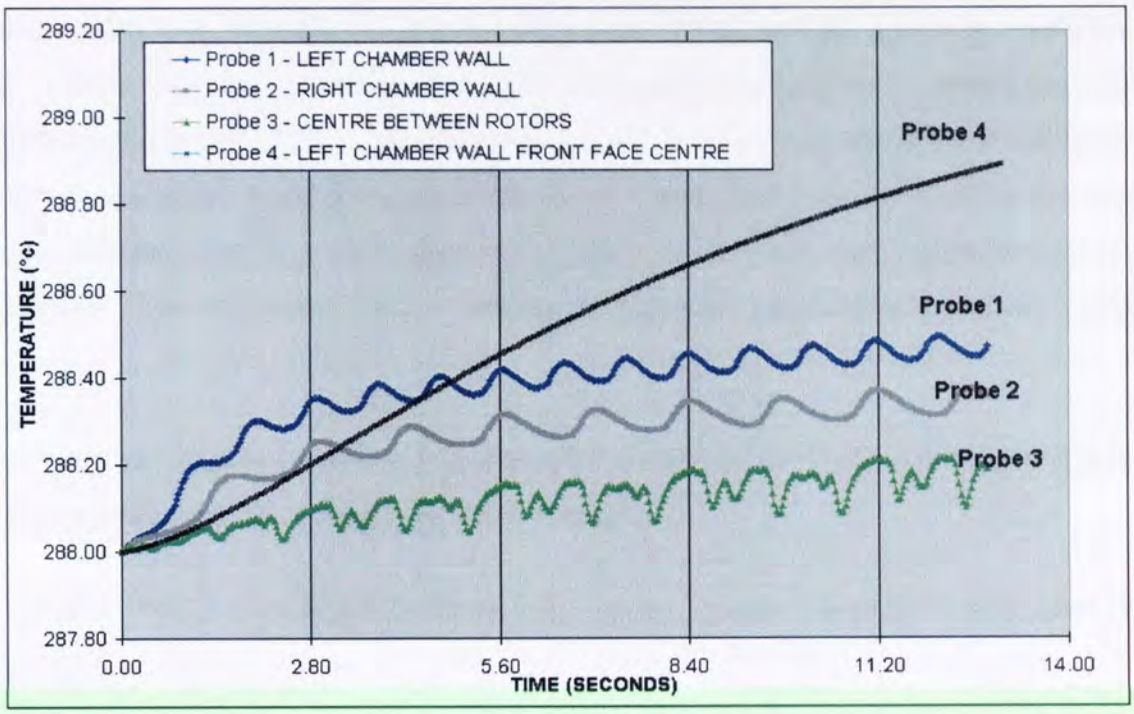

Figure 8-19 ***Predicted temperature change for points representing key positions within the domain at low speed.***

Temperature and Density

The Boussinesq approximation (equation 8-6) is used to describe the relationship between temperature and density. The coefficient of thermal expansion β_e is typical 20 x 10^{-5}°C^{-1} for polymer melts[133]. Therefore a ten degree rise in temperature will produce a decrease of 2 kgm^{-3} (or 0.2%).

$$\rho = \rho_0\{1-\beta_e(T-T_0)\} \tag{8-6}$$

Since I have confirmed that the inertia term is not significant for fluids with a high viscosity any small changes in density will have a negligible effect on the flow field. The forces arising from density gradients, given by equation 8-7, will have little effect since the fluid motion is dominated by the forced convection motion induced by the action of the rotors.

$$\boldsymbol{B} = (\rho-\rho_0)\boldsymbol{g} \tag{8-7}$$

Where $\boldsymbol{B}$ is the buoyancy force and ρ_0 is a mean density.

Temperature and Viscosity

As mentioned previously the viscosity is highly dependent on temperature and the relationship can be represented by the Arrhenius law (equation 8-2). If the temperature of a fluid being processed was to increase uniformly then the viscosity change would be uniform. Therefore viscosity gradients would only be caused by the shear field and the mixing performance would remain the same. A significant factor to consider arises if high thermal gradients exist since their impact on the viscosity may be huge. This will undoubtedly alter the flow patterns and hence the performance of the mixer. The large temperature gradients produced by both the viscous heating and from heat transfer fluids at the wall may cause a very low viscosity close to the chamber. Therefore, this fluid will flow easily and act as a lubricant, in effect, causing the bulk of the fluid to slip freely. This will tend to reduce mixture homogeneity, increase process time and energy costs.

Another point to consider is that a temperature change, which effects the viscosity, will affect the shear stresses and the dispersive mixing performance.

Heat transfer from the boundaries and/or from energy changes associated with chemical or physical change of the fluid is an area which could be targeted for future investigation.

8.6 Rotor Design

8.6.1 Rotor Curvature and Axial Flow

In Chapter 7 the effect on the system of varying equipment design was considered and, as previously noted, the inherent mesh restrictions made it difficult to adjust the blade design. The unmatched mesh approach, however, makes rotor design alteration relatively easy. The axial mixing in the Hampden RAPRA Torque Rheometer has been shown to be poor so in an effort to perhaps improve on this the left rotor design has been be altered as shown in Figure 8-20. The curvature of the blade has been approximately doubled. The effect of this modification on axial flow is shown in Figure 8-21 where an isothermal simulation of a Newtonian fluid has been performed when *both* rotors are rotating at 3.414rad s^{-1}. One can conclude from this a qualitative analysis that the increased rotor curvature prompts greater mass flux in the main void regions either side of the blade. The slice depicted in Figure 8-21 is taken at z = 8mm where the increase in mass flux is most noticeable; as the front face is approached, i.e. z ≈ 25mm, the improvement is less pronounced. In an attempt to pursue a quantitative pathway to determine the improvement in axial activity a 'USER FORTRAN' programme has been created. This programme calculates the total of the axial velocity magnitude from the centres of each cell within the 'rotating' blocks unstructured patch around each rotor. Since both rotors have been created with the same number of cells this approach is valid for comparative purposes. The programme can be found in Appendix 9. Figure 8-22 plots the results from the simulation of a Newtonian fluid and a generalized Newtonian fluid which represents the shear dependency of a typical polymer i.e. n=0.3. The difference in axial flow induced by both the original rotor design and the new and possibly improved design can be observed for the whole rotor cycle. The original rotor cycle lasts approximately 2.8s, however, since the rotors turn at the same speed for these simulations, the complete cycle takes approximately 0.9 seconds to complete. The simulations were repeated but this time polymer wall slip was included. Figure 8-23 depicts the results from the simulations. The average increase in axial flow over the rotor cycle is given in Table 8-7. From these results it can be deduced that the improvement in axial flow due to doubling the rotor curvature is significant for Newtonian fluids (8.1%). This improvement in performance decreases to 5.1% when a typical polymeric fluid is simulated, however, a performance increase of 21.4% is predicted for Newtonian fluids with slip at the wall. Figure 8-23 also shows how the distributive mixing performance may *decrease* when slip is introduced at the wall not *increase* as suggested by the probe data presented in Figure 8-16.

Note: A time step of 0.02s was used for all simulations.

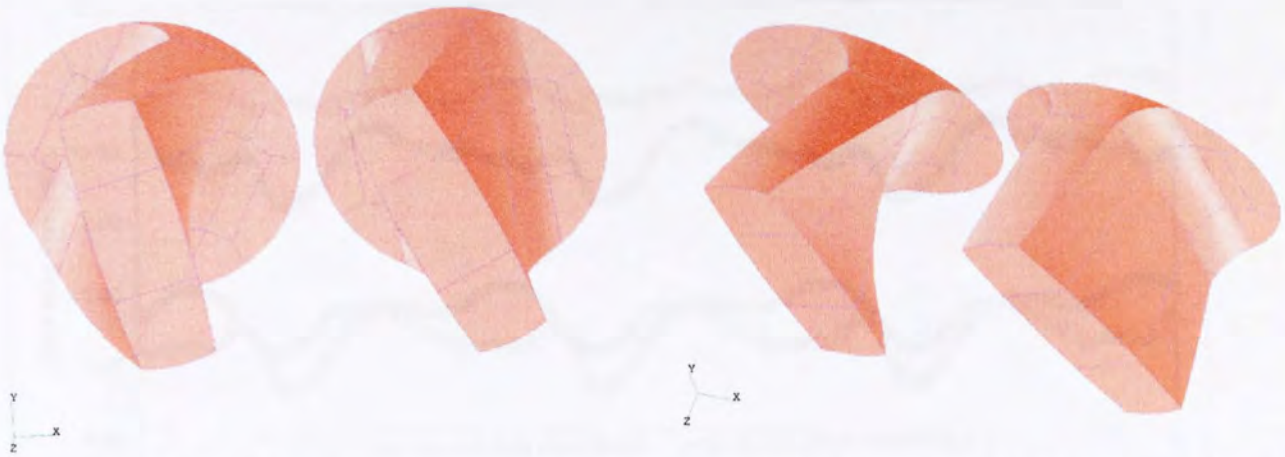

Figure 8-20a and b) ***Rotors taken from the 'sliding grid' simulation showing the original rotor design (right hand rotor) and the new rotor with increased curvature (left hand rotor) – view 1 and view2***

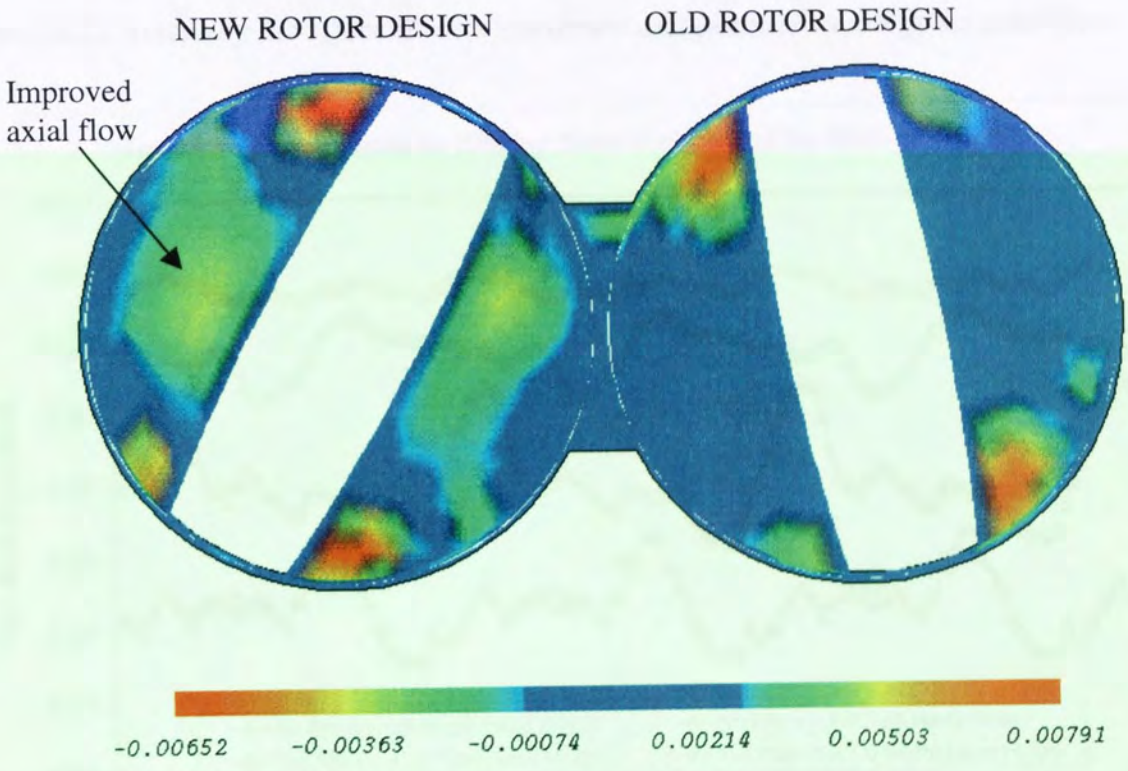

Figure 8-21 ***Axial flow contours on a slice through the computed flow field at z = 8 mm***

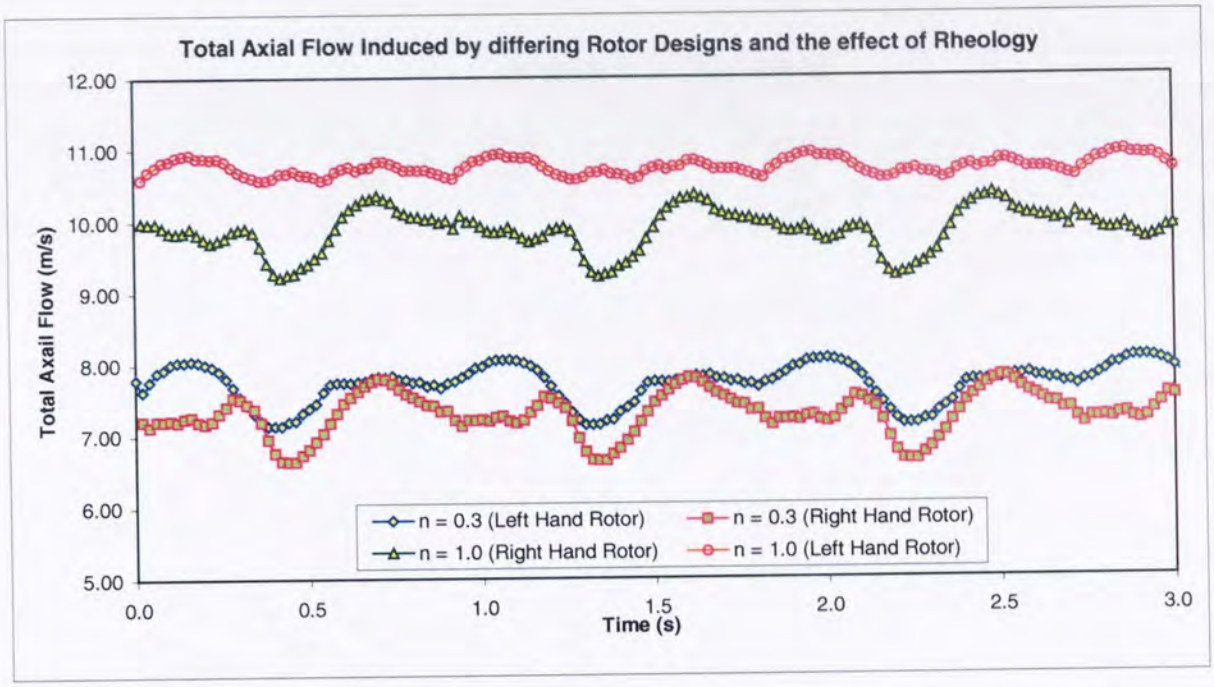

Figure 8-22 *Assessing the effect of rotor curvature and polymer rheology on axial flow*

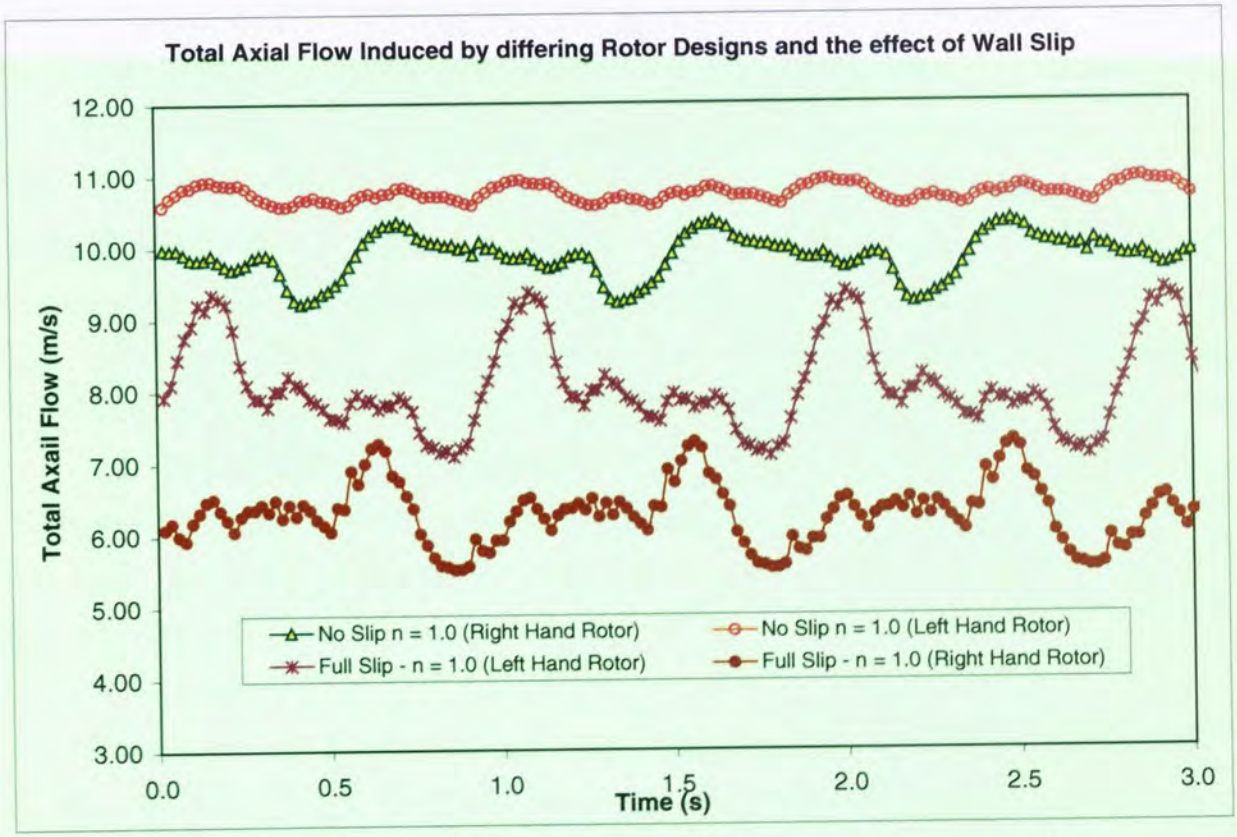

Figure 8-23 *Assessing the effect of rotor curvature and polymer slip on axial flow*

Table 8-7 *The difference (improvement) in axial flow between two rotor designs and the effect of polymer rheology and polymer slip.*

Average Axial Flow (mm/s)								
n = 1.0 with no slip			n = 0.3 with no slip			n = 1.0 with slip		
left rotor	right rotor	Difference	left rotor	right rotor	difference	left rotor	right rotor	difference
10.728	9.855	**0.873**	7.684	7.292	**0.391**	7.971	6.274	**1.707**
		(8.1%)			(5.1%)			(21.4%)

8.6.2 Rotor Clearance Optimisation and Automatic Geometry Parameterisation (AGP)

Rotor curvature is only one of several parameters that require careful consideration when the issue of equipment design is raised. In section 7.4 the subject of rotor clearance was introduced. The investigations were limited by two factors:

1. The inflexibility of the Polyflow code.

   The rigidity of this code prevents the addition of new programmes and therefore the flow of the material over the rotors experiencing the high shear could not be accurately calculated. As an alternative the volume of the fluid between the rotor tip and the outer chamber was inspected as a possible means to determine an optimum rotor clearance.

2. The difficult nature of mesh generation.

   Only four geometries with varying rotor clearances were created due to the difficult and time-consuming nature if the mesh generation process for complex three-dimensional domains of this type.

Having created a new simulation using the unmatched and sliding grid techniques, and using the USER FORTRAN capability of CFX4.2, the first of these limitations was overcome. Appendix 10 contains the programme written to calculate a parameter to assess the relative dispersive mixing effectivity of a rotor design. This parameter is the product of the total mass flow over the rotor tip at any point in time and the average shear stress magnitude experienced by that body of fluid. One obstacle still remained. In fact, one of the major limitations encountered by researchers studying internal mixers is the lengthy process of mesh generation. This is especially true for precise three-dimensional geometries which present the seemlingly insurmountable task of generating large numbers of computational grids for the many configurations one may wish to simulate. Sliding grids can be of enormous benefit in terms of automatic gridding, however, there still remains the task of optimising geometries. After all, to get the most out of a simulation one would hope to be able to examine key variables such as rotor clearance, rotor thickness, rotor separation etc.

So clearly there is still room for improvement in the current simulation methodology. Overcoming the limitation of the high man-hour input required for optimisation was seen by the author as a subject which was worthy of devoting much research time to, since, overcoming this obstacle could really extend the potential of the simulation. To this end a new technique was assessed.

AGP - Automatic Geometry Parameterisation

The CFX pre-processor, CFX4-Build, is based around the PATRAN command language (PCL). Each command made whilst constructing a geometry, including such things as changing the viewing perspective, is written to a file in chronological order. This text file is called a journal file. These files are used to recreate geometry or mesh on different platforms to overcome the problem of portability of binary database files (CFX4-Build files). The idea that these files can be played back by the software presents an interesting opportunity. The journal file can be manipulated by a user – for example a modified journal file can be used to rebuild a geometry prior to mesh generation by simply deleting the final commands which call for the mesh to be created. With forward planning this quality of the journal file can be used to great effect with respect to the optimisation of an internal mixer geometry.

AGP Procedure

It was conceived that the internal mixer geometry could be rebuilt simultaneously producing a journal file that would allow automatic parameterisation of the internal mixer geometry with respect to any desired variable. The variables I chose for the purposes of demonstrating this technique for geometry optimisation are:

1. The clearance variable 'clearance'
2. The thickness of the rotor 'landwidth'
3. The separation of the two rotor axes 'rotor separation'

To understand how this technique works it is easiest to consider what happens for the simplest parameter, which in this case is the 'rotor separation' variable. This real variable, defined at the start of the construction of the geometry, is used in place of an 'x' co-ordinate that is used to define the centre of the right hand rotor. After the left hand rotor has been constructed the pre-processor is instructed to create the right hand rotor by copying the existing rotor and translating these entities by the value of the x co-ordinate defined by the variable 'rotor separation' (see Figure 8-24). After the right hand rotor has been created then the central or bridge region is created connecting the two separate halves of the geometry. Therefore, a working mesh can be built for any value of the 'rotor separation' variable as long as the two rotors do not intersect each other.

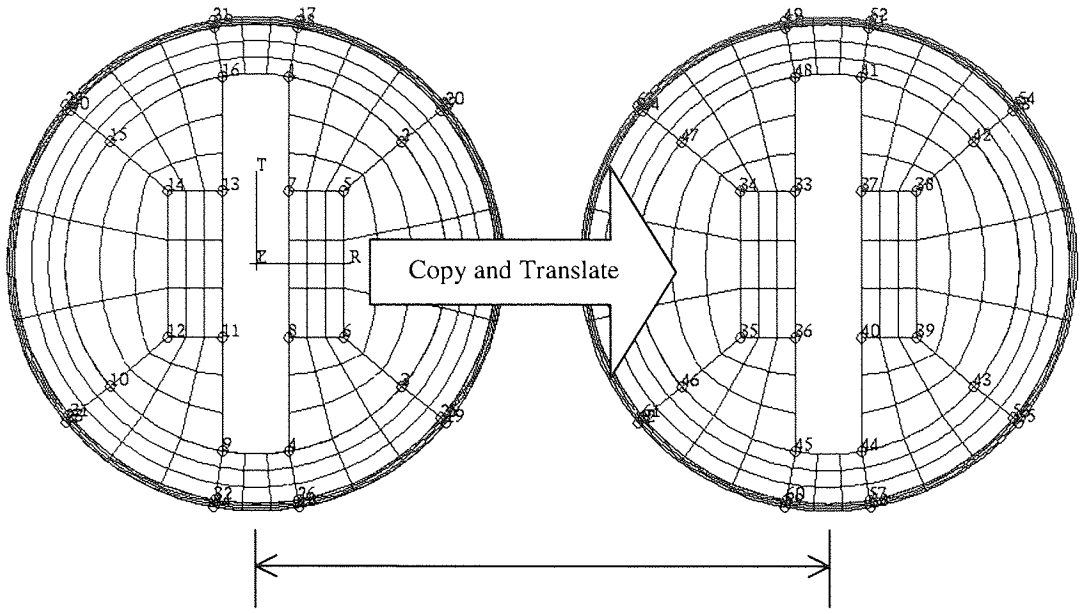

Figure 8-24 ***The AGP variable 'rotor separation'***

Note, the hatching on the cross-section taken from the geometry is for display purposes only and does not represent the computational mesh.

Unfortunately, it is impractical to optimise an existing complex geometry that has not been created from the beginning with the intention of optimising using PCL. The journal file for new the AGP internal mixer geometry created for the work presented in this section is given in Appendix 11.

The time required to produce a new working sliding grid internal mixer geometry using the AGP technique, once the 'original' geometry has been created, is dependent on manual input and the CPU time to rebuild the geometry. The former takes less than one minute, as it involves merely using a text editor to change the value of a variable, and the latter takes less than five minutes on a DEC 500au workstation. Figure 8-25 and 8-26 illustrate how a variety of different geometries can be defined using the 'rotor separation', 'landwidth' and 'clearance' variables. The variables do have their limits, for example the rotors should not be defined so that they extend past the sliding grid boundary. For sensible values the cell form is very good but if the form is set more toward the extremes the computational cell can have very high aspect ratios and become more deformed.

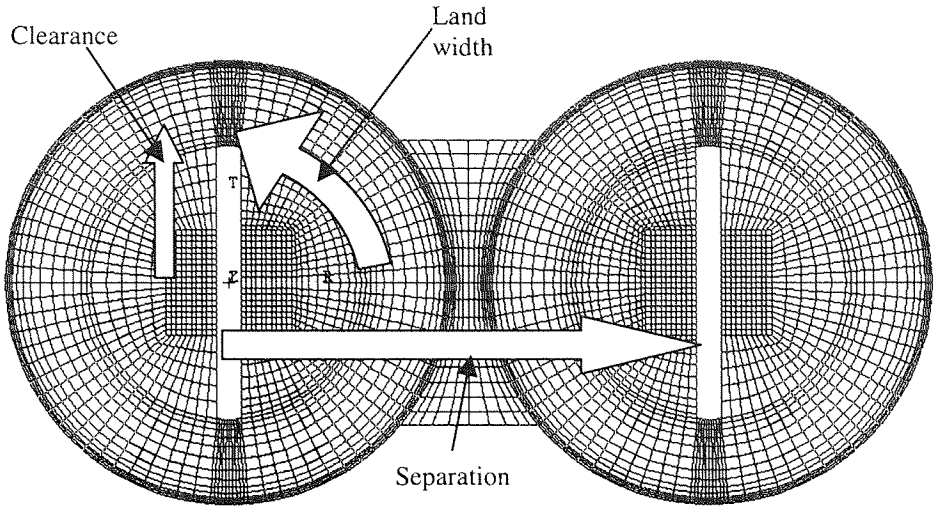

Figure 8-25 ***A small bladed internal mixer AGP computational mesh****

* Clearance = 0.8
Landwidth = 85 degrees
Separation = 2.8

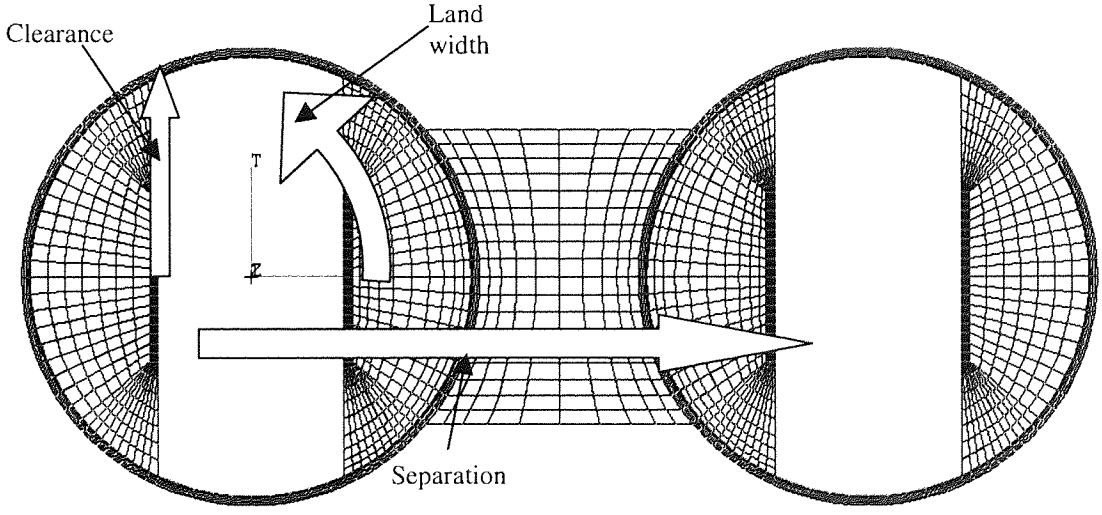

Figure 8-26 ***A large bladed internal mixer AGP computational mesh with a large rotor separation****

* Clearance = 1.25
Landwidth = 65 degrees
Separation = 3.5

Optimisation results using AGP geometries

As a final step in the mesh creation process a user is given the opportunity to scale the geometry. In order to make the mesh generating process easier the geometry was constructed in metres and three other AGP variables were defined in the new internal mixer journal file. These were the scaling factors in the three co-ordinate direction. An arbitrary value of 0.05 was used for these simulations (except for the investigation into the effect of geometry scale on optimum rotor clearance). This resulted in a rotor chamber with a radius of 6.5cm. Also, a rotor speed of 3.414 $rads^{-1}$ was selected for both rotors to simplify the vector field and therefore facilitating trend identification. The investigations into rotor clearance using seven different geometries created using the AGP technique were fourfold:

1. Optimum rotor clearance and power law exponents

   The optimum rotor clearance was examined for varying power law exponents of typical viscous fluids. For low shear-dependent fluids an optimisation peak on the stress/flow rate graph (Figure 8-27) was discovered at regions relatively close to the chamber wall. When the high shear-dependent fluids were examined the characteristics of the peak was seen to vary. Instead of a sharp peak a gentler curve is produced peaking further away from the chamber wall.

2. Optimum rotor clearance and power law factors

   The optimum rotor clearance was examined for varying power law factors of typical viscous fluids. For high 'viscosity' fluids an optimisation peak on the stress/flow rate graph (Figure 8-28) was discovered at regions relatively far from the chamber wall compared to the lower 'viscosity' fluids which produced a peak closer to the chamber wall. As the 'viscosity' increases it appears that the initial portion of the curve follows a linear law (Note that line representing the trend produced by a fluid corresponding to K=1000 in Figure 8-28 is the same as the line representing the trend produced by a fluid corresponding to n=0.5 in Figure 8-27).

3. Optimum rotor clearance and wall-slip

   Optimum rotor clearance was examined for varying wall slip coefficients as used in section 8.4. As the shear dependency of slip increases the optimisation peak on the stress/flow rate graph (Figure 8-29) retains its form but appears lower down on the scale as the average shear magnitude decreases more than the gain in mass flow rate. As the magnitude of the slip tends toward full slip the curve does eventually vary its form to a small degree.

   Appendix 13 holds the appropriate data tables where one can see how the mass flow rates and average stresses vary individually.

Figures 8-30, 8-31 provide a vector plot comparison for identical simulations with the exception of rotor clearance. Figures 8-30, 8-32 provide a vector plot comparison for identical simulations with the exception of power law factor. Figures 8-30, 8-33 provide a vector plot comparison for identical simulations with the exception of wall slip.

4. Optimum rotor clearance and geometry scale.

   Optimum rotor clearance was examined for varying wall geometry scales. For this investigation 42 different AGP geometries were used. As the geometry scale decreases the ratio of optimum rotor clearance to rotor chamber radius increases (see Figure 8-34). The trends of the curves are similar to that found in investigation 2 where it appears that a change of the variable in question changes the linearity of the plots.

   Figure 8-35 illustrates a vector plot for a small-scale geometry.

Discussion

Using this technique it is clear how the optimum value of rotor clearance for dispersive mixing can be obtained and also how trends due to various factors influence the position of this value. The general explanation for the 'peak' phenomenon found in the investigations can be attributed to the fact that a low viscosity (relative to the bulk viscosity) at the rotor tips results in a fluid that is prepared to flow over the rotors more readily outweighing the increases in stress up to a point. This point is called the optimum condition beyond which the gain in fluid flow, when increasing the rotor clearance, is no longer out weighing the loss in stress.

An explanation for the high linearity of some of the data plots may arise by appreciating a topic briefly touched upon in section 7.2.1. In this section it was found that at a certain point, corresponding to an increased Reynolds number brought about by simulating the flow of a fluid with a low viscosity, the inertial forces start to have an effect on the flow field. This phenomenon was not observed again until now because the geometry scales/velocities simulated were not large enough to generate significant inertial flow contributions. In the case of the AGP simulations, however, the scale has been large enough for inertial terms to become consequential. If we consider again the Reynolds number, defined by equation 4.23, but this time using the rotor clearance as the characteristic length and the maximum fluid velocity for the velocity term, an explanation arises.

- As clearance/characteristic length decreases the Reynolds number decreases. This is partly compensated by a corresponding decrease in 'viscosity' and a small increase in velocity. Although the Reynolds number decreases as we move from the largest clearance modelled

here to the smallest it remains in the same order of magnitude. This change in Reynolds number is shown diagrammatically on Figure 8-27.

- As the power law exponent 'n' decreases then 'viscosity' will decrease. This will result in a decrease in viscous forces and therefore an increase in the Reynolds number. This change in Reynolds number is also shown diagrammatically on Figure 8-27.
- As the power law factor 'K' increases then the 'viscosity' also increases resulting in a decrease in the Reynolds number. This change in Reynolds number is depicted on Figure 8-28.
- As the scale decreases the Reynolds number decreases. The trend of Reynolds number variation is given in Figure 8-34

The onset of the non-negligible inertia forces impacting on the flow field manifests itself in two ways. The first is due to the migration from a linear clearance/stress-term relationship to a non-linear relationship and the second is the character of the velocity vector plot. In this section the velocity vector plots reveal 'back-flow' over the rotor tip as opposed to the more regular planar couette flow type found in previous simulations. This *is* a result of the increased Reynolds numbers of the larger-scale simulation and not just a result of having a larger rotor clearance (although the Reynolds number does increase with a larger clearance). This statement is affirmed by Figure 8-35 which shows that there is no 'back-flow' over the rotor tips even though the rotor clearance is large. This is because the small scale suppresses the Reynolds number.

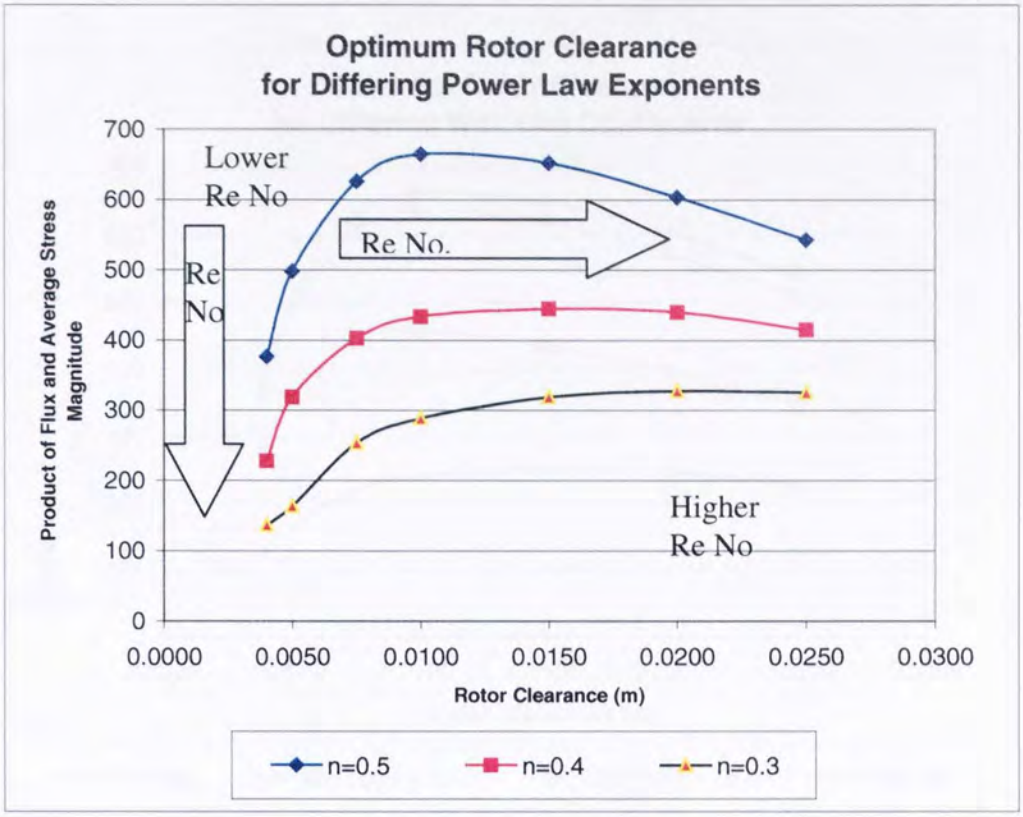

Figure 8-27 *Rotor Clearance optimisation for a variety of power law exponents*

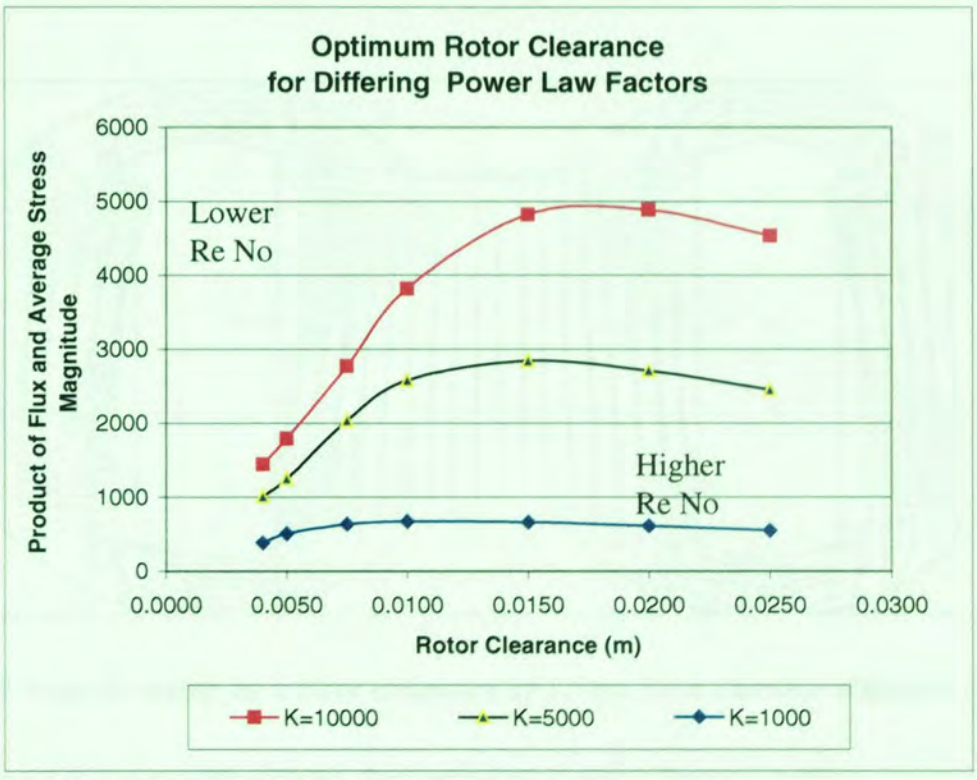

Figure 8-28 *Rotor Clearance optimisation for a variety of power law factors*

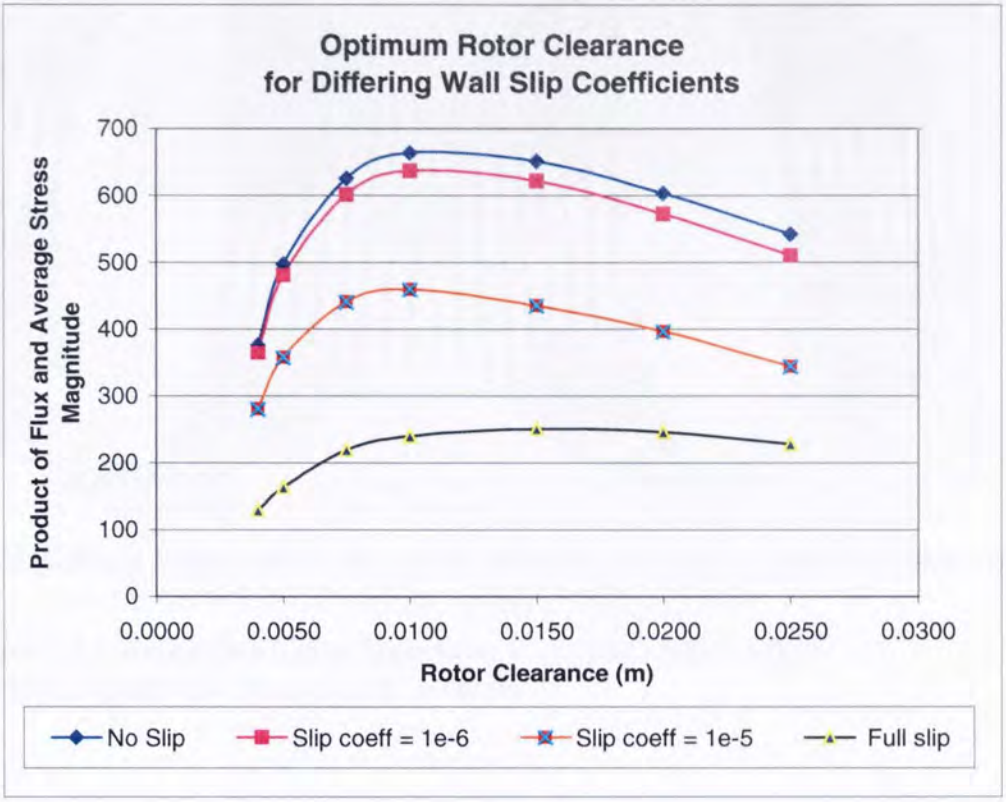

Figure 8-29 ***Rotor Clearance optimisation for a variety of wall-slip conditions***

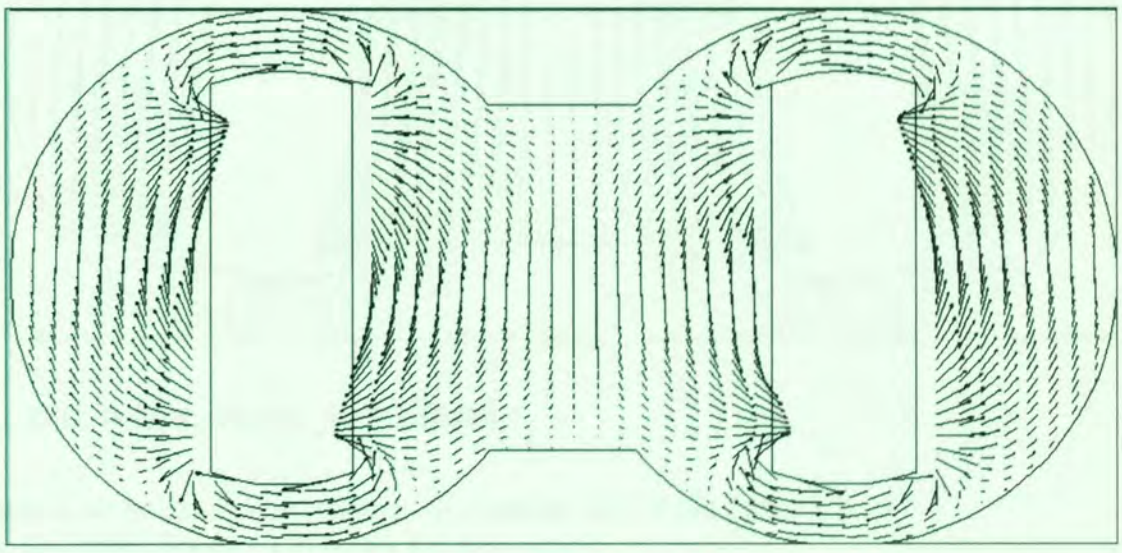

Figure 8-30 ***Velocity vector for a rotor clearance of 1.5 cm for a chamber diameter of 13 cm****

* Clearance =1.0, Landwidth =70deg, Separation =2.7, Scale factor = 0.05
n=0.5, K=1000, Speed =3.414rad/s for both rotors

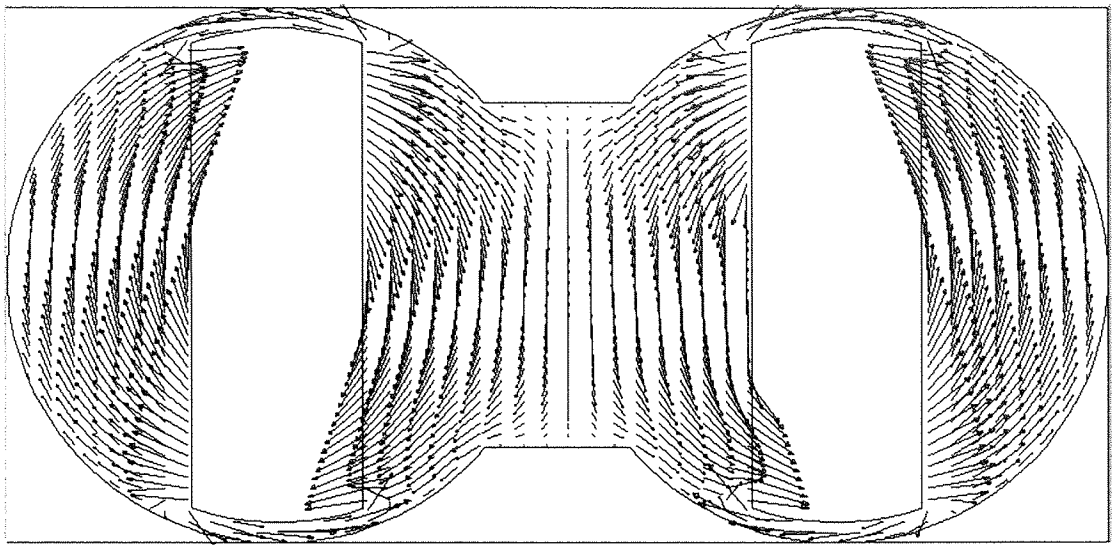

Figure 8-31 ***Velocity Vectors for a rotor clearance of 0.5cm for a chamber diameter of 13cm****

*Clearance =1.2, Landwidth =70deg, Separation =2.7, Scale factor = 0.05
n=0.5, K=1000, Speed =3.414rad/s for both rotors

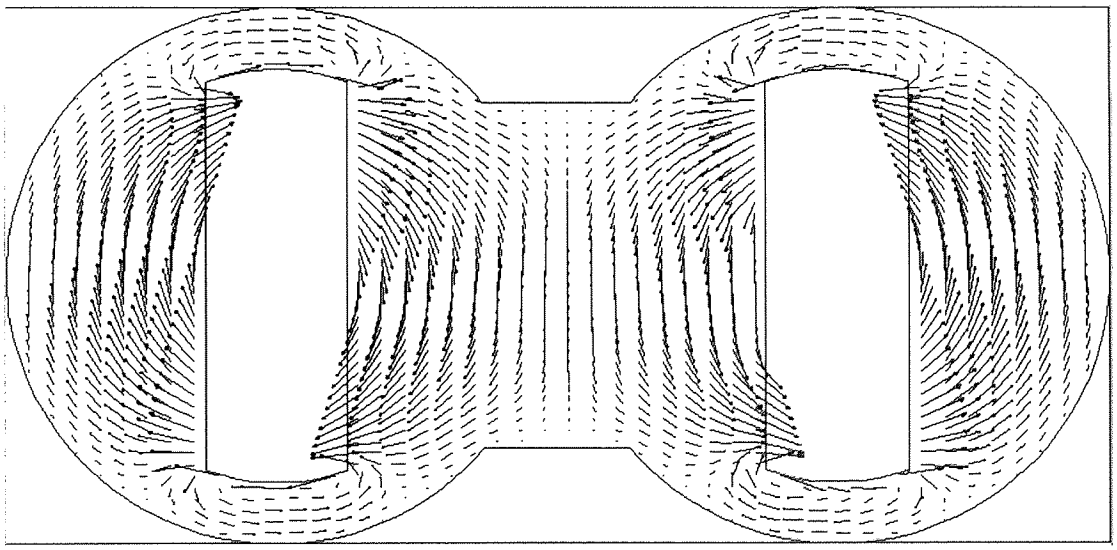

Figure 8-32 ***Velocity Vectors for K =10000 ****

*Clearance =1.0, Landwidth =70deg, Separation =2.7, Scale factor = 0.05
n=0.5, K=10000, Speed =3.414rad/s for both rotors

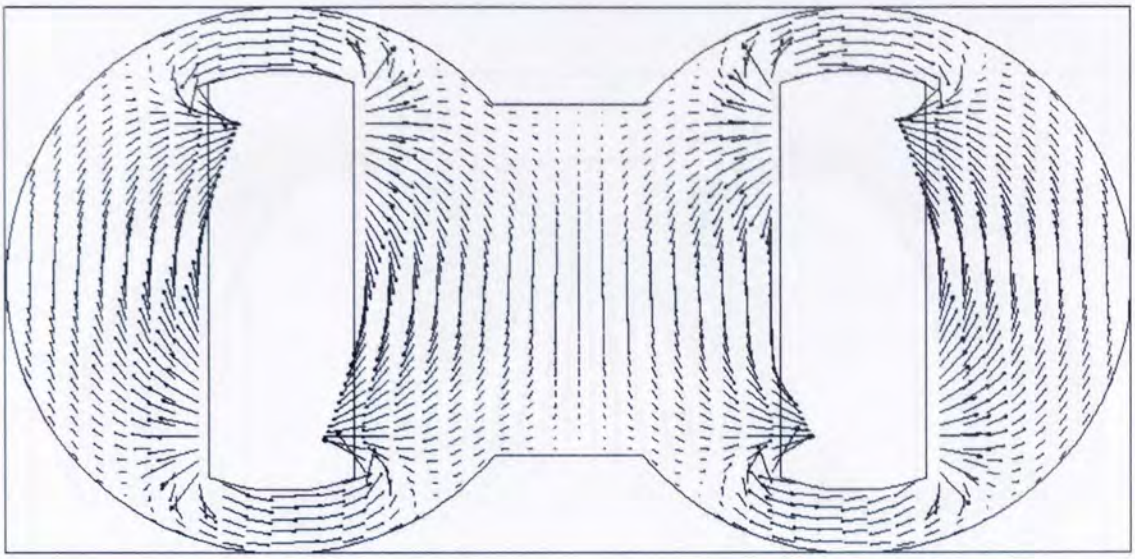

Figure 8-33 ***Velocity Vectors for a geometry with a full wall slip****

*Slip Coeff 5 e-5
Clearance =1.0, Landwidth =70deg, Separation =2.7, Scale factor = 0.05
n=0.5, K=1000, Speed =3.414rad/s for both rotors

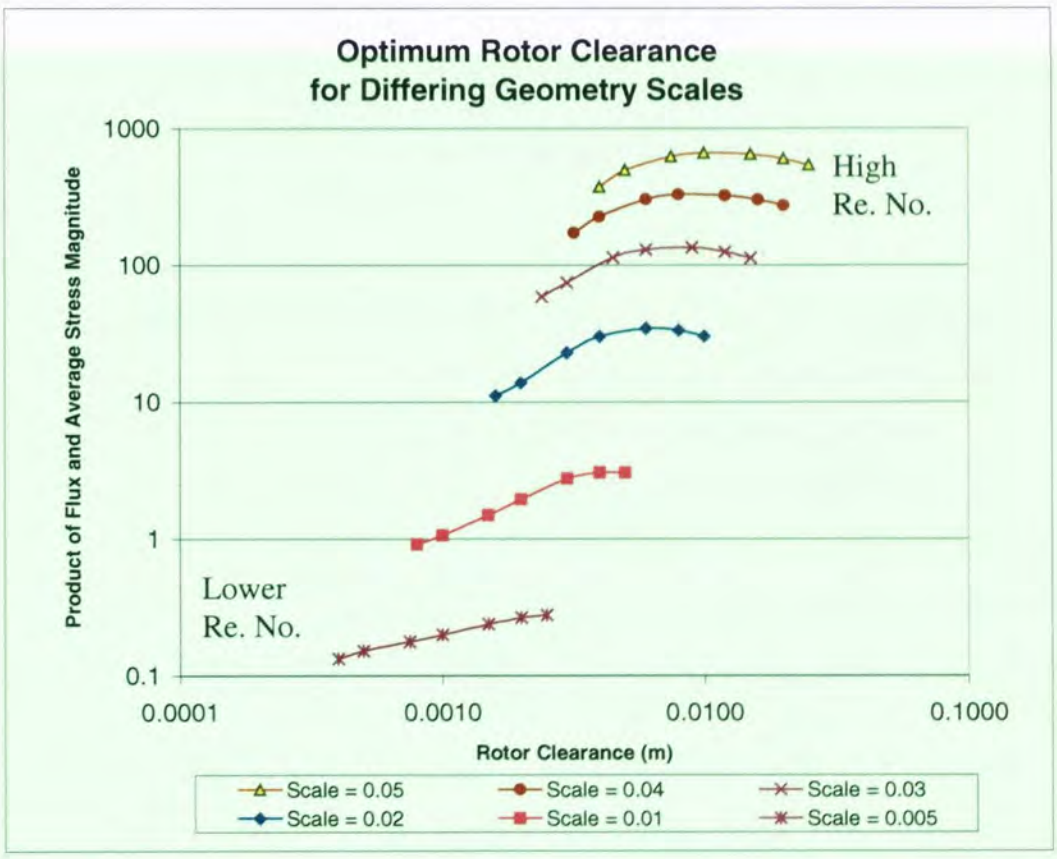

Figure 8-34 Rotor Clearance optimisation for a variety of geometry scales

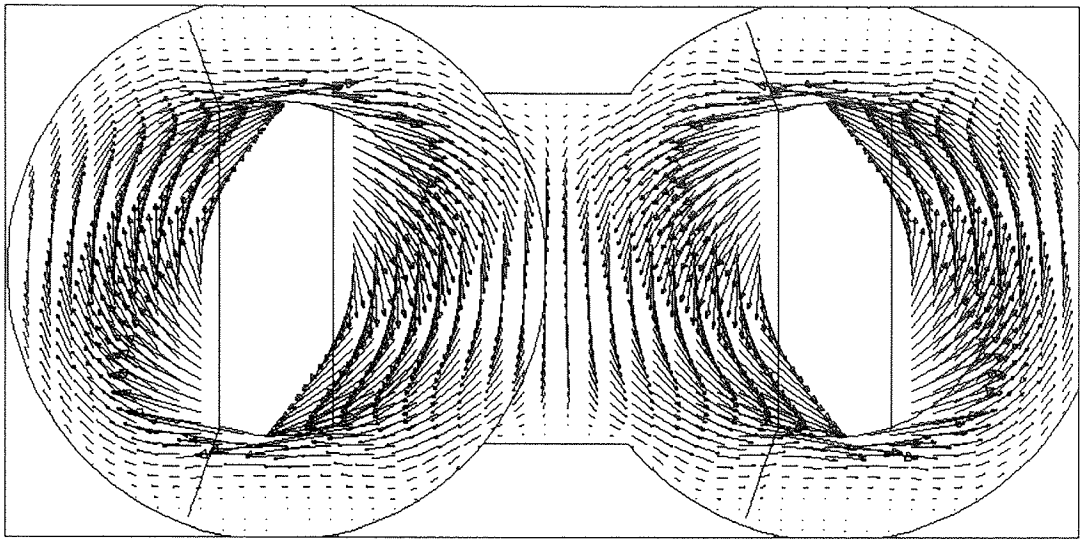

Figure 8-35 ***Velocity Vectors for a rotor clearance of 0.5cm for a chamber diameter of 1.3cm (scaling factor of 0.005)****

* Clearance =1.0, Landwidth =70deg, Separation =2.7, Scale factor = 0.005
n=0.5, K=1000, Speed =3.414rad/s for both rotors

9. Discussion

We have seen that the work presented in this thesis has, when appropriate, already been discussed to some extent. This section presents an initial brief summary of this research and leads into a compilation and expansion of the more important subjects raised, and a discussion of some new issues.

The aim of this research was to establish the potential of simulation to support efforts to benefit those processing industries associated with high viscosity materials in laminar flow. The primary goals of producing simulations of these processes are to improve homogenisation and therefore product performance and reliability, and to reduce operational costs and to improve time to market for novel processes or products. To determine the capabilities of a simulation the first step adopted in this research was to address each complexity involved with modelling the designated processing operation. An assessment of the numerical methods used to solve the mathematical representations of these complexities was attempted as was an assessment of the impact of any assumption made in order to obtain the possible virtual representation of the situation in question. Validation and verification, by comparison with experiment, as it should, then followed, not in any small part due to the fact that the creation of a highly complex simulation can be a minefield of potential errors each detrimental to model accuracy. To address these issues of mathematical limitations, modelling practicalities, result accuracy and of course model uses, as stated in the 'project statement' (see section 2.2), a suitable process was identified; this process being the mixing in a Hampden RAPRA Torque Rheometer laboratory internal mixer. This process offered the advantages of being a real mixing geometry yet remaining relatively simple in terms of rotor design. This particular process also permitted good flow visualisation normal to the plane of rotation. Verification was aided by the fact that this internal mixer measures rotor torque. Also beneficial to this investigation was the small scale or low volume of the mixer which consequently leads to near isothermal operation (see section 4.2.2) for the majority of the mixing cycle. Mathematical limitations, modelling practicalities, result accuracies and model uses identified from this process were believed to be transferable to various processes of a similar vein, for example, twin screw extruders which have previously been modelled by other researchers and then found to be difficult to validate due to inherent difficulties (see section 4.2.2).

One of the most common simplifications used for internal mixer simulation is to reduce the flow domain to two-dimensions and sometimes even to extend this simplification by only analysing a portion of a cross-section as reported on in section 4.2.2. This reduces the time and effort required to create a discretised geometry, reduces the complexity of the codes and minimises CPU time and other demands placed on hardware. This third dimension is, of course, of great importance if one requires accurate flow field patterns, shear stresses and elongational flow components as discussed in section 4.2.2 (p55) and to be able to carry out a full investigation of equipment performance. We have, for example, seen in chapter 8 that axial mixing is a subject worthy of investigation. The third dimension is not only important for internal mixers but also for other processing geometries. Due to the computational demands, an accurate three-dimensional model can limit the number of simulations and, therefore, the types of theoretical experiments which are practicable to perform. The author is still of the belief, however, that it is vital to pursue complex simulation now more than ever, since it is plainly evident that three-dimensional simulations are becoming more and more practical as researchers continue their work and both hardware and software capabilities continue to improve beyond expectation. In the author's opinion the inclusion of the third-dimension will be the future of all CFD internal mixer investigations, hence the decision to pursue this direction (and also in light of the discussion below).

From the author's own experience and from the internal mixer simulations reviewed in the literature survey, it is clear how important flow domain geometry set up can be; in particular boundary conditions and mesh form. Incorrect boundary assumptions can be avoided by careful consideration. As discussed in section 4.2.2, analysing only parts of the geometry, for example, has lead researchers to define fluid boundaries incorrectly, resulting in flow fields that will not accurately represent reality. This extends to fluid boundaries in continuous processes. Bruce *et al* addressed the three-dimensional mixing zones within a twin-screw extruder (TSE) relying on the assumptions that the fluid enters the domain normal to the radial plane and the outlet can be represented by a constant pressure. Both assumptions cause the flow field to deviate from real flow conditions. These limitations can be alleviated by including conveying sections before and after the mixing elements (although this increases the computational demands). Another problematic assumption commonly made in order to obtain a transient simulation is the assumption that the outer chamber wall boundary rotates around a stationary rotor (as discussed on page 54). Simulations that use inappropriate assumptions can still have their uses, for

example, to calculate shearing at the rotor tips where the rest of the flow field commonly. but not always as we have seen in section 8.6.2, has only a small effect on the result. High degrees of accuracy, however, are often required, for example, if particle-tracking simulations were to be used to assess distributive mixing. The wall boundary condition is an important issue that needs to be addressed with some caution, for example, slip at the wall can depend on the material of the wall and on the fluid character, as well as, pressure, temperature and the shear stress values at the wall. The incorporation of full slip conditions into the simulations presented in this thesis show to what extent the prediction of dispersive mixing maybe affected; for example, shear stresses at the rotor tip decrease by over 60% (as derived from the data shown in Figure 8-15). A designer wishing to improve the dispersive component of mixing could increase rotor land-width, decrease rotor clearance, use a lower temperature or challenge the slipping process by using different materials for the rotors and chamber walls. The full slip assumption also leads to decreasing distributive mixing. Evidence of this comes from Figure 8-13 where the axial flow activity decreases by approximately 40% in a simulation of a Newtonian fluid with full slip at the walls. Wall slip may, however, be an advantage. For example, in areas least influenced by the action of the rotors i.e. the upper and lower bridge position – see probe 5 in Figure 8-13 and 8-17. At this location the shear rate can be seen to increase by a factor of two and this desirable outcome could be engineered into the mixer design and therefore benefit equipment performance. A linear relationship was used to describe the relationship between wall slip velocity and the wall shear stress. A linear relationship was chosen as the coloured clay fluids, used in the flow visualisation and verification experiments, are likely to follow this regime since they are essentially a highly filled fluid and not a polymeric fluid which may follow a complex power law relationship with several characteristic slip regions (as discussed in section 8.4.1). The visualisation experiments were used to determine the Navier slip coefficient at the rotor wall for the low pressure clay/Perspex system ($2*10^{-6}$m.Pa^{-1}s^{-1} - which equates to a slip speed of approximately 16mm.s^{-1}). The value of this coefficient is approximately one order higher than that of that calculated by *Kalyon et al.* The reason this value is high is perhaps because of the very smooth Perspex walls and rotor surfaces, the possible presence of grease from hands and the low pressure of the fluid. It is clear, however, that by accounting for slip the simulation mimics the behaviour of the experimental trial more closely (see Figure 8-12a and 8-12b). Also, it has been shown that introducing the slip conditions defined by *Kalyon's* value ($\beta = 8.9*10^{-8}$ m.Pa^{-1}s^{-1}) into the model does not influence the flow substantially in the Hampden RAPRA Torque Rheometer (see Figure 8-11). This indicates that slip may not be significantly detrimental to equipment performance in

this low shear mixer, however, the slip phenomena will become more consequential for larger higher shear mixers.

Grid design for complex geometries requires considerable thought and skill, and the performance of the simulation can be drastically reduced if optimum meshing is not achieved (as shown in section 5.6). It is well known that grid form and node distribution can affect convergence levels and CPU time significantly. The complex three-dimensional blocks shown within this thesis (see Figure 5-12) illustrate how difficult complex rotor design can be to model and how skewed the element form can be. Poor block design is thought to have limited the complexity of the work on mixing elements in a TSE carried out by Bruce *et al* who could not find a converged solution when modelling typical non-Newtonian fluids with a power law index less than 0.5. The form of my own blocks, practicable mesh density and mesh construction time were all benefited greatly by the move to unmatched grids and the CFX software. The unmatched grid capabilities of CFX allowed the uses of regular 'O rings' and 'H grids' which offer the opportunity of constructing a mesh with low skewed elements and an even node density. Approximations incurred from the use of unmatched grids were investigated and have been, to some extent, shown not to affect the simulation accuracy noticeably as the discussion on verification later in this chapter suggests.

The workers on this subject have tackled simulating rotor movement in a number of ways. Initially, this research involved assigning an angular velocity to the rotor boundaries on separate meshes for different rotor configurations. This pseudo steady-state representation of a transient operation assumes that the inertial effects do not contribute to the flow significantly. This research has shown, for the Hampden RAPRA Torque Rheometer, that this is the case for fluids with a viscosity greater than approximately 1 Pa.s (see Table 7.2). Below this value, as the non-linear inertia term begins to contribute to the vector field, it becomes more difficult to find a converged solution to the simulation with the Polyflow solver. In pursuing this course I discovered that, although model accuracy is good, limitations are encountered. The main limitation is to do with the amount of work involved in setting up each separate geometry which represents the whole rotor cycle. Each domain must be meshed from scratch, as the block structure for differing time steps can be very dissimilar. The time required to create the mesh for each time step was of the order of weeks rather than days. As concluded within this report, values for key parameters averaged over the whole domain do not vary too greatly (see Table 5-1), so some understanding of the flow situation and the effect of altering variables was obtained from studies on one geometry; this was not an ideal situation. Other researchers, especially those

using mesh to mesh interpolation or Arbitrary Lagrangian Eulerian techniques to link their steady state 'snap shots' to yield a more useful 'transient' simulation, would have also realised that a new geometry should be created for at least every five degree increment of the whole rotor cycle if a reasonable level of accuracy was to be achieved. Researchers in this field, who have had their work kerbed by this limitation, have resorted to either analysing two-dimensional domains, using only a small number of time steps (to represent only a small portion of the whole cycle) or decreasing model accuracy by using geometries every 20 or 30 degrees. For friction ratios of 1:1 a relatively small number of geometries would be required (72 for 5 degree increments), however, for ratios that may give more chaotic flow patterns such as 1:125 it would be necessary to construct nine times as many. This problem is compounded by the number of new geometries required if the study/optimisation of rotor geometry is to be effectively carried out. It was clear that the issue of mesh generation was a major stumbling block preventing these simulations from becoming a practical engineering tool. Research into this matter uncovered two new ways forward which had not be used, as far as the author is aware, to model a complex three-dimensional internal mixer at the time this study was under way. Essentially, both methods presented an opportunity to automatically model any of the configurations of the rotor cycle from one original mesh. The first was the sliding mesh technique which was developed for modelling stirred tank reactors. Since the internal mixer in question is essentially two stirred chambers linked by a central bridge region it was thought that this method could be applied to this process. This technique and the CFX software that offered this facility was found to be very efficient computationally and in terms of man-hours, although, it can only model non-intermeshing rotors. The second opportunity, the mesh superposition technique (MST), had, at the time of this investigation, only just been developed by Polyflow to tackle such problems with intermeshing and non-intermeshing mixers and extruders and was to be made available in the next software release. The efficiency of the Polyflow codes were, however, still limiting and the approximations and factors, such as the penalty coefficient and the compression factor, used in order to obtain a working MST simulation had not been experimentally verified to the author's knowledge. This technique may become very important for modelling intermeshing rotor as the code and hardware develop in the future, however, the decision was made by the author to proceed along the sliding grid route. The practicality of having to generate complex and time consuming meshes to represent the numerous rotor configurations one finds with the whole rotor cycle was hugely improved by using the sliding grid technique. This, however, was not seen as the end of the subject. There was still the matter of geometry manipulations in terms of investigating and optimising the mixer design. If the rotor clearance of a geometry was to be

investigated, for example, separate geometries still had to be made for each individual case. This was found to be very time consuming; for example, the number of separate 'rotor clearance' geometries created, and reported in section 7.4, where the Polyflow code was used, was limited to only four due to the extent of this obstructing problem. Geometry optimisation is clearly one of the primary benefits of this type of simulation and, therefore, it was seen as a primary goal to try and reduce or even eliminate this problem and hence produce a methodology for rotor design that was highly practical. To this end a new technique for this area of research was developed. The Automatic Geometry Parameterisation (AGP) technique was used to successfully create the multiple geometries in the more conclusive CFX rotor clearance investigation, presented in section 8.6.2. This technique relied on the underlying pre-processor programming code (Patran Command Language - PCL) which can be used to instruct the pre-processor to carry out a variety of commands (an example of the coding used for this research is given in Appendix 11). By manipulating the code, and with careful forward planning (see section 8.6.2) various 'controllable' parameters were engineered into the simulation. Using this technique, and after investing the time to recreate the simulation to incorporate the controllable parameters, it was possible to create a new working mesh in under five 5 minutes of CPU time and under one minute of man time. If we consider that it took 42 separate geometries to create Figure 8-24 it is easy to see that a great deal of time was saved using the AGP technique. As an aside, this technique (which stemmed from the latent capability of the post processor software) did not have a name as such and was not a well promote feature of the software. This was surprising as the technique could be very useful in a number of situations. Since it was only referred to as PCL the author felt it appropriate to give the technique the more descriptive AGP moniker. Perhaps this technique is not as well known or widely used[134] because it is quite difficult to use effectively.

A low volume laboratory mixer generates relatively low amounts of viscous heating when processing fluids with a shear/viscosity relationship of fluids such as common polymers melts at 200 °C and the coloured clays used in experimental trials as mentioned previously in the discussion. This isothermal nature means that the energy can be ignored in the simulation. This, however, is an assumption that one should be aware of (especially if one is to model a larger volume mixer) since polymer melt fluid viscosity is very sensitive to temperature change, as demonstrated in section 8.3.3. Constant fluid density is an assumption, also related to energy change, which has been made. The combined effects of the errors introduced from all the assumptions made and errors originating from numerical methods used in the simulation were put to the test by a number of qualitative and quantitative validation experiments.

A reliable method of assessing model predictions involved comparing flow and mixing patterns. Two similar viscous fluids of different colours were packed into the mixer chambers whilst the rotors are configured 'vertically'. The minor phase, in the form of a thin horizontal plane, was positioned within the bulk or major phase. When the rotors were turned the mixing patterns formed were revealed by an examination of various clay slices. In the simulation this horizontal plane of the minor phase was modelled by inserting a number of new blocks within the discretized domain. Within each new block a mass scalar was defined representing a theoretical dye. The results of these trials revealed that the predictive model yields very similar patterns to that obtained from the experimental model (see Figure 8-4 and Figure 8-5). The discrepancy between the two is largely due to wall slip. This was successfully compensated for by adding an appropriate slip factor into the simulations (see Figure 8-12). The author observed, both experimentally and numerically that the speed of the rotor does not make any difference to the trajectories of the velocity vectors and their gradients, and hence the mixing patterns. This has been attributed to the high viscosity of the fluid damping inertial effects.

The rotor design of the Hampden RAPRA Torque Rheometer allowed excellent visual access when encased in a transparent mixer chamber. Using the 'Perspex mechanical model' quantitative experiments involving the mixing of a transparent viscous gel (having a similar shear dependency on viscosity as common polymer melts) and inert coloured particles (1mm in diameter) were performed. The 'x' and 'y' components of the particle trajectory and velocity magnitude were calculated using a high-speed video camera with a macro lens and a built in timer. The motion of the particle was assessed by comparing two 'frames' differing by a small increment in rotor position. The results indicate good model validity. Over ninety percent of the trajectories, measured in degrees, of a number of unique points within the flow field of the pseudo steady-state Polyflow simulation, the CFX sliding mesh simulation and the experimental model are within 1.1 % of each other. The magnitudes of the velocity vector determined experimentally were, as expected, lower than that predicted by both models. The differences range from 1.0 – 11.2 mms^{-1} with 78% of the results being under 5.3mms^{-1}. This discrepancy has been attributed to 'drag'. Hypothetical particles in the models (i.e. point velocities) can be thought of as moving as one with the fluid and hence do not experience drag. This quantitative technique may only be suitable for validating the Hampden RAPRA Torque Rheometer. It is thought that velocity components of other internal mixers would be very difficult to verify experimentally and this may be the reason that the author is unaware of any other serious

attempts from other researchers. Laser Doppler Anemometry LDA, a technique which is quite commonly used for stirred tank model validation, has been applied to processing corn syrup in a twin screw extruder by Sernas *et al*[135]. The numerically predicted velocity profiles were compared to those found in the axial and azimuthal direction from the LDA experiments. They yielded only 'fairly close agreement' (no quantitative figure to summarise the level of accuracy was given).

The verification techniques mentioned above involve analysing components of the velocity. The pressure term is the other primary variable which should be verified. Past researchers such as Ghoreishy, Nassehi and Cheng[136] have validated their work using pressure sensors on chamber walls. Although this can add to the body of evidence collected in order to build confidence in their models it only validates the tip clearance sections. A more apt validation technique is the use of torque measurements. The interactive nature of CFX affords researchers excellent flexibility. This meant that the sliding grid simulation could be partly validated by using a FORTRAN program created by the author to calculate the torque over the rotors. The predictions were compared directly to torque data produce from the Hampden RAPRA Torque Rheometer from real processing situation. The predictions were reasonable (see Table 8-3) although real processes presented an inherent difficulty associated with accurate temperature measurement, therefore, it was very difficult to designate accurate viscosity data for the simulation.

It is important to note that these experiments validate the simulations at point approaching a complete representation of the real system. The main deviations from reality at this point include the lack of elastic character representation modelling and the absence of voids in the domain. In visualisation experiments fill factors of around 0-15% volume made little observable difference to the flow patterns. The voids tend to break up into small discrete air pockets with a proportion collecting behind each rotor tip rather than between the rotor tip and the chamber wall affecting dispersive mixing (see Figure 6-15). On the same theme Manas-Zloczower *et al* have commented how the presence of voids does not affect the values of key variables averaged over the whole domain. At lower fill factors complex free surfaces and fluid folding begin to occur. These are expected to be difficult to tackle using current CFD techniques. The elastic components of polymeric materials, on the other hand, is thought to be an extremely important point which ideally should not be ignored. Polymers and rubbers can exhibit strong viscoelastic character when sheared. The problem of representing this accurately is accentuated when we consider the non-isotropic nature of polymer properties. The extra stresses generated when a

viscoelastic fluid is sheared at realistic rotor speeds are, section 7.2.4 indicates, expected to be significant. At very low rotor speeds the shear stresses dominate. However, with increasing rotor speed, the normal stresses increase more rapidly than shear stresses. The highly non-linear solutions that exist for even simple viscoelastic models make finding a converged solution for real processing situations difficult. The difficulty in finding a converged solution for rotor speeds above 0.1 $rad.s^{-1}$ with the Polyflow solver is perhaps to a large extent due to the complex geometry and the high percentage of skewed elements in the mesh, as solutions to viscoelastic fluid simulations can be found more readily for regular geometries. Perhaps viscoelastic simulations would better lend themselves to the more regular and more CPU efficient CFX sliding mesh simulation for real complex geometries, although CFX 4.2 does not have viscoelastic functionality it may be possible to program in this capability; this however, was deemed beyond the scope of this project as it was necessary to explore more important avenues. It is clear, however, that one should exercise caution when assessing stresses for the evaluation dispersive mixing when neglecting the contributions from the viscoelastic component of a polymeric fluid; although, for the comparison of various equipment configurations and operating conditions, the model may still reveal useful trends.

When defining a simulation it may be difficult to set some of the parameters representing the desired situation accurately. These are the mean density, constants in the energy equation and the power law coefficients for the wall slip and viscosity models after the initial period of the cycle. The difficulty will arise from combining species, reacting species, chain lysis, the presence of gases and the presence of additives and impurities all of which are very stochastic in their occurrence in the fluid domain. The chaotic nature of other factors such as fluid voids and fluid types (in multi-fluid domains) mean that researchers addressing these issues have had to assign their initial position to random locations in two-dimensional models. The sliding mesh simulation could incorporate several sub-domains each one defined by differing rheologies of the fluid contain within, although, it may be interesting to observe the change in resultant flow field, a realistic representation of a stochastic situation can not be obtained by analysing a few random situation. Modelling reactions between various species, although possible, presents similar problems associated with the stochastic nature of the mixing process. The initial peak in the torque graphs obtained from the reactive processing of polymer melts within Hampden RAPRA Torque Rheometer (*Al-Malaika et al*) corresponds to reaction initiation and propagation. The rapid decay of the peak may suggest that it is reasonable to assume that the majority of the reactions taking place may be terminated before entering the main homogenisation period of the

mixing cycle and therefore perhaps they can be ignored without fear of substantial loss of model accuracy.

On the subject of practicalities, i.e. the potential of CFD for the use by engineers for design purposes, several important factors have been considered. In the author's opinion the CPU time for simulations in no longer such an important factor and neither is convergence for these laminar non-viscoelastic models. Even viscoelastic models may benefit in terms of convergence by techniques such as under relaxation and by designing a low skewed element mesh. Mesh construction time can be reduced by eliminating the need to remesh for different rotor configurations and geometries by using the sliding grid and AGP techniques demonstrated in this research. The level of difficulty, especially of the mesh generation procedures and simulation mathematics, may be an issue for design engineers. Commercial CFD codes make every effort to constantly improve their products and one of their aims is to improve user friendliness; this means that an engineer need have little knowledge of the theory behind the system to be modelled or the equations being solved etc. This could lead to errors and the generation of inaccurate models. The skills required to use and manipulate these models in order to generate useful results take a significant amount of time to acquire. This time will decrease given the right guidance. Ideally, to facilitate the whole modelling process, a number of studies, like this one, and even access to a library of ready made meshes (from which a number of basic or specific rotor or screw designs could be chosen to be used in an appropriate chamber) and an extensive fluid property database should be made available. The cost is also an important practicality. This type of investigation could be realistically set up by industrial companies if the expense of the man hours, code licence fee (approximately £15,000p/a) and suitable hardware (£8,000 +VAT – SPECfp95 52.2*) could be justified.

Potential uses for a simulation of this type spans a wide a spectrum from investigating 'black box' operations in terms of key variables and specialist parameters, to investigating the effect of changing variables on the system, optimisation and to comparing different systems for process transfer and scale up. The majority of this research has been geared towards addressing assumptions and developing a methodology from which all simulations of this type can be used bestowing confidence in both the capabilities and accuracies. Also, within the research strategy (section 2.2.3) a number of potential uses were envisaged involving the simulation aiding in:

- predicting and understand flow patterns accurately (in conjunction with mechanical models)

- analysing the effect of changing process variables
- understanding mixing mechanisms qualitatively
- understanding mixing mechanisms quantitatively
- predicting equipment performance
- optimising process equipment
- scaling up a batch operation
- transferring a batch process to a continuous process confidently

From the work presented in the main body of this thesis one can see that these areas can indeed be assisted by the simulation methodology developed. Analysing the effect of altering process conditions and understanding the effect on mixing has been carried out for several important factors. Most interesting is the effect of non-Newtonian fluid behaviour. The assumption of Newtonian behaviour in internal mixer models has been used by some researchers. Some (White et al) have even reverted back to Newtonian models commenting on how the introduction of non-Newtonian behaviour in their models has had only a minor effect on the flow field and have removed this complication possibly to improve solution convergence and reduce CPU time. Typical power law exponent for viscous fluids processed in internal mixers range from 0.5 to 0.1. Above the value of 0.6 it is evident that the changes in the flow field are minor and the increase in model complexities may not be justified. The effect of decreasing the power law exponent will depend on the flow situation in question, however, from my investigation, it is evident that the flow field can alter considerably (see section 7.2). The vector field in the azimuthal direction varies significantly, however, the most noticeable effect is on flow in the axial direction. A decrease of 26% is observed for the average axial flow of the fluid around a rotor for a simulation using a power law exponent of 0.3 compared to its Newtonian counterpart (as derived from the data in Table 8-7, see also Figure 7-21). As an aside, it was the discovery of this poor axial flow resulting from the mixing of shear thinning fluids and the Hampden RAPRA Torque Rheometer blade design that enabled the 'x' and 'y' velocity vector components to be measured experimentally to a reasonable degree of accuracy. The effect of decreasing the power law exponent on the mixing index parameter is also noteworthy. The investigation brought to light a decrease in dispersive mixing effectiveness with decreasing power law exponent, see Figure 7-10, (in assessing dispersive mixing the shear stress magnitude must also be taken into account).

* Compaq Workstation XP1000 – March 1999

Also it was found that the average shear rate decreased by 20% when comparing simulations where n=1.0 to n=0.1 (see Table 7-3).

Considering model accuracies again, the accuracy of the fluid behaviour by any model, such as the Boussinesq (equation 8-6) or Arhenius approximation (equation 8-2) depends on the material being processed but, more importantly, on the degree of change of the primary variable (in this case temperature for equations 8-6 and 8-2). This is an important point which should be kept in mind when addressing situations with large variable gradients. The same is true for the power law model for shear dependent viscosity. Depending on the material it has been shown that the power law model holds true as long as the primary variable (shear rate) does not expand over many orders of magnitude. The shear rate range in the Hampden RAPRA Torque Rheometer , 0.5 – 100 s^{-1}, the power law model will be sufficiently accurate. The shear rate range may be much larger in other equipment, for example, a shear rate range of 4 – 1000s^{-1} for a twin screw extruder[137]. If this situation exists it may be necessary, depending of the shear rate / viscosity data, to employ a composite model with power law constants corresponding to specific shear rate regions. Figure 9-1 illustrates this point more clearly by demonstrating how two separate power law region many represent reality more accurately.

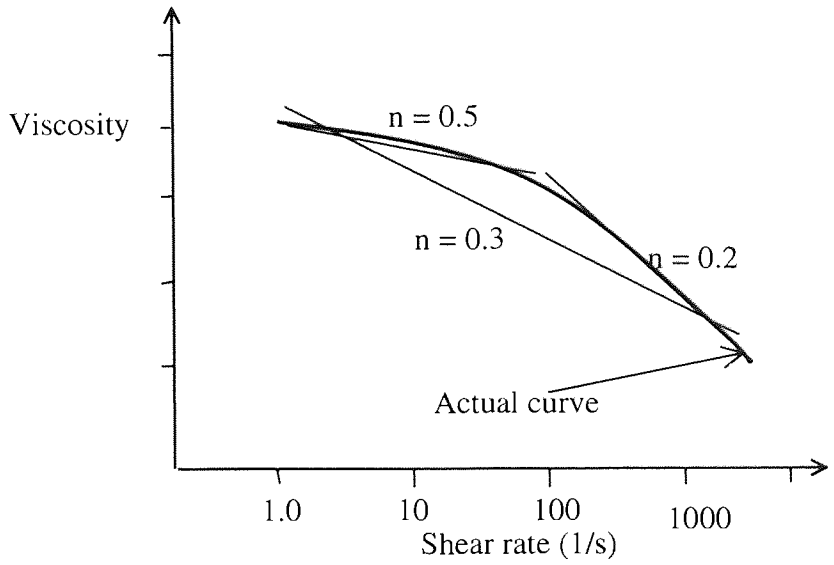

Figure 9- 1 ***Shear rate / viscosity plot highlight the inaccuracy of the power law over large shear rate ranges.***

The Newtonian plateaux occurring at very high and very low shear rates should also been taken into account, if the shear conditions or rheology dictates, as should significant yield stresses

which may result in flow dead spots. This work highlights the point that process operation conditions and equipment design should be optimised for the specific rheology in question and not for any typical test fluid as mixing performance is strongly rheology dependent.

The potential to quantify the effect of operating conditions, such as rotor speed, has been demonstrated. The equation of the various trends can be used for equipment design, for example, to determine the viscous heating energy that needs to be removed by the heat transfer fluid (which ideally should be kept to a minimum). Each point generated for these types of plots required considerable hardware resources and CPU time due to the fact that the Polyflow code was used. The number of points was kept to a minimum and in some cases some of the graphs within this report have been made, to an extent, to highlight the potential of the simulation. This research has also addressed optimisation and geometry scale up, for example, using the AGP technique presented in section 8.6.2, where optimum rotor clearances were revealed for a number of flow situations and the inertia terms was revealed to effect the flow field when the scale of the geometry increases. In addition, rotor curvature has been addressed and improved axial flow has been achieved by increasing the curvature as shown in Figure 8-21. These types of investigations could be extended to new 'concept' rotor designs.

Apart from velocity vectors and streamlines the simulation offers other alternatives to further understanding of the fluid flow in the complex geometry. The dye tracing model reveals the mixing patterns, although, they are perhaps best suited for the validation purposes of this research as the number of rotor turns are limited. Tracer 'blobs' may be more useful especially for understanding the flow within continuous mixer sections. Quantitative appreciation of mixing mechanisms can be obtained by calculating fluxes, stress magnitudes, the mixing index or by particle tracking. Probes, fluxes and average values have been used to assess the mixing index, shear stress magnitudes and transport criteria. Probes do have their uses, however, confidence in their ability to represent regions within the domain are improved if they are used in conjunction with other data outputs such as contour plots, as discussed in section 8.4.4. Perhaps, to obtain a more comprehensive picture of the flow field, more probes than have been used in this work should be employed. One technique that has been found to be quite useful is animation. An animation was created to show axial flow contours on a fixed slice through the domain using a number of time steps representing the whole rotor cycle. If the increments are small enough (approximately 5 degrees) and the animation is engineered to 'loop' the effects are quite impressive and yield a good qualitative appreciation. Another animation was also created as

before but this time involving temperature contours plotted on the slice. As the fluid was mixed the viscous heating effect was followed for a several seconds of real mixing time. Mass fluxes, as used in chapter 8, appear a quite successful method to quantify material flow. Ideally, fluxes should be obtained in all directions, *a la* White *et al,* however, this could be extended to obtaining fluxes for smaller characteristic regions appropriate to the mixer geometry. Average values of a parameter can also yield useful results as observed in the work reported on in chapter 7. More weight could be added to the usefulness of these results by defining the character of the flow in terms of maximum and minimum values as well as a property distribution break down as demonstrated in Figure 9-2. For example, for process transfer purposes, it is desirable to have similar dynamic and kinematic character in the commercial scale to that achieved in the primary product trails in order to obtained the desired product specification. Hence, process transfer may be aided by considering maximum and minimum values and results in the form illustrated by Figure 9-2. Features like average values and numerical breakdowns were currently not available through the standard GUI (graphical user interface) of the Polyflow and CFX4.2 commercial codes. An understanding of the inner structure of the relevant files are required in order to be able to manipulate the data in the correct manner to obtain the desired output. Since CFD is becoming more geared towards producing more useful results features similar to these are expected to become more readily available.

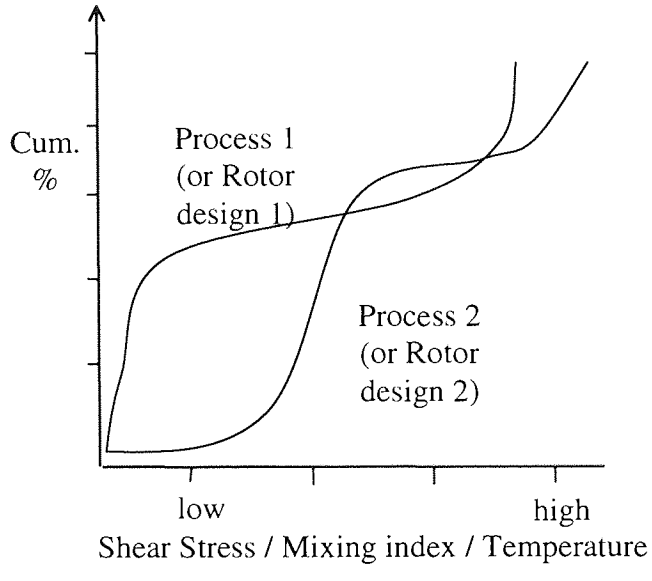

Figure 9-2 ***Diagrammatic plots of percentage of key parameters within the domain of two processes to compare equipment performance***

Taking the example of mixing index we can see how the mixing character of different processes compare. The average mixing index of the Hampden RAPRA Torque Rheometer is 0.393 when

n=0.2 (Table 7-3) and 0.575 for the Banbury mixer when n=0.22 (Manas-Zloczower *et al*)[138]. This difference implies that the Banbury BB-2 Banbury type exhibits better dispersive mixing performance. This value for the Banbury mixer is reported to fall to 0.50 for a two-dimension simulation.

As mentioned earlier, a quantitative appreciation of mixing can be obtained using a particle tracking analysis. Distributive mixing in internal mixers has been analysed by researchers who have tracked a number of particle flocs starting from a variety of locations within the fluid domain. The potential for these investigations is, in the author's opinion, large. Not only can they be used to compare rotor designs or for process transfer and scale up but for optimisation of friction ratios and to take account of the affect of particle density on viscosity *a la* Nassehi and Ghoreishy (viscosity changes due to the presence particles may be small in comparison to viscosity changes induced by shear and temperature gradients). The accuracy of particle tracking investigations in three-dimensional domains has been limited in the past as discussed previously. These limitations can be overcome by use sliding mesh simulations, for example, particle tracking is improved by a high-density mesh consisting of low skew elements and by defining small increments between each mesh representing the whole rotor cycle all of which are a pragmatic option using the methodology adopted in this research. It should be noted that the random initial position of particulates in real life mixing simulations might make speculation on the initial starting position difficult. Also, the particle tracking investigation performed by internal mixer simulations to date do not take into account of the breaking up of flocs only the transportation of particles. It is thought, however, that simulated mixing situations that are found by particle tracking studied to have good relative distributed mixing character will correspond to actual improved mixing in the real life situation. Standard particle tracking is an option not available for transient unmatched sliding grid simulations in CFX4.2, however, software development is an important issue. For example, CFX4.3 (released in November/December 1999) saw the added relevant capabilities of particle tracking with transient flows, solidification and increased performance in terms of CPU time per iteration. CFX4.4 (available in November 2000) will see introduction of particle tracking to unmatched grid, and CFX4.5 should have particle tracking capability with fully sliding unmatched grids[139]. These, and other future developments, combined with the simulations presented within this thesis present many opportunities to further knowledge substantially in this area (see section 10.2).

10. Conclusion & Recommendations for Future Research

10.1 Conclusions

In an attempt to apply a mathematical tool to increase understanding and aid in the development, design and optimisation of viscous fluid processing equipment this research has been carried out with a view to establishing model accuracies, limitations, practicalities and uses. The Hampden RAPRA Torque Rheometer has been simulated as it was thought to be conducive to model validation and its small fluid domain aided investigative modelling. As this research progressed, via 'snap-shot' analysis using the finite element commercial code Polyflow, it was evident that the model was of some worth and is in good agreement with validation experiments, however, several major restrictions were identified. The limitations included poor element form and high man-hour requirements for the construction of each geometry. Also, the absence of time in these models has its own limitations as previously discussed. All, or at least some, of these limitations can be found in the numerous attempts to model internal mixers in accurate geometries by other researchers. At that time it was clear that there was no generally accepted methodology to provide a practical model which had been validated. This research, unlike the others, has presented a full complex three-dimensional, transient, non-isothermal, generalised non-Newtonian simulation with wall slip which overcomes these limitations using unmatched gridding and sliding mesh technology adapted from CFX codes. Overcoming these limitations has been shown to improve element form which influences solution convergence. This stands future research into viscoelasticity in good stead since attempts made to model viscoelasticity during the course of this research have been made difficult partly due to high element skew. Also, the number of configurations used to represent the complete rotor cycle can be very easily altered as can the friction ratio. Another important innovation is the Automatic Geometry Parameterisation technique that has been used to allow extremely quick and easy mesh generation for wide variety of geometries based around an initial design. This AGP technique, combined with the sliding grid simulation, has been used to addressed optimisation and geometry scale up, for example, where optimum rotor clearances were revealed for a number of flow situations and the inertia terms was revealed to effect the flow field when the scale of the geometry increases. The CFX code has also proved to be of superior performance compared to its predecessor in terms of overall CPU time per simulation and hardware memory requirements. Moreover, the code's inherent flexibility has been demonstrated to be invaluable enabling unique features to be

added to the simulation to either improve the model's representation of reality or to produce additional useful results by the addition of user defined programmes.

Model validation has been pursued in terms of qualitative and quantitative velocity vector analysis of the isothermal, full-fill mixing of generalised non-Newtonian fluids as well as torque comparisons with a relatively high degree of success. These investigations indicate that CFD models of this type can be quite accurate and perhaps have not been validated to this extent previously because of the inherent difficulties arising from most real processes.

Researchers wishing to continue this type of investigation should keep in mind of several important factors. These include the viscoelastic nature of some fluid, the low fill factor of some operations and the difficulty that may arise in obtaining correct fluid physical properties to reliably represent a desired rheology. Should a researcher wish to model intermeshing equipment the new mesh superposition technique (Polyflow) appears to be an interesting prospect.

To summarise, this work, as it stands, presents opportunities for future researchers to confidently explore areas such as non-isothermal behaviour, equipment design using the highly practical AGP techinique, distributive mixing (in terms of particle tracking investigations) and to provide a good opportunity to deal with the effects of viscoelastic fluid behaviour which is thought to be important when assessing dispersive mixing efficiency – see section 10.2. From a pragmatic perspective one can see the potential of these simulations for design and optimisation of process conditions and equipment design for a variety of rheologies and situations and for assisting in the task of process transfer and scale-up. Superior product homogeneity, by improving mixing and reducing flow dead spots and degradation, and minimising processing time and energy costs may follow from these simulations.

10.2 Future work - Short term

- To fully explore non-isothermal situations using the Arhenius model for fluid viscosity and incorporating boundary conditions representing energy exchange from heat transfer fluid over large time scales and then extending this to large-scale geometries.
- To add to the body of evidence collected to date using:
  1. further torque comparisons
  2. using polymeric materials for visualisation purposes
  3. temperature comparisons
- To investigate the effect of using a more accurate wall slip model to give a better representation of a polymeric material.

10.3 Future work - Medium – Long term

- To model further geometry variations using the AGP technique, additional user defined programmes and extend this to other rotor designs.
- To investigate optimising mass transfer between chambers in terms of improving this flow without overly decreasing the shearing area.
- To use the mesh superposition technique for intermeshing rotor designs and to assess accuracy and limitations of the type of model.
- To use particle tracking for distributive mixing analysis.
- To investigate friction ratios fully.
- To investigate phase changes, reaction and multi-fluid domains
- To investigate viscoelastic behaviour using user defined programmes and to assess the impact of viscoelasticity on flow patterns and stress magnitudes.
- To use the model in conjunction with continuous mixer design and operation.

References

[1] Matthew G., Polymer Mixing Technology, Applied Science Publishers, 1982, Essex, England.

[2] Meissner K., Poltersdorf B., Model Development for an Internal Mixer, International Polymer Processing VII, No. 1, p.2, (1992)

[3] Thomas D. K., Developments in Polymer Stabilisation-1, Scott G., Ed., p.137, 1979, Applied Science Publishers, London.

[4] Scott G., Developments in Polymer Stabilisation-1, Scott G., Ed., p.181, 1981, Applied Science Publishers, London.

[5] Williams D. F., Biocompatability of Orthopaedic Implants, Vols. I and II, CRC Press, 1982, Boca Raton, FL.

[6] Walker A., Phthalates face European ban in soft toys for children, The Chemical Engineer, Issue 672, p. 3, 14th Jan 1999

[7] Ajiboye O., Scott G., Polym. Deg. Stab., Vol 4, p 397 (1982)

[8] Chakraborty K. B., Scott G., Tavakoli S. M., Advances in Elastomers and Rubber Elasticity, Lal J., Mark J. E. Eds., Plenum Press, p.189, 1986, New York.

[9] Coulson J. M. Richardson J. F., Chemical Engineering Vol. 1, p. 528, 4th Ed., Pergamon Press, 1993, Oxford, England.

[10] Fluent Europe Inc. (http://www.fluent.com/) Holmwood House, CortworthRoad, Sheffield S11 9LP.

[11] AEA Technology (CFX) (http://www.aeat.co.uk/cfx/cfxapp.htm) 329 Harwell, Didcot, Oxfordshire, OX11 0RA, United Kingdom.

[12] Computational Dynamics Ltd. (http://www.cd.co.uk/) Computational Dynamics Limited, Olympic House, 317 Latimer Road, London, W10 6RA, England.

[13] ICEM (http://icemcfd.com/) Berkeley, CA (Main office) 2855 Telegraph Ave., Suite 501, Berkeley, CA 94705.

[14] Concentration, Heat and Momentum Ltd. (http://CHAM.co.uk) Bakery House, 40 High Street, Wimbledon Village, London. SW19 5AU, UK.

[15] Amtec Engineering Inc. (INCA) (http://www.amtec.com/) P.O. Box 3633. Bellevue, WA 98009- 3633 USA.

[16] ADINA R & D, Inc. (http://world.std.com/~adina/transp.html) 71 Elton Avenue, Watertown, MA 02172, USA.

[17] PolyDynamics, Inc. (http://www.polydynamics.com/pdintro.htm) 1685 Main Street West, Suite 305, Hamilton, Ontario, Canada L8S 1G5

[18] Polyflow package, (http://www.polyflow.be/) Polyflow SA., Place de l'Universite 16, Louvain-la-Neuve, Belgium.

[19] Bruce D.P., PhD Thesis, Aston University (1997).

[20] The Chemical Engineer, p. 22,.24 June 1993,

[21] Scott Blair G.W., *Rheol.* Acta, Vol. 4, 53 (1968)

[22] Lenk R. S., Polymer Rheology, p.10, Applied Science Publishers (1978).

[23] The Chemical Engineer , p. 24, 24 June 1993.

[24] Bird R.B. Armstrong R.C. Hassager O. Dynamics of Polymeric liquids. Vol.1, p.62, Ed. 2, John Wiley & sons Press (1987).

[25] The Chemical Engineer, p. 23, 24 June 1993

[26] Bird R.B. Armstrong R.C. Hassager O. Dynamics of Polymeric liquids. Vol.1. Ed. 2. John Wiley & sons Press (1987).

[27] Fell N., The Chemical Engineer, p.17-18, 9 Oct 1997.

[28] Manas-Zloczower I., Tadmor Z., Mixing and Compounding of Polymers: Theory and Practice, Ch 18, Hanser, (1994) Munich .

[29] Meissner K., Poltersdorf B., Model Development for an Internal Mixer, International Polymer Processing VII, No.1, p.1, (1992)

[30] White J. L., Development of Internal Mixer Technology For The Rubber Industry, Rubber Chemistry Technology, Vol. 65, p.527-579 (1992)

[31] Manas-Zloczower I., Tadmor Z., Mixing and Compounding of Polymers: Theory and Practice, p.621, Hanser, (1994), Munich.

[32] Matthews G., Polymer Mixing Technology, Applied Science Publishers, (1982).

[33] Manas-Zloczower I., Tadmor Z., Mixing and Compounding of Polymers: Theory and Practice, Hanser, (1994), Munich.

[34] Coulson J. M., Richardson J. F., Chemical Engineering Vol. 1, p. 230, 4th Ed., (1993) Pergamon Press, Oxford, England.

[35] Coulson J. M., Richardson J. F., Chemical Engineering Vol. 1, p. 231, 4th Ed., (1993) Pergamon Press, Oxford, England.

[36] Carley J. F., McKelvey, Ind. Eng. Chem., 45, p. 985 (1953).

[37] Maddock B. H., SPE J., 15, p. 983 (1959).

[38] Manas-Zloczower I., Tadmor Z., Mixing and Compounding of Polymers: Theory and Practice, Ch. 8, Hanser, (1994) Munich.

[39] Computational fluid dynamics without complex mathematics: the advantage for thermofluids education, Process Instn Mech Engrs., Vol. 205, p13 (1991).

[40] Computational fluid dynamics without complex mathematics: the advantage for thermofluids education, Process Instn Mech Engrs., Vol. 205, p14 (1991).

[41] Bird R. B., Stewart W. E., Lightfoot E. N., Transport Phenomena, p.76, John Wiley International, (1960) New York.

[42] Matthews G., Polymer Mixing Technology, p.127, Applied Science Publishers (1982), Essex, England.

[43] Matthews G., Polymer Mixing Technology, p.127, Applied Science Publishers (1982), Essex, England.

[44] Kim J. K., White J. L., Non Newtonian and Non-Isothermal Modelling of 3D-Flow in an Internal mixer, Intern. Polymer Processing VI, No. 2, p.103-110 (1991).

[45] Cheng J. J., Manas-Zloczower I., Hydrodynamic Analysis of a Banbury Mixer - 2-D Flow Simulations for the Entire Mixing Chamber, Polymer Engineering Science, Vol.29, No. 15 p.1059-1065 (1989)

[46] Ghoreishy M. H. R., A Transient Finite Element Model of Mixing of Rubber Compounds in a Banbury Mixer, Iranian Polymer Journal, Vol. 5, No.1, p.30-41 (1996)

[47] Ghoreishy M. H. R., A Transient Finite Element Model of Mixing of Rubber Compounds in a Banbury Mixer, Iranian Polymer Journal, Vol. 5, No.1, p.30-41 (1996)

[48] Nassehi V., Freakley P. K., Spreader Blade Analogy of flow past an Internal Mixer Rotor, Intern. Polymer Processing VI, No.2, p.91-97 (1991).

[49] Freakly P. K., Patel S. R., Rubber Chem. Technol., Vol. 58. p.751 (1985)

[50] Nassehi V., Ghoreishy M. H. R., Modelling the Transient Flow of Rubber Compounds in the Dispersive Section of an Internal Mixer with Slip-Stick Boundary Conditions. Advances in Polymer Technology, Vol. 16, No. 1, p.45-68 (1997)

[51] Nassehi V. Salemi R., Finite Element Modelling of Non-isothermal Viscometric Flows in Rubber Mixing, Intern. Polymer Processing IX, No.3, p.199-204 Hanser Publishers, Munich (1994)

[52] Nassehi V., Ghoreishy M. H. R , Freakley P. K., Clarke J. Development of Validated, Predictive Mathematical Model for Rubber Mixing, Plastics, Rubber and Composites Processing and Applications, Vol. 26, No. 3, p.103-112 (1997)

[53] Nassehi V., Ghoreishy M. H. R., Simulation of Free Surface Flow in Partially Filled Internal Mixers, Intern. Polymer Processing XII, No. 4, p.347-353 Hanser Publishers, Munich (1997)

[54] Nassehi V., Ghoreishy M. H. R., Finite Element Analysis of Mixng in Partially Filled Twin Blade Internal Mixers, Intern. Polymer Processing XIII, No.3, p.231-238, (1998)

[55] Yang H. H., Manas Zloczower I., 3D Flow Field Analysis of a Banbury Mixer, Intern. Polymer Processing VII, No.3, p.195-203, (1992)

[56] Cheng J. J., Manas-Zloczower I, Hydrodynamic Analysis of a Banbury Mixer - 2-D Flow Simulations for the Entire Mixing Chamber, Polymer Engineering Science, Vol. 29, No.15 p.1059-1065 (1989)

[57] Wong T, Manaszloczower I., 2-Dimensional Dynamic Study Of The Distributive Mixing In An Internal Mixer, International Polymer Processing,Vol.9, No.1, pp.3-10 (1994)

[58] Yang H. H., Manas Zloczower I., Analysis of Mixing Performance in a VIC Mixer, Intern. Polymer Processing IX, 4, p291-302 (1994).

[59] Manas-Zloczower I., Cheng H., Chaotic Feature of Flow in Polymer Processing Equipment-Relevance to Distributive Mixing, Intern. Polymer Processing XII, 2, p83--91 (1997).

[60] Wong T. H., Manas Zloczower I., Numerical Studies of the Flow Field in Partially Filled Mixing Equipment ANTEC '92 p1788-p1795 (1992).

[61] Kim J. K., White J. L., Non Newtonian and Non-Isothermal Modelling of 3D-Flow in an Internal mixer, Intern. Polymer Processing VI, 2, p103-110 (1991).

[62] White J. L., Hu B., Simulation of Flow in an Internal Mixer of Evaluate Rotor Design: Effect of Non-Newtonian Behaviour, Kautschuk Gummi Kunststoffe 49, Jahrgang, Vol. 49 No. 4 pp285-288 (1996)

[63] White J. L., Kim P. S. K., Simulation of Flow in an Intermeshing Internal Mixer and comparison of Rotor Design, Rubber Chemistry and Technology, Vol. 69, No. 4, pp686-695 (1996)

[64] Min K. Suh K. G., Experiments and Modelling of Flow of Elastomers in an Internal Mixer with Intermeshing Rotor, Polymer Engineering and Science, Vol. 31, No. 11, pp779-788 (1991)

[65] Osswald T. A., Gramann P.J. Simulating Polymer Processes Using the Boundary Element Method, Intern. Polymer Processing VII, 4, p303-313 (1992).

[66] Gramann P.J., Matzig J.C., Osswald T.A., Simulating the Non-isothermal mixing of polymer blends using the boundary element method, Journal of Reinforced Plastics and Composites, Vol.12, No. 7, pp787-799 (1993)

[67] Stradins L. Osswald T. A., Predicting the effect of viscosity ratio on the mixing of Polymer Blends using the Boundary Element Method, Polymer Engineering and Science, Vol. 36, No. 7, pp979-984 (1996)

[68] Malkin A. Ya., Baranov, A. V., Dakhin O. Kh., Non-isothermal Dispersive Flow of a Rubber Mixture Inside an Internal Mixer, International Polymer Processing Vol. 10, No. 2, pp99-104 (1995)

[69] Shinzi H., J., Soc. Rheol. Jap., 15, p.123 (1987)

[70] Meisser K., Poltersdorf B., Model Development for an Internal Mixer, International Polymer Processing, Vol. 9, No. 1, pp 3-14 (1992)

[71] Wilson, M.P., Al-Malaika, S. and Bruce, D.P., *IChemE Research Event*, **1**, 367 (1996).

[72] Wilson, M.P., Al-Malaika, S., Generalis, S.C. and Bruce, D.P., *Fluid Mixing V: Symposium Series*, p.140, p. 237 (1996).

[73] Wilson, M.P., Al-Malaika, S., Generalis, S.C. and Bruce, D.P., *AIChemE 5th World Congress*, Vol. 4, p.509 (1996).

[74] Bruce, D.P., *ATLAS*, Vol. 4, p.3, (1996).

[75] Bruce D.P.Flow field Analysis of Some Mixing and Conveying Screw Element Regions Within a Closely Intermeshing Co-Rotating Twin Screw Extruder, PhD Thesis, Aston University (1997).

[76] Chicheng W., Manas-Zloczower I., Flow Field Analysis of a Cavity Transfer Mixer Polymer Engineering and Science, mid-August 1994, Vol.34, No.15,1224-1230.

[77] PolyCEM Training Example – A Tutorial for the geometry creation and the Mesh Generation, Polyflow s.a., April 1995.

[78] Gramann P. J., Osswald T.A., Simulating Polymer Mixing Processes Using the Boundary Element Method, Intern. Polymer Processing VII, 4, p.304, 1992.

[79] Yang H. H., Manas-Zloczower I., Analysis of Mixing Performance in a VIC Mixer, Intern. Polymer Processing IX, 4, p291-302 (1994).

[80] Chicheng W, Manas-Zloczower I., "Flow Field Analysis of a Cavity Transfer Mixer", Polymer Engineering and Science, mid-August 1994, Vol.34, No.15, p.1224-1230.

[81] Avalosse Th., Crochet M. J., Finite Element Simulation of Mixing: Three-dimensional Flow Through a Kenics Mixer, AICHE Journal, Vol. 43, No. 3, pp588-597 (1996).

[82] Ghoreishy M. H. R., A Transient Finite Model of Mixing of Rubber Compounds in a Banbury Mixer, Iranian Polymer Journal, Vol 5, No. 1, p30 – 41, (1996).

[83] Nassehi V., Salemi R., Finite Element Modelling of Non-isothermal Viscometric Flows in Rubber Mixing, Intern. Polymer Processing *IX* ,3, p199-204, (1994).

[84] Cheng J., Manas-Zloczower I., Hydrodynamic Analysis of a Banbury Mixer – 2-D Flow Simulations for the Entire Mixing Chamber, Polymer Engineering and Science, Mid-August, Vol.29, No 19 p1059-1065 (1989).

[85] Sernas V., Karwe M.V, Jaluria Y., Chiruvella R.V., Transport in a twin screw extruder for the processing of polymers, Polymer Engineering Science, Mid June 1996, Vol.36, No 11, p1531-1540.

[86] Karwe M.V., Chandrasekaren M., Measurement of velocity profiles in reverse-screw elements of a twin screw, AIChE Journal, Oct 1997, Vol.43, No.10 , P2424-2431.

[87] Jaworski Z., Wyszynski M. L., Moore I. P. T., Nienow A. W., Sliding mesh computational fluid dynamics – a predictive tool in stirred tank design, Proc. Instn Mech. Engr. Vol 211 Part E (1997)

[88] White J.C., Min K., Rubber Chem. Technol., Vol. 58, 1024 (1985).

[89] Min K., Suh K. G., Experiments and modelling of flow of elastomers in an internal mixer with intermeshing rotors, Polymer Engineering and Science, Mid June 1991, Vol 31, No. 11, p 779-788.

[90] Bird R. B., Armstrong R. C., Hassager O., Dynamics of Polymeric Liquids, 2nd Ed., Vol. 1, p-446, John Wiley & Sons (1987).

[91] Ottino J. M., Chella R., Laminar Mixing of Polymeric Liquids; A Brief Review and Recent Theoretical Developments. Polymer Engineering and Science, Vol. 23, No7, (May 1983).

[92] Manas-Zloczower I., Tadmor Z., Mixing and Compounding of Polymers: Theory and Practice, p.175, Hanser, Munich (1994).

[93] Cheng J., Manas-Zloczower I., Hydrodynamic Analysis of a Banbury Mixer – 2-D Flow Simulations for the Entire Mixing Chamber, Polymer Engineering and Science, Mid-August, Vol.29, No. 19, p.1059-1065 (1989).

[94] Ghoreishy M. H. R., A Transient Finite Model of Mixing of Rubber Compounds in a Banbury Mixer, Iranian Polymer Journal, Vol. 5, No. 1, p. 30 – 41, (1996).

[95] Nassehi V., Salemi R., Finite Element Modelling of Non-isothermal Viscometric Flows in Rubber Mixing, Intern. Polymer Processing *IX* , No.3, p. 199-204, (1994).

[96] Harnby N., Edwards M. F., Nienow A., Mixing in the Process Industries, Butterworths Series in Chemical Engineering, p.191, (1985).

[97] Kappel M., International Chemical Engineering, Vol. 19, No.1, p. 96 (1979).

98 Metzner A. B., Otto R. E., AIChE., Vol. 3, No. 1, p. 3 (1957).

99 Kajiwara T., Negashima Y., Nakano Y., Funatsu K., Numerical Study of Twin-Screw Extruder by Three-dimensional Flow Analysis - Development of Analysis Technique and Evaluation of Mixing Performance for Full Flight Screws, Polymer Engineering and Science, Vol. 36, No. 16, p. 2142-2152, (Aug 1996).

100 Manas-Zloczower I., Feke, D. L., International Polymer Processing, Vol. 2, p.185 (1988)

101 Manas Zloczower I., Feke, D. L., Analysis of Agglomeration Rupture in Linear Flow Fields, International Polymer Processing, Vol. 4, p.3-8 (1988)

102 Elmendorp J. J., A Study of Polymer Blending Rheology, Polymer Engineering Science, Vol 26, No. 6, p. 418-427 (1986)

103 Nagata S., Yanagimoto M., Yokiyama T., Mem. Fac Eng. Kyoto Univ., 18, p. 444 (1956).

104 Hoogendorn C. J., den Hartog A. P., Chem. Eng. Sci. 22, p.1689 (1967).

105 Harnby N., Edwards M. F., Nienow A., Mixing in the Process Industries, Butterworths Series in Chemical Engineering, p.200 (1985).

106 Nagata S., Yanagimoto M., Yokiyama T., Mem. Fac Eng. Kyoto Univ., 18, p.444 (1956).

107 Hoogendorn C. J., den Hartog A. P., Chem. Eng. Sci. 22, p.1689 (1967).

108 Polyflow User's Manual, Version 3.5.0, Polyflow SA., Place de l'Universite 16, Louvain-la-Neuve, Belgium

109 Kaylon D. M. Lawal L., A non-isothermal extrusion flow of viscoplastic fluids with wall slip. International Journal of Heat and Mass Transfer, Vol. 40, No 16 pp3883-3884 (1997)

110 Kim J. K., White J. L., Non Newtonian and Non-Isothermal Modelling of 3D-Flow in an Internal mixer, Intern. Polymer Processing VI, No. 2, p.103-110 (1991).

111 White J. L., Chen Z., Simulation of Non-Isothermal Flow in Modular Co-Rotating Twin Screw Extrusion Polymer Engineering Science, Mid February 1994, Vol.34, No.3. p229-p237

112 CFX package, Version 4.2, CFX International, AEA Technology, 8.19 Harwell, Didcot, Oxfordshire, UK.

113 Al-Malaika S., Ibrahim, M. J., Rao, Scott G., Mechanisms of Antioxidant Action: Photoantioxidant Activity of Polymer-Bound Hindered Amines, Journal of Applied Polymer Science, Vol. 44, p1287-1296 (1992).

114 Al-Malaika S., Artus K., Chemical Modification of Polymer Blends by Reactive Processing: In Situ Reactions of Interlinking Agents in PS/EPDM Blends, Journal of Applied Polymer Science, Vol. 69, p.1933-1951 (1998).

[115] Griskey R. G., Polymer Process Engineering, p. 129, Chapman and Hall press (1995)

[116] Salamore J. C., Polymeric Materials Encyclopedia, Vol. 9, p. 6614, CRC press (1996)

[117] Agassant J. F., Avenas P., Sergent J., Carreau P.J., Polymer Processing – Principles and Modeling, p. 362, Oxford University press (1991)

[118] Mooney M., Journal of Rheology, Vol. 2, p. 210 (1931)

[119] Black W. B. Graham M. D., Wall Slip in Polymer-Melt Flow Instabilities, Physical Review Letters, Volume 77, Number 5, p. 956 (1996).

[120] Hatzikiririakos S.G., Dealy J.M., Journal of Rheology, Vol. 35, p. 497 (1991)

[121] Ramamurthy A.V., Journal of Rheology, Vol. 30, p.337 (1986)

[122] Hatzikiririakos S.G., Dealy J.M., Journal of Rheology, Vol. 36, p. 845 (1992)

[123] Hill D.A. Hasegawa T. Denn M.M. , Journal of Rheology, Vol.34, p. 891 (1990)

[124] Lawal A. and D. M. Kalyon. Non-isothermal extrusion flow of viscoplastic fluids with wall slip. Journal of Heat and Mass Transfer, Vol. 40, No 6, p. 3883-3897 (1997)

[125] Kaylon. D. M. Yilmazer U., Slip effects in capillary and parallel disk torsional flow of highly filled suspensions. Journal of Rheology, Vol. 50, p1169-1177 (1993)

[126] Kalyon D. M., Yaras P., Aral B., Yilmazer U., Rhelogical behaviour of a concentrated suspension: a solid rocket fuel simulant. Journal of Rheology, Vol. 37, p.35-53 (1993)

[127] Hill D. A. Wall Slip in polymer melts: A pseudo chemical model, Journal of Rheology, Vol. 42, No. 3, p. 581-601 (1998)

[128] Mhetar V. and Archer L. A., Slip in entangled polymer solutions., Macromolecules 1998, Vol. 31, No. 19, p. 6639-6649 (1998)

[129] Leger L., Hervet H., Massey G. and Durliat E. Wall Slip in Polymer melts, Journal of Physics and condensed matter, Vol. 9, p. 7719-7740 (1997).

[130] Archer L. A., Larson R. G., and Chen Y.L., Direct measurements of slip in sheared polymer solutions, Journal of Fluid Mechanics, Vol. 301, p. 133-151 (1995).

[131] Soltani F., Yilmazer U. Slip Velocity and Slip Layer Thickness in Flow of concentrated suspensions, Journal of Applied Polymer Science, Vol. 70, No 3, p. 515-522 (1998).

[132] Polyflow Version 3.5.0, Reference Manual, p8, Polyflow SA., Place de l'Universite 16, Louvain-la-Neuve, Belgium (May 1996)

[133] Polyflow Version 3.5.0, Reference Manual, p8, Polyflow SA., Place de l'Universite 16, Louvain-la-Neuve, Belgium (May 1996)

[134] Ian Jones, Head of Consultancy at CFX International, 8.19 Harwell, Oxon., Private Communication (2000).

[135] Sernas V., Karwe M.V, Jaluria Y., Chiruvella R.V., Transport in a twin screw extruder for the processing of polymers, Polymer Engineering Science, Vol.36, No. 11, p1531-1540 (1996).

[136] Cheng J., Manas-Zloczower I., Hydrodynamic Analysis of a Banbury Mixer – 2-D Flow Simulations for the Entire Mixing Chamber, Polymer Engineering and Science, Mid-August, Vol.29, No. 19, p.1059-1065 (1989).

[137] Brandao J., Spieth E, Lekakou C., Extrusion of Polypropylene. Part 1: Melt Rheology, Polymer Engineering and Science, Vol. 36, No. 1, p.49-55 (1996)

[138] Yang H. H., Manas Zloczower I., 3D Flow Field Analysis of a Banbury Mixer, Intern. Polymer Processing VII, 3, p195-p203, (1992)

[139] Nigel Wiles, CFX4 Project Manager at CFX International, 8.19 Harwell, Oxon., Private Communication (2000).

Nomenclature

Lower Case Roman Characters

a	Material element extension
a_v	Interfacial area per unit volume
c_i	Concentration of species i
c_i'	Deviation from the average concentration i.e. $c_i - \overline{c_i}$
$\overline{c_i}$	Average concentration of species i
g	Gravitational force vector
g_x	Gravitational force in x direction
g_y	Gravitational force in y direction
g_z	Gravitational force in z direction
h	Material element dimension
k	Turbulence energy
k	Thermal conductivity
k_s	Proportionality constant
l	Original material element length
m	Bird-Carreau model exponent (1-n)
n	Power law exponent
p	Pressure
q	Heat flux vector
q_x	Heat flux in x direction
q_y	Heat flux in y direction
q_z	Heat flux in z direction
r	Position vector
r_a	Point distance from axis
s	Surface area
t	Time
u_s	Wall slip velocity
v	Velocity vector
v_x	Velocity in x direction
v_y	Velocity in y direction
v_z	Velocity in z direction
x	Co-ordinate vector
y	Co-ordinate vector
z	Co-ordinate vector

Upper Case Roman Characters

$\mathbf{A}$	Model dependent tensor function for differential viscoelastic models
A	User defined variable in wall slip model
$\mathbf{B}$	Buoyancy force
B	User defined variable in wall slip model
C	User defined variable in wall slip model
C_p	Specific heat capacity at constant pressure
$\mathbf{D}$	Deformation tensor
E	Activation energy
F	Force
$\mathbf{I}$	Unit tensor
J	Striation thickness
K	Power law factor or consistence
K_p	Geometrical constant
L	Characteristic length of rotor (diameter)
N	Rotor speed
Po	Power number
R	Ideal gas constant
R(|r|)	Two point correlation function
Re	Reynolds number
S	Scale-up factor
S_i	Interfacial area
S_L	Source term for mass scalar in laminar flow equation
$\mathbf{T}$	Torque
$\mathbf{T}_e$	Differential viscolelastic (extra) stress tensor
T	Temperature
T_0	Original temperature
$\mathbf{U}$	Displacement gradient
U	Displacement in x direction
$\hat{U}$	Internal energy per unit mass.
V_{mix}	Volume of fluid being mixed
V	Displacement in y direction
W	Displacement in z direction

Lower Case Greek Characters

α	Einstein's viscosity equation constant

β	Wall slip coefficient or Navier's wall slip coefficient
β_e	Thermal expansion coefficient
$\dot{\gamma}$	Shear rate
ε	Dissipation rate of turbulence energy
ε	Strain
ζ	Constant in differential viscoelastic models
η	Viscosity for generalised non-Newonian fluids
η_e	Viscosity for extra stress component
η_D	Dispersion phase viscosity
η_L	Major liquid phase viscosity
κ	Bird-Carreau model constant
λ	Mixing index or mixing efficiency
λ_r	Relaxation time
μ	Viscosity
μ_0	Viscosity at zero shear rate
μ_∞	Viscosity at infinite shear rates
μ_a	Viscosity at an average shear rate
μ_n	Newtonian viscosity
ρ	Density
ρ_0	Original density (at T_0)
σ	Shear stress
σ_y	Yield stress
τ	Stress tensor
τ_w	Stress at the wall
ϕ	Volume fraction of dispersed phase
ω	Vorticity tensor

Upper Case Greek Characters

Φ	Mass scalar
Γ_Φ	Diffusion coefficient of minor phase 'Φ' into bulk phase

Other symbols

∇	Vector differential operator or divergence

Appendix 1. Quantification of Mixing

If the reader is interested in extending the model presented in this thesis to incorporate a mixing analyse, some useful terms are given below.

Scale of Segregation is a measure of the average separation between regions consisting of the same component and is used to characterise mixing. This statistical measure introduced by Danckwerts in 1952[i] is given by

$$\chi = \int_0^\infty R(|r|) \cdot d|r| \qquad \text{(A1-1)}$$

Where
R(|r|) is given by

$$R(|r|) = \frac{\overline{c_i(x+r) \cdot c_i(x)}}{\overline{(c_i')^2}} \qquad \text{(A1-2)}$$

Where

R(|r|)	=	two point correlation function (gives the probability that concentration fluctuations in two volume elements will be correlated)
c_i	=	concentration of species i
c_i'	=	deviation from the average concentration i.e. $c_i - \overline{c_i}$
$\overline{c_i}$	=	Average concentration of species i
r	=	position vector
x	=	co-ordinate vector

At R(0) $\overline{c_i} = 1$; and for larger values of |r|, R(|r|) $\Rightarrow$ 0 (unless long range order exists). It should therefore be noted that for lamellar or other periodic structures, R(|r|) will not decay but oscillate, exhibiting a periodic variation.

Intensity of Segregation is also used as a statistical measure[ii] and is given by

$$I = \frac{\overline{c_A'^2}}{\overline{c_A'} \cdot \overline{c_B'}} \qquad \text{(A1-3)}$$

The intensity of segregation, I, measures the deviation of the concentrations at any point in the segregated phases from the mean value. *I* does not depend on the scale of segregation but reflects the extent to which interdiffusion of components occurs. For immiscible systems *I* is always at its maximum value of 1. Conversely when *I* = 0 perfect mixing or complete homogenisation has been achieved. As diffusion proceeds the intensity decays. For regular lamellar structures *I* decays exponentially with time. For irregular lamellar structures the behaviour is more complex [iii].

Scale of Scrutiny, also referred to as the limit of resolution, is a parameter that must be defined before mixing analysis can begin. This is the smallest length scale within which concentration differences could be distinguished and is usually set not by the resolution of the measuring instrument but by the intent of the mixing process. For example, for blending colours, the scale of scrutiny corresponds to the resolving power of the eye.

These statistical measures have their limitations; they are only useful for systems with no large-scale non-uniformities and it is difficult to relate them directly to fluid mechanics[iv].

Interfacial Area has been used to characterise the mixing process

$$a_v = \lim_{v \to 0} \frac{S}{V_{mix}} \qquad \text{(A1-4)}$$

Where

a_v = interfacial area per unit volume (m^{-1})

S_i = interfacial area in given volume (V_{mix})

This parameter is inversely proportional to the striation thickness. The average striation thickness 'J', which may be correlated to the scale of segregation, is the average distance between interfaces.

$$J = \frac{2V_{mix}}{S_i} \qquad \text{(A1-5)}$$

Rate of Mixing

The mixing time, which is a useful way of comparing processing device efficiency, can be defined as the time required to produce a mixture or a product of predetermined quality. It follows that the mixing rate is defined as the rate at which mixing progresses towards a final state. The final state must, of course, be defined prior to mixing rate analysis.

The concentration of a tracer, added to a single phase miscible liquid in a stirred tank, may be measured by a suitable device at a given point. A plot of tracer concentration against time will show the mixing time. Figure 3-6 is what we might typically expect from such an experiment.

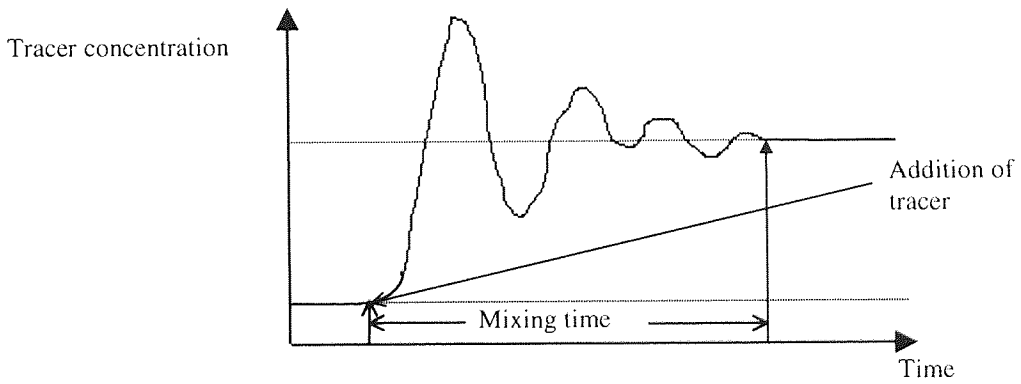

Figure A1-1 ***Mixing-time measurement curve.***

Since it is clear that mixture composition depends on the location of the detector and where the point source in introduced into the system it is desirable to record concentrations at many locations. This type of data can be manipulated by statistical means. The mixing time can be obtained if the variance of the concentration is plotted against time. The effect of various processing variables on the mixing time can be determined experimentally using this method. However, the approach to the fully mixed condition is asymptotic i.e. there is no one value of mixing time. This will inevitably lead to potentially large errors in the estimation of mixing time.

Appendix 2. Sample Data-Sheet

Run No.		Date:	
Aim / Comment:			
File Name:			

Data Specified			
Fluid Name:			
Fluid Model :	Newtonian:	Power Law:	Viscoelastic:
Model Parameters:	e.g. Factor:	Exponent (n)	
Density	g/mm^3 (	kg/m^3)@	°c
Pressure	@	co-ordinates	

Iteration Scheme	Newton Rhapson	Picard	Evolution
Max No. of Iterations			
Convergence Limit	* 10$^-$		
Av. Values included	Yes	No	
Rotor Speed			

Mesh Data						
No. of Nodes	(before merging)					
Max. Frontal Width						
No. of Active Variables						
No. of Static Variables						
Av. Frontal width						
Calculated "swap space"	Mb					
Predicted Time (s per iteration)						
Results						
Actual time taken		Iterations:		T/iteration:		
Convergence reached						
Average Values:						
Local Shear Rate (s^{-1})						
Mixing Index						
Stress Tensor						
Comments:						

Hampden RAPRA Torque Rheometer Model Units

The CAD skeleton for the Polyflow model was defined in millimetres for convenience. As a consequence the units used for the equations which describe the flow in the simulations must be converted to a consistent set as detailed in Table A2-1 [v].

Table A2-1 ***Units used for the Polyflow simulation***

	Conventional SI Units	Conversion Factor	Model Units
Length	M	* 1000	mm
Mass	Kg	* 1000	g
Time	s	* 1	s
Density	$kg\ m^{-3}$	* 0.000,001	$g\ mm^{-3}$
Viscosity	$kg\ m^{-1}\ s^{-1}$	* 1	$g\ mm^{-1}\ s^{-1}$
Viscosity (power law)	$kg\ m^{-1}\ s^{n-1}$	* 1	$g\ mm^{-1}\ s^{n-1}$
Force	$kg\ m\ s^{-2}$	* 1,000,000	$g\ mm\ s^{-2}$
Pressure	$kg\ m^{-1}\ s^{-2}$	* 1	$g\ mm^{-1}\ s^{-2}$
Torque	$kg\ m^{2}\ s^{-2}$ (N m)	* 1,000,000,000	$g\ mm^{2}\ s^{-2}$
Shear Rate	s^{-1}	* 1	s^{-1}
Shear Stress	$kg\ m^{-1}\ s^{-2}$	* 1	$g\ mm^{-1}\ s^{-2}$

Appendix 3. The Motion of the Internal Mixer

The motion of the Hampden RAPRA Torque Rheometer has been broken down into 36 separate configurations each differing by an angle of 20 degrees for the right (slower) rotor and 30 degrees for the left (faster) rotor. The patterns is repeated after the left rotor and right rotor have rotated through 1080 degrees and 720 degrees respectively. As we can see configuration 1 is identical configuration to configuration 37. Also we can observe that a pattern occurs every 19 configurations with the *bottom* of the left rotor (in configuration 19) in the place previously held by the *top* of the left rotor (in configuration 1).

Figure A3-1 ***The Motion of the Hampden RAPRA Torque Rheometer Internal Mixer***

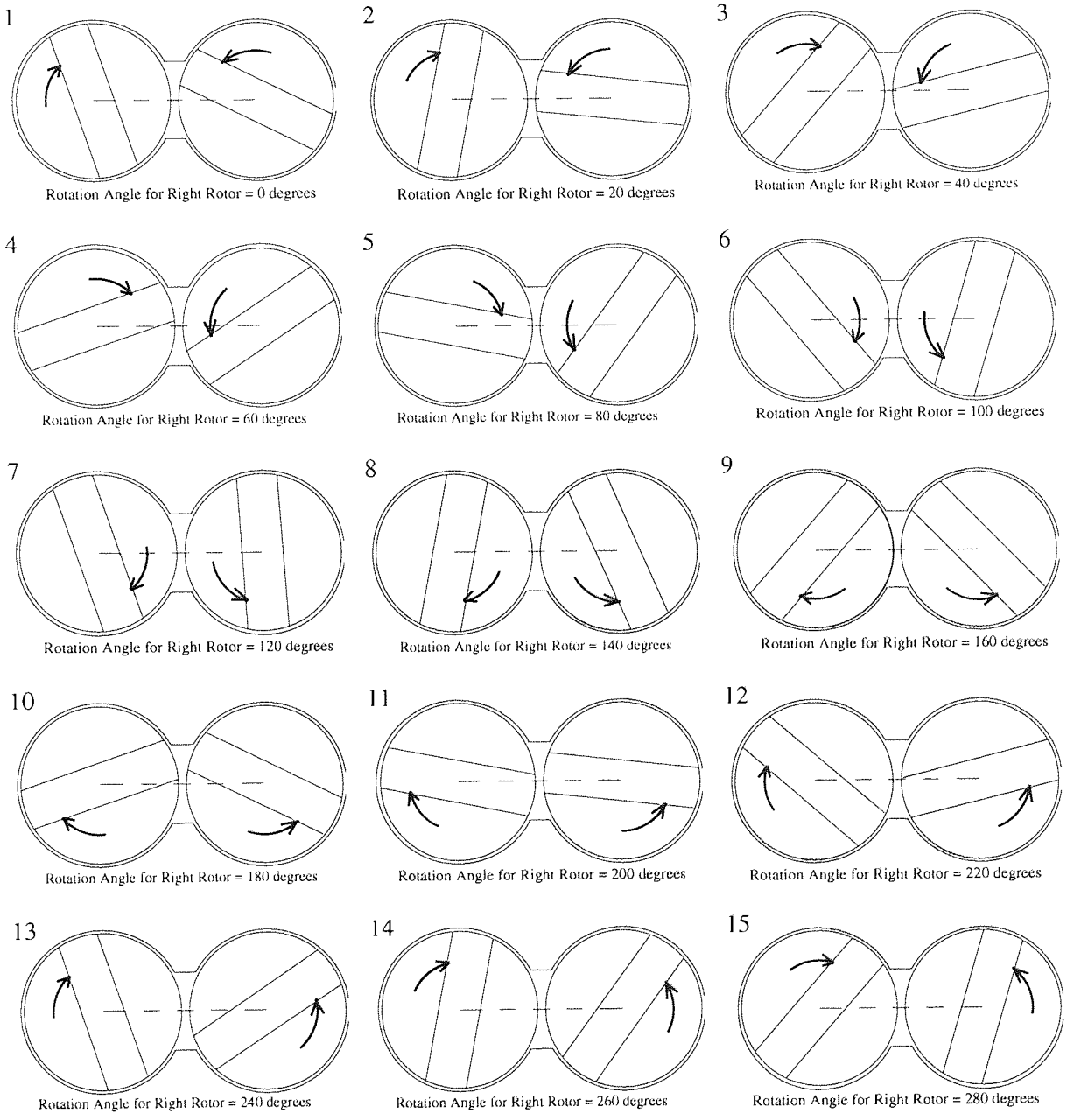

16

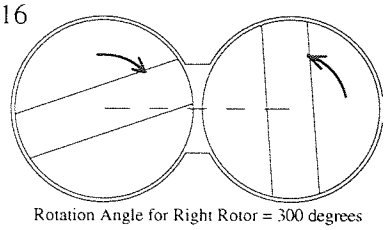

Rotation Angle for Right Rotor = 300 degrees

17

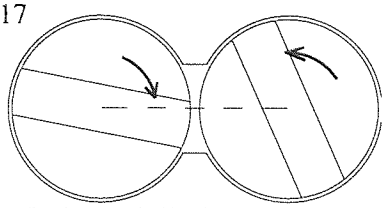

Rotation Angle for Right Rotor = 320 degrees

18

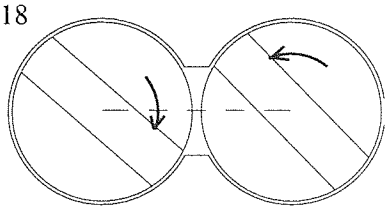

Rotation Angle for Right Rotor = 340 degrees

19

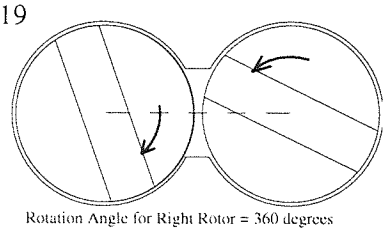

Rotation Angle for Right Rotor = 360 degrees

20

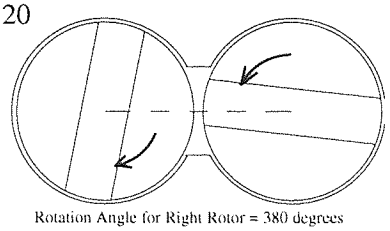

Rotation Angle for Right Rotor = 380 degrees

21

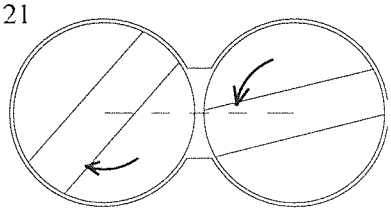

Rotation Angle for Right Rotor = 400 degrees

23

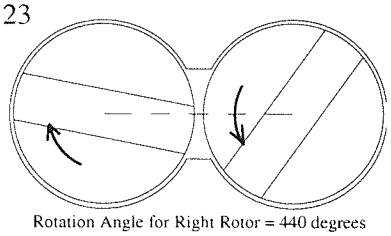

Rotation Angle for Right Rotor = 440 degrees

22

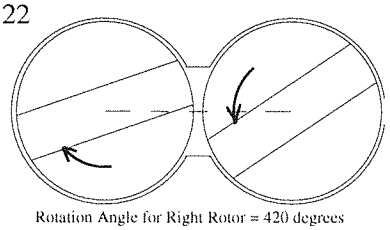

Rotation Angle for Right Rotor = 420 degrees

24

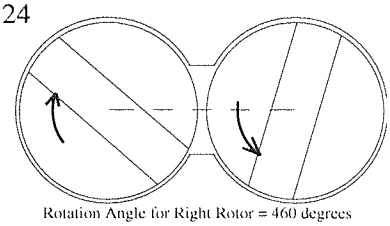

Rotation Angle for Right Rotor = 460 degrees

25

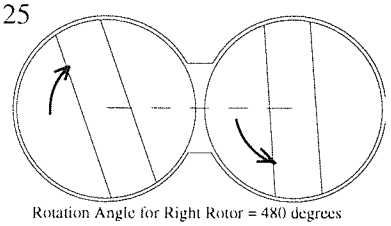

Rotation Angle for Right Rotor = 480 degrees

26

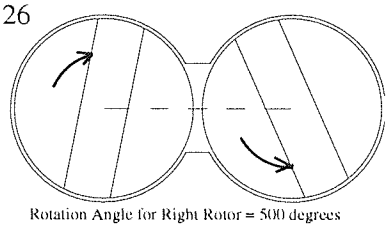

Rotation Angle for Right Rotor = 500 degrees

27

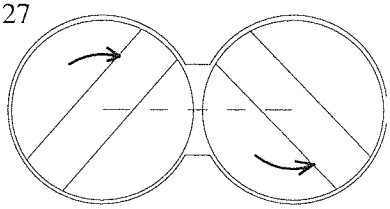

Rotation Angle for Right Rotor = 520 degrees

28

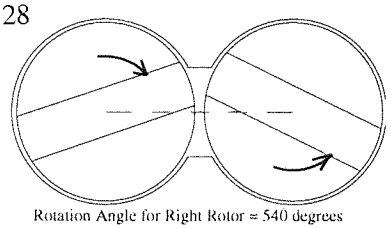

Rotation Angle for Right Rotor = 540 degrees

29

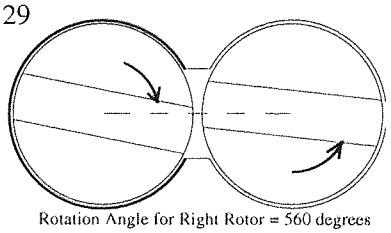

Rotation Angle for Right Rotor = 560 degrees

30

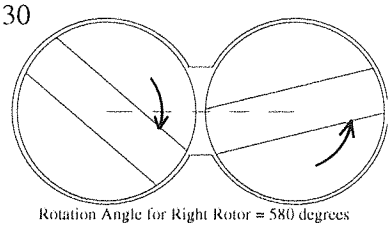

Rotation Angle for Right Rotor = 580 degrees

31

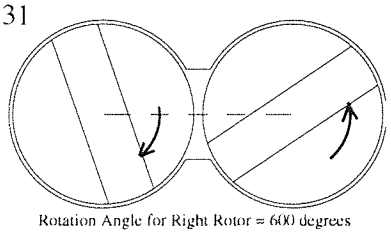

Rotation Angle for Right Rotor = 600 degrees

32

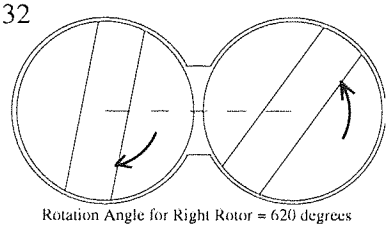

Rotation Angle for Right Rotor = 620 degrees

33

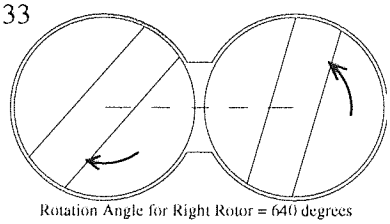

Rotation Angle for Right Rotor = 640 degrees

34

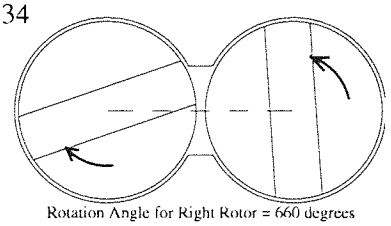

Rotation Angle for Right Rotor = 660 degrees

35

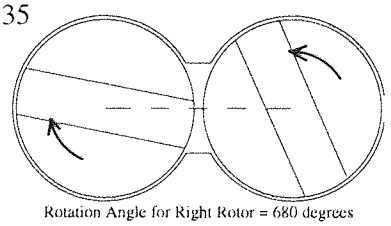

Rotation Angle for Right Rotor = 680 degrees

36

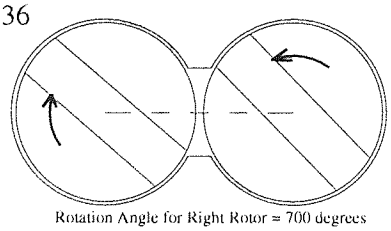

Rotation Angle for Right Rotor = 700 degrees

37

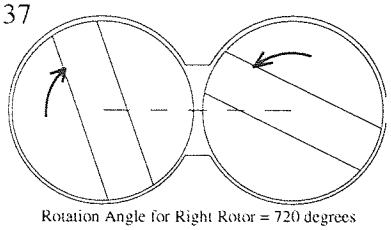

Rotation Angle for Right Rotor = 720 degrees

Appendix 4. Mesh Optimisation Data

Table A4-1 *Mesh size and its affect on swap space and CPU requirement for the three rotor configurations*

Rotor Configuration1		
Mesh Size (Nodes)	Swap Space (Mb)	Predicted Time per Iteration (mins)
714	88.2	1.8
933	148.6	3.2
1645	330.6	7.6
2394	801.9	19.0
2898	942.3	22.4
3744	1529.4	36.6
4151	2034.3	48.8
4500	2154.9	52.6
4684	2241.9	53.9
5400	3471.1	83.6

Rotor Configuration2				
Mesh Size (Nodes)	Swap Space (Mb)	Predicted Time per Iteration (mins)	Actual Time (min per iteration)	
			real	user
2325	585.6	13.8	36.93	27.38
3066	895.4	21.3	55.06	45.42
4390	1600.8	38.4	145.63	115.86
5060	1966.7	47.2	155.23	138.01
5300	2254.0	52.8	179.87	162.10
5595	2461.9	59.2	252.42	213.97

Rotor Configuration3		
Mesh Size (Nodes)	Swap Space (Mb)	Predicted Time per Iteration (mins)
1914	301.3	6.9
2601	576.9	13.6
3509	970.9	22.6
4123	1308.4	30.4
4548	1583.6	37.9

(n=1.0, K=3000, low rotor speed)

Note: The swap space requirement of a particular flow problem is directly proportional the total number of variables and the maximum frontal width. The CPU demand is directly proportional the total number of variables, the maximum frontal width and a constant relating to the specific speed of a computer.

Table A4-2 *Mesh size and its affect on average parameter values for the three Rotor Configurations*

Rotor Configuration 1		
No. of Nodes	Shear Rate(1/s)	Mixing Index
714	16.1990	0.52940
933	13.1018	0.52799
1645	12.8883	0.52072
2394	12.4596	0.52584
2898	12.2816	0.52263
3744	12.3335	0.52210
4151	12.0777	0.52409
4500	12.0760	0.52320
4684	12.0750	0.52316

Rotor Configuration 2		
No. of Nodes	Shear Rate(1/s)	Mixing Index
2325	12.1733	0.52301
3066	11.9631	0.52323
4390	11.9184	0.52222
5060	11.9008	0.52192
5300	11.8401	0.52201
5595	11.8180	0.52235

Rotor Configuration 3		
No. of Nodes	Shear Rate(1/s)	Mixing Index
1914	12.4226	0.51911
2601	12.3837	0.51857
3509	12.1001	0.51867
4123	12.0795	0.51897
4548	12.0775	0.51897

(n=1.0, K=3000, low rotor speed)

Appendix 5. Determination of the Rheological Properties

The experimental trials for quantitatively assessing the 'x' and 'y' components of the velocity vectors in the Hampden RAPRA Torque Rheometer domain used a completely transparent and bubble free viscous gel – 'Boots' own lubricating gel. The data obtained from a recently calibrated Haake viscometer (Table A5-1) was plotted on a $\log_{10}$ /$\log_{10}$ scale (Figure A5-1) and the equation of the trendline (power type) was calculated. We can see that the trendline gives reasonable fit over a shear rate range of 0 – 6000. However, when we consider a shear rate range more suitable an internal mixer, as cited in the literature and calculated using the simulation and by hand, the opportunity to truncate the shear rate range to an appropriate value of 1.0 - 130s^{-1} is presented. If the fit of the trendline of the new plot, Figure A5-2, is examined a great improvement is seen. The power law factor is calculated to be **54.57** and the value of 'n' is **0.4114** for the clear gel over a shear range of 1.0 – 130s^{-1}.

A similar graph for 'Coloured Clay' is presented (Figure A5-3). The power law factor is calculated to be **1933.5** and the value of 'n' is **0.3585**.

Table A5-1 ***Viscosity and shear rate data for the 'Clear Gel' obtained from the Haake Viscometer***

Viscosity	Shear Rate	Viscosity
mPa s	s^{-1}	g/mm s
14674	10	14.674
7630	25	7.63
6236	40	6.236
4559	70	4.559
3146	130	3.146
1520	281	1.52
930	507	0.93
673	732	0.673
502	1018	0.502
411	1304	0.411
355	1605	0.355
326	1801	0.326
260	2267	0.26
215	2824	0.215
197	3335	0.197
175	3907	0.175
144	4629	0.144
134	5397	0.134
114	6059	0.114

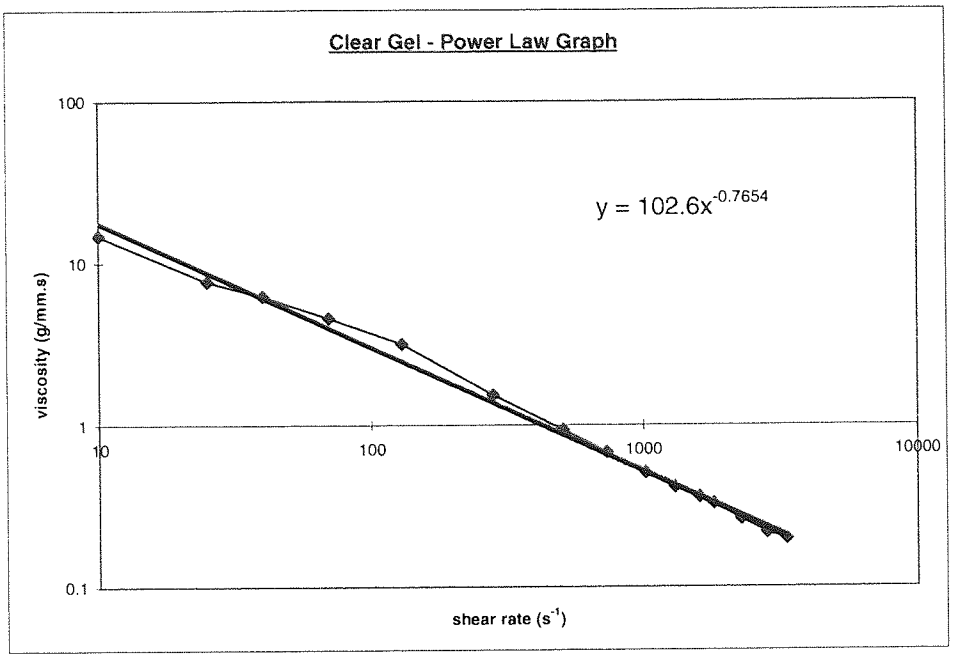

Figure A5-1 *A graph to calculate the power law constants for the 'Clear Gel' over shear rate range of 1.0 – 6000 s^{-1}*

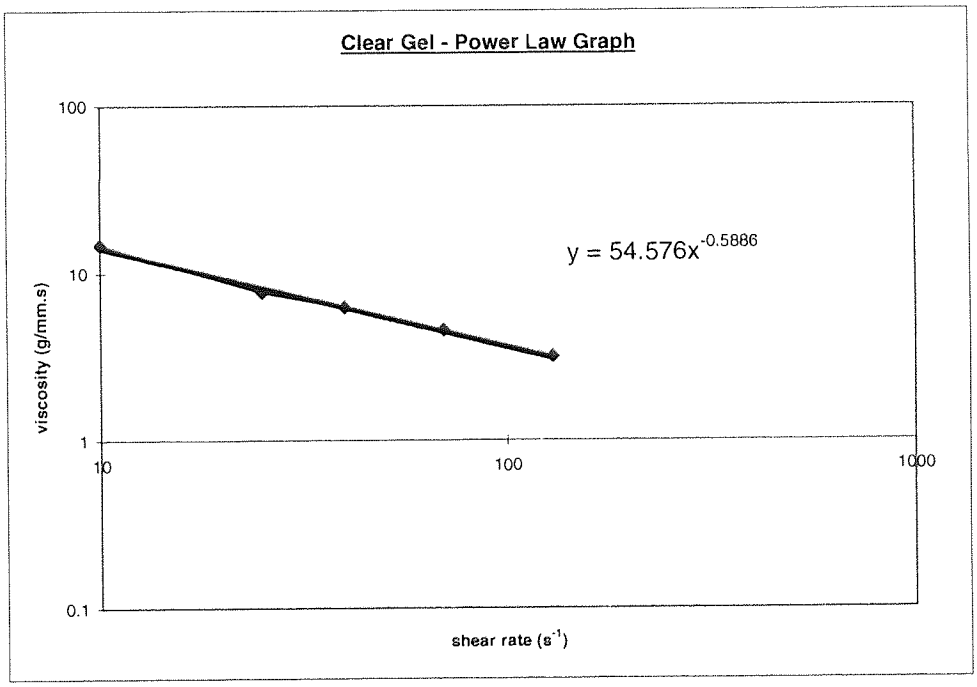

Figure A5-2 *A graph to calculate the power law constants for the 'Clear Gel' over shear rate range of 1.0 – 130 s^{-1}*

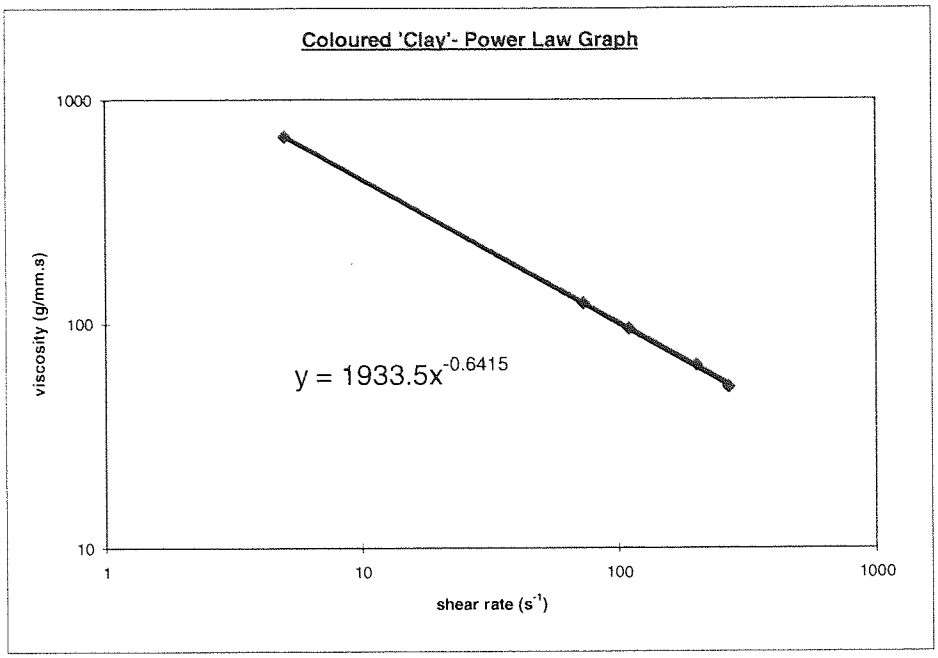

Figure A5-3 ***A graph to calculate the power law constants for the 'Coloured Clay'***

Appendix 6. Viscoelastic - Shear and Normal Stress Data

Differential models
The general form of differential models is written in the form

$$\mathbf{A}(T_e,\lambda_r)\cdot\mathbf{T}_e+\lambda_r(\dot{\gamma},T)\frac{\delta\mathbf{T}_e}{\delta t}=2\eta_e(\dot{\gamma},T)\mathbf{D} \qquad \text{(A6-1)}$$

where the λ_r is the relaxation time and η_e is the viscosity coefficient.

$$\frac{\delta\mathbf{T}_e}{\delta t}=\frac{\zeta}{2}\overset{\Delta}{\mathbf{T}}_e+\left(1-\frac{\zeta}{2}\right)\overset{\nabla}{\mathbf{T}}_e \qquad \text{(A6-2)}$$

The lower and upper convected derivative of the extra-stress is given by (A6-3) and (A6-4) respectively.

$$\overset{\Delta}{\mathbf{T}}_e=\frac{D\mathbf{T}_e}{Dt}+\mathbf{T}_e\cdot\nabla\mathbf{v}^T+\nabla\mathbf{v}\cdot\mathbf{T}_e \qquad \text{(A6-3)}$$

$$\overset{\nabla}{\mathbf{T}}_e=\frac{D\mathbf{T}_e}{Dt}+\mathbf{T}_e\cdot\nabla\mathbf{v}^T-\nabla\mathbf{v}\cdot\mathbf{T}_e \qquad \text{(A6-4)}$$

The simplest differential viscoelastic model is the upper convected Maxwell (**A**=unit tensor (**I**) and ζ =2) model which is given by:

$$\mathbf{T}_e+\lambda_r\overset{\nabla}{\mathbf{T}}_e=2\eta_e\mathbf{D} \qquad \text{(A6-5)}$$

The Oldroyd-B involves the same equation for the extra stress tensor but includes the shear stress tensor. The White Metzner involves the same equation for the extra stress tensor again but the shear stress tensor is included however, this time, represented by the power law or Bird-Carreau law since both the relaxation time and the viscosity coefficient can be a function of shear rate and temperature.

Viscometric data indicate that suitable data for ζ lie between 0 and 0.2[vi] and values of λ range from 0.01 – 1.0[vii]

Two, more complicated models, are the Phan Thein Tanner and the Giesekus, respectively defined by

$$\mathbf{A}=\exp\left[\frac{\varepsilon\lambda_r}{\eta_e}\mathrm{trace}(\mathbf{T}_e)\right]\mathbf{I} \qquad (0\le\zeta\le2) \qquad \text{(A6-6)}$$

$$\mathbf{A}=\mathbf{I}+\frac{\alpha\lambda_r}{\eta_e}\mathbf{T}_e \qquad (\zeta=0) \qquad \text{(A6-7)}$$

where ε and α are dimensionless material parameters

Table A6-1 *Total and extra stress components for the viscoelastic investigation for different rotor speeds*

		Point1		Point2		Point 3		Point4	
Speed		Extra stress	Total Stress	Extra stress	Total Stress	Extra stress	Total Stress	Extra stress	Total Stress
(rad/s)	xx	1.6700E-06	7.6200E-03	6.8400E-06	2.5384E-01	1.8600E-04	5.4731E-01	1.5144E-06	-9.6500E-02
0.000015	yy	4.2700E-06	-4.7000E-02	7.3900E-06	-2.3800E-01	1.5100E-05	-4.3700E-01	3.5000E-06	1.6600E-01
	zz	5.5890E-07	5.5500E-02	1.6000E-06	4.9500E-02	-2.3180E-07	1.2800E-03	-3.0400E-07	-3.3900E-02
	xy	-4.3300E-06	6.9300E-02	-8.3000E-06	-3.4400E-02	-4.8300E-05	7.5100E-01	1.8700E-06	-2.5000E-02
	yz	1.1600E-03	1.1600E-02	-3.5300E-07	1.1610E-03	2.6800E-06	1.5600E-02	4.3500E-07	-1.2000E-02
	zx	2.6300E-07	1.6300E-02	-4.4700E-03	-4.4700E-03	5.7400E-07	6.8900E-03	-1.9600E-07	-1.5900E-01
	Scalar*	2.3200E-03	1.9129E-01	8.9400E-03	6.0921E-01	2.7108E-04	1.9278E+00	6.0513E-06	4.6582E-01
		Point1		Point2		Point 3		Point4	
Speed		Extra stress	Total Stress	Extra stress	Total Stress	Extra stress	Total Stress	Extra stress	Total Stress
(rad/s)	xx	-1.6930E-02	7.4511E-01	6.9090E-02	2.5480E+01	1.8632E+00	4.7578E+01	1.5180E-02	-9.6410E+00
0.0015	yy	4.1950E-02	-4.6628E+00	7.3940E-02	-2.3766E+01	1.5048E-01	-4.3533E+01	3.5020E-02	1.6666E+01
	zz	5.3700E-03	5.5580E+00	1.5900E-02	4.9614E+00	-2.2000E-03	1.2189E-01	3.0200E-03	-3.3954E+00
	xy	-4.3000E-02	6.8866E+00	-8.2800E-02	-3.5200E+00	-4.8196E-01	7.4671E+01	1.8800E-02	-2.4838E+00
	yz	-1.1210E-02	1.1528E+00	-3.4700E-03	1.5551E-01	2.7840E-02	1.5838E+00	4.3600E-03	-1.1959E+00
	zx	2.5800E-03	1.6403E+00	-1.4900E-03	4.4276E-01	5.2200E-03	6.9737E-01	-1.9700E-03	-1.5929E+00
	Scalar*	1.1501E-01	1.9043E+01	1.8358E-01	6.1007E+01	2.7145E+00	1.8648E+02	5.5415E-02	3.4264E+01
		Point1		Point2		Point 3		Point4	
Speed		Extra stress	Total Stress	Extra stress	Total Stress	Extra stress	Total Stress	Extra stress	Total Stress
(rad/s)	xx	-1.6738E+00	5.9392E+00	7.6343E+00	2.5929E+02	1.8911E+02	6.5483E+02	1.5577E+00	-9.5138E+01
0.015	yy	3.5984E+00	-4.3709E+01	7.4871E+00	-2.3084E+02	1.4878E+01	-4.2168E+02	3.5420E+00	1.7046E+02
	zz	3.4800E-01	5.6295E+01	1.4468E+00	5.0595E+01	-7.9900E-02	7.9700E-01	-2.7770E-01	-3.3954E+01
	xy	-4.0733E+00	6.5372E+01	-8.1476E+00	-4.2725E+01	-4.7744E+01	7.0296E+02	1.9715E+00	-2.3487E+01
	yz	-1.0915E+00	1.0655E+01	-3.1580E-01	1.0460E+00	3.6841E+00	1.8862E+01	4.4553E-01	-1.1800E+01
	zx	2.1100E-01	1.6831E+01	-1.8800E-01	-4.1299E+00	6.1200E-02	7.2252E+00	-1.9900E-01	-1.6241E+01
	Scalar*	1.0666E+01	1.8353E+02	1.8463E+01	6.0857E+02	2.7486E+02	1.9348E+03	6.1964E+00	3.4625E+02
		Point1		Point2		Point 3		Point4	
Speed		Extra stress	Total Stress	Extra stress	Total Stress	Extra stress	Total Stress	Extra stress	Total Stress
(rad/s)	xx	-3.8512E+01	2.5989E+00	3.1047E+02	1.5327E+03	5.2272E+03	7.4091E+03	4.7276E+01	-4.4626E+02
0.075	yy	4.9270E+01	1.9326E+02	1.9699E+02	-9.8475E+02	3.0861E+02	1.7954E+03	9.6153E+01	9.5970E+02
	zz	-6.6497E+00	2.7538E+02	2.0659E+01	2.6273E+02	1.6449E+01	1.5197E+01	-2.3017E+00	-1.6397E+02
	xy	4.9279E+01	2.6824E+02	-2.0607E+02	-3.8082E+02	-1.1381E+03	2.4443E+03	6.6204E+01	-7.4766E+01
	yz	-2.3313E+01	3.7522E+01	-8.3670E+00	-3.6820E+00	1.9429E+02	2.6442E+02	1.2873E+01	-5.6155E+01
	zx	1.3775E+00	8.6378E+01	-6.8648E-01	-1.4658E+01	-3.9675E+01	1.5012E+01	-2.0323E+00	-8.8220E+01
	Scalar*	1.5409E+02	6.6393E+02	5.4599E+02	3.1761E+03	7.5344E+03	1.0655E+04	1.8097E+02	1.8399E+03
		Point1		Point2		Point 3		Point4	
Speed		Extra stress	Total Stress	Extra stress	Total Stress	Extra stress	Total Stress	Extra stress	Total Stress
(rad/s)	xx	-6.0258E+01	-3.6500E+00	6.0600E+02	2.2100E+03	1.0346E+04	1.3147E+04	9.4370E+01	-4.5900E+02
0.1	yy	7.4371E+01	-2.5600E+02	3.3800E+02	-1.2064E+03	6.8500E+02	-2.2060E+03	1.8585E+02	1.3704E+03
	zz	1.7998E+01	3.5800E+02	2.6970E+01	3.4706E+02	3.1210E+01	4.4580E+01	5.6100E-01	-2.1100E+02
	xy	1.2705E+02	3.3500E+02	-3.6710E+02	-5.8000E+02	-1.9935E+03	2.6010E+03	1.3722E+02	-5.6770E+01
	yz	3.8200E+01	4.4400E+01	-1.7900E+01	-1.0500E+01	5.2000E+02	6.2500E+02	2.4880E+01	-7.7900E+01
	zx	5.9990E-01	1.1500E+02	3.0477E+00	-1.4600E+01	-1.0598E+02	-8.7600E+01	4.6500E+00	-1.1448E+02
	Scalar*	3.1278E+02	1.0398E+03	1.0219E+03	4.3477E+03	1.4737E+04	2.1003E+04	3.5970E+02	2.4493E+03

Speed (rad/s)	Extra stress	Total Stress	Extra stress (%)	Extra stress	Total Stress	Extra stress (%)
0.000015	0.002320021	0.191293097	1.212809534	0.008940019	0.609214245	1.467467142
0.0015	0.115010968	19.04339305	0.603941576	0.183580348	61.00706447	0.300916541
0.015	10.66583466	183.5279672	5.811558219	18.46256047	608.5738101	3.033742196
0.075	154.0878849	663.9291168	23.20848431	545.9921723	3176.120884	17.190535
0.1	312.7828484	1039.784922	30.08149489	1021.864881	4347.685202	23.50365387

Speed (rad/s)	Extra stress	Total Stress	Extra stress (%)	Extra stress	Total Stress	Extra stress (%)
0.000015	0.000271083	1.927763373	0.014062026	6.05126E-06	0.465816509	0.001299066
0.0015	2.714485468	186.4781532	1.455658704	0.055414919	34.26437037	0.161727526
0.015	274.8593509	1934.779092	14.20623946	6.196392262	346.2516698	1.789563142
0.075	7534.43702	10655.10879	70.71196707	180.9734936	1839.874923	9.836184586
0.1	14737.02654	21002.55052	70.16779474	359.6951398	2449.264143	14.68584517

$$(4*((xy)^2 + (yz)^2 + (zx)^2) + (xx - yy)^2 + (yy - zz)^2 + (zz - xx)^2)^0.5$$

Appendix 7. FORTRAN Torque Programme

The FORTRAN programme written to calculate the torque for the area of a specific rotor in the CFX simulation.

```
C   WRITTEN BY ALAN HARRIES ON 1.3.99
C
SUBROUTINE USRTRN(U,V,W,P,VFRAC,DEN,VIS,TE,ED,RS,T,H,RF,SCAL,
     +                  XP,YP,ZP,VOL,AREA,VPOR,ARPOR,WFACT,CONV,IPT,
     +                  IBLK,IPVERT,IPNODN,IPFACN,IPNODF,IPNODB,IPFACB,
     +                  WORK,IWORK,CWORK)
C
C***********************************************************************
C
C   USER SUBROUTINE TO ALLOW USERS TO MODIFY OR MONITOR THE SOLUTION AT
C   THE END OF EACH TIME STEP
C   THIS SUBROUTINE IS CALLED BEFORE THE START OF THE RUN AS WELL AS AT
C   THE END OF EACH TIME STEP
C
C   >>> IMPORTANT                                                    <<<
C   >>>                                                             <<<
C   >>> USERS MAY ONLY ADD OR ALTER PARTS OF THE SUBROUTINE WITHIN  <<<
C   >>> THE DESIGNATED USER AREAS                                   <<<
C
C***********************************************************************
C
C   THIS SUBROUTINE IS CALLED BY THE FOLLOWING SUBROUTINES
C      CUSR  TRNMOD
C
C***********************************************************************
C   CREATED
C      27/04/90  ADB
C   MODIFIED
C      05/08/91  IRH  NEW STRUCTURE
C      01/10/91  DSC  REDUCE COMMENT LINE GOING OVER COLUMN 72.
C      29/11/91  PHA  UPDATE CALLED BY COMMENT, ADD RF ARGUMENT,
C                     CHANGE LAST DIMENSION OF RS TO 6 AND IVERS TO 2
C      05/06/92  PHA  ADD PRECISION FLAG AND CHANGE IVERS TO 3
C      03/07/92  DSC  CORRECT COMMON MLTGRD.
C      23/11/93  CSH  EXPLICITLY DIMENSION IPVERT ETC.
C      03/02/94  PHA  CHANGE FLOW3D TO CFDS-FLOW3D
C      22/08/94  NSW  MOVE 'IF(IUSED.EQ.0) RETURN' OUT OF USER AREA
C      19/12/94  NSW  CHANGE FOR CFX-F3D
C      02/07/97  NSW  UPDATE FOR CFX-4
C
C***********************************************************************
C
C   SUBROUTINE ARGUMENTS
C
C     U       - U COMPONENT OF VELOCITY
C     V       - V COMPONENT OF VELOCITY
C     W       - W COMPONENT OF VELOCITY
C     P       - PRESSURE
C     VFRAC   - VOLUME FRACTION
C     DEN     - DENSITY OF FLUID
C     VIS     - VISCOSITY OF FLUID
C     TE      - TURBULENT KINETIC ENERGY
C     ED      - EPSILON
C     RS      - REYNOLD STRESSES
C     T       - TEMPERATURE
C     H       - ENTHALPY
C     RF      - REYNOLD FLUXES
C     SCAL    - SCALARS (THE FIRST 'NCONC' OF THESE ARE MASS FRACTIONS)
C     XP      - X COORDINATES OF CELL CENTRES
C     YP      - Y COORDINATES OF CELL CENTRES
C     ZP      - Z COORDINATES OF CELL CENTRES
C     VOL     - VOLUME OF CELLS
C     AREA    - AREA OF CELLS
C     VPOR    - POROUS VOLUME
C     ARPOR   - POROUS AREA
C     WFACT   - WEIGHT FACTORS
C     CONV    - CONVECTION COEFFICIENTS
```

```
C
C      IPT     - 1D POINTER ARRAY
C      IBLK    - BLOCK SIZE INFORMATION
C      IPVERT  - POINTER FROM CELL CENTERS TO 8 NEIGHBOURING VERTICES
C      IPNODN  - POINTER FROM CELL CENTERS TO 6 NEIGHBOURING CELLS
C      IPFACN  - POINTER FROM CELL CENTERS TO 6 NEIGHBOURING FACES
C      IPNODF  - POINTER FROM CELL FACES TO 2 NEIGHBOURING CELL CENTERS
C      IPNODB  - POINTER FROM BOUNDARY CENTERS TO CELL CENTERS
C      IPFACB  - POINTER FROM BOUNDARY CENTERS TO BOUNDARY FACESS
C
C      WORK    - REAL WORKSPACE ARRAY
C      IWORK   - INTEGER WORKSPACE ARRAY
C      CWORK   - CHARACTER WORKSPACE ARRAY
C
C    SUBROUTINE ARGUMENTS PRECEDED WITH A '*' ARE ARGUMENTS THAT MUST
C    BE SET  BY THE USER IN THIS ROUTINE.
C
C    NOTE THAT OTHER DATA MAY BE OBTAINED FROM CFX-4 USING THE
C    ROUTINE GETADD, FOR FURTHER DETAILS SEE THE VERSION 4
C    USER MANUAL.
C***********************************************************************
C
C
       LOGICAL LDEN,LVIS,LTURB,LTEMP,LBUOY,LSCAL,LCOMP
      +        ,LRECT,LCYN,LAXIS,LPOROS,LTRANS
C
       CHARACTER*(*) CWORK
C
C+++++++++++++++++ USER AREA 1 ++++++++++++++++++++++++++++++++++++++++
C---- AREA FOR USERS EXPLICITLY DECLARED VARIABLES
C
C+++++++++++++++++ END OF USER AREA 1 ++++++++++++++++++++++++++++++++++
C
       COMMON
      + /ALL/     NBLOCK,NCELL,NBDRY,NNODE,NFACE,NVERT,NDIM
      + /ALLWRK/ NRWS,NIWS,NCWS,IWRFRE,IWIFRE,IWCFRE
      + /ADDIMS/ NPHASE,NSCAL,NVAR,NPROP
      +          ,NDVAR,NDPROP,NDXNN,NDGEOM,NDCOEF,NILIST,NRLIST,NTOPOL
      + /CHKUSR/ IVERS,IUCALL,IUSED
      + /CONC/    NCONC
      + /DEVICE/ NREAD,NWRITE,NRDISK,NWDISK
      + /IDUM/    ILEN,JLEN
      + /LOGIC/   LDEN,LVIS,LTURB,LTEMP,LBUOY,LSCAL,LCOMP
      +          ,LRECT,LCYN,LAXIS,LPOROS,LTRANS
      + /MLTGRD/ MLEVEL,NLEVEL,ILEVEL
      + /SGLDBL/ IFLGPR,ICHKPR
      + /SPARM/   SMALL,SORMAX,NITER,INDPRI,MAXIT,NODREF,NODMON
      + /TIMUSR/ DTUSR
      + /TRANSI/ NSTEP,KSTEP,MF,INCORE
      + /TRANSR/ TIME,DT,DTINVF,TPARM
C+++++++++++++++++ USER AREA 2 ++++++++++++++++++++++++++++++++++++++++
C---- AREA FOR USERS TO DECLARE THEIR OWN COMMON BLOCKS
C      THESE SHOULD START WITH THE CHARACTERS 'UC' TO ENSURE
C      NO CONFLICT WITH NON-USER COMMON BLOCKS
C+++++++++++++++++ END OF USER AREA 2 ++++++++++++++++++++++++++++++++++
C
       DIMENSION
      + U(NNODE,NPHASE),V(NNODE,NPHASE),W(NNODE,NPHASE),P(NNODE,NPHASE)
      +,VFRAC(NNODE,NPHASE),DEN(NNODE,NPHASE),VIS(NNODE,NPHASE)
      +,TE(NNODE,NPHASE),ED(NNODE,NPHASE),RS(NNODE,NPHASE,6)
      +,T(NNODE,NPHASE),H(NNODE,NPHASE),RF(NNODE,NPHASE,4)
      +,SCAL(NNODE,NPHASE,NSCAL)
       DIMENSION
      + XP(NNODE),YP(NNODE),ZP(NNODE)
      +,VOL(NCELL),AREA(NFACE,3),VPOR(NCELL),ARPOR(NFACE,3)
      +,WFACT(NFACE),CONV(NFACE,NPHASE)
      +,IPT(*),IBLK(5,NBLOCK)
      +,IPVERT(NCELL,8),IPNODN(NCELL,6),IPFACN(NCELL,6),IPNODF(NFACE,4)
      +,IPNODB(NBDRY,4),IPFACB(NBDRY)
      +,IWORK(*),WORK(*),CWORK(*)
C
C+++++++++++++++++ USER AREA 3 ++++++++++++++++++++++++++++++++++++++++
C---- AREA FOR USERS TO DIMENSION THEIR ARRAYS
```

```
       DIMENSION ALP(3),ALS(3),TOR(3)
C---- AREA FOR USERS TO DEFINE DATA STATEMENTS
C+++++++++++++++++ END OF USER AREA 3 +++++++++++++++++++++++++++++++++++
C---- STATEMENT FUNCTION FOR ADDRESSING
      IP(I,J,K)=IPT((K-1)*ILEN*JLEN+(J-1)*ILEN+I)
C----VERSION NUMBER OF USER ROUTINE AND PRECISION FLAG
      IVERS=3
      ICHKPR = 1
C+++++++++++++++++ USER AREA 4 +++++++++++++++++++++++++++++++++++++++++
C---- TO USE THIS USER ROUTINE FIRST SET IUSED=1
       IUSED=1
C+++++++++++++++++ END OF USER AREA 4 +++++++++++++++++++++++++++++++++++
       IF (IUSED.EQ.0) RETURN
C---- FRONTEND CHECKING OF USER ROUTINE
       IF (IUCALL.EQ.0) RETURN
C+++++++++++++++++ USER AREA 5 +++++++++++++++++++++++++++++++++++++++++
C---- EXAMPLE (SET TIME INCREMENT FOR NEXT TIME STEP)
C     DTUSR = 0.1
C----END OF EXAMPLE
C+++++++++++++++++ END OF USER AREA 5 +++++++++++++++++++++++++++++++++++
C
      open (unit=9,file='results.out',status='unknown')
C
      CALL IPALL('WALLLEFT1','WALL','PATCH','CENTRES',
     +IPT,NPT,CWORK,IWORK)
C
C     LOOP OVER ALL INTERIOR CELLS
      DO 100 I=1,NPT
C
C     USE ARRAY IPT TO GET ADDRESS
         INODE=IPT(I)

      UCMODULUS = (AREA(NPT,1)**2 + AREA(NPT,2)**2
     @ + AREA(NPT,3)**2)**0.5
C
           ALP(1) = YP(INODE)*P(INODE,NPHASE)*AREA(NPT,3) -
     *       ZP(INODE)*P(INODE,NPHASE)*AREA(NPT,2)
           ALP(2) = ZP(INODE)*P(INODE,NPHASE)*AREA(NPT,1) -
     >       XP(INODE)*P(INODE,NPHASE)*AREA(NPT,3)
           ALP(3) = XP(INODE)*P(INODE,NPHASE)*AREA(NPT,2) -
     %      YP(INODE)*P(INODE,NPHASE)*AREA(NPT,1)
C
           ALS(1) = (YP(INODE)*SCAL(INODE,NPHASE,3)-ZP(INODE)
     <       *SCAL(INODE,NPHASE,2))*UCMODULUS
           ALS(2) = (ZP(INODE)*SCAL(INODE,NPHASE,1)-XP(INODE)
     $      *SCAL(INODE,NPHASE,3))*UCMODULUS
           ALS(3) = (XP(INODE)*SCAL(INODE,NPHASE,2)-YP(INODE)
     ^      *SCAL(INODE,NPHASE,1))*UCMODULUS
C
           TOR(1)= ALP(1)+ALS(1)
           TOR(2)= ALP(2)+ALS(2)
           TOR(3)= ALP(3)+ALS(3)
           SCAL(INODE,NPHASE,4)=(TOR(1)**2+TOR(2)**2+TOR(3)
     @     **2)**0.5
C
C
 100   CONTINUE
C
            TSUM=0.0
C
          DO 200 I=1,NPT
             INODE=IPT(I)
             TSUM=TSUM+SCAL(INODE,NPHASE,4)
C
 200   CONTINUE
              write(9,111)TSUM
C             write(6,*)'total torque',TSUM
 111      format(1h,'total torque = ',d23.16)
C
C+++++++++++++++++ END OF USER AREA 5 +++++++++++++++++++++++++++++++++++
      RETURN
C
      END
```

Appendix 8. Simulation Command File

A general CFX command file for the transient – sliding mesh simulation

```
>>CFX4
 >>SET LIMITS
 TOTAL CHARACTER WORK SPACE 13000
 >>OPTIONS
  user scalar equations 5
   UNMATCHED GRIDS
   CARTESIAN COORDINATES
   NON NEWTONIAN FLOW
   LAMINAR FLOW
   INCOMPRESSIBLE FLOW
/*  HEAT TRANSFER*/
   TRANSIENT FLOW
   TRANSIENT GRID
 /* VISCOUS HEATING*/
  >>VARIABLE NAMES
   USER SCALAR1 'SHEAR RATE'
 /*  USER SCALAR2 'X SHEAR STRESS'
     USER SCALAR3 'Y SHEAR STRESS'
    USER SCALAR4 'Z SHEAR STRESS'*/
    USER SCALAR2 'xy nodal shear stress'
    USER SCALAR3 'yz nodal shear stress'
    USER SCALAR4 'zx nodal shear stress'
    USER SCALAR5 'z mass flux'
>>MODEL TOPOLOGY
 >>GLUE PATCHES FOR UNMATCHED GRIDS
   FIRST PATCH NAMES 'BLKBDYLEFTSIDE1'
   SECOND PATCH NAMES 'BLKBDYLEFTSIDE2'
 >>GLUE PATCHES FOR UNMATCHED GRIDS
   FIRST PATCH NAMES 'BLKBDYRIGHTSIDE1'
   SECOND PATCH NAMES 'BLKBDYRIGHTSIDE2'
>>MODEL DATA
 >>SET INITIAL GUESS
  /* >>INPUT FROM FILE*/
   /*  READ DUMP FILE*/
   /* TIME STEP 7*/
 >>PHYSICAL PROPERTIES
   >>FLUID PARAMETERS
    VISCOSITY 1.0000E+04
    DENSITY 8.0000E+02
   >>GRID MOTION PARAMETERS
    PATCH NAME 'USER3DRIGHT'
    POSITION VECTOR ON MOTION AXIS 0.039860 0.000000E+00 0.000000E+00
    DIRECTION VECTOR ON MOTION AXIS 0.000000E+00 0.000000E+00 1.000000E+00
    ROTATION SPEED 2.276
    TRANSLATION SPEED 0.0000E+00
   >>GRID MOTION PARAMETERS
    PATCH NAME 'USER3DLEFT'
    POSITION VECTOR ON MOTION AXIS 0.000000E+00 0.000000E+00 0.000000E+00
    DIRECTION VECTOR ON MOTION AXIS 0.000000E+00 0.000000E+00 1.000000E+00
    ROTATION SPEED -3.4140E+00
    TRANSLATION SPEED 0.0000E+00
 /*  >>HEAT TRANSFER PARAMETERS*/
 /*    THERMAL CONDUCTIVITY 5.0000E-01*/
 /*    FLUID SPECIFIC HEAT 2500.0*/
 /*    ENTHALPY REFERENCE TEMPERATURE 2.88E+02*/
   >>NON NEWTONIAN PARAMETERS
    >>NON NEWTONIAN MODEL
     NON NEWTONIAN MODEL 'POWER LAW'
    >>NON NEWTONIAN CONSTANTS
```

```
      POWER LAW INDEX 0.4114
      CONSISTENCY 54.0
      MINIMUM SHEAR RATE LIMIT 1.0000E-01
      MAXIMUM SHEAR RATE LIMIT 1.0000E+03
      INITIAL VISCOSITY GUESS 54.0
   >>TRANSIENT PARAMETERS
    >>FIXED TIME STEPPING
      TIME STEPS 1 * 0.001
>>SOLVER DATA
 >>PROGRAM CONTROL
   MAXIMUM NUMBER OF ITERATIONS 500
 /*  MAXIMUM CPU TIME 30000*/
   MASS SOURCE TOLERANCE 1.0000E-08
>>MODEL BOUNDARY CONDITIONS
/*  >>WALL BOUNDARIES*/
/*  PATCH NAME 'WALL'*/
   /*VELOCITY ABC 0.0 1.0E-9 0.0 0.0 0.0  */
/*  PATCH NAME 'WALLLEFT'*/
   /*VELOCITY ABC 0.0 1.0E-9 0.0 0.0 0.0  */
/*  PATCH NAME 'WALLRIGHT'*/
   /*VELOCITY ABC 0.0 1.0E-9 0.0 0.0 0.0  */
 /*  PATCH NAME 'WALL'*/
   /*TEMPERATURE ABC 1.0 2.0 500.0 */
>>OUTPUT OPTIONS
   >>DUMP FILE FORMAT
   >>dump file options
     scal1
     scal2
     scal3
     scal4
     scal5
  /* scal6*/
  /* scal7*/
  /* scal8*/
     TIME STEP INTERVAL 1
      all variables
      geometry data
 /* >>LINE GRAPH DATA
   XYZ 0.0 -0.0195 -0.0125
   EACH TIME STEP
   FILE NAME 'ALSPLOT1S'
   TEMPERATURE
   DENSITY
   VISCOSITY
   ALL VARIABLES
  >>LINE GRAPH DATA
   XYZ 0.04 -0.0195 -0.0125
   EACH TIME STEP
   FILE NAME 'ALSPLOT2S'
   TEMPERATURE
   DENSITY
   VISCOSITY
   ALL VARIABLES
  >>LINE GRAPH DATA
   XYZ 0.0199 0.0 -0.0125
   EACH TIME STEP
   FILE NAME 'ALSPLOT3S'
   TEMPERATURE
   DENSITY
   VISCOSITY
   ALL VARIABLES
  >>LINE GRAPH DATA
   XYZ 0.0 0.015 -0.0125
   EACH TIME STEP
   FILE NAME 'ALSPLOT4S'
```

```
  TEMPERATURE
  DENSITY
  VISCOSITY
  ALL VARIABLES
 >>LINE GRAPH DATA
  XYZ 0.0 0.0 0.0005
  EACH TIME STEP
  FILE NAME 'ALSPLOT5S'
  TEMPERATURE
  DENSITY
  VISCOSITY
  ALL VARIABLES
 >>LINE GRAPH DATA
  XYZ 0.015 0.0 0.0005
  EACH TIME STEP
  FILE NAME 'ALSPLOT6S'
  TEMPERATURE
  DENSITY
  VISCOSITY
  ALL VARIABLES
 >>PRINT OPTIONS
  >>WHAT
   SHORT UNMATCHED GRID INFORMATION
   PATCH UNMATCHED GRID INFORMATION
  >>WHEN
   EACH STEP*/
>>STOP
```

Appendix 9. FORTRAN Axial Flow Programme

The FORTRAN programme written to calculate the total axial flow for the volume around a specific rotor in the CFX simulation

```
C   WRITTEN BY ALAN HARRIES ON 1.3.99
C
C
SUBROUTINE USRTRN(U,V,W,P,VFRAC,DEN,VIS,TE,ED,RS,T,H,RF,SCAL,
     +                  XP,YP,ZP,VOL,AREA,VPOR,ARPOR,WFACT,CONV,IPT,
     +                  IBLK,IPVERT,IPNODN,IPFACN,IPNODF,IPNODB,IPFACB,
     +                  WORK,IWORK,CWORK)
C
C***********************************************************************
C
C   USER SUBROUTINE TO ALLOW USERS TO MODIFY OR MONITOR THE SOLUTION AT
C   THE END OF EACH TIME STEP
C   THIS SUBROUTINE IS CALLED BEFORE THE START OF THE RUN AS WELL AS AT
C   THE END OF EACH TIME STEP
C
C   >>> IMPORTANT                                                    <<<
C   >>>                                                             <<<
C   >>> USERS MAY ONLY ADD OR ALTER PARTS OF THE SUBROUTINE WITHIN  <<<
C   >>> THE DESIGNATED USER AREAS                                   <<<
C
C***********************************************************************
C
C   THIS SUBROUTINE IS CALLED BY THE FOLLOWING SUBROUTINES
C      CUSR  TRNMOD
C
C***********************************************************************
C   CREATED
C      27/04/90  ADB
C   MODIFIED
C      05/08/91  IRH  NEW STRUCTURE
C      01/10/91  DSC  REDUCE COMMENT LINE GOING OVER COLUMN 72.
C      29/11/91  PHA  UPDATE CALLED BY COMMENT, ADD RF ARGUMENT,
C                     CHANGE LAST DIMENSION OF RS TO 6 AND IVERS TO 2
C      05/06/92  PHA  ADD PRECISION FLAG AND CHANGE IVERS TO 3
C      03/07/92  DSC  CORRECT COMMON MLTGRD.
C      23/11/93  CSH  EXPLICITLY DIMENSION IPVERT ETC.
C      03/02/94  PHA  CHANGE FLOW3D TO CFDS-FLOW3D
C      22/08/94  NSW  MOVE 'IF(IUSED.EQ.0) RETURN' OUT OF USER AREA
C      19/12/94  NSW  CHANGE FOR CFX-F3D
C      02/07/97  NSW  UPDATE FOR CFX-4
C
C***********************************************************************
C
C   SUBROUTINE ARGUMENTS
C
C     U      - U COMPONENT OF VELOCITY
C     V      - V COMPONENT OF VELOCITY
C     W      - W COMPONENT OF VELOCITY
C     P      - PRESSURE
C     VFRAC  - VOLUME FRACTION
C     DEN    - DENSITY OF FLUID
C     VIS    - VISCOSITY OF FLUID
C     TE     - TURBULENT KINETIC ENERGY
C     ED     - EPSILON
C     RS     - REYNOLD STRESSES
C     T      - TEMPERATURE
C     H      - ENTHALPY
C     RF     - REYNOLD FLUXES
C     SCAL   - SCALARS (THE FIRST 'NCONC' OF THESE ARE MASS FRACTIONS)
C     XP     - X COORDINATES OF CELL CENTRES
C     YP     - Y COORDINATES OF CELL CENTRES
C     ZP     - Z COORDINATES OF CELL CENTRES
C     VOL    - VOLUME OF CELLS
C     AREA   - AREA OF CELLS
```

```
C     VPOR    - POROUS VOLUME
C     ARPOR   - POROUS AREA
C     WFACT   - WEIGHT FACTORS
C     CONV    - CONVECTION COEFFICIENTS
C
C     IPT     - 1D POINTER ARRAY
C     IBLK    - BLOCK SIZE INFORMATION
C     IPVERT - POINTER FROM CELL CENTERS TO 8 NEIGHBOURING VERTICES
C     IPNODN - POINTER FROM CELL CENTERS TO 6 NEIGHBOURING CELLS
C     IPFACN - POINTER FROM CELL CENTERS TO 6 NEIGHBOURING FACES
C     IPNODF - POINTER FROM CELL FACES TO 2 NEIGHBOURING CELL CENTERS
C     IPNODB - POINTER FROM BOUNDARY CENTERS TO CELL CENTERS
C     IPFACB - POINTER FROM BOUNDARY CENTERS TO BOUNDARY FACESS
C
C     WORK    - REAL WORKSPACE ARRAY
C     IWORK   - INTEGER WORKSPACE ARRAY
C     CWORK   - CHARACTER WORKSPACE ARRAY
C
C   SUBROUTINE ARGUMENTS PRECEDED WITH A '*' ARE ARGUMENTS THAT MUST
C   BE SET  BY THE USER IN THIS ROUTINE.
C
C   NOTE THAT OTHER DATA MAY BE OBTAINED FROM CFX-4 USING THE
C   ROUTINE GETADD, FOR FURTHER DETAILS SEE THE VERSION 4
C   USER MANUAL.
C
C*********************************************************************
C
C
      LOGICAL LDEN,LVIS,LTURB,LTEMP,LBUOY,LSCAL,LCOMP
     +       ,LRECT,LCYN,LAXIS,LPOROS,LTRANS
C
      CHARACTER*(*) CWORK
C
C+++++++++++++++++ USER AREA 1 ++++++++++++++++++++++++++++++++++++++++
C---- AREA FOR USERS EXPLICITLY DECLARED VARIABLES
C
C+++++++++++++++++ END OF USER AREA 1 +++++++++++++++++++++++++++++++++
C
      COMMON
     + /ALL/     NBLOCK,NCELL,NBDRY,NNODE,NFACE,NVERT,NDIM
     + /ALLWRK/ NRWS,NIWS,NCWS,IWRFRE,IWIFRE,IWCFRE
     + /ADDIMS/ NPHASE,NSCAL,NVAR,NPROP
     +         ,NDVAR,NDPROP,NDXNN,NDGEOM,NDCOEF,NILIST,NRLIST,NTOPOL
     + /CHKUSR/ IVERS,IUCALL,IUSED
     + /CONC/    NCONC
     + /DEVICE/ NREAD,NWRITE,NRDISK,NWDISK
     + /IDUM/    ILEN,JLEN
     + /LOGIC/   LDEN,LVIS,LTURB,LTEMP,LBUOY,LSCAL,LCOMP
     +          ,LRECT,LCYN,LAXIS,LPOROS,LTRANS
     + /MLTGRD/ MLEVEL,NLEVEL,ILEVEL
     + /SGLDBL/ IFLGPR,ICHKPR
     + /SPARM/   SMALL,SORMAX,NITER,INDPRI,MAXIT,NODREF,NODMON
     + /TIMUSR/ DTUSR
     + /TRANSI/ NSTEP,KSTEP,MF,INCORE
     + /TRANSR/ TIME,DT,DTINVF,TPARM
C
C+++++++++++++++++ USER AREA 2 ++++++++++++++++++++++++++++++++++++++++
C---- AREA FOR USERS TO DECLARE THEIR OWN COMMON BLOCKS
C     THESE SHOULD START WITH THE CHARACTERS 'UC' TO ENSURE
C     NO CONFLICT WITH NON-USER COMMON BLOCKS
C
C+++++++++++++++++ END OF USER AREA 2 +++++++++++++++++++++++++++++++++
C
      DIMENSION
     + U(NNODE,NPHASE),V(NNODE,NPHASE),W(NNODE,NPHASE),P(NNODE,NPHASE)
     +,VFRAC(NNODE,NPHASE),DEN(NNODE,NPHASE),VIS(NNODE,NPHASE)
     +,TE(NNODE,NPHASE),ED(NNODE,NPHASE),RS(NNODE,NPHASE,6)
     +,T(NNODE,NPHASE),H(NNODE,NPHASE),RF(NNODE,NPHASE,4)
     +,SCAL(NNODE,NPHASE,NSCAL)
      DIMENSION
     + XP(NNODE),YP(NNODE),ZP(NNODE)
     +,VOL(NCELL),AREA(NFACE,3),VPOR(NCELL),ARPOR(NFACE,3)
     +,WFACT(NFACE),CONV(NFACE,NPHASE)
```

```
     +,IPT(*),IBLK(5,NBLOCK)
     +,IPVERT(NCELL,8),IPNODN(NCELL,6),IPFACN(NCELL,6),IPNODF(NFACE,4)
     +,IPNODB(NBDRY,4),IPFACB(NBDRY)
     +,IWORK(*),WORK(*),CWORK(*)
C
C+++++++++++++++++ USER AREA 3 ++++++++++++++++++++++++++++++++++++++++++
C---- AREA FOR USERS TO DIMENSION THEIR ARRAYS
C
C        DIMENSION AXMODULUS(1)
C
C---- AREA FOR USERS TO DEFINE DATA STATEMENTS
C
C+++++++++++++++++ END OF USER AREA 3 +++++++++++++++++++++++++++++++++++
C
C---- STATEMENT FUNCTION FOR ADDRESSING
      IP(I,J,K)=IPT((K-1)*ILEN*JLEN+(J-1)*ILEN+I)
C
C----VERSION NUMBER OF USER ROUTINE AND PRECISION FLAG
C
      IVERS=3
      ICHKPR = 1
C
C+++++++++++++++++ USER AREA 4 ++++++++++++++++++++++++++++++++++++++++++
C---- TO USE THIS USER ROUTINE FIRST SET IUSED=1
C
       IUSED=1
C
C+++++++++++++++++ END OF USER AREA 4 +++++++++++++++++++++++++++++++++++
C
       IF (IUSED.EQ.0) RETURN
C
C---- FRONTEND CHECKING OF USER ROUTINE
       IF (IUCALL.EQ.0) RETURN
C
C+++++++++++++++++ USER AREA 5 ++++++++++++++++++++++++++++++++++++++++++
C
C---- EXAMPLE (SET TIME INCREMENT FOR NEXT TIME STEP)
C
C     DTUSR = 0.1
C
C----END OF EXAMPLE
C
C+++++++++++++++++ END OF USER AREA 5 +++++++++++++++++++++++++++++++++++
C
      open (unit=9,file='resultsaxial.out',status='unknown')
C
      CALL IPALL('USER3DLEFT','*','PATCH','CENTRES',
     +IPT,NPT,CWORK,IWORK)
C
C     LOOP OVER ALL INTERIOR CELLS
      DO 100 I=1,NPT
C
C     USE ARRAY IPT TO GET ADDRESS
      INODE=IPT(I)
C
      SCAL(INODE,NPHASE,1) = ((W(INODE,1))**2)**0.5
C
  100   CONTINUE
C
          AXSUM=0.0
C
          DO 200 I=1,NPT
             INODE=IPT(I)
             AXSUM=AXSUM+SCAL(INODE,NPHASE,1)
C
 200   CONTINUE
              write(9,111)AXSUM
C             write(6,*)'LEFT AXIAL FLOW TOTAL',AXSUM
 111      format(1h,'LEFT AXIAL FLOW TOTAL = ',d23.16)
C
C+++++++++++++++++ END OF USER AREA 5 +++++++++++++++++++++++++++++++++++
      RETURN
      END
```

Appendix 10. FORTRAN Rotor Clearance Optimisation Programme

This is the FORTRAN programme written to calculate the parameter used for optimising rotor clearance in the CFX simulation

```
C   Written by Alan Harries
C
C
      SUBROUTINE USRTRN(U,V,W,P,VFRAC,DEN,VIS,TE,ED,RS,T,H,RF,SCAL,
     +                  XP,YP,ZP,VOL,AREA,VPOR,ARPOR,WFACT,CONV,IPT,
     +                  IBLK,IPVERT,IPNODN,IPFACN,IPNODF,IPNODB,IPFACB,
     +                  WORK,IWORK,CWORK)
C
C***********************************************************************
C
C   USER SUBROUTINE TO ALLOW USERS TO MODIFY OR MONITOR THE SOLUTION AT
C   THE END OF EACH TIME STEP
C   THIS SUBROUTINE IS CALLED BEFORE THE START OF THE RUN AS WELL AS AT
C   THE END OF EACH TIME STEP
C
C   >>> IMPORTANT                                                   <<<
C   >>>                                                            <<<
C   >>> USERS MAY ONLY ADD OR ALTER PARTS OF THE SUBROUTINE WITHIN  <<<
C   >>> THE DESIGNATED USER AREAS                                  <<<
C
C***********************************************************************
C
C   THIS SUBROUTINE IS CALLED BY THE FOLLOWING SUBROUTINES
C      CUSR  TRNMOD
C
C***********************************************************************
C   CREATED
C      27/04/90  ADB
C   MODIFIED
C      05/08/91  IRH  NEW STRUCTURE
C      01/10/91  DSC  REDUCE COMMENT LINE GOING OVER COLUMN 72.
C      29/11/91  PHA  UPDATE CALLED BY COMMENT, ADD RF ARGUMENT,
C                     CHANGE LAST DIMENSION OF RS TO 6 AND IVERS TO 2
C      05/06/92  PHA  ADD PRECISION FLAG AND CHANGE IVERS TO 3
C      03/07/92  DSC  CORRECT COMMON MLTGRD.
C      23/11/93  CSH  EXPLICITLY DIMENSION IPVERT ETC.
C      03/02/94  PHA  CHANGE FLOW3D TO CFDS-FLOW3D
C      22/08/94  NSW  MOVE 'IF(IUSED.EQ.0) RETURN' OUT OF USER AREA
C      19/12/94  NSW  CHANGE FOR CFX-F3D
C      02/07/97  NSW  UPDATE FOR CFX-4
C
C***********************************************************************
C
C   SUBROUTINE ARGUMENTS
C
C     U       - U COMPONENT OF VELOCITY
C     V       - V COMPONENT OF VELOCITY
C     W       - W COMPONENT OF VELOCITY
C     P       - PRESSURE
C     VFRAC   - VOLUME FRACTION
C     DEN     - DENSITY OF FLUID
C     VIS     - VISCOSITY OF FLUID
C     TE      - TURBULENT KINETIC ENERGY
C     ED      - EPSILON
C     RS      - REYNOLD STRESSES
C     T       - TEMPERATURE
C     H       - ENTHALPY
C     RF      - REYNOLD FLUXES
C     SCAL    - SCALARS (THE FIRST 'NCONC' OF THESE ARE MASS FRACTIONS)
C     XP      - X COORDINATES OF CELL CENTRES
C     YP      - Y COORDINATES OF CELL CENTRES
C     ZP      - Z COORDINATES OF CELL CENTRES
C     VOL     - VOLUME OF CELLS
C     AREA    - AREA OF CELLS
C     VPOR    - POROUS VOLUME
C     ARPOR   - POROUS AREA
```

```
C     WFACT  - WEIGHT FACTORS
C     CONV   - CONVECTION COEFFICIENTS
C
C     IPT    - 1D POINTER ARRAY
C     IBLK   - BLOCK SIZE INFORMATION
C     IPVERT - POINTER FROM CELL CENTERS TO 8 NEIGHBOURING VERTICES
C     IPNODN - POINTER FROM CELL CENTERS TO 6 NEIGHBOURING CELLS
C     IPFACN - POINTER FROM CELL CENTERS TO 6 NEIGHBOURING FACES
C     IPNODF - POINTER FROM CELL FACES TO 2 NEIGHBOURING CELL CENTERS
C     IPNODB - POINTER FROM BOUNDARY CENTERS TO CELL CENTERS
C     IPFACB - POINTER FROM BOUNDARY CENTERS TO BOUNDARY FACESS
C
C     WORK   - REAL WORKSPACE ARRAY
C     IWORK  - INTEGER WORKSPACE ARRAY
C     CWORK  - CHARACTER WORKSPACE ARRAY
C
C   SUBROUTINE ARGUMENTS PRECEDED WITH A '*' ARE ARGUMENTS THAT MUST
C   BE SET  BY THE USER IN THIS ROUTINE.
C
C   NOTE THAT OTHER DATA MAY BE OBTAINED FROM CFX-4 USING THE
C   ROUTINE GETADD, FOR FURTHER DETAILS SEE THE VERSION 4
C   USER MANUAL.
C
C*********************************************************************
C
C
      LOGICAL LDEN,LVIS,LTURB,LTEMP,LBUOY,LSCAL,LCOMP
     +       ,LRECT,LCYN,LAXIS,LPOROS,LTRANS
C
      CHARACTER*(*) CWORK
C
C+++++++++++++++++ USER AREA 1 ++++++++++++++++++++++++++++++++++++++++
C---- AREA FOR USERS EXPLICITLY DECLARED VARIABLES
C
C+++++++++++++++++ END OF USER AREA 1 +++++++++++++++++++++++++++++++++
C
      COMMON
     + /ALL/     NBLOCK,NCELL,NBDRY,NNODE,NFACE,NVERT,NDIM
     + /ALLWRK/ NRWS,NIWS,NCWS,IWRFRE,IWIFRE,IWCFRE
     + /ADDIMS/ NPHASE,NSCAL,NVAR,NPROP
     +         ,NDVAR,NDPROP,NDXNN,NDGEOM,NDCOEF,NILIST,NRLIST,NTOPOL
     + /CHKUSR/ IVERS,IUCALL,IUSED
     + /CONC/    NCONC
     + /DEVICE/ NREAD,NWRITE,NRDISK,NWDISK
     + /IDUM/    ILEN,JLEN
     + /LOGIC/  LDEN,LVIS,LTURB,LTEMP,LBUOY,LSCAL,LCOMP
     +         ,LRECT,LCYN,LAXIS,LPOROS,LTRANS
     + /MLTGRD/ MLEVEL,NLEVEL,ILEVEL
     + /SGLDBL/ IFLGPR,ICHKPR
     + /SPARM/  SMALL,SORMAX,NITER,INDPRI,MAXIT,NODREF,NODMON
     + /TIMUSR/ DTUSR
     + /TRANSI/ NSTEP,KSTEP,MF,INCORE
     + /TRANSR/ TIME,DT,DTINVF,TPARM
C
C+++++++++++++++++ USER AREA 2 ++++++++++++++++++++++++++++++++++++++++
C---- AREA FOR USERS TO DECLARE THEIR OWN COMMON BLOCKS
C     THESE SHOULD START WITH THE CHARACTERS 'UC' TO ENSURE
C     NO CONFLICT WITH NON-USER COMMON BLOCKS
C
C+++++++++++++++++ END OF USER AREA 2 +++++++++++++++++++++++++++++++++
C
      DIMENSION     +
U(NNODE,NPHASE),V(NNODE,NPHASE),W(NNODE,NPHASE),P(NNODE,NPHASE)
     +,VFRAC(NNODE,NPHASE),DEN(NNODE,NPHASE),VIS(NNODE,NPHASE)
     +,TE(NNODE,NPHASE),ED(NNODE,NPHASE),RS(NNODE,NPHASE,6)
     +,T(NNODE,NPHASE),H(NNODE,NPHASE),RF(NNODE,NPHASE,4)
     +,SCAL(NNODE,NPHASE,NSCAL)
      DIMENSION
     + XP(NNODE),YP(NNODE),ZP(NNODE)
     +,VOL(NCELL),AREA(NFACE,3),VPOR(NCELL),ARPOR(NFACE,3)
     +,WFACT(NFACE),CONV(NFACE,NPHASE)
     +,IPT(*),IBLK(5,NBLOCK)
     +,IPVERT(NCELL,8),IPNODN(NCELL,6),IPFACN(NCELL,6),IPNODF(NFACE,4)
```

```
     +,IPNODB(NBDRY,4),IPFACB(NBDRY)
     +,IWORK(*),WORK(*),CWORK(*)
C
C+++++++++++++++++ USER AREA 3 ++++++++++++++++++++++++++++++++++++++++++
C---- AREA FOR USERS TO DIMENSION THEIR ARRAYS
C23456
      DIMENSION SGNWL(6)
C     DATA SGNWL /1.0 1.0 1.0 -1.0 -1.0 -1.0/
C---- AREA FOR USERS TO DEFINE DATA STATEMENTS
C
C+++++++++++++++++ END OF USER AREA 3 +++++++++++++++++++++++++++++++++++
C
C---- STATEMENT FUNCTION FOR ADDRESSING
      IP(I,J,K)=IPT((K-1)*ILEN*JLEN+(J-1)*ILEN+I)
C
C----VERSION NUMBER OF USER ROUTINE AND PRECISION FLAG
C
      IVERS=3
      ICHKPR = 1
C
C+++++++++++++++++ USER AREA 4 ++++++++++++++++++++++++++++++++++++++++++
C---- TO USE THIS USER ROUTINE FIRST SET IUSED=1
C
       IUSED=1
C
C+++++++++++++++++ END OF USER AREA 4 +++++++++++++++++++++++++++++++++++
C
       IF (IUSED.EQ.0) RETURN
C
C---- FRONTEND CHECKING OF USER ROUTINE
       IF (IUCALL.EQ.0) RETURN
C
C+++++++++++++++++ USER AREA 5 ++++++++++++++++++++++++++++++++++++++++++
C
C---- EXAMPLE (SET TIME INCREMENT FOR NEXT TIME STEP)
C
C     DTUSR = 0.1
C
C----END OF EXAMPLE
C
C+++++++++++++++++ END OF USER AREA 5 +++++++++++++++++++++++++++++++++++
C
      OPEN (UNIT=9,FILE='RESULTSSTRESS.OUT',STATUS='UNKNOWN')
C
C   ***********************************************
C   CALCULATE MASS FLOW THROUGH PATCH USER2DSTRESS
C
       DATA SGNWL / 1.0, 1.0, 1.0, -1.0, -1.0, -1.0 /
C
      FLUX=0.0
C
C
C
      CALL IPALL('USER2DSTRESS','*'
     *   ,'PATCH','CENTRES',IPT,NPT,CWORK,IWORK)
C
C      LOOP OVER ALL INTERIOR CELLS
C
      DO 100 I=1,NPT
C
C     USE ARRAY TO GET ARRAY IPT TO GET ADDRESS
      INODE=IPT(I)
C
      IBDRY=INODE-NCELL
      IWL=IPNODB(IBDRY,3)
      IFACE=IPFACN(IBDRY,IWL)
      FLUX=SGNWL(IWL)*CONV(IFACE,1) + FLUX
 100  CONTINUE
C
      WRITE(0,*)'MASS FLUX',FLUX
C
C
C     *********************************
```

```
C      STRESSMAGNITUDE ON USER3DSTRESS
C
       AVERAGE STRESS = 0.0
C
       CALL IPALL('USER3DSTRESS','*'
     *    ,'PATCH','CENTRES',IPT,NPT,CWORK,IWORK)
C
       DO 200 I=1,NPT
C
C
C      USE ARRAY TO GET ARRAY IPT TO GET ADDRESS
       INODE=IPT(I)
C
C
C
       SCAL(INODE,NPHASE,4) = (SCAL(INODE,NPHASE,1)**2.0 +
      %     SCAL(INODE,NPHASE,2)**2.0  +
      &     SCAL(INODE,NPHASE,3)**2)**0.5
C
C      CALCULATION AVERAGE VALUE OF CELL CENTRES IN PATCH
C      NPT = NUMBER OF CELLS IN PATCH
C
       AVERAGESTRESS = AVERAGESTRESS + (SCAL(INODE,NPHASE,4)/NPT)
C
 200   CONTINUE
C
C
       WRITE(0,*)'AVERAGE SHEAR STRESS',AVERAGESTRESS
C
C      ********************************
C      PRODUCT OF AVERAGESTRESS AND FLUX
C
C
C
       PRODUCT=AVERAGESTRESS * FLUX
C
       WRITE(0,*)'AVERAGESTRESS * FLUX',PRODUCT


       RETURN
C
C
       END
C
```

Appendix 11. Internal Mixer Automatic Geometry Parameterisation (AGP) Journal File

```
#   Written by Alan Harries
#
#
STRING asm_create_cord_3po_created_ids[VIRTUAL]
asm_const_coord_3point( "1", "Coord 0", 2, "[0 0 0]", "[0 0 1]", "[1 0 0 ]",   @
   asm_create_cord_3po_created_ids )
$# 1 Coord created: Coord 1
real sx
sx = 0.05
real sy
sy = 0.05
real sz
sz = 0.05
real clearance
clearance = 1.15
real landwidth
landwidth = 70.0
real separation
separation = 2.70
STRING asm_create_grid_xyz_created_ids[VIRTUAL]
asm_const_grid_xyz( "1", "['clearance' 'landwidth' 0]", "Coord 1 ",      @
asm_create_grid_xyz_created_ids )
$# Error reported from application APP
$#     Unable to process list: "['clearance' 'landwidth' 0]"
$? NO 16000101
asm_const_grid_xyz( "1", "[`clearance` `landwidth` 0]", "Coord 1 ",      @
asm_create_grid_xyz_created_ids )
$# 1 Point created: Point 1
point_size( 9 )
point_label( TRUE )
asm_const_grid_xyz( "2", "[`clearance` 40 0]", "Coord 1 ",      @
asm_create_grid_xyz_created_ids )
$# 1 Point created: Point 2
asm_const_grid_xyz( "3", "[`clearance` -40 0]", "Coord 1 ",      @
asm_create_grid_xyz_created_ids )
$# 1 Point created: Point 3
asm_const_grid_xyz( "4", "[`clearance` -`landwidth` 0]", "Coord 1 ",      @
asm_create_grid_xyz_created_ids )
$# 1 Point created: Point 4
STRING sgm_transform_point_created_ids[VIRTUAL]
asm_transform_grid_scale( "5", "[0 0 0]", [0.60000002, 0.60000002, 0.60000002] @
    , "Coord 0", 1, FALSE, FALSE, "Point 2 3 ",  @
sgm_transform_point_created_ids )
$# 2 Points created: Grid 5,6
STRING asm_line_2point_created_ids[VIRTUAL]
asm_const_line_2point( "1", "Point 1 ", "Point 4 ", 0, "", 50., 1,      @
asm_line_2point_created_ids )
$# 1 Line created: Line 1
asm_const_line_2point( "2", "Point 5 ", "Point 6 ", 0, "", 50., 1,      @
asm_line_2point_created_ids )
$# 1 Line created: Line 2
STRING sgm_curve_break_poi_created_ids[VIRTUAL]
sgm_edit_curve_break_point( "3", "Point 5 ", "Curve 1 ", TRUE,      @
sgm_curve_break_poi_created_ids )
$# 2 Lines Created: Lines 3,4
$# Question from application SGM
$#     Do you wish to delete the original curves?
$? YES 38000217
$# 1 Curve Deleted: Curve 1
sgm_edit_curve_break_point( "5", "Point 6 ", "Curve 4 ", TRUE,      @
sgm_curve_break_poi_created_ids )
$# 2 Lines Created: Lines 5,6
$# Question from application SGM
$#     Do you wish to delete the original curves?
$? YES 38000217
$# 1 Curve Deleted: Curve 4
STRING sgm_transform_point_created_ids[VIRTUAL]
asm_transform_grid_mirror( "9", "Coord 0.3", 0., FALSE,      @
"Point 1 2 7 5 8 6 3 4 ", sgm_transform_point_created_ids )
```

```
$# Question in application SGM by application ASM
$#     Point 1 already exists at the specified location to create the next
$# Point. Do you wish to create a duplicate Point?
$? NO 1000034
$# Duplicate Point was not created at users request.
$# Question in application SGM by application ASM
$#     Point 2 already exists at the specified location to create the next
$# Point. Do you wish to create a duplicate Point?
$? NOFORALL 1000034
$# Duplicate Point was not created at users request.
$# Duplicate Point was not created at users request.
$# Duplicate Point was not created at users request.
$# Duplicate Point was not created at users request.
$# Duplicate Point was not created at users request.
$# Duplicate Point was not created at users request.
$# Duplicate Point was not created at users request.
$# 0 Points created.
asm_transform_grid_mirror( "9", "Coord 0.3", 0., FALSE,      @
"Point 1 2 7 5 8 6 3 4 ", sgm_transform_point_created_ids )
$# Question in application SGM by application ASM
$#     Point 1 already exists at the specified location to create the next
$# Point. Do you wish to create a duplicate Point?
$? NOFORALL 1000034
$# Duplicate Point was not created at users request.
$# Duplicate Point was not created at users request.
$# Duplicate Point was not created at users request.
$# Duplicate Point was not created at users request.
$# Duplicate Point was not created at users request.
$# Duplicate Point was not created at users request.
$# Duplicate Point was not created at users request.
$# Duplicate Point was not created at users request.
$# 0 Points created.
asm_transform_grid_mirror( "9", "Coord 0.3", 0., FALSE,      @
"Point 1 2 7 5 8 6 3 4 ", sgm_transform_point_created_ids )
$# Question in application SGM by application ASM
$#     Point 1 already exists at the specified location to create the next
$# Point. Do you wish to create a duplicate Point?
$? NOFORALL 1000034
$# Duplicate Point was not created at users request.
$# Duplicate Point was not created at users request.
$# Duplicate Point was not created at users request.
$# Duplicate Point was not created at users request.
$# Duplicate Point was not created at users request.
$# Duplicate Point was not created at users request.
$# Duplicate Point was not created at users request.
$# Duplicate Point was not created at users request.
$# 0 Points created.
STRING sgm_transform_point_created_ids[VIRTUAL]
asm_transform_grid_rotate( "9", "Coord 0.3", 180., 0., "Coord 0", 1, FALSE,    @
  "Point 1 2 7 5 8 6 3 4 ", sgm_transform_point_created_ids )
$# 8 Points created: Grid 9:16
STRING asm_line_2point_created_ids[VIRTUAL]
asm_const_line_2point( "7", "Point 16 ", "Point 13 ", 0, "", 50., 1,      @
asm_line_2point_created_ids )
$# 1 Line created: Line 7
asm_const_line_2point( "8", "Point 13 ", "Point 11 ", 0, "", 50., 1,      @
asm_line_2point_created_ids )
$# 1 Line created: Line 8
asm_const_line_2point( "9", "Point 11 ", "Point 9 ", 0, "", 50., 1,       @
asm_line_2point_created_ids )
$# 1 Line created: Line 9
asm_const_line_2point( "10", "Point 14 ", "Point 12 ", 0, "", 50., 1,      @
asm_line_2point_created_ids )
$# 1 Line created: Line 10
STRING sgm_surface_2curve_created_ids[VIRTUAL]
sgm_const_surface_2curve( "1", "Curve 8 ", "Curve 10 ",      @
sgm_surface_2curve_created_ids )
$# 1 Surface Created: Surface 1
sgm_const_surface_2curve( "2", "Curve 5 ", "Curve 2 ",      @
sgm_surface_2curve_created_ids )
$# 1 Surface Created: Surface 2
ga_display_lines_set( "general", 2 )
STRING sgm_create_curve_2d_created_ids[VIRTUAL]
```

```
sgm_const_curve_2d_arc2point_v2( "11", 1, 0., FALSE, FALSE, 1, "Coord 0.3",    @
  "[0 0 0]", "Point 16 ", "Point 1 ", FALSE, sgm_create_curve_2d_created_ids )
$# 1 Curve Created: Curve 11
sgm_const_curve_2d_arc2point_v2( "12", 1, 0., FALSE, FALSE, 1, "Coord 0.3",    @
  "[0 0 0]", "Point 1 ", "Point 2 ", FALSE, sgm_create_curve_2d_created_ids )
$# 1 Curve Created: Curve 12
sgm_const_curve_2d_arc2point_v2( "13", 1, 0., FALSE, FALSE, 1, "Coord 0.3",    @
  "[0 0 0]", "Point 2 ", "Point 3 ", FALSE, sgm_create_curve_2d_created_ids )
$# 1 Curve Created: Curve 13
sgm_const_curve_2d_arc2point_v2( "14", 1, 0., FALSE, FALSE, 1, "Coord 0.3",    @
  "[0 0 0]", "Point 3 ", "Point 4 ", FALSE, sgm_create_curve_2d_created_ids )
$# 1 Curve Created: Curve 14
sgm_const_curve_2d_arc2point_v2( "15", 1, 0., FALSE, FALSE, 1, "Coord 0.3",    @
  "[0 0 0]", "Point 4 ", "Point 9 ", FALSE, sgm_create_curve_2d_created_ids )
$# 1 Curve Created: Curve 15
sgm_const_curve_2d_arc2point_v2( "16", 1, 0., FALSE, FALSE, 1, "Coord 0.3",    @
  "[0 0 0]", "Point 9 ", "Point 10 ", FALSE, sgm_create_curve_2d_created_ids )
$# 1 Curve Created: Curve 16
sgm_const_curve_2d_arc2point_v2( "17", 1, 0., FALSE, FALSE, 1, "Coord 0.3",    @
  "[0 0 0]", "Point 15 ", "Point 10 ", FALSE, sgm_create_curve_2d_created_ids )
$# 1 Curve Created: Curve 17
sgm_const_curve_2d_arc2point_v2( "18", 1, 0., FALSE, FALSE, 1, "Coord 0.3",    @
  "[0 0 0]", "Point 16 ", "Point 15 ", FALSE, sgm_create_curve_2d_created_ids )
$# 1 Curve Created: Curve 18
sgm_const_surface_2curve( "3", "Surface 2.1 ", "Curve 12 ",      @
sgm_surface_2curve_created_ids )
$# 1 Surface Created: Surface 3
sgm_const_surface_2curve( "4", "Curve 2 ", "Curve 13 ",      @
sgm_surface_2curve_created_ids )
$# 1 Surface Created: Surface 4
sgm_const_surface_2curve( "5", "Surface 2.3 ", "Curve 14 ",      @
sgm_surface_2curve_created_ids )
$# 1 Surface Created: Surface 5
sgm_const_surface_2curve( "6", "Surface 1.3 ", "Curve 16 ",      @
sgm_surface_2curve_created_ids )
$# 1 Surface Created: Surface 6
sgm_const_surface_2curve( "7", "Curve 10 ", "Curve 17 ",      @
sgm_surface_2curve_created_ids )
$# 1 Surface Created: Surface 7
sgm_const_surface_2curve( "8", "Surface 1.1 ", "Curve 18 ",      @
sgm_surface_2curve_created_ids )
$# 1 Surface Created: Surface 8
sgm_const_surface_2curve( "9", "Surface 1.1 ", "Curve 18 ",      @
sgm_surface_2curve_created_ids )
$# Question in application SGM by application ASM
$#     Surface 8 already exists at the specified location to create the next
$# Surface. Do you wish to create a duplicate Surface?
$? NO 1000034
$# Duplicate Surface was not created at users request.
$# No Geometry Created.
ga_view_zoom_set( 2.4354348 )
STRING asm_create_grid_xyz_created_ids[VIRTUAL]
asm_const_grid_xyz( "17", "[1.3 `landwidth` 0]", "Coord 1 ",      @
asm_create_grid_xyz_created_ids )
$# 1 Point created: Point 17
asm_const_grid_xyz( "18", "[1.3 -`landwidth` 0]", "Coord 1 ",      @
asm_create_grid_xyz_created_ids )
$# 1 Point created: Point 18
asm_const_grid_xyz( "19", "[1.3 -40 0]", "Coord 1 ",      @
asm_create_grid_xyz_created_ids )
$# 1 Point created: Point 19
asm_const_grid_xyz( "20", "[1.3 40 0]", "Coord 1 ",      @
asm_create_grid_xyz_created_ids )
$# 1 Point created: Point 20
STRING sgm_transform_point_created_ids[VIRTUAL]
asm_transform_grid_rotate( "21", "Coord 0.3", 180., 0., "Coord 0", 1, FALSE,   @
   "Point 18:20 17 ", sgm_transform_point_created_ids )
$# 4 Points created: Grid 21:24
sgm_const_curve_2d_arc2point_v2( "19", 1, 0., FALSE, FALSE, 1, "Coord 0.3",    @
  "[0 0 0]", "Point 21 ", "Point 17 ", FALSE, sgm_create_curve_2d_created_ids )
$# 1 Curve Created: Curve 19
sgm_const_curve_2d_arc2point_v2( "20", 1, 0., FALSE, FALSE, 1, "Coord 0.3",    @
  "[0 0 0]", "Point 22 ", "Point 21 ", FALSE, sgm_create_curve_2d_created_ids )
```

```
$# 1 Curve Created: Curve 20
sgm_const_curve_2d_arc2point_v2( "21", 1, 0., FALSE, FALSE, 1, "Coord 0.3",    @
  "[0 0 0]", "Point 22 ", "Point 23 ", FALSE, sgm_create_curve_2d_created_ids )
$# 1 Curve Created: Curve 21
sgm_const_curve_2d_arc2point_v2( "22", 1, 0., FALSE, FALSE, 1, "Coord 0.3",    @
  "[0 0 0]", "Point 24 ", "Point 23 ", FALSE, sgm_create_curve_2d_created_ids )
$# 1 Curve Created: Curve 22
sgm_const_curve_2d_arc2point_v2( "23", 1, 0., FALSE, FALSE, 1, "Coord 0.3",    @
  "[0 0 0]", "Point 24 ", "Point 18 ", FALSE, sgm_create_curve_2d_created_ids )
$# 1 Curve Created: Curve 23
sgm_const_curve_2d_arc2point_v2( "24", 1, 0., FALSE, FALSE, 1, "Coord 0.3",    @
  "[0 0 0]", "Point 19 ", "Point 18 ", FALSE, sgm_create_curve_2d_created_ids )
$# 1 Curve Created: Curve 24
sgm_const_curve_2d_arc2point_v2( "25", 1, 0., FALSE, FALSE, 1, "Coord 0.3",    @
  "[0 0 0]", "Point 19 ", "Point 18 ", FALSE, sgm_create_curve_2d_created_ids )
$# Question in application SGM by application ASM
$#     Curve 24 already exists at the specified location to create the next
$# Curve. Do you wish to create a duplicate Curve?
$? NO 1000034
$# Duplicate Curve was not created at users request.
$# No Geometry Created.
sgm_const_curve_2d_arc2point_v2( "25", 1, 0., FALSE, FALSE, 1, "Coord 0.3",    @
  "[0 0 0]", "Point 19 ", "Point 20 ", FALSE, sgm_create_curve_2d_created_ids )
$# 1 Curve Created: Curve 25
sgm_const_curve_2d_arc2point_v2( "26", 1, 0., FALSE, FALSE, 1, "Coord 0.3",    @
  "[0 0 0]", "Point 17 ", "Point 20 ", FALSE, sgm_create_curve_2d_created_ids )
$# 1 Curve Created: Curve 26
STRING sgm_transform_curve_created_ids[VIRTUAL]
sgm_transform_scale( "27", "curve", [0.97000003, 0.97000003, 0.97000003],      @
"[0 0 0]", "Coord 0", 1, FALSE, "Curve 24:26 19:23 ",      @
sgm_transform_curve_created_ids )
$# 8 Curves Created: Curves 27:34
STRING sgm_surface_2curve_created_ids[VIRTUAL]
sgm_const_surface_2curve( "9", "Curve 19 ", "Curve 30 ",      @
sgm_surface_2curve_created_ids )
$# 1 Surface Created: Surface 9
sgm_const_surface_2curve( "10", "Curve 26 ", "Curve 29 ",      @
sgm_surface_2curve_created_ids )
$# 1 Surface Created: Surface 10
sgm_const_surface_2curve( "11", "Curve 25 ", "Curve 28 ",      @
sgm_surface_2curve_created_ids )
$# 1 Surface Created: Surface 11
sgm_const_surface_2curve( "12", "Curve 24 ", "Curve 27 ",      @
sgm_surface_2curve_created_ids )
$# 1 Surface Created: Surface 12
sgm_const_surface_2curve( "13", "Curve 23 ", "Curve 34 ",      @
sgm_surface_2curve_created_ids )
$# 1 Surface Created: Surface 13
sgm_const_surface_2curve( "14", "Curve 22 ", "Curve 33 ",      @
sgm_surface_2curve_created_ids )
$# 1 Surface Created: Surface 14
sgm_const_surface_2curve( "15", "Curve 21 ", "Curve 32 ",      @
sgm_surface_2curve_created_ids )
$# 1 Surface Created: Surface 15
sgm_const_surface_2curve( "16", "Curve 20 ", "Curve 31 ",      @
sgm_surface_2curve_created_ids )
$# 1 Surface Created: Surface 16
sgm_const_surface_2curve( "17", "Curve 30 ", "Curve 11 ",      @
sgm_surface_2curve_created_ids )
$# 1 Surface Created: Surface 17
sgm_const_surface_2curve( "18", "Curve 29 ", "Curve 12 ",      @
sgm_surface_2curve_created_ids )
$# 1 Surface Created: Surface 18
sgm_const_surface_2curve( "19", "Curve 28 ", "Curve 13 ",      @
sgm_surface_2curve_created_ids )
$# 1 Surface Created: Surface 19
sgm_const_surface_2curve( "20", "Curve 27 ", "Curve 14 ",      @
sgm_surface_2curve_created_ids )
$# 1 Surface Created: Surface 20
sgm_const_surface_2curve( "21", "Curve 34 ", "Curve 15 ",      @
sgm_surface_2curve_created_ids )
$# 1 Surface Created: Surface 21
sgm_const_surface_2curve( "22", "Curve 33 ", "Curve 16 ",      @
```

```
sgm_surface_2curve_created_ids )
$# 1 Surface Created: Surface 22
sgm_const_surface_2curve( "23", "Curve 32 ", "Curve 17 ",      @
sgm_surface_2curve_created_ids )
$# 1 Surface Created: Surface 23
sgm_const_surface_2curve( "24", "Curve 31 ", "Curve 18 ",      @
sgm_surface_2curve_created_ids )
$# 1 Surface Created: Surface 24
ga_view_zoom_set( 3.132 )
STRING sgm_transform_surf__created_ids[VIRTUAL]
sgm_transform_translate( "25", "surface", "<`separation` 0 0>", "Coord 0", 1,  @
   FALSE, "Surface 1:24 ", sgm_transform_surf__created_ids )
$# 24 Surfaces Created: Surfaces 25:48
ga_view_center_set( -0.037850, 0.087056 )
ga_view_zoom_set( 1.305839 )
STRING sgm_surface_2curve_created_ids[VIRTUAL]
sgm_const_surface_2curve( "49", "Surface 39.4 ", "Curve 25 ",     @
sgm_surface_2curve_created_ids )
$# 1 Surface Created: Surface 49
ga_view_zoom_set( 2.6116776 )
STRING sgm_sweep_solid_ext_created_ids[VIRTUAL]
sgm_const_solid_extrude( "1", "<0 0 1>", 1., 0., "[0 0 0]", "Coord 0",     @
"Surface 1:49 ", sgm_sweep_solid_ext_created_ids )
$# 49 Solids Created: Solids 1:49
point_label( FALSE )
solid_label( TRUE )
volume_label( TRUE )
body_label( TRUE )
uil_toolbar.labels_off(  )
solid_label( TRUE )
volume_label( TRUE )
body_label( TRUE )
gm_visibility_widget( "Solids 1:8", FALSE )
ga_view_aa_set( 18.908808, 11.679482, -0.256313 )
ga_view_aa_set( 28.105305, -4.626776, 1.294134 )
gm_visibility_widget( "Solids 1:8", FALSE )
ga_view_aa_set( 3.073791, 1.833842, -1.722998 )
gm_visibility_widget( "Solid 1:8  25:31", FALSE )
gm_visibility_widget( "Solid 1:8  25:32", FALSE )
gm_visibility_widget( "Solid 1:8  25:32", FALSE )
gm_visibility_widget( "curve 1:", FALSE )
gm_visibility_widget( "curve 1:40", FALSE )
gm_visibility_widget( "curve 1:100", FALSE )
gm_visibility_widget( "Curve 1:100", FALSE )
gm_visibility_widget( "Surface 1:", FALSE )
gm_visibility_widget( "Surface 1:100", TRUE )
gm_visibility_widget( "Surface 1:100", FALSE )
gm_visibility_widget( "solids 9-16", FALSE )
gm_visibility_widget( "solid 9-16", FALSE )
gm_visibility_widget( "solid 9:16", FALSE )
ga_view_aa_set( 11.976768, 6.920885, 4.282290 )
gm_visibility_widget( "solid 33-40", FALSE )
gm_visibility_widget( "solid 33:40", FALSE )
ga_view_aa_set( 3.888700, 4.971751, 4.907196 )
gm_visibility_widget( "solid49", TRUE )
gm_visibility_widget( "solid49", FALSE )
cfx4_db.put_item( "BLKBDYLEFTROTOR", "UNMATCHED_BDRY", ["FACES"], [2], [87], [ @
   FALSE], [0.], ["Solid 17.1 Solid 24.1 Solid 23.5 Solid 22.1 Solid 21.3 " // @
"Solid 20.1 Solid 19.4 Solid 18.2"] )
cfx4_db.put_item( "BLKBDYRIGHTROTOR", "UNMATCHED_BDRY", ["FACES"], [2], [87],  @
   [FALSE], [0.], ["Solid 41.1 Solid 48.1 Solid 47.3 Solid 46.1 Solid 45.3" // @
" Solid 44.1 Solid 43.3 Solid 42.1"] )
gm_visibility_widget( " Point 1:128 Curve 2:3 5:34 Surface 1:49 Solid 1:49",   @
  TRUE )
ui_exec_function( "mesh_seed_display_mgr", "init" )
mesh_seed_display_mgr.erase(  )
mesh_seed_create( "Solid 9.4.3 ", 1, 3, 0., 0., 0. )
mesh_seed_create( "Solid 39.6.1 ", 1, 3, 0., 0., 0. )
mesh_seed_create( "Solid 47.6.1 18.6.2 ", 5, 10, 2.5, 0., 0. )
mesh_seed_create( "Solid 49.3.3 ", 5, 10, 2.5, 0., 0. )
mesh_seed_create( "Solid 31.6.4 3.2.2 ", 5, 10, 2.5, 0., 0. )
mesh_seed_create( "Solid 2.6.1 25.6.4 26.1.2 1.6.4 ", 1, 10, 0., 0., 0. )
ga_view_aa_set( 5.407943, 1.404990, 1.693465 )
```

```
mesh_seed_create( "Solid 2.6.1 25.6.4 26.1.2 1.6.4 41.2.2 45.4.3 17.2.2 21" // @
".4.3 ", 1, 10, 0., 0., 0. )
ga_view_aa_set( 47.690514, 20.950775, -7.189257 )
mesh_seed_create( "Solid 39.1.1 ", 1, 1, 0., 0., 0. )
ga_view_aa_set( 43.231606, 16.728264, -2.685001 )
gu_fit_view( )
ga_view_aa_set( 0., 0., 0. )
mesh_seed_display_mgr.erase( )
ga_view_aa_set( 22.286224, 10.290486, -0.007098 )
gm_visibility_widget( " Node 1:13822 Element 1:10380", FALSE )
ga_display_lines_set( "general", 0 )
ga_view_aa_set( 0., 0., 0. )
cfx4_patch_create( "USER3DLEFTROTOR", FALSE, "",     @
"Solid 18 17 3 4 2 19 20 5 21 22 6 1 8 24 23 7 " )
$# PATCH USER3DLEFTROTOR created.
cfx4_patch_create( "USER3DRIGHTROTOR", FALSE, "",     @
"Solid 32 48 31 47 46 30 45 44 29 26:28 43:41:-1 " )
$# PATCH USER3DRIGHTROTOR created.
ga_view_aa_set( 13.181753, 4.684066, -2.579100 )
cfx4_patch_create( "USER3DSTRESS", FALSE, "", "Solid 9 17 " )
$# PATCH USER3DSTRESS created.
ga_view_aa_set( 0., 0., 0. )
cfx4_db.del_item( "BLKBDYLEFTROTOR", "UNMATCHED_BDRY" )
gm_visibility_widget( "Surface 48 41 42 27 32 25 31 47:43:-1 24 17:19 4 3 " // @
"8 7 23 1 Curve 16 Surface 5 20 22 21 ", FALSE )
gm_visibility_widget( "Surface 48 41 42 27 32 25 31 47:43:-1 24 17:19 4 3 " // @
"8 7 23 1 Curve 16 Surface 5 20 22 21 ", FALSE )
gm_visibility_widget( "Surface 48 41 42 27 32 25 31 43:47 24 17:19 4 3 8 7" // @
" 23 1 Curve 16 Surface 5 20 22 21 Point 33:40 97:104 Surface 26 28:30 Sol" // @
"id 25:32 42:48:2 Point 5:8 11:14 65:72 Curve 2 3 5:10 12 14 18 Surface 2 " // @
"6 Solid 1:8 18:24:2 Coord 1 ", FALSE )
ga_view_aa_set( -1.000000, 0.000000, 0.000000 )
gm_visibility_widget( "Solid 47 41:45:2 19 17 23 21 49 ", FALSE )
ga_view_aa_set( 3.035311, 2.080006, 0.077659 )
gm_visibility_widget( "Curve 11 ", FALSE )
point_size( 1 )
ga_view_aa_set( 20.395100, 10.424175, -3.308625 )
cfx4_db.put_item( "BLKBDYRIGHTROTOROUTSIDE", "UNMATCHED_BDRY", ["FACES"], [2], @
    [87], [FALSE], [0.], ["Solid 33.2 Solid 34.2 Solid 35.4 Solid 36.2 Sol" // @
"id 37.4 Solid 38.2 Solid 39.4 Solid 40.2"] )
cfx4_db.put_item( "BLKBDYLEFTROTOROUTSIDE", "UNMATCHED_BDRY", ["FACES"], [2],  @
   [86], [FALSE], [0.], ["Solid 9.2 Solid 10.2 Solid 11.4 Solid 12.2 Solid" // @
" 13.4 Solid 14.2 Solid 15.4 Solid 16.2"] )
gm_visibility_widget( " Point 1:128 Curve 2:3 5:34 Surface 1:49 Solid 1:49",   @
  TRUE )
ga_view_aa_set( 0., 0., 0. )
ga_view_aa_set( 14.000001, 1.000000, 0.000000 )
gm_visibility_widget( "Solid 9 10 16 11:15 ", FALSE )
ga_view_aa_set( 15.150346, 13.701810, -2.129498 )
gm_visibility_widget( "Surface 1:100 ", FALSE )
ga_view_aa_set( 19.995625, 6.071087, -0.742705 )
gm_visibility_widget( "Curve 1:100 ", FALSE )
ga_view_aa_set( 20.076801, 8.008136, -1.231505 )
ga_view_center_set( -2.038056, -0.194101 )
ga_view_aa_set( 15.651733, 4.531422, 4.370502 )
cfx4_db.put_item( "BLKBDYLEFTROTORINSIDE", "UNMATCHED_BDRY", ["FACES"], [2], [ @
   87], [FALSE], [0.], ["Solid 17.1 Solid 18.1 Solid 19.3 Solid 20.1 Solid" // @
" 21.3 Solid 22.1 Solid 23.3 Solid 24.1"] )
gm_visibility_widget( " Point 1:128 Curve 2:3 5:34 Surface 1:49 Solid 1:49",   @
  TRUE )
ga_view_aa_set( 0., 0., 0. )
gm_visibility_widget( "Curve 1:100 ", FALSE )
ga_view_aa_set( 23.213167, 8.661576, -2.164256 )
$# Session file stopped playing (level 1)
ui_exec_function( "mesh_seed_display_mgr", "init" )
mesh_seed_display_mgr.erase( )
cfx4_patch_create( "USER2DSTRESS", TRUE, "Solid 17.3 ", "" )
$# 1 Surface Created: Surface 50
$# PATCH USER2DSTRESS created.
ga_view_center_set( -1.592822, 0.910184 )
ga_view_zoom_set( 0.553112 )
cfx4_patch_delete( "USER2DSTRESS" )
cfx4_patch_create( "USER2DSTRESS", TRUE, "Surface 50 Solid 9.3 ", "" )
```

```
$# 1 Surface Created: Surface 51
$# PATCH USER2DSTRESS created.
gm_visibility_widget( " Node 1:13822 Element 1:10380", TRUE )
ga_view_aa_set( 0., 0., 0. )
repaint_graphics(  )
#now for the analysis form
mesh_seed_display_mgr.erase(  )

*******************************
SURFACE MESH MUST NOW BE CREATED
*******************************
Now continue…

cfx4_anal_apply.apply3( "Solid 1:49 ", 2., 4., 4., 8, ["USER2DSTRESS",  @
"USER3DLEFTROTOR", "USER3DRIGHTROTOR", "USER3DSTRESS", "BLKBDYRIGHTROTOR",  @
"BLKBDYRIGHTROTOROUTSIDE", "BLKBDYLEFTROTOROUTSIDE", "BLKBDYLEFTROTORINSIDE"], @
 "", TRUE, FALSE, FALSE, FALSE, TRUE, "(x,y,z)", `sx`, `sy`, `sz` )
$# Realigning database with new node numbers...
$# Database realignment completed.
$# Geometric equivalencing completed. 4248 nodes deleted.
$# Number of elements to be created in solids is: 4612
$# Number of 3d hexahedral elements is: 0
$# Total number of elements will be: 4612
$# Running  /CFX/4.2/build/4.2/IRIS_R4K/bin/runvolmsh file.jba
$# Journal file stopped recording at 05-Mar-:0 15:06:04
```

Appendix 12. Optimum Rotor Clearance Data

Table A12-1 *Optimum rotor clearance data for varying power exponents, factors and wall-slip conditions.*

* =(Chamber Radius = 1.3metres) – 'clearance') * (Scale Factor = 0.05))

'landwidth' = 70 deg - 'separation' =2.7 m - rotor speed = 3.414 rad/s - for all simulations

n=0.5 K=1000 no Slip

Clearance Value (m)	Actual Clearance* (m)	Flux (kg/s)	Av. Stress Mag. (Pa)	Product of Flux and Stress
0.80	0.0250	0.2350	2308.143	542.413605
0.90	0.0200	0.2055	2934.879	603.1176345
1.00	0.0150	0.1699	3835.21	651.602179
1.10	0.0100	0.1242	5345.42	663.901164
1.15	0.0075	0.0952	6567.806	625.2551312
1.20	0.0050	0.0596	8342.732	497.2268272
1.22	0.0040	0.03968	9475.817	376.0004186

n=0.4 K=1000 no Slip

Clearance Value (m)	Actual Clearance* (m)	Flux (kg/s)	Av. Stress Mag. (Pa)	Product of Flux and Stress
0.80	0.0250	0.2365	1752.739	414.5227735
0.90	0.0200	0.2074	2120.346	439.7597604
1.00	0.0150	0.1695	2621.64	444.36798
1.10	0.0100	0.1274	3403.178	433.5648772
1.15	0.0075	0.09921	4055.2	402.316392
1.20	0.0050	0.06428	4964.193	319.098326
1.22	0.0040	0.04236	5380.96	227.9374656

n=0.3 K=1000 no Slip

Clearance Value (m)	Actual Clearance* (m)	Flux (kg/s)	Av. Stress Mag. (Pa)	Product of Flux and Stress
0.80	0.0250	0.23780	1367.723	325.2445294
0.90	0.0200	0.20890	1567.978	327.5506042
1.00	0.0150	0.17420	1830.499	318.8729258
1.10	0.0100	0.13000	2219.301	288.50913
1.15	0.0075	0.10220	2479.53	253.407966
1.20	0.0050	0.05468	2998.228	163.943107
1.22	0.0040	0.04359	3129.296	136.4060126

n=0.5 K=10000 no Slip

Clearance Value (m)	Actual Clearance* (m)	Flux (kg/s)	Av. Stress Mag. (Pa)	Product of Flux and Stress
0.80	0.0250	0.21350	21231.56	4532.93806
0.90	0.0200	0.18090	26976.99	4880.137491
1.00	0.0150	0.13910	34639.58	4818.365578
1.10	0.0100	0.08682	43920.44	3813.172601
1.15	0.0075	0.05776	47899.13	2766.653749
1.20	0.0050	0.02879	62047.88	1786.358465
1.22	0.0040	0.01865	77073.61	1437.422827

n=0.5 K=5000 no Slip

Clearance Value (m)	Actual Clearance* (m)	Flux (kg/s)	Av. Stress Mag. (Pa)	Product of Flux and Stress
0.80	0.0250	0.22320	10967.94	2448.044208
0.90	0.0200	0.19180	14101.8	2704.72524
1.00	0.0150	0.15340	18499.61	2837.840174
1.10	0.0100	0.103	25016.8	2576.7304
1.15	0.0075	0.07108	28585.11	2031.829619
1.20	0.0050	0.03725	33389.39	1243.754778
1.22	0.0040	0.02396	41861.25	1002.99555

n=0.5 K=1000 - Beta = 1*e-6 Slip

Clearance Value (m)	Actual Clearance* (m)	Flux (kg/s)	Av. Stress Mag. (Pa)	Product of Flux and Stress
0.80	0.0250	0.23520	2166.400	509.53728
0.90	0.0200	0.20580	2778.736	571.8638688
1.00	0.0150	0.17020	3650.120	621.250424
1.10	0.0100	0.12460	5107.941	636.4494486
1.15	0.0075	0.09574	6275.483	600.8147424
1.20	0.0050	0.06029	7964.963	480.2076193
1.22	0.0040	0.04025	9054.269	364.4343273

n=0.5 K=1000 - Beta = 1*e-5 Slip

Clearance Value (m)	Actual Clearance* (m)	Flux (kg/s)	Av. Stress Mag. (Pa)	Product of Flux and Stress
0.80	0.0250	0.23680	1451.595	343.737696
0.90	0.0200	0.20760	1908.335	396.170346
1.00	0.0150	0.17240	2519.783	434.4105892
1.10	0.0100	0.12760	3594.395	458.644802
1.15	0.0075	0.09931	4432.185	440.1602924
1.20	0.0050	0.06470	5522.748	357.3217956
1.22	0.0040	0.04395	6374.659	280.1662631

n=0.5 K=1000 - Beta = 5*e-5 Slip

Clearance Value (m)	Actual Clearance* (m)	Flux (kg/s)	Av. Stress Mag. (Pa)	Product of Flux and Stress
0.80	0.0250	0.23850	955.454	227.8758267
0.90	0.0200	0.20970	1173.318	246.0447846
1.00	0.0150	0.17520	1432.623	250.9955496
1.10	0.0100	0.13140	1826.268	239.9716152
1.15	0.0075	0.10390	2109.012	219.1263468
1.20	0.0050	0.07024	2320.128	162.9657907
1.22	0.0040	0.04872	2635.891	128.4206095

n=0.5 K=1000 - Full Slip

Clearance Value (m)	Actual Clearance* (m)	Flux (kg/s)	Av. Stress Mag. (Pa)	Product of Flux and Stress
0.80	0.0250	0.23920	1039.166	248.5685072
0.90	0.0200	0.21070	1234.091	260.0229737
1.00	0.0150	0.17640	1456.086	256.8535704
1.10	0.0100	0.13310	1724.520	229.533612
1.15	0.0075	0.10620	1898.596	201.6308952
1.20	0.0050	0.07270	2020.58	146.896166
1.22	0.0040	0.05037	2038.174	102.6628244

Data for different geometry scales

* =(Chamber Radius = 1.3metres) – 'clearance') * (**Scale Factor**))

n = 0.5 - K = 1000 - 'landwidth' = 70 deg - 'separation' =2.7 m - rotor speed = 3.414 rad/s - for all simulations

Scale Factor = 0.04

Clearance Value (m)	Actual Clearance* (m)	Flux (kg/s)	Av. Stress Mag. (Pa)	Product of Flux and Stress
0.80	0.0200	0.11920	2302.271	274.4307032
0.90	0.0160	0.10390	2919.422	303.3279458
1.00	0.0120	0.08539	3805.878	324.9839224
1.10	0.0080	0.06150	5370.222	330.268653
1.15	0.0060	0.04646	6559.073	304.7345316
1.20	0.0040	0.02830	8044.103	227.6481149
1.22	0.0032	0.01848	9355.237	172.8847798

Scale Factor = 0.03

Clearance Value (m)	Actual Clearance* (m)	Flux (kg/s)	Av. Stress Mag. (Pa)	Product of Flux and Stress
0.80	0.0150	0.0497500	2273.836	113.123341
0.90	0.0120	0.0431700	2907.565	125.5195811
1.00	0.0090	0.0351100	3839.258	134.7963484
1.10	0.0060	0.0246300	5304.191	130.6422243
1.15	0.0045	0.0179300	6366.908	114.1586604
1.20	0.0030	0.0100700	7419.101	74.71034707
1.22	0.0024	0.0065540	8992.054	58.93392192

Scale Factor = 0.02

Clearance Value (m)	Actual Clearance* (m)	Flux (kg/s)	Av. Stress Mag. (Pa)	Product of Flux and Stress
0.80	0.0100	0.0141100	2157.727	30.44552797
0.90	0.0080	0.0120600	2784.154	33.57689724
1.00	0.0060	0.0095510	3627.876	34.64984368
1.10	0.0040	0.0062820	4830.429	30.34475498
1.15	0.0030	0.0042590	5403.770	23.01465643
1.20	0.0020	0.0021500	6473.333	13.91766595
1.22	0.0016	0.0013840	8079.118	11.18149931

Scale Factor = 0.01

Clearance Value (m)	Actual Clearance* (m)	Flux (kg/s)	Av. Stress Mag. (Pa)	Product of Flux and Stress
0.80	0.0050	0.0015820	1931.203	3.055163146
0.90	0.0040	0.0012960	2371.465	3.07341864
1.00	0.0030	0.0009592	2880.943	2.763400526
1.10	0.0020	0.0005696	3430.864	1.954220134
1.15	0.0015	0.0003712	4057.333	1.50608201
1.20	0.0010	0.0001819	5892.860	1.071911234
1.22	0.0008	0.0001240	7400.514	0.917663736

Scale Factor = 0.005

Clearance Value (m)	Actual Clearance* (m)	Flux (kg/s)	Av. Stress Mag. (Pa)	Product of Flux and Stress
0.80	0.0025	0.0001769	1578.376	0.279214714
0.90	0.0020	0.0001409	1886.908	0.265865337
1.00	0.0015	0.0001022	2338.410	0.238985502
1.10	0.0010	0.0000614	3255.813	0.199776686
1.15	0.0008	0.0000430	4135.075	0.177808225
1.20	0.0005	0.0000261	5820.422	0.152029423
1.22	0.0004	0.0000174	7676.669	0.133497274

References for Appendices

[i] Danckwerts P.V., Appl. Sci. Res., A3, 279 (1952).

[ii] Manas-Zloczower I., Tadmor Z., Mixing and Compounding of Polymers: Theory and Practice, p.4, Hanser, (1994) Munich.

[iii] Manas-Zloczower I., Tadmor Z., Mixing and Compounding of Polymers: Theory and Practice, p.5 Hanser, (1994) Munich.

[iv] Manas-Zloczower I., Tadmor Z., Mixing and Compounding of Polymers: Theory and Practice, p.5 Hanser, (1994) Munich.

[v] Private communication from Polyflow, Polyflow SA., Place de l'Universite 16, Louvain-la-Neuve, Belgium

[vi] Theoretical Background, p.9, Version 3.5.0, Polyflow SA., Place de l'Universite 16, Louvain-la-Neuve, Belgium

[vii] Reference manual, p.8, Version 3.5.0, Polyflow SA., Place de l'Universite 16, Louvain-la-Neuve, Belgium